



**UCGE Reports
Number 20198**

Department of Geomatics Engineering

**Ionosphere Tomographic Modeling and Applications
Using Global Positioning System (GPS) Measurements**

(URL: <http://www.geomatics.ucalgary.ca/links/GradTheses.html>)

by

Zhizhao Liu

June 2004



**UNIVERSITY OF
CALGARY**

UNIVERSITY OF CALGARY

**Ionosphere Tomographic Modeling and Applications Using
Global Positioning System (GPS) Measurements**

by

Zhizhao Liu

A THESIS

SUBMITTED TO THE FACULTY OF GRADUATE STUDIES
IN PARTIAL FULFILMENT OF THE REQUIREMENTS FOR THE
DEGREE OF DOCTOR OF PHILOSOPHY

DEPARTMENT OF GEOMATICS ENGINEERING

CALGARY, ALBERTA

June, 2004

© Zhizhao Liu 2004

Abstract

Precise ionosphere modeling is crucial and remains as a challenge for GPS positioning and navigation as well as many other Earth Observation Systems. This research develops and analyzes a new ionospheric modeling system based on a multiple-layer tomographic technique using spherical harmonic functions and empirical orthogonal functions in combination with Kalman filter estimator to perform real-time ionospheric modeling and perform ionospheric TEC predictions. A close form expression that links the smoothed TEC measurements and the tomographic model has been developed, which allows the simultaneous execution of TEC smoothing and model estimation and ionospheric TEC prediction. This system is feasible for real-time implementation to generate TEC predictions to support real-time GPS positioning and other real-time applications. In order to assess the accuracies of the ionospheric TEC prediction data, three quantitative indicators are proposed to evaluate the prediction performance. The tomographic model proposed in this research is function-based, which is computationally more efficient than tomographic models that are based on voxel concept and overcomes the limitations associated with single-layer ionospheric models.

Comprehensive data analyses have been conducted to assess the model using data from different types of GPS networks and acquired under both ionosphere quiet and disturbed conditions. The model performance has been assessed using different elevation angles and prediction intervals. The numerical results at the independent user station show that over a local area GPS network using an elevation cutoff of 15° , the vertical TEC data predicted at 5-min or 10-min interval have an accuracy of 3.5~4.3 TECU during ionospheric quiet time period. An accuracy of 5.9 TECU can be obtained using a 30-min prediction interval. Over a wide area GPS network using an elevation cutoff of 15° , the 5-min and 10-min VTEC predictions have an accuracy about 5.0~5.8 TECU and the 30-min predictions about 5.5~5.9 TECU during ionospheric quiet day. During ionospheric disturbed day, the 5-min and 10-min VTEC predictions have an accuracy about 5.2~6.1

TECU and the vertical TEC prediction accuracy is about 5.8~6.7 TECU using a 30-min prediction interval.

Acknowledgements

I would like to thank my supervisor Dr. Yang Gao for the guidance and support throughout my graduate studies. His door is always open to me for a discussion. I am grateful for the freedom, encouragement, understanding and patience Dr. Gao has given to me which allow me to enjoy the research and study during the years. I am very grateful for Dr. Klaus-Peter Schwarz who initially gave me the opportunity to study at the University of Calgary.

My sincere appreciation and gratitude also go to Dr. Gérard Lachapelle, Dr. Susan Skone, Dr. Naser El-Sheimy in the Department of Geomatics Engineering and Dr. David Irvine-Halliday from the Department of Electrical and Computer Engineering for their various helps and supports to me throughout the years. Two other examiners are Dr. A. O. Fapojuwo and Dr. A. Bruton. They are greatly thanked for their service in the committee.

Meanwhile, I also would like to thank the members in the group of Positioning and Mobile Information Systems for creating a nice research environment and sharing the thoughts through the discussions. I also thank a lot of my friends for their great helps during my living and studies in Calgary including Dr. Yong Hu, Dr. Zhiling Fei, Mr. Zhe Liu, Dr. Quanke Wang, Mr. Wuji Yang, Dr. Chaowei Yang and Dr. Qiaoping Zhang, to name a few.

Last but not least, I am deeply in debit to my parents who always back up me since my first day in school. I cannot express my gratitude to them in my describable words. I thank my dear wife, Mrs. Jiehong Chen, for her constant understanding and support, especially in the difficult time.

The supports from NSERC strategic grant, J.B. Hyne Research Innovation Award (UC 2003), KIS-94 Graduate Scholarship (UC 2003, donated by Drs. Elizabeth Cannon and Gérard Lachapelle), Graduate Student Chapter Award (ION 2003), Student Competition Paper Award (ION 2003), Graduate Research Scholarships (Dept. of Geomatics Eng. 2001 & 2002), The PCI Best Paper Award (GEOIDE 2002) and several travel grants from the Department, GEOIDE and the University are very appreciated.

Table of Contents

Approval Page	ii
Abstract.....	iii
Acknowledgements	v
Table of Contents	vi
List of Tables	xii
List of Figures.....	xv
List of Symbols	xxxii
List of Abbreviations	xxxvi
CHAPTER 1 INTRODUCTION	1
1.1 BACKGROUND	1
1.2 OBJECTIVES AND CONTRIBUTIONS	3
1.3 OUTLINES.....	5
CHAPTER 2 OVERVIEW OF GLOBAL POSITIONING SYSTEM	7
2.1 GPS COMPONENTS.....	7
2.1.1 <i>Space segment</i>	8
2.1.2 <i>Ground control segment</i>	8
2.1.3 <i>User segment</i>	9
2.2 GPS OBSERVABLES	9
2.3 GPS REFERENCE SYSTEM AND TIME STANDARD	10
2.4 GPS ERROR SOURCES	10
2.4.1 <i>Orbit error</i>	12
2.4.2 <i>Satellite clock error</i>	12
2.4.3 <i>Ionosphere error</i>	13
2.4.4 <i>Troposphere error</i>	14
2.4.5 <i>Receiver clock error</i>	15
2.4.6 <i>Multipath error</i>	16

2.4.7 Receiver noise	16
2.5 IONOSPHERIC EFFECTS ON GPS SIGNALS	17
2.5.1 The ionospheric storm effect.....	17
2.5.2 The scintillation effect.....	18
CHAPTER 3 IONOSPHERE AND ITS MEASUREMENTS	20
3.1 FORMATION OF IONOSPHERE.....	20
3.2 STRATIFICATION OF IONOSPHERE.....	22
3.2.1 D-region.....	23
3.2.2 E-region	24
3.2.3 F-region	24
3.3 SOLAR ACTIVITIES AND SPACE ENVIRONMENT	25
3.3.1 Solar radiation and energetic particles	25
3.3.2 Magnetic field	26
3.3.3 The plasma.....	27
3.4 IONOSPHERE PHENOMENA AND SOLAR ACTIVITIES	29
3.5 VARIOUS TEC MEASURING TECHNIQUES	32
3.5.1 Ionosonde	32
3.5.2 Incoherent scatter radar	34
3.5.3 Dual frequency GPS receivers.....	34
3.6 IMPACTS OF IONOSPHERE	35
3.6.1 The impact on GPS/GNSS.....	35
3.6.2 The impact on other systems.....	36
CHAPTER 4 IONOSPHERE TOMOGRAPHIC MODELING	37
4.1 CONCEPT OF IONOSPHERE MODELING.....	37
4.2 OVERVIEW OF 2D MODELS AND LIMITATIONS.....	38
4.2.1 Broadcast model	39
4.2.2 Grid model	40
4.2.3 Polynomial function model	41

4.3 OVERVIEW OF OTHER MODELS BASED ON TOMOGRAPHY AND LIMITATIONS	44
4.4 DEVELOPMENT OF THE IONOSPHERE TOMOGRAPHIC MODELING METHOD	50
4.4.1 TEC observations.....	54
4.4.2 TEC smoothed by carrier phase measurements.....	60
4.4.3 Tomographic model development.....	66
4.5 IONOSPHERE TOMOGRAPHIC MODEL PARAMETER ESTIMATION	74
4.6 IONOSPHERIC TEC PREDICTION AND EVALUATION.....	82
4.6.1 Evaluation indicator one: vertical TEC error	84
4.6.2 Evaluation indicator two: relative error.....	86
4.6.3 Evaluation indicator three: recovering efficiency	87
4.7 SOFTWARE DEVELOPMENT AND IMPLEMENTATION	88
4.8 ADVANTAGES OF TOMOGRAPHIC MODELING.....	91
4.9 APPLICATIONS OF IONOSPHERE TOMOGRAPHIC MODELING.....	92
4.9.1 Single frequency GPS receiver positioning and navigation	93
4.9.2 Other space-based Earth observation systems (EOS)	93
4.9.3 Radio frequency selection	94
4.9.4 Space weather research.....	94
CHAPTER 5 IONOSPHERE TOMOGRAPHIC MODELING OVER A LOCAL	
AREA GPS REFERENCE NETWORK	96
5.1 TOMOGRAPHIC MODELING WITH A LOCAL AREA GPS NETWORK.....	97
5.2 DATA DESCRIPTION	98
5.3 DATA ANALYSIS STRATEGY.....	100
5.4 IMPACTS OF VARIOUS PARAMETERS	101
5.4.1 Prediction interval	101
5.4.2 Elevation cutoff angle.....	102
5.5 DATA ANALYSIS AND RESULTS.....	103
5.5.1 Results of low elevation cutoff angle (15°).....	103
5.5.1.1 Results of Scheme 1 (15°, 5 min)	103
5.5.1.2 Results of Scheme 2 (15°, 10 min)	108

5.5.1.3 Results of Scheme 3 (15°, 30 min)	112
5.5.2 <i>Results of medium elevation cutoff angle (20°)</i>	116
5.5.2.1 Results of Scheme 4 (20°, 5 min)	116
5.5.2.2 Results of Scheme 5 (20°, 10 min)	118
5.5.2.3 Results of Scheme 6 (20°, 30 min)	120
5.5.3 <i>Results of high elevation cutoff angle (25°)</i>	122
5.5.3.1 Results of Scheme 7 (25°, 5 min)	122
5.5.3.2 Results of Scheme 8 (25°, 10 min)	125
5.5.3.3 Results of Scheme 9 (25°, 30 min)	127
5.6 APPLICATION OF PREDICTED IONOSPHERIC TEC CORRECTIONS TO SPP	130
5.6.1 <i>SPP results using 5-min TEC predictions</i>	131
5.6.2 <i>SPP results using 10-min TEC predictions</i>	137
5.6.3 <i>SPP results using 30-min TEC predictions</i>	141

CHAPTER 6 IONOSPHERE TOMOGRAPHIC MODELING OVER A WIDE

AREA GPS REFERENCE NETWORK146

6.1 DATA DESCRIPTION	147
6.2 DATA ANALYSIS STRATEGY	151
6.3 DATA ANALYSIS AND RESULTS	153
6.3.1 <i>Results of low elevation cutoff angle (15°)</i>	155
6.3.1.1 Results of Scheme 1 (15°, 5 min)	155
6.3.1.1.1 Results on ionosphere quiet day DOY 089	156
6.3.1.1.2 Results on ionosphere disturbed day DOY 090	163
6.3.1.2 Results of Scheme 2 (15°, 10 min)	169
6.3.1.2.1 Results on ionosphere quiet day DOY 089	169
6.3.1.2.2 Results on ionosphere disturbed day DOY 090	175
6.3.1.3 Results of Scheme 3 (15°, 30 min)	182
6.3.1.3.1 Results on ionosphere quiet day DOY 089	182
6.3.1.3.2 Results on ionosphere disturbed day DOY 090	188
6.3.2 <i>Results of medium elevation cutoff angle (20°)</i>	194

6.3.2.1 Results of Scheme 4 (20°, 5 min)	194
6.3.2.1.1 Results on ionosphere quiet day DOY 089	194
6.3.2.1.2 Results on ionosphere disturbed day DOY 090	198
6.3.2.2 Results of Scheme 5 (20°, 10 min)	202
6.3.2.2.1 Results on ionosphere quiet day DOY 089	202
6.3.2.2.2 Results on ionosphere disturbed day DOY 090	205
6.3.2.3 Results of Scheme 6 (20°, 30 min)	209
6.3.2.3.1 Results on ionosphere quiet day DOY 089	209
6.3.2.3.2 Results on ionosphere disturbed day DOY 090	213
6.3.3 Results of high elevation cutoff angle (25°).....	217
6.3.3.1 Results of Scheme 7 (25°, 5 min)	217
6.3.3.1.1 Results on ionosphere quiet day DOY 089	217
6.3.3.1.2 Results on ionosphere disturbed day DOY 090	220
6.3.3.2 Results of Scheme 8 (25°, 10 min)	224
6.3.3.2.1 Results on ionosphere quiet day DOY 089	224
6.3.3.2.2 Results on ionosphere disturbed day DOY 090	228
6.3.3.3 Results of Scheme 9 (25°, 30 min)	232
6.3.3.3.1 Results on ionosphere quiet day DOY 089	232
6.3.3.3.2 Results on ionosphere disturbed day DOY 090	235
6.3.4 Summary.....	239
6.3.5 SPP results.....	241
6.3.5.1 SPP results on DOY 089	242
6.3.5.1.1 Use of 5-min TEC Prediction	242
6.3.5.1.2 Use of 10-min TEC Prediction	249
6.3.5.1.3 Use of 30-min TEC Prediction	254
6.3.5.2 SPP results on DOY 090	260
6.3.5.2.1 Use of 5-min TEC Prediction	261
6.3.5.2.2 Use of 10-min TEC Prediction	267
6.3.5.2.3 Use of 30-min TEC Prediction	272

6.3.5.3 Summary	278
CHAPTER 7 CONCLUSIONS AND RECOMMENDATIONS	281
7.1 CONCLUSIONS	281
7.2 RECOMMENDATIONS	286
REFERENCES	288

List of Tables

Table 2.1 Approximate GPS Satellite Parameters	8
Table 2.2 GPS Error Source Budget (Skone, 1998)	11
Table 5.1 GPS Station Coordinates of the Local Area GPS Network	99
Table 5.2 GPS Receiver and Antenna Types	99
Table 5.3 Baseline Lengths in the Local Area GPS Network (km)	100
Table 5.4 Data Analysis Schemes.....	102
Table 5.5 Error Statistics for 5-min VTEC Prediction with Cutoff 15° on DOY 136....	105
Table 5.6 Error Statistics for 10-min VTEC Prediction with Cutoff 15° on DOY 136..	110
Table 5.7 Error Statistics for 30-min VTEC Prediction with Cutoff 15° on DOY 136..	114
Table 5.8 Error Statistics for 5-min VTEC Prediction with Cutoff 20° on DOY 136....	118
Table 5.9 Error Statistics for 10-min VTEC Prediction with Cutoff 20° on DOY 136..	119
Table 5.10 Error Statistics for 30-min VTEC Prediction with Cutoff 20° on DOY 136	122
Table 5.11 Error Statistics for 5-min VTEC Prediction with Cutoff 25° on DOY 136..	125
Table 5.12 Error Statistics for 10-min VTEC Prediction with Cutoff 25° on DOY 136	127
Table 5.13 Error Statistics for 30-min VTEC Prediction with Cutoff 25° on DOY 136	130
Table 5.14 Single-frequency Single Point Positioning RMS Error at 6 Stations Using Tomographic Corrections Predicted at 15° and 5- min Interval (m)	134
Table 5.15 Ionospheric Recovering Efficiency of 5- min TEC Predictions	136
Table 5.16 Single-frequency Single Point Positioning RMS Error at 6 Stations Using Tomographic Corrections Predicted at 15° and 10- min Interval (m)	139
Table 5.17 Ionospheric Recovering Efficiency of 10- min TEC Predictions	140
Table 5.18 Single-frequency Single Point Positioning RMS Error at 6 Stations Using Tomographic Corrections Predicted at 15° and 30- min Interval (m)	143
Table 5.19 Ionospheric Recovering Efficiency of 30- min TEC Predictions	144
Table 6.1 Coordinates of GPS Station in Wide Area GPS Reference Network	147
Table 6.2 Baseline Distances between GPS Stations in GPS Network (km)	150
Table 6.3 GPS Receive and Antenna Types	151

Table 6.4 Error Statistics for 5-min VTEC Prediction with Cutoff 15° on DOY 089....	159
Table 6.5 Error Statistics for 5-min VTEC Prediction with Cutoff 15° on DOY 090....	165
Table 6.6 Error Statistics for 10-min VTEC Prediction with Cutoff 15° on DOY 089..	172
Table 6.7 Error Statistics for 10-min VTEC Prediction with Cutoff 15° on DOY 090..	179
Table 6.8 Error Statistics for 30-min VTEC Prediction with Cutoff 15° on DOY 089..	185
Table 6.9 Error Statistics for 30-min VTEC Prediction with Cutoff 15° on DOY 090..	191
Table 6.10 Error Statistics for 5-min VTEC Prediction with Cutoff 20° on DOY 089..	198
Table 6.11 Error Statistics for 5-min VTEC Prediction with Cutoff 20° on DOY 090..	201
Table 6.12 Error Statistics for 10-min VTEC Prediction with Cutoff 20° on DOY 089	205
Table 6.13 Error Statistics for 10-min VTEC Prediction with Cutoff 20° on DOY 090	209
Table 6.14 Error Statistics for 30-min VTEC Prediction with Cutoff 20° on DOY 089	212
Table 6.15 Error Statistics for 30-min VTEC Prediction with Cutoff 20° on DOY 090	216
Table 6.16 Error Statistics for 5-min VTEC Prediction with Cutoff 25° on DOY 089..	220
Table 6.17 Error Statistics for 5-min VTEC Prediction with Cutoff 25° on DOY 090..	224
Table 6.18 Error Statistics for 10-min VTEC Prediction with Cutoff 25° on DOY 089	227
Table 6.19 Error Statistics for 10-min VTEC Prediction with Cutoff 25° on DOY 090	231
Table 6.20 Error Statistics for 30-min VTEC Prediction with Cutoff 25° on DOY 089	235
Table 6.21 Error Statistics for 30-min VTEC Prediction with Cutoff 25° on DOY 090	238
Table 6.22 VTEC Prediction Accuracy Statistics for All Schemes on DOY 089	239
Table 6.23 STEC Prediction Relative Error Statistics for All Schemes on DOY 089.....	239
Table 6.24 VTEC Prediction Accuracy Statistics for All Schemes on DOY 090	240
Table 6.25 STEC Prediction Relative Error Statistics for All Schemes on DOY 090.....	240
Table 6.26 Single-frequency Single Point Positioning RMS Error at 6 Stations Using Tomographic Corrections Predicted at 15° and 5- min Interval (m)	246
Table 6.27 Ionospheric Recovering Efficiency of 5- min TEC Predictions	248
Table 6.28 Single-frequency Single Point Positioning RMS Error at 6 Stations Using Tomographic Corrections Predicted at 15° and 10- min Interval (m)	252
Table 6.29 Ionospheric Recovering Efficiency of 10- min TEC Predictions	252

Table 6.30 Single-frequency Single Point Positioning RMS Error at 6 Stations Using Tomographic Corrections Predicted at 15° and 30-min Interval (m)	258
Table 6.31 Ionospheric Recovering Efficiency of 30-min TEC Predictions	258
Table 6.32 Single-frequency Single Point Positioning RMS Error at 6 Stations Using Tomographic Corrections Predicted at 15° and 5-min Interval (m)	264
Table 6.33 Ionospheric Recovering Efficiency of 5-min TEC Predictions	265
Table 6.34 Single-frequency Single Point Positioning RMS Error at 6 Stations Using Tomographic Corrections Predicted at 15° and 10-min Interval (m)	270
Table 6.35 Ionospheric Recovering Efficiency of 10-min TEC Predictions	270
Table 6.36 Single-frequency Single Point Positioning RMS Error at 6 Stations Using Tomographic Corrections Predicted at 15° and 30-min Interval (m)	275
Table 6.37 Ionospheric Recovering Efficiency of 30-min TEC Predictions	276
Table 6.38 Summary of Recovering Efficiency for DOY 089 and 090	278
Table 6.39 Summary of Recovering Efficiency for DRAO and DAM2 Predictions	280

List of Figures

Figure 3.1 Illustration of Ionization Process (From NRL, 2003)	21
Figure 3.2 Atmosphere and Ionospheric Multiple Layers	22
Figure 3.3 Electron Density and Temperature Profiles (From ION, 2004)	23
Figure 3.4 Earth's Magnetic Field Encountering Solar Wind (From UTK, 2003a)	26
Figure 3.5 Spiraling Motion of Charged Particles in Geomagnetic Field (From UTK, 2003b) ...	29
Figure 4.1 Illustration of Ionospheric TEC Observation in GPS Network	54
Figure 4.2 Electron Density Profile Obtained from IRI90 Model.....	70
Figure 4.3 EOF #1 Derived from Electron Density Profiles	71
Figure 4.4 EOF #2 Derived from Electron Density Profiles	71
Figure 4.5 EOF #3 Derived from Electron Density Profiles	71
Figure 4.6 Configuration File Used in IonoTomo	89
Figure 4.7 Ionospheric TEC Prediction Results from IonoTomo	90
Figure 5.1 GPS Station Distribution of the Local Area GPS Network.....	98
Figure 5.2 Geomagnetic Kp Index Values on May 15, 2000	100
Figure 5.3 Comparison of Observed and Predicted TEC for PRN 02 at SPK1 Station on DOY 136 at 15° Cutoff and 5-min Prediction Interval.....	104
Figure 5.4 Comparison of Observed and Predicted TEC for PRN 02 at LEEP Station on DOY 136 at 15° Cutoff and 5-min Prediction Interval.....	104
Figure 5.5 Comparison of Observed and Predicted TEC for PRN 02 at CIT1 Station on DOY 136 at 15° Cutoff and 5-min Prediction Interval.....	104
Figure 5.6 Comparison of Observed and Predicted TEC for PRN 19 at LEEP Station on DOY 136 at 15° Cutoff and 5-min Prediction Interval.....	107
Figure 5.7 Comparison of Observed and Predicted TEC for PRN 02 at LEEP Station on DOY 136 at 15° Cutoff and 5-min Prediction Interval.....	107
Figure 5.8 Comparison of Observed and Predicted TEC for PRN 02 at SPK1 Station on DOY 136 at 15° Cutoff and 10-min Prediction Interval.....	109

Figure 5.9 Comparison of Observed and Predicted TEC for PRN 02 at LEEP Station on DOY 136 at 15° Cutoff and 10-min Prediction Interval.....	109
Figure 5.10 Comparison of Observed and Predicted TEC for PRN 02 at CIT1 Station on DOY 136 at 15° Cutoff and 10-min Prediction Interval.....	110
Figure 5.11 Comparison of Observed and Predicted TEC for PRN 19 at LEEP Station on DOY 136 at 15° Cutoff and 10-min Prediction Interval.....	111
Figure 5.12 Comparison of Observed and Predicted TEC for PRN 02 at LEEP Station on DOY 136 at 15° Cutoff and 10-min Prediction Interval.....	111
Figure 5.13 Comparison of Observed and Predicted TEC for PRN 02 at SPK1 Station on DOY 136 at 15° Cutoff and 30-min Prediction Interval.....	112
Figure 5.14 Comparison of Observed and Predicted TEC for PRN 02 at LEEP Station on DOY 136 at 15° Cutoff and 30-min Prediction Interval.....	113
Figure 5.15 Comparison of Observed and Predicted TEC for PRN 02 at CIT1 Station on DOY 136 at 15° Cutoff and 30-min Prediction Interval.....	113
Figure 5.16 Comparison of Observed and Predicted TEC for PRN 19 at LEEP Station on DOY 136 at 15° Cutoff and 30-min Prediction Interval.....	114
Figure 5.17 Comparison of Observed and Predicted TEC for PRN 02 at LEEP Station on DOY 136 at 15° Cutoff and 30-min Prediction Interval.....	115
Figure 5.18 Comparison of Observed and Predicted TEC for PRN 02 at SPK1 Station on DOY 136 at 20° Cutoff and 5-min Prediction Interval.....	116
Figure 5.19 Comparison of Observed and Predicted TEC for PRN 02 at LEEP Station on DOY 136 at 20° Cutoff and 5-min Prediction Interval.....	116
Figure 5.20 Comparison of Observed and Predicted TEC for PRN 02 at CIT1 Station on DOY 136 at 20° Cutoff and 5-min Prediction Interval.....	117
Figure 5.21 Comparison of Observed and Predicted TEC for PRN 02 at SPK1 Station on DOY 136 at 20° Cutoff and 10-min Prediction Interval.....	118
Figure 5.22 Comparison of Observed and Predicted TEC for PRN 02 at LEEP Station on DOY 136 at 20° Cutoff and 10-min Prediction Interval.....	119

Figure 5.23 Comparison of Observed and Predicted TEC for PRN 02 at CIT1 Station on DOY 136 at 20° Cutoff and 10-min Prediction Interval.....	119
Figure 5.24 Comparison of Observed and Predicted TEC for PRN 02 at SPK1 Station on DOY 136 at 20° Cutoff and 30-min Prediction Interval.....	121
Figure 5.25 Comparison of Observed and Predicted TEC for PRN 02 at LEEP Station on DOY 136 at 20° Cutoff and 30-min Prediction Interval.....	121
Figure 5.26 Comparison of Observed and Predicted TEC for PRN 02 at CIT1 Station on DOY 136 at 20° Cutoff and 30-min Prediction Interval.....	121
Figure 5.27 Comparison of Observed and Predicted TEC for PRN 02 at SPK1 Station on DOY 136 at 25° Cutoff and 5-min Prediction Interval.....	124
Figure 5.28 Comparison of Observed and Predicted TEC for PRN 02 at LEEP Station on DOY 136 at 25° Cutoff and 5-min Prediction Interval.....	124
Figure 5.29 Comparison of Observed and Predicted TEC for PRN 02 at CIT1 Station on DOY 136 at 25° Cutoff and 5-min Prediction Interval.....	124
Figure 5.30 Comparison of Observed and Predicted TEC for PRN 02 at SPK1 Station on DOY 136 at 25° Cutoff and 10-min Prediction Interval.....	126
Figure 5.31 Comparison of Observed and Predicted TEC for PRN 02 at LEEP Station on DOY 136 at 25° Cutoff and 10-min Prediction Interval.....	126
Figure 5.32 Comparison of Observed and Predicted TEC for PRN 02 at CIT1 Station on DOY 136 at 25° Cutoff and 10-min Prediction Interval.....	127
Figure 5.33 Comparison of Observed and Predicted TEC for PRN 02 at SPK1 Station on DOY 136 at 25° Cutoff and 30-min Prediction Interval.....	129
Figure 5.34 Comparison of Observed and Predicted TEC for PRN 02 at LEEP Station on DOY 136 at 25° Cutoff and 30-min Prediction Interval.....	129
Figure 5.35 Comparison of Observed and Predicted TEC for PRN 02 at CIT1 Station on DOY 136 at 25° Cutoff and 30-min Prediction Interval.....	129
Figure 5.36 Positioning Error at SPK1 Station Using Three Ionospheric Models, Tomographic Correction Predicted at 15° and 5-min Interval.....	132

Figure 5.37 Positioning Error at LEEP Station Using Three Ionospheric Models, Tomographic Correction Predicted at 15° and 5-min Interval.....	133
Figure 5.38 Positioning Error at CIT1 Station Using Three Ionospheric Models, Tomographic Correction Predicted at 15° and 5-min Interval.....	133
Figure 5.39 Positioning Error at LEEP Station Using Three Ionospheric Models, Tomographic Correction Predicted at 15° and 5-min Interval.....	137
Figure 5.40 Positioning Error at SPK1 Station Using Three Ionospheric Models, Tomographic Correction Predicted at 15° and 10-min Interval.....	138
Figure 5.41 Positioning Error at LEEP Station Using Three Ionospheric Models, Tomographic Correction Predicted at 15° and 10-min Interval.....	138
Figure 5.42 Positioning Error at CIT1 Station Using Three Ionospheric Models, Tomographic Correction Predicted at 15° and 10-min Interval.....	138
Figure 5.43 Positioning Error at LEEP Station Using Three Ionospheric Models, Tomographic Correction Predicted at 15° and 10-min Interval.....	141
Figure 5.44 Positioning Error at SPK1 Station Using Three Ionospheric Models, Tomographic Correction Predicted at 15° and 30-min Interval.....	142
Figure 5.45 Positioning Error at LEEP Station Using Three Ionospheric Models, Tomographic Correction Predicted at 15° and 30-min Interval.....	142
Figure 5.46 Positioning Error at CIT1 Station Using Three Ionospheric Models, Tomographic Correction Predicted at 15° and 30-min Interval.....	142
Figure 5.47 Positioning Error at LEEP Station Using Three Ionospheric Models, Tomographic Correction Predicted at 15° and 30-min Interval.....	145
Figure 6.1 GPS Station Distribution within Wide Area GPS Reference Network	148
Figure 6.2 Geomagnetic Kp Index Values during March 30-31, 2001	148
Figure 6.3 Comparison of Satellite Biases on DOY 089.....	154
Figure 6.4 Comparison of Satellite Biases on DOY 090	154
Figure 6.5 Comparison of Receiver Biases for DOY 089 and 090	155
Figure 6.6 Comparison of Observed and Predicted TEC for PRN 02 at CARR Station on DOY 089 at 15° Cutoff and 5-min Prediction Interval.....	157

Figure 6.7 Comparison of Observed and Predicted TEC for PRN 02 at COSO Station on DOY 089 at 15° Cutoff and 5-min Prediction Interval.....	157
Figure 6.8 Comparison of Observed and Predicted TEC for PRN 03 at AMC2 Station on DOY 089 at 15° Cutoff and 5-min Prediction Interval.....	157
Figure 6.9 Comparison of Observed and Predicted TEC for PRN 03 at CASP Station on DOY 089 at 15° Cutoff and 5-min Prediction Interval.....	158
Figure 6.10 Comparison of Observed and Predicted TEC for PRN 31 at PRDS Station on DOY 089 at 15° Cutoff and 5-min Prediction Interval.....	158
Figure 6.11 Comparison of Observed and Predicted TEC for PRN 04 at FAIR Station on DOY 089 at 15° Cutoff and 5-min Prediction Interval.....	158
Figure 6.12 Comparison of Observed and Predicted TEC for PRN 31 at DRAO Station on DOY 089 at 15° Cutoff and 5-min Prediction Interval.....	160
Figure 6.13 Comparison of Observed and Predicted TEC for PRN 03 at DRAO Station on DOY 089 at 15° Cutoff and 5-min Prediction Interval.....	160
Figure 6.14 Comparison of Observed and Predicted TEC for PRN 02 at DAM2 Station on DOY 089 at 15° Cutoff and 5-min Prediction Interval.....	162
Figure 6.15 Comparison of Observed and Predicted TEC for PRN 27 at DAM2 Station on DOY 089 at 15° Cutoff and 5-min Prediction Interval.....	162
Figure 6.16 Comparison of Observed and Predicted TEC for PRN 02 at CARR Station on DOY 090 at 15° Cutoff and 5-min Prediction Interval.....	163
Figure 6.17 Comparison of Observed and Predicted TEC for PRN 02 at COSO Station on DOY 090 at 15° Cutoff and 5-min Prediction Interval.....	163
Figure 6.18 Comparison of Observed and Predicted TEC for PRN 03 at AMC2 Station on DOY 090 at 15° Cutoff and 5-min Prediction Interval.....	164
Figure 6.19 Comparison of Observed and Predicted TEC for PRN 03 at CASP Station on DOY 090 at 15° Cutoff and 5-min Prediction Interval.....	164
Figure 6.20 Comparison of Observed and Predicted TEC for PRN 31 at PRDS Station on DOY 090 at 15° Cutoff and 5-min Prediction Interval.....	164

Figure 6.21 Comparison of Observed and Predicted TEC for PRN 04 at FAIR Station on DOY 090 at 15° Cutoff and 5-min Prediction Interval.....	165
Figure 6.22 Comparison of Observed and Predicted TEC for PRN 31 at DRAO Station on DOY 090 at 15° Cutoff and 5-min Prediction Interval.....	167
Figure 6.23 Comparison of Observed and Predicted TEC for PRN 03 at DRAO Station on DOY 090 at 15° Cutoff and 5-min Prediction Interval.....	167
Figure 6.24 Comparison of Observed and Predicted TEC for PRN 02 at DAM2 Station on DOY 090 at 15° Cutoff and 5-min Prediction Interval.....	167
Figure 6.25 Comparison of Observed and Predicted TEC for PRN 17 at DAM2 Station on DOY 090 at 15° Cutoff and 5-min Prediction Interval.....	168
Figure 6.26 Comparison of Observed and Predicted TEC for PRN 02 at CARR Station on DOY 089 at 15° Cutoff and 10-min Prediction Interval.....	170
Figure 6.27 Comparison of Observed and Predicted TEC for PRN 02 at COSO Station on DOY 089 at 15° Cutoff and 10-min Prediction Interval.....	170
Figure 6.28 Comparison of Observed and Predicted TEC for PRN 03 at AMC2 Station on DOY 089 at 15° Cutoff and 10-min Prediction Interval.....	170
Figure 6.29 Comparison of Observed and Predicted TEC for PRN 03 at CASP Station on DOY 089 at 15° Cutoff and 10-min Prediction Interval.....	171
Figure 6.30 Comparison of Observed and Predicted TEC for PRN 31 at PRDS Station on DOY 089 at 15° Cutoff and 10-min Prediction Interval.....	171
Figure 6.31 Comparison of Observed and Predicted TEC for PRN 04 at FAIR Station on DOY 089 at 15° Cutoff and 10-min Prediction Interval.....	171
Figure 6.32 Comparison of Observed and Predicted TEC for PRN 31 at DRAO Station on DOY 089 at 15° Cutoff and 10-min Prediction Interval.....	174
Figure 6.33 Comparison of Observed and Predicted TEC for PRN 03 at DRAO Station on DOY 089 at 15° Cutoff and 10-min Prediction Interval.....	174
Figure 6.34 Comparison of Observed and Predicted TEC for PRN 02 at DAM2 Station on DOY 089 at 15° Cutoff and 10-min Prediction Interval.....	175

Figure 6.35 Comparison of Observed and Predicted TEC for PRN 27 at DAM2 Station on DOY 089 at 15° Cutoff and 10-min Prediction Interval.....	175
Figure 6.36 Comparison of Observed and Predicted TEC for PRN 02 at CARR Station on DOY 090 at 15° Cutoff and 10-min Prediction Interval.....	176
Figure 6.37 Comparison of Observed and Predicted TEC for PRN 02 at COSO Station on DOY 090 at 15° Cutoff and 10-min Prediction Interval.....	177
Figure 6.38 Comparison of Observed and Predicted TEC for PRN 03 at AMC2 Station on DOY 090 at 15° Cutoff and 10-min Prediction Interval.....	177
Figure 6.39 Comparison of Observed and Predicted TEC for PRN 03 at CASP Station on DOY 090 at 15° Cutoff and 10-min Prediction Interval.....	177
Figure 6.40 Comparison of Observed and Predicted TEC for PRN 31 at PRDS Station on DOY 090 at 15° Cutoff and 10-min Prediction Interval.....	178
Figure 6.41 Comparison of Observed and Predicted TEC for PRN 04 at FAIR Station on DOY 090 at 15° Cutoff and 10-min Prediction Interval.....	178
Figure 6.42 Comparison of Observed and Predicted TEC for PRN 31 at DRAO Station on DOY 090 at 15° Cutoff and 10-min Prediction Interval.....	180
Figure 6.43 Comparison of Observed and Predicted TEC for PRN 03 at DRAO Station on DOY 090 at 15° Cutoff and 10-min Prediction Interval.....	181
Figure 6.44 Comparison of Observed and Predicted TEC for PRN 02 at DAM2 Station on DOY 090 at 15° Cutoff and 10-min Prediction Interval.....	181
Figure 6.45 Comparison of Observed and Predicted TEC for PRN 17 at DAM2 Station on DOY 090 at 15° Cutoff and 10-min Prediction Interval.....	181
Figure 6.46 Comparison of Observed and Predicted TEC for PRN 02 at CARR Station on DOY 089 at 15° Cutoff and 30-min Prediction Interval.....	182
Figure 6.47 Comparison of Observed and Predicted TEC for PRN 02 at COSO Station on DOY 089 at 15° Cutoff and 30-min Prediction Interval.....	183
Figure 6.48 Comparison of Observed and Predicted TEC for PRN 03 at AMC2 Station on DOY 089 at 15° Cutoff and 30-min Prediction Interval.....	183

Figure 6.49 Comparison of Observed and Predicted TEC for PRN 03 at CASP Station on DOY 089 at 15° Cutoff and 30-min Prediction Interval.....	183
Figure 6.50 Comparison of Observed and Predicted TEC for PRN 31 at PRDS Station on DOY 089 at 15° Cutoff and 30-min Prediction Interval.....	184
Figure 6.51 Comparison of Observed and Predicted TEC for PRN 04 at FAIR Station on DOY 089 at 15° Cutoff and 30-min Prediction Interval.....	184
Figure 6.52 Comparison of Observed and Predicted TEC for PRN 31 at DRAO Station on DOY 089 at 15° Cutoff and 30-min Prediction Interval.....	187
Figure 6.53 Comparison of Observed and Predicted TEC for PRN 26 at DRAO Station on DOY 089 at 15° Cutoff and 30-min Prediction Interval.....	187
Figure 6.54 Comparison of Observed and Predicted TEC for PRN 02 at DAM2 Station on DOY 089 at 15° Cutoff and 30-min Prediction Interval.....	187
Figure 6.55 Comparison of Observed and Predicted TEC for PRN 31 at DAM2 Station on DOY 089 at 15° Cutoff and 30-min Prediction Interval.....	188
Figure 6.56 Comparison of Observed and Predicted TEC for PRN 02 at CARR Station on DOY 090 at 15° Cutoff and 30-min Prediction Interval.....	189
Figure 6.57 Comparison of Observed and Predicted TEC for PRN 02 at COSO Station on DOY 090 at 15° Cutoff and 30-min Prediction Interval.....	189
Figure 6.58 Comparison of Observed and Predicted TEC for PRN 03 at AMC2 Station on DOY 090 at 15° Cutoff and 30-min Prediction Interval.....	189
Figure 6.59 Comparison of Observed and Predicted TEC for PRN 03 at CASP Station on DOY 090 at 15° Cutoff and 30-min Prediction Interval.....	190
Figure 6.60 Comparison of Observed and Predicted TEC for PRN 31 at PRDS Station on DOY 090 at 15° Cutoff and 30-min Prediction Interval.....	190
Figure 6.61 Comparison of Observed and Predicted TEC for PRN 04 at FAIR Station on DOY 090 at 15° Cutoff and 30-min Prediction Interval.....	190
Figure 6.62 Comparison of Observed and Predicted TEC for PRN 31 at DRAO Station on DOY 090 at 15° Cutoff and 30-min Prediction Interval.....	193

Figure 6.63 Comparison of Observed and Predicted TEC for PRN 03 at DRAO Station on DOY 090 at 15° Cutoff and 30-min Prediction Interval.....	193
Figure 6.64 Comparison of Observed and Predicted TEC for PRN 02 at DAM2 Station on DOY 090 at 15° Cutoff and 30-min Prediction Interval.....	194
Figure 6.65 Comparison of Observed and Predicted TEC for PRN 17 at DAM2 Station on DOY 090 at 15° Cutoff and 30-min Prediction Interval.....	194
Figure 6.66 Comparison of Observed and Predicted TEC for PRN 02 at CARR Station on DOY 089 at 20° Cutoff and 5-min Prediction Interval.....	195
Figure 6.67 Comparison of Observed and Predicted TEC for PRN 02 at COSO Station on DOY 089 at 20° Cutoff and 5-min Prediction Interval.....	196
Figure 6.68 Comparison of Observed and Predicted TEC for PRN 03 at AMC2 Station on DOY 089 at 20° Cutoff and 5-min Prediction Interval.....	196
Figure 6.69 Comparison of Observed and Predicted TEC for PRN 03 at CASP Station on DOY 089 at 20° Cutoff and 5-min Prediction Interval.....	196
Figure 6.70 Comparison of Observed and Predicted TEC for PRN 31 at PRDS Station on DOY 089 at 20° Cutoff and 5-min Prediction Interval.....	197
Figure 6.71 Comparison of Observed and Predicted TEC for PRN 04 at FAIR Station on DOY 089 at 20° Cutoff and 5-min Prediction Interval.....	197
Figure 6.72 Comparison of Observed and Predicted TEC for PRN 02 at CARR Station on DOY 090 at 20° Cutoff and 5-min Prediction Interval.....	199
Figure 6.73 Comparison of Observed and Predicted TEC for PRN 02 at COSO Station on DOY 090 at 20° Cutoff and 5-min Prediction Interval.....	199
Figure 6.74 Comparison of Observed and Predicted TEC for PRN 03 at AMC2 Station on DOY 090 at 20° Cutoff and 5-min Prediction Interval.....	200
Figure 6.75 Comparison of Observed and Predicted TEC for PRN 03 at CASP Station on DOY 090 at 20° Cutoff and 5-min Prediction Interval.....	200
Figure 6.76 Comparison of Observed and Predicted TEC for PRN 31 at PRDS Station on DOY 090 at 20° Cutoff and 5-min Prediction Interval.....	200

Figure 6.77 Comparison of Observed and Predicted TEC for PRN 04 at FAIR Station on DOY 090 at 20° Cutoff and 5-min Prediction Interval.....	201
Figure 6.78 Comparison of Observed and Predicted TEC for PRN 02 at CARR Station on DOY 089 at 20° Cutoff and 10-min Prediction Interval.....	203
Figure 6.79 Comparison of Observed and Predicted TEC for PRN 02 at COSO Station on DOY 089 at 20° Cutoff and 10-min Prediction Interval.....	203
Figure 6.80 Comparison of Observed and Predicted TEC for PRN 03 at AMC2 Station on DOY 089 at 20° Cutoff and 10-min Prediction Interval.....	203
Figure 6.81 Comparison of Observed and Predicted TEC for PRN 03 at CASP Station on DOY 089 at 20° Cutoff and 10-min Prediction Interval.....	204
Figure 6.82 Comparison of Observed and Predicted TEC for PRN 31 at PRDS Station on DOY 089 at 20° Cutoff and 10-min Prediction Interval.....	204
Figure 6.83 Comparison of Observed and Predicted TEC for PRN 04 at FAIR Station on DOY 089 at 20° Cutoff and 10-min Prediction Interval.....	204
Figure 6.84 Comparison of Observed and Predicted TEC for PRN 02 at CARR Station on DOY 090 at 20° Cutoff and 10-min Prediction Interval.....	206
Figure 6.85 Comparison of Observed and Predicted TEC for PRN 02 at COSO Station on DOY 090 at 20° Cutoff and 10-min Prediction Interval.....	207
Figure 6.86 Comparison of Observed and Predicted TEC for PRN 03 at AMC2 Station on DOY 090 at 20° Cutoff and 10-min Prediction Interval.....	207
Figure 6.87 Comparison of Observed and Predicted TEC for PRN 03 at CASP Station on DOY 090 at 20° Cutoff and 10-min Prediction Interval.....	207
Figure 6.88 Comparison of Observed and Predicted TEC for PRN 31 at PRDS Station on DOY 090 at 20° Cutoff and 10-min Prediction Interval.....	208
Figure 6.89 Comparison of Observed and Predicted TEC for PRN 04 at FAIR Station on DOY 090 at 20° Cutoff and 10-min Prediction Interval.....	208
Figure 6.90 Comparison of Observed and Predicted TEC for PRN 02 at CARR Station on DOY 089 at 20° Cutoff and 30-min Prediction Interval.....	210

Figure 6.91 Comparison of Observed and Predicted TEC for PRN 02 at COSO Station on DOY 089 at 20° Cutoff and 30-min Prediction Interval.....	210
Figure 6.92 Comparison of Observed and Predicted TEC for PRN 03 at AMC2 Station on DOY 089 at 20° Cutoff and 30-min Prediction Interval.....	211
Figure 6.93 Comparison of Observed and Predicted TEC for PRN 03 at CASP Station on DOY 089 at 20° Cutoff and 30-min Prediction Interval.....	211
Figure 6.94 Comparison of Observed and Predicted TEC for PRN 31 at PRDS Station on DOY 089 at 20° Cutoff and 30-min Prediction Interval.....	211
Figure 6.95 Comparison of Observed and Predicted TEC for PRN 04 at FAIR Station on DOY 089 at 20° Cutoff and 30-min Prediction Interval.....	212
Figure 6.96 Comparison of Observed and Predicted TEC for PRN 02 at CARR Station on DOY 090 at 20° Cutoff and 30-min Prediction Interval.....	214
Figure 6.97 Comparison of Observed and Predicted TEC for PRN 02 at COSO Station on DOY 090 at 20° Cutoff and 30-min Prediction Interval.....	214
Figure 6.98 Comparison of Observed and Predicted TEC for PRN 03 at AMC2 Station on DOY 090 at 20° Cutoff and 30-min Prediction Interval.....	214
Figure 6.99 Comparison of Observed and Predicted TEC for PRN 03 at CASP Station on DOY 090 at 20° Cutoff and 30-min Prediction Interval.....	215
Figure 6.100 Comparison of Observed and Predicted TEC for PRN 31 at PRDS Station on DOY 090 at 20° Cutoff and 30-min Prediction Interval.....	215
Figure 6.101 Comparison of Observed and Predicted TEC for PRN 04 at FAIR Station on DOY 090 at 20° Cutoff and 30-min Prediction Interval.....	215
Figure 6.102 Comparison of Observed and Predicted TEC for PRN 02 at CARR Station on DOY 089 at 25° Cutoff and 5-min Prediction Interval.....	217
Figure 6.103 Comparison of Observed and Predicted TEC for PRN 02 at COSO Station on DOY 089 at 25° Cutoff and 5-min Prediction Interval.....	218
Figure 6.104 Comparison of Observed and Predicted TEC for PRN 03 at AMC2 Station on DOY 089 at 25° Cutoff and 5-min Prediction Interval.....	218

Figure 6.105 Comparison of Observed and Predicted TEC for PRN 03 at CASP Station on DOY 089 at 25° Cutoff and 5-min Prediction Interval.....	218
Figure 6.106 Comparison of Observed and Predicted TEC for PRN 31 at PRDS Station on DOY 089 at 25° Cutoff and 5-min Prediction Interval.....	219
Figure 6.107 Comparison of Observed and Predicted TEC for PRN 04 at FAIR Station on DOY 089 at 25° Cutoff and 5-min Prediction Interval.....	219
Figure 6.108 Comparison of Observed and Predicted TEC for PRN 02 at CARR Station on DOY 090 at 25° Cutoff and 5-min Prediction Interval.....	221
Figure 6.109 Comparison of Observed and Predicted TEC for PRN 02 at COSO Station on DOY 090 at 25° Cutoff and 5-min Prediction Interval.....	222
Figure 6.110 Comparison of Observed and Predicted TEC for PRN 03 at AMC2 Station on DOY 090 at 25° Cutoff and 5-min Prediction Interval.....	222
Figure 6.111 Comparison of Observed and Predicted TEC for PRN 03 at CASP Station on DOY 090 at 25° Cutoff and 5-min Prediction Interval.....	222
Figure 6.112 Comparison of Observed and Predicted TEC for PRN 31 at PRDS Station on DOY 090 at 25° Cutoff and 5-min Prediction Interval.....	223
Figure 6.113 Comparison of Observed and Predicted TEC for PRN 04 at FAIR Station on DOY 090 at 25° Cutoff and 5-min Prediction Interval.....	223
Figure 6.114 Comparison of Observed and Predicted TEC for PRN 02 at CARR Station on DOY 089 at 25° Cutoff and 10-min Prediction Interval.....	225
Figure 6.115 Comparison of Observed and Predicted TEC for PRN 02 at COSO Station on DOY 089 at 25° Cutoff and 10-min Prediction Interval.....	225
Figure 6.116 Comparison of Observed and Predicted TEC for PRN 03 at AMC2 Station on DOY 089 at 25° Cutoff and 10-min Prediction Interval.....	226
Figure 6.117 Comparison of Observed and Predicted TEC for PRN 03 at CASP Station on DOY 089 at 25° Cutoff and 10-min Prediction Interval.....	226
Figure 6.118 Comparison of Observed and Predicted TEC for PRN 31 at PRDS Station on DOY 089 at 25° Cutoff and 10-min Prediction Interval.....	226

Figure 6.119 Comparison of Observed and Predicted TEC for PRN 04 at FAIR Station on DOY 089 at 25° Cutoff and 10-min Prediction Interval.....	227
Figure 6.120 Comparison of Observed and Predicted TEC for PRN 02 at CARR Station on DOY 090 at 25° Cutoff and 10-min Prediction Interval.....	229
Figure 6.121 Comparison of Observed and Predicted TEC for PRN 02 at COSO Station on DOY 090 at 25° Cutoff and 10-min Prediction Interval.....	229
Figure 6.122 Comparison of Observed and Predicted TEC for PRN 03 at AMC2 Station on DOY 090 at 25° Cutoff and 10-min Prediction Interval.....	229
Figure 6.123 Comparison of Observed and Predicted TEC for PRN 03 at CASP Station on DOY 090 at 25° Cutoff and 10-min Prediction Interval.....	230
Figure 6.124 Comparison of Observed and Predicted TEC for PRN 31 at PRDS Station on DOY 090 at 25° Cutoff and 10-min Prediction Interval.....	230
Figure 6.125 Comparison of Observed and Predicted TEC for PRN 04 at FAIR Station on DOY 090 at 25° Cutoff and 10-min Prediction Interval.....	230
Figure 6.126 Comparison of Observed and Predicted TEC for PRN 02 at CARR Station on DOY 089 at 25° Cutoff and 30-min Prediction Interval.....	232
Figure 6.127 Comparison of Observed and Predicted TEC for PRN 02 at COSO Station on DOY 089 at 25° Cutoff and 30-min Prediction Interval.....	233
Figure 6.128 Comparison of Observed and Predicted TEC for PRN 03 at AMC2 Station on DOY 089 at 25° Cutoff and 30-min Prediction Interval.....	233
Figure 6.129 Comparison of Observed and Predicted TEC for PRN 03 at CASP Station on DOY 089 at 25° Cutoff and 30-min Prediction Interval.....	233
Figure 6.130 Comparison of Observed and Predicted TEC for PRN 31 at PRDS Station on DOY 089 at 25° Cutoff and 30-min Prediction Interval.....	234
Figure 6.131 Comparison of Observed and Predicted TEC for PRN 04 at FAIR Station on DOY 089 at 25° Cutoff and 30-min Prediction Interval.....	234
Figure 6.132 Comparison of Observed and Predicted TEC for PRN 02 at CARR Station on DOY 090 at 25° Cutoff and 30-min Prediction Interval.....	236

Figure 6.133 Comparison of Observed and Predicted TEC for PRN 02 at COSO Station on DOY 090 at 25° Cutoff and 30-min Prediction Interval.....	236
Figure 6.134 Comparison of Observed and Predicted TEC for PRN 03 at AMC2 Station on DOY 090 at 25° Cutoff and 30-min Prediction Interval.....	237
Figure 6.135 Comparison of Observed and Predicted TEC for PRN 03 at CASP Station on DOY 090 at 25° Cutoff and 30-min Prediction Interval.....	237
Figure 6.136 Comparison of Observed and Predicted TEC for PRN 31 at PRDS Station on DOY 090 at 25° Cutoff and 30-min Prediction Interval.....	237
Figure 6.137 Comparison of Observed and Predicted TEC for PRN 04 at FAIR Station on DOY 090 at 25° Cutoff and 30-min Prediction Interval.....	238
Figure 6.138 Positioning Error at CARR Station Using Three Ionospheric Models, Tomographic Correction Predicted at 15° and 5-min Interval.....	243
Figure 6.139 Positioning Error at COSO Station Using Three Ionospheric Models, Tomographic Correction Predicted at 15° and 5-min Interval.....	244
Figure 6.140 Positioning Error at AMC2 Station Using Three Ionospheric Models, Tomographic Correction Predicted at 15° and 5-min Interval.....	244
Figure 6.141 Positioning Error at CASP Station Using Three Ionospheric Models, Tomographic Correction Predicted at 15° and 5-min Interval.....	244
Figure 6.142 Positioning Error at PRDS Station Using Three Ionospheric Models, Tomographic Correction Predicted at 15° and 5-min Interval.....	245
Figure 6.143 Positioning Error at FAIR Station Using Three Ionospheric Models, Tomographic Correction Predicted at 15° and 5-min Interval.....	245
Figure 6.144 Positioning Error at DRAO Station Using Three Ionospheric Models, Tomographic Correction Predicted at 15° and 5-min Interval.....	249
Figure 6.145 Positioning Error at DAM2 Station Using Three Ionospheric Models, Tomographic Correction Predicted at 15° and 5-min Interval.....	249
Figure 6.146 Positioning Error at CARR Station Using Three Ionospheric Models, Tomographic Correction Predicted at 15° and 10-min Interval.....	250

Figure 6.147 Positioning Error at COSO Station Using Three Ionospheric Models, Tomographic Correction Predicted at 15° and 10-min Interval.....	250
Figure 6.148 Positioning Error at AMC2 Station Using Three Ionospheric Models, Tomographic Correction Predicted at 15° and 10-min Interval.....	250
Figure 6.149 Positioning Error at CASP Station Using Three Ionospheric Models, Tomographic Correction Predicted at 15° and 10-min Interval.....	251
Figure 6.150 Positioning Error at PRDS Station Using Three Ionospheric Models, Tomographic Correction Predicted at 15° and 10-min Interval.....	251
Figure 6.151 Positioning Error at FAIR Station Using Three Ionospheric Models, Tomographic Correction Predicted at 15° and 10-min Interval.....	251
Figure 6.152 Positioning Error at DRAO Station Using Three Ionospheric Models, Tomographic Correction Predicted at 15° and 10-min Interval.....	254
Figure 6.153 Positioning Error at DAM2 Station Using Three Ionospheric Models, Tomographic Correction Predicted at 15° and 10-min Interval.....	254
Figure 6.154 Positioning Error at CARR Station Using Three Ionospheric Models, Tomographic Correction Predicted at 15° and 30-min Interval.....	255
Figure 6.155 Positioning Error at COSO Station Using Three Ionospheric Models, Tomographic Correction Predicted at 15° and 30-min Interval.....	256
Figure 6.156 Positioning Error at AMC2 Station Using Three Ionospheric Models, Tomographic Correction Predicted at 15° and 30-min Interval.....	256
Figure 6.157 Positioning Error at CASP Station Using Three Ionospheric Models, Tomographic Correction Predicted at 15° and 30-min Interval.....	256
Figure 6.158 Positioning Error at PRDS Station Using Three Ionospheric Models, Tomographic Correction Predicted at 15° and 30-min Interval.....	257
Figure 6.159 Positioning Error at FAIR Station Using Three Ionospheric Models, Tomographic Correction Predicted at 15° and 30-min Interval.....	257
Figure 6.160 Positioning Error at DRAO Station Using Three Ionospheric Models, Tomographic Correction Predicted at 15° and 30-min Interval.....	260

Figure 6.161 Positioning Error at DAM2 Station Using Three Ionospheric Models, Tomographic Correction Predicted at 15° and 30-min Interval.....	260
Figure 6.162 Positioning Error at CARR Station Using Three Ionospheric Models, Tomographic Correction Predicted at 15° and 5-min Interval.....	262
Figure 6.163 Positioning Error at COSO Station Using Three Ionospheric Models, Tomographic Correction Predicted at 15° and 5-min Interval.....	262
Figure 6.164 Positioning Error at AMC2 Station Using Three Ionospheric Models, Tomographic Correction Predicted at 15° and 5-min Interval.....	263
Figure 6.165 Positioning Error at CASP Station Using Three Ionospheric Models, Tomographic Correction Predicted at 15° and 5-min Interval.....	263
Figure 6.166 Positioning Error at PRDS Station Using Three Ionospheric Models, Tomographic Correction Predicted at 15° and 5-min Interval.....	263
Figure 6.167 Positioning Error at FAIR Station Using Three Ionospheric Models, Tomographic Correction Predicted at 15° and 5-min Interval.....	264
Figure 6.168 Positioning Error at DRAO Station Using Three Ionospheric Models, Tomographic Correction Predicted at 15° and 5-min Interval.....	266
Figure 6.169 Positioning Error at DAM2 Station Using Three Ionospheric Models, Tomographic Correction Predicted at 15° and 5-min Interval.....	267
Figure 6.170 Positioning Error at CARR Station Using Three Ionospheric Models, Tomographic Correction Predicted at 15° and 10-min Interval.....	268
Figure 6.171 Positioning Error at COSO Station Using Three Ionospheric Models, Tomographic Correction Predicted at 15° and 10-min Interval.....	268
Figure 6.172 Positioning Error at AMC2 Station Using Three Ionospheric Models, Tomographic Correction Predicted at 15° and 10-min Interval.....	268
Figure 6.173 Positioning Error at CASP Station Using Three Ionospheric Models, Tomographic Correction Predicted at 15° and 10-min Interval.....	269
Figure 6.174 Positioning Error at PRDS Station Using Three Ionospheric Models, Tomographic Correction Predicted at 15° and 10-min Interval.....	269

Figure 6.175 Positioning Error at FAIR Station Using Three Ionospheric Models, Tomographic Correction Predicted at 15° and 10-min Interval.....	269
Figure 6.176 Positioning Error at DRAO Station Using Three Ionospheric Models, Tomographic Correction Predicted at 15° and 10-min Interval.....	272
Figure 6.177 Positioning Error at DAM2 Station Using Three Ionospheric Models, Tomographic Correction Predicted at 15° and 10-min Interval.....	272
Figure 6.178 Positioning Error at CARR Station Using Three Ionospheric Models, Tomographic Correction Predicted at 15° and 30-min Interval.....	273
Figure 6.179 Positioning Error at COSO Station Using Three Ionospheric Models, Tomographic Correction Predicted at 15° and 30-min Interval.....	273
Figure 6.180 Positioning Error at AMC2 Station Using Three Ionospheric Models, Tomographic Correction Predicted at 15° and 30-min Interval.....	274
Figure 6.181 Positioning Error at CASP Station Using Three Ionospheric Models, Tomographic Correction Predicted at 15° and 30-min Interval.....	274
Figure 6.182 Positioning Error at PRDS Station Using Three Ionospheric Models, Tomographic Correction Predicted at 15° and 30-min Interval.....	274
Figure 6.183 Positioning Error at FAIR Station Using Three Ionospheric Models, Tomographic Correction Predicted at 15° and 30-min Interval.....	275
Figure 6.184 Positioning Error at DRAO Station Using Three Ionospheric Models, Tomographic Correction Predicted at 15° and 30-min Interval.....	278
Figure 6.185 Positioning Error at DAM2 Station Using Three Ionospheric Models, Tomographic Correction Predicted at 15° and 30-min Interval.....	278

List of Symbols

$a_{0,r}$	parameter for the spatial linear model
$a_{1,r}$	parameter for the spatial linear model
$a_{2,r}$	parameter for the spatial linear model
a_{f0}	clock bias coefficient
a_{f1}	clock drift coefficient
a_{f2}	clock drift rate coefficient
a_{nk}^m	tomographic model coefficient
A	amplitude term in Klobuchar model
b_i	receiver inter-frequency bias in carrier phase measurement
b^p	satellite inter-frequency bias in carrier phase measurement
$b_{i,j}$	receiver instrumental delay in carrier phase measurement
b_j^p	satellite instrumental delay in carrier phase measurement
b_{nk}^m	tomographic model coefficient
B	magnetic field
B_i	receiver inter-frequency bias in code measurement
B^p	satellite inter-frequency bias in code measurement
$B_{i,j}$	receiver instrumental delay in code measurement
B_j^p	satellite instrumental delay in code measurement
c	speed of light in vacuum
d^o	observed ionospheric slant TEC data vector
d^p	predicted ionospheric slant TEC data vector
d_i^o	observed ionospheric slant TEC
d_i^p	predicted ionospheric slant TEC

d_{orb}	satellite orbit error
Δd_i	slant TEC prediction error
Δd_i^v	vertical TEC prediction error
Δd_{rms}^v	vertical TEC prediction RMS error
DC	night-time constant offset term in Klobuchar
e	satellite orbit eccentricity or charge on an electron
ele	elevation angle
f_c	ionosphere critical frequency
f_i	GPS frequency
G^p	predicted geometry matrix
H_k	design matrix
i	satellite orbit Inclination or subscript index
ΔI_i	ionospheric delay on GPS frequency f_i
K	highest order of empirical orthogonal functions
m	is the mass of an electron
m_p	multipath effect on code pseudorange measurement
M	highest order of spherical harmonics functions
M_p	multipath effect on code pseudorange measurement
M(ele)	mapping function converting slant ionospheric delay to vertical delay
N	ambiguity for carrier phase measurement
$N_0(\lambda, \phi, z)$	approximate electron density
$N_e(\lambda, \phi, z)$	electron density
$\delta N_e(\lambda, \phi, z)$	correction to electron density
P	period of Klobuchar model
P_i	GPS pseudorange measurement

$\bar{P}_n^m(\square)$	associated Legendre polynomial
Q_k	process noise covariance matrix
r_{CS}	satellite semimajor axis
R_k	observation noise covariance matrix
$R.E._i$	relative error of predicted slant TEC
Recov	ionospheric recovering efficiency of tomographic model
SPP_{rms_dual}	positioning RMS error using dual-frequency model
SPP_{rms_tomo}	positioning RMS error using tomographic model
SPP_{rms_zero}	positioning RMS error using zero model
t	local mean solar time at subionospheric point
dt	GPS satellite clock error
t_{oc}	reference time for satellite clock correction
Δt_R	satellite clock relativistic correction
$\Delta t_{SV,L1}$	satellite clock corrections for L1 measurement
$\Delta t_{SV,L2}$	satellite clock corrections for L2 measurement
T	tropospheric refraction delay
T_{GD}	group delay
TEC	slant TEC measurement
TEC_R	code-derived slant TEC measurement
$TEC_{SM,N}$	smoothed slant TEC measurement at epoch N
TEC_ϕ	carrier phase-derived slant TEC measurement
ΔTEC	offset between TEC_R and TEC_ϕ
δTEC	difference between TEC measurement and approximate
dT	GPS receiver clock error
v_k	measurement error vector

VTEC	vertical TEC delay
w_{k-1}	system noise vector
W	IGP grid weight function
x_k	system state vector
x^P	predicted state vector
z	geographical height
z_k	measurement vector
$Z_k(z)$	empirical orthogonal functions
σ	standard deviation
β	reciprocal of correlation time
γ	square of ratio of L1 to L2 frequencies
ε_p	code pseudorange measurement noise
ε_ϕ	carrier phase measurement noise
λ	Sun-fixed longitude
λ_i	GPS carrier phase signal wavelength
$d\lambda$	Sun-fixed longitude difference
ρ	geometrical distance
ϕ	geomagnetic latitude
Φ	carrier phase measurement
$\Phi_{k,k-1}$	transition matrix
$d\phi_{r_i}^s$	geomagnetic latitude difference
ω_s	satellite angular velocity

List of Abbreviations

BIH	Bureau International de l'Heure
BTS	BIH terrestrial system
C/A-code	coarse acquisition code
CC	composite clock
CME	coronal mass ejection
CODE	center for orbit determination in Europe
DoD	Department of Defence
DoT	Department of Transportation
DOY	day of year
EGNOS	European geostationary navigation overlay service
EME	electromagnetic emission
EOF	empirical orthogonal function
EOS	Earth observation systems
EUV	extreme ultraviolet
FAA	Federal Aviation Administration
FOC	full operational capability
GEONET	GPS Earth observation network
GPS	global positioning system
IGP	ionospheric grid point
IGS	international GPS service for geodynamics
IMF	interplanetary magnetic field
IOC	initial operational capability
IPP	ionospheric pierce point
IRI	international reference ionosphere
ISR	incoherent scatter radar
ITRF	international terrestrial reference frame
JPL	jet propulsion laboratory

LUF	lowest usable frequency
MC	master clock
MSAS	MTSAT satellite based augmentation system
MTSAT	multi-functional transport satellite
MUF	maximum usable frequency
NAVSTAR	navigation satellite timing and ranging
NNSS	navy navigation satellite system
NRT	near real time
PCA	polar cap absorption
P-code	precise code
POD	precise orbit determination
PPS	precise positioning service
RF	radio frequency
RMS	root mean squares
RTK	real-time kinematic
SA	selective availability
SBAS	satellite based augmentation system
SCIGN	southern California integrated GPS network
SHF	spherical harmonics function
SID	sudden ionospheric disturbance
SIMRSN	Singapore integrated multiple reference station network
SPP	single point positioning
SPS	standard positioning service
TEC	total electron content
TECU	total electron content unit
TOA	time of arrival
T/P	TOPEX/Poseidon
USNO	United States naval observatory
VLBI	very long baseline interferometry

VLF	very low frequency
VTEC	vertical total electron content
WAAS	wide area augmentation system
WADGPS	wide area differential GPS
WGS84	world geodetic system 1984
WRS	WAAS reference station

CHAPTER 1

INTRODUCTION

This chapter states the research background, the current ionospheric modeling problems, research motivation and objectives.

1.1 Background

The ionosphere is a part of the upper atmosphere where free electrons are concentrated and affect the propagation of radio frequency electromagnetic waves. Ionosphere is located between 60 and 1500 km above the Earth. The electron production in the ionosphere is controlled by ionization processes that primarily depend on a wide spectrum of solar X-ray and extreme ultraviolet (EUV) radiation which varies with the Sun's activity (Rishbeth and Garriott, 1969). Ionosphere medium is highly variable in space and time and its structure and peak densities in the ionosphere vary greatly with time (sunspot cycle, seasonally, and diurnally), with geographical location (polar, auroral zones, mid-latitudes, and equatorial regions), and with certain solar-related ionospheric disturbances. Ionosphere research attracts significant attention from the global positioning system (GPS) community because ionospheric range delay on GPS signals is a major error source in GPS positioning and navigation. Since selective availability (SA) was turned off on May 1st, 2000, the ionospheric delay has actually become the biggest error for single frequency GPS applications (Skone et al., 2002; Gao et al., 2002a).

The current Global Positioning System (GPS) broadcasts RF signals on L1 (1575.42 MHz) and L2 (1227.60 MHz) frequencies. After GPS modernization by about 2005, a third frequency L5 (1176.45 MHz) will be added to GPS satellites. Prior to the reception by the receiver antenna, GPS signals transmitted from satellites travel through the ionosphere. The ionosphere is dispersive at GPS frequencies. Due to the existence of ample free electrons, the GPS signals are significantly affected by ionosphere. This effect

is usually referred to as ionospheric delay or ionospheric error by GPS users. The magnitude of ionospheric delay is proportional to the total electron content (TEC) and inversely proportional to the square of transmission frequency. TEC is defined by the integral of electron density in a 1-m² column along the signal transmission path. Ionospheric delays of 38~52 m were observed at low-latitude region during high solar activity period at an elevation cutoff angle 10° (Komjathy et al., 2002). Fortunately there are two frequencies used by GPS and will be three after GPS modernization in 2005. The TEC can be readily determined by employing the measurements from L1 and L2 frequencies (Klobuchar, 1996) and subsequently almost all of the ionospheric errors can be removed once the TEC is determined. For applications where TEC observations are not available like single frequency GPS users or for regions where the measurement of TEC is not possible, an empirical ionosphere model however should be used to minimize the ionosphere errors. The GPS control segment broadcasts eight coefficients of the Klobuchar model which can provide the ionosphere error correction for the single frequency GPS users on a global basis. However the model is quoted as a 50-percent root-sum square correction on a global basis (Klobuchar, 1987). Compared to the broadcast ionospheric model, the models established using data from GPS networks can compensate the ionospheric error with much higher accuracies.

To date various ionosphere models based on GPS observations have been proposed (Klobuchar, 1987; Walker, 1989; Coster et al., 1992; El-Arini et al., 1993 and 1994; Komjathy, 1997; Skone, 1998; Schaer, 1999; Liao, 2000; Hansen et al., 1997; Hanse, 1998; Hernández-Pajares et al., 1999 and 2000; Liu and Gao, 2001a; Colombo et al., 2000 and 2002). A common characteristic of most of these models is that they are constructed based on the assumption that the electrons in the ionosphere are concentrated in a single thin ionosphere shell with a fixed altitude, typically selected between 250 and 450 km, above the Earth's surface. Although most free electrons are indeed concentrated within a region ranging from 250-450 km in height, this assumption is not physically true. Free electrons are actually distributed irregularly within the entire ionosphere that

approximately covers a region between 60 and 1500 km above the Earth's surface. Such a single layer assumption could introduce modeling errors up to several TEC units (TECU) (Komjathy, 1997). The ionosphere models based on the single-layer concept, such as the grid and harmonic models, are essentially constructed on a two-dimensional basis. Hence those single-layer ionospheric models are inherently insufficient to describe the ionosphere in the vertical dimension. As a result, they are unable to provide a whole structure of ionosphere and subsequently they lack the capability to describe the spatial variations of the ionosphere as well as the presence of heterogeneities. Some proposed tomographic models overcome the limitations of two-dimensional models (Hansen et al., 1997; Hansen, 1998, Hernández-Pajares et al., 1999 and 2000; Colombo et al., 2000 and 2002) and they could model the ionosphere in three-dimensional (3D) mode. A number of drawbacks however still exist in these models. A more detailed analysis of these models will be elaborated in Chapter 4. Therefore, there is a need for the development of a new three-dimensional (3D) ionospheric modeling system that is able to characterize the spatial structure through the stratification of multiple layers in the ionosphere and to overcome the drawbacks of previous 3D models.

1.2 Objectives and Contributions

The objectives of this research will focus on the development of a close form new ionospheric modeling system using a tomography technique applied to GPS data and evaluate this modeling system by using GPS reference networks observed under different conditions. Using this modeling system, GPS measurements from GPS reference network can be processed to construct the ionosphere tomographic model and predict ionospheric TEC using the constructed model in a real-time mode, which allows GPS users to make use of the TEC predictions in their real-time applications. Different from the previous single-layer models, this model is able to model the ionospheric electron density function in three dimensions. The new model is constructed using multiple layers to model the ionosphere electron density field and it can overcome the limitations in single-layer ionospheric models as well as existing tomographic models. Unlike 2D ionospheric

models, the ionosphere tomographic model uses the ionospheric electron density as the variable to be modeled, which is a more fundamental variable describing the property of the ionosphere than the variable total electron content (TEC) used by the single-layer ionospheric models. The new modeling system will also overcome the drawbacks associated with previous tomographic modeling methods. The research contributions of this thesis include:

- 1) A new modeling system has been developed for modeling the ionosphere using function-based tomography technique to construct a 3D model of the ionosphere with smoothed GPS-derived TEC data from operational GPS reference networks. The system is able to conduct real-time ionospheric estimation and ionospheric TEC predictions based on Kalman filtering. A pseudo TEC observation has been introduced to establish a reference for estimating inter-frequency biases.
- 2) The formulas for smoothing the code-derived total electron content (TEC) using carrier phase measurements and the formula for recursive estimation of the error of smoothed TEC measurements have been derived.
- 3) A close form analytical expression that establishes the link between function-based tomographic model and smoothed TEC data have been developed which allows the ionospheric TEC smoothing and tomographic modeling to run in parallel in real-time implementation.
- 4) Three quantitative indicators have been proposed to assess the performances of the ionospheric predictions by the tomographic model.
- 5) The developed function-based tomographic modeling system has been tested with respect to both local area and wide area GPS networks. Data analysis has been conducted to assess the accuracy of the model predicted ionospheric TEC data in a real-time fashion using different testing schemes and under different ionospheric conditions including extremely disturbed ionospheric conditions ($K_p=8\sim 9$). The performance of the ionospheric TEC predictions has been evaluated in both TEC measurement domain and position domain.

- 6) A software package has been developed to implement the proposed ionosphere tomographic modeling system.

1.3 Outlines

Chapter 1 states the research background, current problems in ionospheric modeling, the research motivation and the specific objectives that are treated. The significance of establishing three-dimensional ionospheric model is also discussed. An overview is given in Chapter 2 of theory of the Global Positioning System and of GPS error sources. The ionospheric effects on GPS are also summarized.

Chapter 3 discusses the characteristics of the ionosphere and their impact on navigation and positioning using GPS. The techniques of measuring ionospheric electron density are discussed as well. Chapter 4 first overviews and analyzes the drawbacks associated with current ionospheric models and then describes the development of a methodology for function-based three-dimensional (3D) tomographic modeling system and prediction of the ionospheric TEC using tomographic technique. Three quantitative indicators for assessing the ionospheric predictions are proposed. The mathematical derivation of the tomographic modeling, prediction and evaluation will be given in details.

The implementation and assessment of the proposed ionosphere tomographic modeling method will be conducted in Chapter 5 using data from a local area GPS network and in Chapter 6 using data from a wide area GPS network. Data collected under various ionospheric conditions will be analyzed. In both Chapters 5 and 6, the performance of the 3D ionospheric model will be examined in both TEC measurement domain and position domain. For assessment in the position domain, the proposed 3D model and other ionospheric models are used to correct ionospheric errors in single point positioning. The performances of 3D model and other ones are evaluated through the examination of the achievable positioning accuracies using a single-frequency receiver.

Chapter 7 summarizes the major conclusions drawn as a result of the development of the 3D ionosphere tomographic modeling system described in this thesis. Recommendations for future work are also provided.

CHAPTER 2

OVERVIEW OF GLOBAL POSITIONING SYSTEM

The Navigation Satellite Timing and Ranging (NAVSTAR) Global Positioning System is an all weather, radio-based, satellite navigation system developed by U.S. Department of Defence (DoD) and Department of Transportation (DoT). It enables the users to accurately determine three-dimensional position, velocity, and time information anywhere on or near the surface of the Earth at any time. The GPS program started in 1973 and on April 27, 1995, the NAVSTAR GPS, containing 24 (21+3 spares) operational satellites, was formally declared as having met the requirement of Full Operational Capability (FOC). Since then, the system has been taken into full use. Prior to GPS FOC, an Initial Operational Capability (IOC) was declared on December 8, 1993 when 24 GPS satellites (Block I/II/IIA) were operating in their assigned orbits, available for navigation use and providing Standard Positioning Service (SPS) levels.

Positioning with GPS is to use one-way ranging measurements from GPS satellites that are also broadcasting their estimated positions. Ranges are measured to four or more satellites simultaneously in view by matching (correlating) the incoming signal with a user-generated replica signal and measuring the received phase against the user's clock (Parkinson, 1996a). With at least four range measurements, typically four unknowns, the receiver's three-dimensional position latitude, longitude, height, and its clock error can be estimated. In the rest of this chapter, the GPS system components, error sources, differential GPS concept as well as ionospheric impact on positioning are overviewed.

2.1 GPS Components

The GPS system is comprised of three primary segments: space segment, ground control segment, and user segment. The GPS satellites continuously transmit ranging signals to

the Earth at two L-band frequencies, a primary signal at 1575.42 MHz (L1) and a secondary broadcast at 1227.60 MHz (L2) (Parkinson, 1996a).

2.1.1 Space segment

The space segment is designed to have a constellation of 24 satellites. The satellites operate in six orbital planes, each plane equally spaced about the equator and inclined at 55° . For multiple access, the GPS satellite orbit was designed to form a constellation that at any place in the world at least four satellites are visible at any time (Spilker and Parkinson, 1996a). The period of the satellites is 12 hours sidereal time and the semi-major axis is 26,561.75 km. The altitude of GPS orbit is 20,162.61 km above the Earth's equatorial radius. The advantage of such a high altitude is that GPS satellites are not subject to atmospheric drag, which is beneficial for the precise orbit determination. The approximate parameters of GPS orbit are summarized in Table 2.1 (Spilker and Parkinson, 1996).

Table 2.1 Approximate GPS Satellite Parameters

Orbit plane	Six equally spaced ascending nodes at 120 deg
Orbit radius r_{CS}	26,561.75 km semimajor axis
Orbit velocity (circular) (ECI)	$= \sqrt{\mu/r_{CS}} = 3.8704 \text{ km/s}$
Eccentricity	Nominally zero, but generally less than $e = 0.02$
ω_s angular velocity	$1.454 \times 10^{-4} \text{ rad/s}$
Period	12 h mean sidereal time
Inclination	$i = 55^\circ$ nominal

2.1.2 Ground control segment

The ground control segment began operation in 1985 and consists of a master control center, four ground antenna upload stations and five widely separated monitoring stations. The ground control network is responsible for tracking the GPS satellites, determining satellite orbits, and periodically uploading almanac ephemeris as well as other system data to the satellites. The navigation messages are retransmitted from satellites to the user segment.

2.1.3 User segment

The user segment consists of the GPS receivers and its related device. The GPS receiver's three-dimensional position is determined by simultaneously observing at least four GPS satellites and taking advantage of the geometric intersection of the simultaneously observed ranges with known satellites coordinates. What the GPS receiver measures is actually the GPS signal's transmission time from the epoch it leaves the satellite's antenna to the epoch it arrives at receiver's antenna. Using code correlation techniques, the transmission time is determined by shifting time for which the code sequence travels from the satellite and correlating it with an identical code generated in the tracking receiver. The receiver code sequence is shifted until maximum correlation value between the two codes is obtained. This shifted time multiplied by the speed of light is the range between GPS receiver to the satellite. The determination of satellite signal transmission time is affected by a variety of errors, such as satellite clock error, receiver clock error, ionospheric error, tropospheric error, satellite orbit error, multipath error and receiver noise. These errors will be discussed in the later part of this chapter.

2.2 GPS Observables

In principle, both signals at the L1 frequency and L2 frequency can each have two modulations at the same time (called "phase quadrature"). Currently there are two modulations on L1 frequency but only one modulation on L2. The two modulations are coarse acquisition code (C/A code) and precise code (P code). The C/A code is broadcast at a chipping rate of 1.023 MHz. This is the principal civilian ranging signal and it is also used to acquire the P code. The use of this signal is called the Standard Positioning Service (SPS). The P code is a much longer code with a chipping rate ten times of C/A code, 10.23 MHz. Because of its higher modulation bandwidth, the P code is more precise than C/A code. The P code is encrypted so that it is unavailable to unauthorized users. The use of this encrypted P code is called Precise Positioning Service (PPS).

2.3 GPS Reference System and Time Standard

The terrestrial reference system used for GPS is the World Geodetic System 1984 (WGS 84). The GPS navigation message includes Earth-fixed satellite ephemerides expressed in this system. WGS 84 is a global geocentric coordinate system defined originally by the DoD based on Doppler observations from the TRANSIT satellite system (a predecessor of GPS) (Bock, 1998). WGS 84 was first determined by aligning the DoD reference frame NSWC-9Z2 as closely as possible with the Bureau International de l'Heure (BIH) Conventional Terrestrial System (BTS) at epoch 1984.0 (Bock, 1998). In order to align WGS 84 with the more accurate International Terrestrial Reference Frame (ITRF), the DoD coordinated ten GPS tracking stations at the epoch 1994.0 using GPS data collected at these stations, a subset of IGS tracking stations whose ITRF91 coordinates being held fixed in the process (Malys and Slater, 1994). This refined WGS 84 frame has been designated as WGS 84 (G730). The 'G' is short for GPS derived and '730' is the GPS week number when these modifications were implemented.

Each GPS satellite carries a precise and stable atomic clock. The accurate atomic clock on satellites is beneficial for keeping precise time standard and for ground users to obtain precise positioning solutions. The time used by GPS is provided by its Composite Clock (CC), which was implemented since June 17, 1990 at 0000 UT. The Composite Clock is comprised of all operational monitor stations and satellite frequency standards. GPS system time in turn uses the Master Clock (MC) at United States Naval Observatory (USNO) as reference and is steered to UTC (USNO) from which system time will not deviate by more than one microsecond (USNO, 2003). UTC (USNO) itself is kept very close to the international benchmark UTC (BIPM) (USNO, 2003).

2.4 GPS Error Sources

The measurements of the time of arrival (TOA) of GPS signals from satellites to receivers are contaminated by a variety of errors. These error sources can be grouped into

three categories, the satellite related errors, the atmosphere related errors, and the receiver related errors. The satellite related errors include satellite clock error, satellite orbit error, and satellite inter-frequency bias. Atmosphere related errors consist of ionospheric delay error and tropospheric delay error. Receiver related errors are comprised of receiver clock error, receiver inter-frequency bias, multipath, and receiver noise. Among these errors the ionospheric delay error is the largest error source after selective availability was turned off (Gao and Liu, 2002; Skone et al., 2002). Under normal ionospheric condition, the influence of ionospheric delay on GPS signals is usually in the range from a few metres to tens of metres but it could reach more than 100 m during severe ionosphere storms (Gao and Liu, 2002). Table 2.2 gives a typical budget of each error source (Skone, 1998).

Table 2.2 GPS Error Source Budget (Skone, 1998)

Type of error	Size of error (m)
Ionosphere	5.0
Troposphere	1.5
SV clock and orbit	5.0
Receiver noise	1.5
Multipath	2.5
Total	7.8

Generally, these error sources can be corrected or mitigated by adopting appropriate procedures or models. For example, the ionospheric error can be mitigated using ionospheric models, e.g. Klobuchar model (Klobuchar, 1987), grid-model (Skone, 1998; Liao, 2000), tomographic model (Hernández-Pajares et al., 1999; Liu and Gao, 2001a). Different ionospheric models have different characteristics and produce different modeling accuracies. The study of this thesis is to develop a high accuracy ionospheric model based on a tomographic technique. Most of other error sources can also be mathematically modeled and alleviated to a minimum degree. For example, the precise orbit determination (POD) and clock estimation conducted by International GPS Service for Geodynamics (IGS) can reach the level of less than 5 cm and 0.1 ns, respectively, in their final products. The tropospheric delay error can also be effectively corrected using certain models (Hopfield, 1969; Saastamoinen, 1973; Lanyi, 1984). The multipath error

can be mitigated by the careful selection of GPS site, receiver (narrow correlators, multipath-estimating multiple-correlator channels), and antenna (e.g. choke ring) (Langley, 1998b). The following subsections describe the characteristics of each type of error sources.

2.4.1 Orbit error

The navigation messages generated at control segment and uploaded by the four ground antennas of the control segment's monitor stations are prediction results based on the past tracking information. Therefore the GPS satellite positions calculated from navigation messages are different from their true positions. This discrepancy between them is called orbit error. Before SA was turned off, the orbit error included an error called "epsilon" which was intentionally imposed within the satellite's navigation messages. The satellite orbit error is therefore much greater. Now the accuracy of broadcast orbit is about 2 m (IGSCB, 2004). Using post-processed orbit data provided by the IGS, the orbit error can be significantly reduced. Currently the IGS final orbits are claimed to have an accuracy of 5 cm (IGSCB, 2004).

2.4.2 Satellite clock error

Although all the GPS satellites are equipped with atomic clocks for the generation of GPS signals, the atomic clock performance still introduces an error to the GPS frequency standard because of its instability. This error can be corrected using the coefficients broadcast from the satellite. These coefficients are uploaded by the GPS control segment and actually several different sets of coefficients are uploaded to the satellite, of which each set is valid over a given time period (Spilker, 1996a). The clock error, Δt_{SV} , can be calculated by the following equation (Spilker, 1996a).

$$\Delta t_{SV} = a_{f0} + a_{f1}(t - t_{oc}) + a_{f2}(t - t_{oc})^2 + \Delta t_R \quad (2.1)$$

where a_{f0} , a_{f1} and a_{f2} are coefficients for clock bias (sec), clock drift (sec/sec), and clock drift rate (sec/sec²) respectively; t is the unbiased space vehicle clock time; t_{oc} is

a reference time for clock correction; Δt_R is the relativistic correction which must be computed by the users.

It should be noted if the users are using a single frequency GPS receiver (L1 or L2) for positioning and navigation, the space vehicle clock correction should be appropriately modified because the clock bias coefficient a_{f_0} estimated by GPS control segment is based on dual-frequency measurements where group delay, T_{GD} , is accounted for. Taking T_{GD} into account, the satellite clock error corrections for L1 or L2 measurements are given by equations (2.2) and (2.3), respectively.

$$\Delta t_{SV,L1} = \Delta t_{SV} - T_{GD} \quad (2.2)$$

$$\Delta t_{SV,L2} = \Delta t_{SV} - \gamma T_{GD} \quad (2.3)$$

where $\Delta t_{SV,L1}$ and $\Delta t_{SV,L2}$ are the satellite clock corrections for L1 and L2 measurement, respectively; T_{GD} is the group delay which is included in the navigation messages from satellites; $\gamma = (f_1/f_2)^2 = (1575.42/1227.60)^2 = (77/60)^2$.

2.4.3 Ionosphere error

The ionosphere is the upper atmosphere part where a large amount of free electrons exist. When the GPS signals propagate through the dense electrons, they are significantly delayed. This error is called ionosphere error. This ionospheric effect on range may vary from more than 100 m to less than a few metres (Wells et al., 1987). The ionospheric delay can change in one order during the course of a day due to ionospheric variability. This characteristic of the ionosphere makes it more difficult to be precisely modeled. Fortunately, the ionosphere is a dispersive medium at GPS frequencies which means the refractive index is a function of the signal frequency. The dual-frequency GPS measurements therefore can take advantage of this property to directly determine the ionospheric error.

The ionospheric delay is proportional to the total electron content and the reciprocal of the square of electromagnetic wave frequency propagating through the ionosphere. TEC is defined as the number of electrons in a column with a 1- m² cross section that extends from the GPS satellite to the observer (Klobuchar, 1996). Mathematically, the ionospheric delay on pseudorange and carrier phase measurements can be expressed at the first order refractive index by

$$\Delta I_i = \frac{40.3 \text{TEC}}{f_i^2} \quad (2.4)$$

where f_i ($i=1,2$) is the frequency of GPS L1 or L2 signals and ΔI_i ($i=1,2$) is the ionospheric delay on L1 or L2 signal. When pseudorange measurements on both L1 and L2 are available and not taking the inter-frequency biases into account, TEC can be determined directly by (Klobuchar, 1996),

$$\text{TEC} = \frac{f_1^2 f_2^2 (P_1 - P_2)}{40.3(f_2^2 - f_1^2)} \quad (2.5)$$

where P_i ($i=1,2$) is the pseudorange measurements on L1 and L2. Although the TEC determined by this formula is noisy because of the noisy code measurements themselves, it however gives the most direct way to determine TEC and thereafter the ionospheric delay ΔI_i ($i=1,2$). The ionospheric effect on GPS signals will be discussed in section 2.5.

2.4.4 Troposphere error

The troposphere is the lower part of atmosphere ranging from the Earth's surface to about 9-16 km in altitude. The signal received from a GPS satellite is refracted by the atmosphere as it travels to the user on or near the Earth's surface. The atmospheric refraction causes a delay that depends upon the actual path (slightly curved) of the ray and the refractive index of the gases along that path (Spilker, 1996b). The magnitude of tropospheric delay error varies between 2 or 3 m in zenith and the typical zenith value is

2.5 m. The tropospheric delay error can be categorized as two components: dry atmosphere effect and wet atmosphere or water vapor effect. The dry component of delay accounts for about 90% of the total error and the water vapor about 10% (Janes et al., 1989). The dry atmosphere zenith delay corresponds to approximately 2.3 m and varies with local temperature and atmospheric pressure in a reasonably predictable manner (Spilker, 1996b). The wet component of tropospheric delay varies over time e.g. 10-20% in a few hours and is less predictable even with surface humidity measurements (Spilker, 1996b). Comparably the dry delay varies less than 1% in a few hours. Although the size of the tropospheric delay error is significantly smaller than that of ionospheric delay, its wet component is difficult to model because of the high variability of the water vapor with location and time. Therefore the modeling error is primarily due to the poor performance of the tropospheric wet delay model. The unmodeled residual is about 3 cm in the zenith (Mendes, 1999). Various tropospheric error correction models are available including the models by Saastamoinen (1973) and Hopfield (1969).

2.4.5 Receiver clock error

The measuring of GPS range is the measuring of the time interval between GPS signal reception and signal transmission. That means the receiver must have a clock inside to precisely measure the time of arrival of GPS signals. For all receivers to have an atomic clock is not realistic because of their large size and very high cost. Therefore most receivers are equipped with a quartz crystal oscillator which is generally small, inexpensive and consumes little power. However some receivers, especially high-precision geodetic types of receivers used at the GPS reference stations, have I/O ports to permit the input of an external frequency standard from a cesium, rubidium, or even a hydrogen maser. When enough GPS satellites are tracked, the receiver clock error can be determined and the receiver clock can be synchronized to GPS time. This synchronization has an error of about 0.1 microsecond under SA and about 0.01 microsecond with SA off. The receiver clock errors can be cancelled out using differential method or estimated as an unknown along with coordinate parameters.

2.4.6 Multipath error

Multipath is a phenomenon where a signal arrives at a receiver's antenna via two or more different paths (Langley, 1998a). The multipath is usually noticeable when the antenna is set up in an environment with large reflecting surfaces such as buildings. To block the interference of the indirect, reflected signals with the direct GPS signals to antenna, a ground plane is considered to be an intrinsic part of the antenna (Langley, 1998a). The theoretical maximum multipath on P-code pseudorange is about 15 m and about 150 m on C/A code measurements (Bishop et al., 1985). The multipath effect on carrier phase measurements is significantly smaller with a maximum of about 5 cm (Seeber, 1993). The multipath effect can be diminished by: 1) careful selection of antenna location to avoid reflecting obstacles; 2) use of carefully designed antennas (choke ring) or use of extended antenna ground planes; 3) use of GPS receivers with special signal processing techniques, such as narrow correlators, multipath-estimating multiple-correlator channels (Langley, 1998a). The combination of the above measures may produce maximum multipath mitigation effects and give best quality of pseudorange and carrier phase measurements.

2.4.7 Receiver noise

The receiver noise level is a good indicator of the quality of GPS receivers. Both code pseudorange and carrier phase measurements from GPS receivers contain noise. But the carrier phase measurements have much lower noise than the code pseudorange ones. That is why in the ionospheric modeling discussed in Chapter 4 the carrier phase measurements are used to smooth the code measurements in order to reduce the noise level of the GPS derived TEC data. The noise level for C/A code measurements is about 0.3 m or even better while the carrier phase measurements is at the level of 2 mm (Parkinson, 1996b; Spilker, 1996c).

2.5 Ionospheric Effects on GPS Signals

The path of a radio wave is influenced by free electrons in the ionosphere when it is propagating through the ionosphere. The refractive index depends on the electron concentration and the magnetic field of the medium and the frequency and polarization of the transmitted wave.

2.5.1 The ionospheric storm effect

An ionospheric storm is caused by the ionospheric electron density turbulence in the F region which is usually due to a sudden burst of radiations from the Sun. It is characterized by the variations in TEC (Skone, 2001). During geomagnetic storms, the energetic particles from solar wind enter into ionosphere-thermosphere system and excite equatorward propagating gravity waves. At the mid-latitudes, the equatorward propagating waves drive the F-region to higher altitudes, resulting in ionization enhancements (Schunk and Nagy, 2000). It consists of three phases: positive phase, negative phase and recovery phase. In the positive phase of ionospheric storm, the ionospheric electron density grows and lasts for a few hours. The temporal characteristics of positive storm effects make them unpredictable and difficult in explaining features of the ionospheric response. In the negative phase, the electron density decreases and this process lasts several days. Negative storm effects are the dominant characteristic of the ionospheric response to geomagnetic activity enhancements (Cander, 1993; Cander and Mihajlovic, 1998) In the recovery phase, the ionospheric electron density returns to normal level before the storm. Ionospheric storms usually but not always occur in conjunction with geomagnetic storms and their phases are not related to the initial and main phases of a geomagnetic storm. They usually last one day and are the results of globally altered circulation caused by enhanced flux of energetic electrons (electron precipitation) into Earth's ionosphere. The behavior of individual storm depends on geomagnetic latitude, season, and local time (Schunk and Nagy, 2000). Ionospheric storms usually are observed at both middle and low latitude (Huang and Cheng, 1991).

During ionospheric storm events, the TEC has significant increase (during positive phase) and decrease (during negative phase) variations. The spatial and temporal variations in TEC results in a rapid spatial decorrelation of the ionospheric range delays between GPS stations. Large-scale gradients in TEC may cause a 1-2 ppm differential ionospheric range delay on L1 (Parkinson and Enge, 1996).

2.5.2 The scintillation effect

Ionospheric scintillation is a rapid change in the phase and/or amplitude of a radio signal as it passes through small-scale plasma density irregularities in the ionosphere, typically on a satellite-to-ground propagation channel (Conker et al., 2003). Scintillations are most common in regions that exhibit the most dynamic ionospheric behavior (Nichols et al., 2000) and are commonly observed in the high latitude auroral region and low latitude equatorial anomaly region (Skone and Knudsen, 2000). The strongest scintillation occurs in the equatorial anomaly regions at approximately $\pm 15^\circ$ latitude on either side of the geomagnetic equator (Nichols et al., 2000). During the daytime, the plasma is drifted due to the dynamo electric field at equatorial region caused by thermospheric winds (Schunk and Nagy, 2000). The plasma is diffused down and away from equator due to gravity and this causes equatorial anomaly or Appleton anomaly (Schunk and Nagy, 2000). During the night time, equatorial scintillation usually begins one hour after local sunset and generally tapers off by local midnight. This activity is caused by a rapid rise in the height of the ionosphere's F2 region above the magnetic equator after local sunset. It produces an instability that grows rapidly, generating irregularities that rise to heights sometimes exceeding 1,000 km.

Scintillation at the high latitudes is created by a different mechanism. Energetic particles from the Sun are trapped by the Earth's magnetic field and travel toward the poles along the magnetic field lines. When the particles reach the ionosphere, their interaction causes secondary ionization, which creates small-scale irregularities. This mechanism also causes phenomenon known as the aurora borealis and aurora australis. The strength and

frequency of polar/auroral scintillation are highly correlated with the 11-year sunspot cycle as well as the periods of high geomagnetic activity.

Scintillation demonstrates its most severe effects in regions like high latitudes (within and poleward of the auroral region) and equatorial area in the post sunset to local time midnight. During periods of solar cycle maxima, amplitude fading at 1.5GHz (GPS frequency) may exceed 20dB for several hours after sunset and in the central polar cap, GPS signals may suffer a fade of larger than 10 dB (Aaron and Basu, 1994; Fu et al., 1999). The scintillation activity adversely affects the satellite signal tracking performance of GPS receivers by causing cycle slips and loss of lock (Nichols et al., 2000) or even loss of GPS signal availability (El-Gizawy and Skone, 2002). Loss of the L2 signal will affect the GPS reference network's, such as WAAS, ability to monitor and correct ionosphere but it basically will not affect the L1 single frequency GPS users because GPS reference networks usually employ both L1 and L2 signals to perform their functions. However loss of the L1 signal will affect both GPS users and GPS reference receivers because most GPS users are equipped with only single-frequency GPS receivers. The L2 signal of codeless receivers is more sensitive to the scintillation activity (Skone, 2001) because of the relatively long signal integration time required to receive an encrypted L2 signal. The use of semicodeless receivers may have an advantage over the pure codeless receivers and can track through higher scintillation because they have some knowledge of encrypted code on the L2 signal.

CHAPTER 3

IONOSPHERE AND ITS MEASUREMENTS

This chapter will describe and analyze the ionosphere from the aspects of its formation, structure, characteristics and impacts. The techniques of measuring ionosphere are also elucidated.

On December 12, 1901 Guglielmo Marconi transmitted a radio signal over the Atlantic from Poldhu, England to Newfoundland, Canada marking the first successful wireless communication over long distance. However this transatlantic radio experiment was not in agreement with the mathematical theory of the diffraction of electromagnetic waves by the Earth's surface (Giraud and Petit, 1978). Three independent studies by Kenelly in the USA, Heaviside in Great Britain and Nagaoka in Japan furnished the correct explanation for the success of Marconi's demonstration. All three hypothesized a permanent conductive layer in the rarefied air which took on the name "Kenelly-Heaviside layer", namely the currently known ionosphere (Giraud and Petit, 1978).

3.1 Formation of Ionosphere

The ionosphere is characterized by the existence of free electrons and positively charged ions. When the molecules and atoms of the atmosphere receive enough external energy, one or more electrons is dissociated from the molecules or atoms. This process is called ionization. The solar extreme ultraviolet (EUV) radiation and particle precipitation are the two primary energy sources in the ionization (Schunk and Nagy, 2000). In the ionization process, the atoms or molecules become positively charged ions while the dissociated electrons become negatively charged free electrons. This forms the ionosphere. Because the number of positively charged ions is approximately equal to that of negatively charged free electrons, the ionosphere is electrically neutral.

Ionospheric ionization depends primarily on the Sun and its activity. In the daytime, the photons coming from solar ultraviolet spectral range or higher cause the neutral gas to produce free electron ion pairs due to the effect of photoionization (Kelley, 1989; Schunk and Nagy, 2000). In addition to photoionization, energetic particle, mainly electron, is another source causing ionization. During nighttime, ionization due to energetic particles maintains the ionosphere while photoionization disappears. The presence and absence of solar radiation cause the ionospheric day and night variations (Kasha, 1969). Figure 3.1 is a simplified explanation of the electron disassociation process when a molecule receives enough energy that exceeds threshold ionization energy.

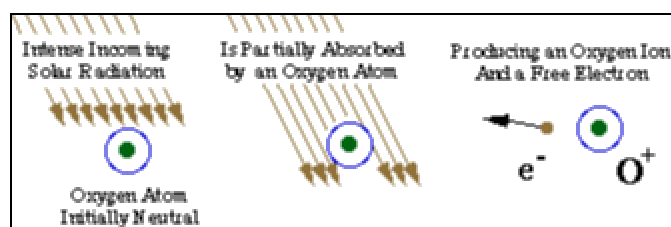


Figure 3.1 Illustration of Ionization Process (From NRL, 2003)

The electron densities in the ionosphere vary greatly with time (universal time, season and solar cycle), location (altitude, latitudes and longitude), and magnetic activities (Schunk and Nagy, 2000). Although the major ionization energy sources are from solar EUV and energetic particles, the magnetosphere also has a significant effect on ionosphere. On the other side, the solar wind pressure and orientation of the interplanetary magnetic field basically determine the strength and form of magnetospheric effect (Schunk and Nagy, 2000). Therefore, the solar activities play a critical role in the formation of ionosphere.

The ionosphere is usually separated into different layers, “D,” “E” and “F” layers, generally according to the maximum electron density at certain altitude. The F layer is further divided into “F1” and “F2” sub-layers. However, these different layers are only distinct in daytime ionosphere at mid-latitudes (Schunk and Nagy, 2000). “F2” layer

decays in the nighttime and a distinct E-F valley can appear to separate E-F2 layers (Schunk and Nagy, 2000).

3.2 Stratification of Ionosphere

The ionosphere, located between 60 and 1500 km above the Earth, is the part of the upper atmosphere where free electrons with sufficient density appreciably have influence on the propagation of radio frequency electromagnetic waves (Schaer, 1999). According to the spatial concentration of electron density, the ionosphere is spatially divided into a few different layers, namely, D, E and F layers, as shown in Figure 3.2.

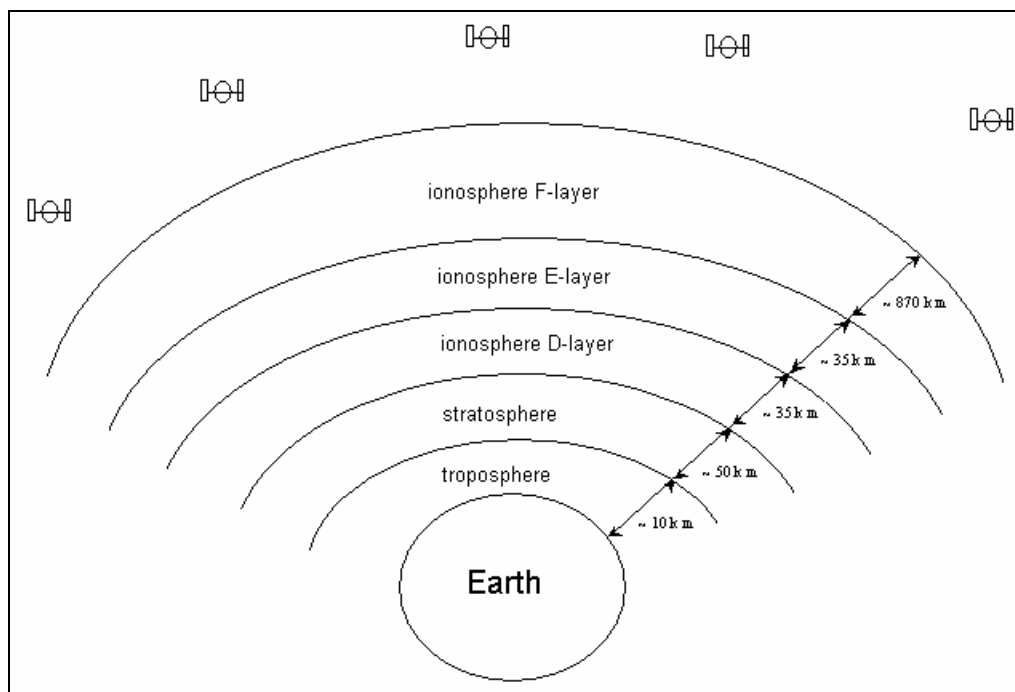


Figure 3.2 Atmosphere and Ionospheric Multiple Layers

The major property of each ionospheric region is the electron density, the number of free electrons per unit volume. It is now known that there are sub-divisions within these layers, particularly in the F layer, which has F1 and F2 layers. The electron density and temperature profiles for different layers are depicted in Figure 3.3. It shows that different layers have different electron density and that the peak electron density occurs in F layer

and can reach the value of 10^6 per cm^3 . The peak of electron concentration typically occurs in the range of 250-400 km (Goodman and Aarons, 1990). The factor that affects the peak density value to become larger is the recombination rate, during which the ions and electrons combine together.

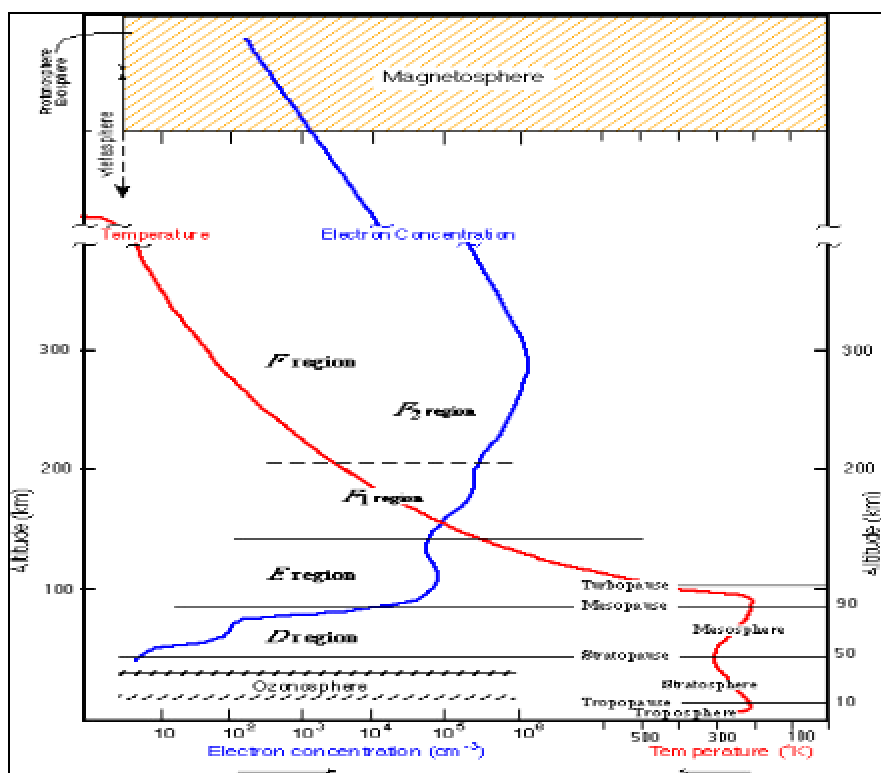


Figure 3.3 Electron Density and Temperature Profiles (From ION, 2004)

3.2.1 D-region

The D layer is the lowest part of the ionosphere and it is referred to the region between about 75 and 95 km above the Earth. This layer is primarily affected by solar radiation and free electron density is greatest shortly after noon and is extremely small at night or even disappears at night (Kasha, 1969; Hargreaves, 1992). Compared to other layers, the D layer is the most complex layer from a chemical point of view because of both its relative high pressure and several different sources contributing to ionization, including Lyman- α radiation, EUV radiation, X-ray, galactic cosmic ray and energetic particles

(Hargreaves, 1992). The D layer is the major place where the radio absorption occurs and the absorption in winter months would exceed the summer one by a factor of two or three, known as winter anomaly of ionospheric radio absorption (Hargreaves, 1992).

3.2.2 E-region

Above the D-region, from 90 to 150 km above sea level, lies the E-layer that is formed mainly by soft X-rays (Kasha, 1969; Kelley, 1989). The E layer is formed by absorbing long wavelength ultraviolet radiations with wavelength approximately 90 nm. At high latitudes, the E layer ionization is significant due to the precipitation of energetic electrons and protons. The electron density can reach 10^5 perm^3 in the daytime but it dramatically reduces to about $5 \times 10^3 \text{ perm}^3$ in the nighttime although it does not vanish (Hargreaves, 1992). The anomaly present in the E layer is sporadic-E phenomenon, which represents an ionization enhancement in the E region. A characteristic feature of sporadic-E is their small size. Its size can be as small as 0.6-2 km in width (Hargreaves, 1992). The principal cause of sporadic-E layer at middle latitude is a variation of wind speed with height (Hargreaves, 1992).

3.2.3 F-region

The F layer is the upper part of the ionosphere and its altitude ranges from 150 km to 500 km (Kelley, 1989). The F-region is formed mainly by solar radiation of about 20-90 nm wavelength (Kasha, 1969). The F layer is usually further divided into F1 and F2 sub-layers. Compared to F1 sub-layer and D and E layers, F2 sub-layer is the of most research interest for radio propagation because of its largest concentration of electrons (Hargreaves, 1992). F2 layer is also the part in ionosphere that is the most variable, anomalous and difficult to predict (Hargreaves, 1992). Because the F2 region has the largest electron concentration in the ionosphere, the single layer ionospheric model based on GPS data usually selects an altitude ranging from 250 to 400 km above the Earth as the height of the single shell to which the slant ionospheric TEC measurements are mapped to the zenith direction.

3.3 Solar Activities and Space Environment

3.3.1 Solar radiation and energetic particles

Sun is a star of radius 696,000 km that continuously output radiation energy that allows the life on the Earth to develop. The solar energy is generated by nuclear fusion of hydrogen into helium in a very hot central core, which is about 16 million kelvin (Schunk and Nagy, 2000). The Sun's atmosphere is composed of three layers, namely photosphere, chromosphere and corona and it extends to a region beyond 10 radii. The photosphere is a thin and cool layer that emits visible radiation. The outer layer, corona, contains very hot ($\sim 10^6$ K) ionized plasma that typically extends several radii from the Sun (Schunk and Nagy, 2000). Due to the effect of high temperature in corona, the plasma continuously outflows from corona away from the Sun. The outflow plasma is called solar wind. While the solar wind rapidly escapes from corona, it also drags the Sun's dipole magnetic field lines with it into interplanetary space although the magnetic field is weak (Schunk and Nagy, 2000). Solar wind is one type of particle outflow that bring energy to the Earth and consequently contributes to the ionization in ionosphere. The solar wind, carrying the interplanetary magnetic field (IMF) with in, has significant impact on the magnetosphere around the Earth (Cowley, 1998), aurora (Akasofu, 1998), and geomagnetic storms (Tsurutani and Gonzalez, 1998) and ionosphere (Richmond, 1998). The interaction of solar wind with the Earth's magnetic field is illustrated in Figure 3.4. The solar wind plasma cannot directly penetrate the outer border of magnetosphere, the magnetopause, but is deflected around it. Figure 3.4 shows that the solar wind is deflected by the Earth's magnetic field when it approaches the Earth. Figure 3.4 shows that the solar wind is first deflected by the bow shock. At the Earth's bow shock, the solar wind is slowed to subsonic velocities (Russell, 1987). The space between the bow shock and the Earth is called magnetosphere. The existence of magnetosphere prevents the energetic particles from direct penetration into the atmosphere. Figure 3.4 also shows that the dipolar terrestrial magnetic field is compressed by the high speed solar wind on the dayside and on the opposite side, the nightside of the Earth, the solar

wind transforms it into a prolonged, tail-like structure, which reaches far beyond the lunar orbit (Kamide and Baumjohann, 1993). Another type of particle outflow from Sun is called coronal mass ejection (CME). CME is caused by the break of one end of solar magnetic flux loop, which is originally rooted in sunspots (Schunk and Nagy, 2000). Before the break of the magnetic loop, the curved magnetic field accumulates hot plasma. Some CME was associated with solar flare, a powerful explosion in the atmosphere above sunspots, but most CME are independent of solar flares (Joselyn, 1998; Schunk and Nagy, 2000). Besides solar wind and CME, both of which transfer energy from the Sun to Earth, another important method of energy transmission is solar electromagnetic radiation. The energy contained in radiation is by far more dominant than both solar wind and CME, several order higher in magnitude (Schunk and Nagy, 2000). In comparison, the solar wind contains only one-millionth of the total energy radiating from the Sun (Lyon, 2000). The radiation is composed of energy from infrared (52%), visible (41%), ultraviolet (<7%) spectral regions and some minor energy contributors like radio, xray emissions, extreme ultraviolet (EUV) (Schunk and Nagy, 2000).

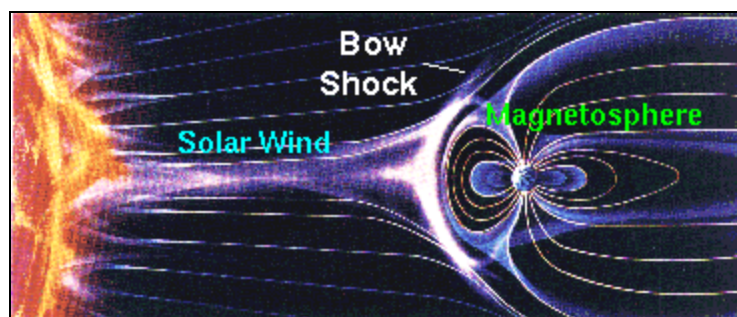


Figure 3.4 Earth's Magnetic Field Encountering Solar Wind (From UTK, 2003a)

3.3.2 Magnetic field

The Earth's magnetic field, approximated as a tilted dipolar field, is produced by the motion of electrical charges (Giraud and Petit, 1978). The magnetic field strength depends on the latitude and the radial distance from the Earth's center. At a given latitude, the magnitude is inversely proportional to the cube of the radial distance. At a

given radial distance (altitude), the induction increases by about a factor of two from the geomagnetic equator to the poles (Giraud and Petit, 1978). The magnetic field at ground level is subject to both quasi-diurnal and irregular short-term time fluctuations, with periods varying from the order of hours to the order of seconds and less. This variation is very small, usually a fraction of one per cent of the total value, and major events can cause 1~2% change. The international Kp index, valued from 0 to 9, is used to define the magnitude of such magnetic perturbations (Giraud and Petit, 1978). The Kp index characterizes the irregular planetary geomagnetic activities. The quasi-diurnal components of magnetic fluctuation include the solar quiet variation, a diurnal oscillation with a period of 24 hours and the lunar variation, a semi-diurnal oscillation with a period of 24.8 hours (Giraud and Petit, 1978).

The Earth's magnetosphere is a cavity filled with hot but low-density plasma which is surrounded by denser but colder solar wind plasma (Kamide and Baumjohann, 1993). The magnetosphere is topographically located between the outer boundary formed by magnetopause and solar wind and inner border formed by ionosphere (Kamide and Baumjohann, 1993). The magnetopause is situated where the geomagnetic pressure of the Earth's magnetic field and the kinetic pressure of the solar wind are in equilibrium (Giraud and Petit, 1978). Between solar wind and ionosphere, Earth's magnetic field acts as wires to relay the energy from solar wind to ionosphere in the form of heat (Lyon, 2000). The heated charged particles are accelerated to circle close to the Earth. The region where the Earth's magnetic field has an effect on the particles is called magnetosphere. The Earth's magnetism is strong enough to keep the charged particles in solar wind from approaching the Earth closer than 10 Earth radii on the sunward side (Lyon, 2000).

3.3.3 The plasma

When the atoms and molecules receive enough energy, the electrons are dissociated from them. The neutral gas becomes a collection of conductive free electrons and ions, which

is the fourth matter state. Sir William Crookes, an English physicist, identified this state of matter, now called plasma, in 1879 (plasma, 2003). The particle density in plasma is required to be low enough so that the short-range collisions are negligible (Parks, 1991). The plasma in Earth's ionosphere includes free electrons, positive charge ions such as N_2^+ , O^+ , NO^+ .

The plasma exhibits two different kinds of properties. One is due to the interaction between the individual particles. The other is due to the collective behavior of all the particles (Parks, 1991). The discrimination of individual particle from collective behavior is the Debye length (λ_D) which is defined as (Schunk and Nagy, 2000):

$$\lambda_D = \left(\frac{\epsilon_0 k T_e}{n_e e^2} \right)^{1/2} \quad (3.1)$$

where ϵ_0 is the permittivity of free space; k is Boltzmann's constant; T_e is electron temperature; n_e is electron density and e is electron charge. Plasma phenomena that vary over distance less than λ_D , the ions and particles can be treated as individual particles. If the distance from the center of an ion is larger than λ_D , there will be no electric field due to the ion (Davies, 1990). That is to say only within this distance, the ion has effects on electrons and ions. When the number of particles in a sphere is sufficiently large, the collective behavior dominate. This sphere, called Debye sphere, is defined by (Schunk and Nagy, 2000):

$$N_{\lambda_D} = \frac{4\pi}{3} \lambda_D^3 n_e \quad (3.2)$$

In the Earth's magnetic field, the movements of charged particles spiral around the magnetic field line in a helical path. The movement velocity of electron can be decomposed as parallel component and perpendicular component, which are parallel to and perpendicular to the magnetic field, respectively (Davies, 1990). The movement parallel to magnetic field is unaffected but the perpendicular component is affected by the

magnetic field with a Lorentz force (Davies, 1990). The projection of the combined result of the parallel component and perpendicular component on a plane is that particles move in a circle. Because of the thermal movement, the electrons and ions are continuously moving in a way spinning in Earth's magnetic field (Davies, 1990). This movement can be illustrated by Figure 3.5.

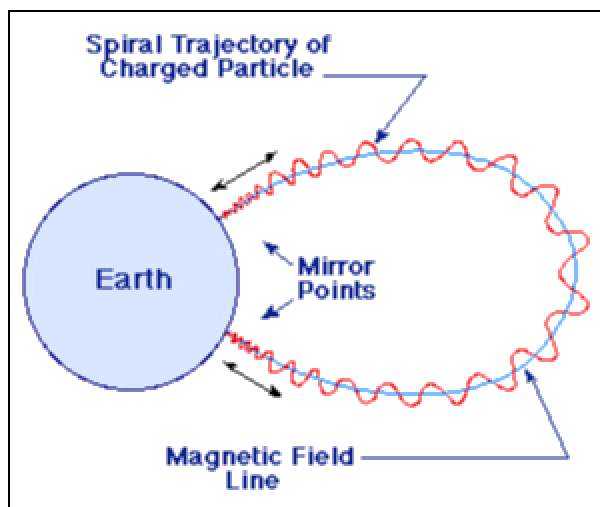


Figure 3.5 Spiraling Motion of Charged Particles in Geomagnetic Field (From UTK, 2003b)

3.4 Ionosphere Phenomena and Solar Activities

The ionosphere and solar activity and the Earth's magnetosphere are highly related. The ionosphere is a particularly variable part of the Earth's atmosphere. Solar activity is highly linked with ionospheric structure and dynamics, stronger activity typically implying enhancement in the maximum electron concentration in the ionospheric layers (Goodman and Aarons, 1990). Two types of solar phenomena affect the Earth: electromagnetic flux radiation from solar flares and the energetic particles which is fed by solar flares, coronal holes, and disappearing filaments (Goodman and Aarons, 1990; Cleveland et al., 1992). The direct electromagnetic radiation travels to the Earth at the speed of light (8 minutes) while the transit time of the solar wind particles ranges from 1 to 6 days. Energy and momentum is transferred from the solar wind to magnetosphere and ionosphere (Lyon, 2000). The Sun emits electromagnetic radiation over a wide

spectral range, a stream of plasma and bursts of energetic particles (Hargreaves, 1992). The Sun is the major energy source that ionizes the ionosphere. The Sun's atmosphere is comprised of three layers: photosphere, chromosphere and corona (Parks, 1991). Because the solar atmosphere is not static equilibrium, the most outer layer, corona, expands into space. This corona is usually what we call solar wind. In addition to electromagnetic energy from the Sun, the particulate energy from solar wind also reaches the proximity of the Earth and has a close effect on the Earth's ionosphere (Davies, 1990; Parks, 1991).

Many ionospheric phenomena are associated with solar activities directly or indirectly. Outside the ionosphere, there exists a magnetosphere that is due to Earth itself is a magnet. When the solar wind approaches the magnetosphere, the geomagnetic field is compressed and the interaction between solar wind and magnetosphere causes the associated ionospheric phenomena. These phenomena include sudden ionospheric disturbances, ionospheric storm, polar cap absorption (PCA) events, traveling ionospheric disturbance (large scale) and associated event in geomagnetic field, aurora, and magnetospheric substorms (Davies, 1990).

The sudden ionospheric disturbances (SID) that are caused by solar flares have various forms, including shortwave fadeout, sudden phase anomaly, sudden frequency deviation, sudden cosmic noise absorption, sudden enhancement/decrease of atmospherics, and sudden increase in total electron content (Davies, 1990). Solar flare is a transient brightening in a small active region on solar surface, which lasting for 3-4 minutes to several hours with an average lifetime of about 30 minutes (Campbell, 2003). The sudden increase in total electron content occurs in D, E and F regions and the increase may amount to 5% of the background electron content (Hargreaves, 1992).

Polar cap absorption (PCA) is caused by intense ionization due to highly energetic protons during large solar flares (Davies, 1990). Its durations can vary from one day to about 10 days. Radio links can be severely disrupted in the polar regions during PCA

events, including effects on aircraft communications (Hargreaves, 1992). In addition to radio absorption effects in polar ionosphere, the proton influx emitted from the solar flares particularly has effects on the condition of very low frequency (VLF) waves. Due to the high sensitivities of VLF to the PCA, it provides a good monitor to the event (Hargreaves, 1992).

The occurrence of ionospheric storm is closely associated with geomagnetic storms, auroral and magnetospheric storms (Davies, 1990). Ionospheric storm is the most important disturbance in terms of its adverse impact on the society due to its duration (several days), geographical distribution and adverse effects on radio spectrum (Davies, 1990). Compared to polar cap absorption and sudden ionospheric disturbances events, PCA events are severe and last long but they are rare and only affect polar cap areas where is sparsely populated; SID events affect populated areas but they are relatively short (Davies, 1990). On the contrary, ionospheric storms affect mid and low latitudes where most radio communication activities occur. Magnetic storms are disturbances of the geomagnetic field and occur when there is a large sudden change in solar wind pressure on the magnetopause. The geomagnetic storm is especially strong when the sudden change is associated with sufficiently large southward IMF component (Baker, 1986). During the start of a geomagnetic storm, the gravity wave can be excited at high latitudes and their propagation to lower latitudes leads to traveling ionospheric disturbance (Schunk and Nagy, 2000). A result after geomagnetic storm is that a large amount of energy is deposited into the ionosphere-thermosphere system at high latitudes during the storm. Responding to this, the ionosphere at high latitudes has a change in electron density (Schunk and Nagy, 2000). If the storm results in an electron density increase, it is called positive ionospheric storm. If it results in an electron density decrease, it is called negative ionospheric storm. Aurora is a result of the entry of energetic particles from magnetosphere to atmosphere. Similar to magnetic storm, aurora is connection with solar wind (Hargreaves, 1992). Auroral zones are relatively narrow belts located between geomagnetic latitude 65° and 70° , with the phenomenon

occurrence rate falling on both equatorward and poleward sides (Hargreaves, 1992). The auroral consist of a series of upper-atmosphere phenomena including luminous aurora, radar aurora, auroral radio absorption, auroral X-rays, magnetic disturbances and electromagnetic emissions (Hargreaves, 1992).

3.5 Various TEC Measuring Techniques

In most ionospheric modeling methods based on GPS measurements, the total electron content values are employed as the observation data for modeling, e.g. Komjathy (1997), Skone (1998) and Schaer (1999). The procurement of these TEC observations can be made via various observing techniques. The mostly used measuring techniques include ionosonde, incoherent scatter radar, and dual frequency GPS data which is the primary TEC source in this thesis.

3.5.1 Ionosonde

Ionosonde or ionospheric sounder is the oldest remote sensing device but still widely used for measuring the ionosphere (Schunk and Nagy, 2000). By 1947, an instrument known as the ionosonde was routinely used in the field to automatically measure the characteristics of the ionosphere. The ionosonde operates according to the principle that refraction index is proportional to the free electron density in the ionosphere. The ionization in the atmosphere forms several horizontal layers, and so does the free electron concentration. Therefore the ionosphere refractive index varies with height. Ionosonde broadcasts a range of frequencies vertically and the reflection takes place when the frequency equals the plasma frequency, which is a function of free electron density (Schunk and Nagy, 2000). The ionosonde measures the time the each frequency takes for a round trip, thus the electron density at the reflected height in ionosphere can be calculated. An ionosonde broadcasts a sweep of frequencies, typically in range of 1-20 MHz (Kelley, 1989). As the frequency increases, each wave is refracted less by the ionization in the layer, and so each penetrates further before it is reflected. As a wave approaches the reflection point, its group velocity approaches zero and this increases the

time-of-flight of the signal. Eventually, a frequency is reached that enables the wave to penetrate the layer without being reflected. Due to the existence of the geomagnetic field, the formula of refractive index has two solutions (Hargreaves, 1992). That means the wave may propagate at two speeds. These are called ordinary wave and extraordinary wave, whose refractive values correspond to the positive and negative values respectively.

The frequency at which a wave just penetrates a layer of ionization is known as the critical frequency of that layer. The critical frequency is related to the electron density by the simple relation (Kelley, 1989):

$$f_c = 8.98\sqrt{N_e} \text{ for the ordinary mode and} \quad (3.3)$$

$$f_c = 8.98\sqrt{N_e} + 0.5Be/m \text{ for the extraordinary mode.} \quad (3.4)$$

where f_c is the critical frequency in Hz, N_e is the electron concentration in $e1/m^3$, B is the magnetic field strength in A/m , e is the charge on an electron in C and m is the mass of an electron in kg .

According to the name of critical frequency, it is understandable that the frequencies that are higher than this critical frequency will not be reflected. The actual ionosonde is more complex. First, ionosonde frequency travels with group velocity rather than speed of light because of the existence of free electrons in ionosphere (Kelley, 1989). The traveling speed of the radio signal itself is a function of the density of free electrons. Thus the height determined by using light speed as radio traveling velocity is called virtual height (Kelley, 1989). Therefore the virtual height will be greater than the true height. Another complication of ionosonde is associated with effect of the geomagnetic field, which results in multiple values of ionospheric refractive index (Kelley, 1989). Although these complications, ionosonde have been used in ionosphere research for decades and still are very useful (Schunk and Nagy, 2000).

3.5.2 Incoherent scatter radar

The incoherent scatter radar (ISR) transmits the radio waves into the ionosphere and the radio waves are reflected back to the transmitter after they meet with the ionospheric electrons (Kelley, 1989). Like most radar systems, ISR transmits pulse to ionosphere and the range to target region is determined by half of return time multiplying the speed of light. Each electron targeted by ISR inherently echoes back a certain amount of energy, thus the strength of the returned signal is proportional to the electron density of the area that is studied by ISR (Kelley, 1989).

Besides the measuring of the electron density, the incoherent scatter radar can also function to measure the doppler shift of echoed pulses. Because the electrons are not stationary in ionosphere but moving in a random thermal motion, the reflected echos will have different frequencies from that of the original transmitted radio waves because of the doppler shift effect. The echoed waves will not be at a single frequency, but a spectrum of frequencies near the transmitter frequency because the various velocities of the electron motions. As the temperature of electrons increases, the average velocity of the electrons increases and the spectrum of the velocities increases as well. In another word, the spectrum of reflected frequencies increases. That is to say the width of the spectrum is a measure of the ionosphere electron temperature (Kelley, 1989). Therefore the incoherent scatter radar can be used as a thermometer of the ionosphere. In addition to the thermal motion of the ionosphere, the velocity of plasma wind (motion of the mixture of ions and electrons) can also be measured by the Doppler shift. Thus an incoherent scatter radar also functions as a wind speedometer.

3.5.3 Dual frequency GPS receivers

Taking advantage of the dispersive property of the ionosphere, the GPS signals operating at two different frequencies can be used to measure the integral of ionosphere density, namely, the total electron content (TEC). TEC is a useful parameter for ionospheric studies and transionospheric systems (Goodman and Aarons, 1990). If not taking the

receiver and satellite inter-frequency biases into account, the TEC can be directly derived from two pseudorange measurements observed at L1 and L2 frequencies (Klobuchar, 1996).

$$\text{TEC} = \frac{f_1^2(P_1 - P_2)}{40.3(1 - \gamma)} \quad (3.5)$$

where $g = \left(\frac{f_1}{f_2}\right)^2 = \left(\frac{1575.42}{1227.6}\right)^2 = \left(\frac{77}{60}\right)^2$ is the squared L1 and L2 frequency ratio. The

advantage of deriving ionospheric TEC from GPS data is that firstly, the TEC can be readily determined from GPS observations based on equation (3.5); secondly the GPS observations can be easily obtained from a dual-frequency GPS receiver. Nowadays a lot of local and regional GPS reference networks are deployed in the world. The accessibility and availability of these GPS reference network observations provide a solid basis for the derivation of TEC data and ionospheric modeling. More detailed derivations can be found in Chapter 4.

3.6 Impacts of Ionosphere

The ionosphere, as an important part of the space weather, may cause serious practical consequences on the people's daily life. The change of current flowing through ionosphere can cause disruption to power distribution system, long-distance telephone networks, and corrosion of pipelines on the ground (Lyon, 2000). The following two sections discuss the ionosphere impacts on GPS/GNSS and other systems.

3.6.1 The impact on GPS/GNSS

GPS signals transmitted from GPS satellites penetrate through the ionosphere and they suffer from an appreciable ionospheric delay due to the existence of large amount of free electrons. During geomagnetic storms, a locally disturbed ionosphere can cause irregular delays to GPS signals. The irregular delays due to geomagnetic storms can represent positioning errors of dozens of metres at a single receiver (Kleusberg, 1993). GPS

receiver signal tracking performance can be degraded during storm events (Knight et al., 1999). Large percentages of data corruption (up to 20%), represented by occurrence of carrier phase cycle slips, were observed at equatorial regions during ionospheric scintillation period (Skone, 2001). Complete loss of GPS signals may occur during some F-region scintillation event (Campbell, 2003). Even using double differencing method (differencing between two receivers and two satellites), the residual ionosphere can still cause about 2 ppm error on geometry-free combination observations on baselines of about 50 km under ionospheric quiet conditions (Alves et al., 2002). More recently, more and more satellite based augmentation systems (SBAS) have been in development, like U.S. Wide Area Augmentation System (WAAS), European Geostationary Navigation Overlay Service (EGNOS) and Japanese Multi-functional Transport Satellite (MTSAT) Satellite Based Augmentation System (MSAS) as well as an initiative of Brazilian testbed (Doherty et al., 2002). The small gradient ionosphere has small effects on SBAS and high capability for ionospheric corrections is available in most time except in rarely extreme geomagnetic storms (Doherty et al., 2002). The ionospheric effects have most serious impact on low latitude SBAS. The test results in South American regions showed that RMS errors of residual ionospheric range could reach 1.9 m under quiet conditions, compared to 0.5 m level at mid latitudes (Komjathy et al., 2002).

3.6.2 The impact on other systems

Besides the significant impact on GPS/GNSS satellite navigation systems, the ionosphere also affects the performance of other systems. Sharp variations in the ionospheric ion and electron densities caused by geomagnetic storms can lead to radio signal fluctuations and even blackouts. The risk level of high energy particle radiation can also threaten or damage satellites and spacecraft microelectronics systems, in particular during geomagnetic storms when a large amount of charged particles are generated. A power blackout occurred on March 13, 1989 to a Hydro-Quebec power system due to the geomagnetic storm (Kappernman and Albertson, 1990).

CHAPTER 4

IONOSPHERE TOMOGRAPHIC MODELING

This chapter will first describe the concept of ionospheric modeling and provide an overview of the existing models using GPS measurements and their limitations. A TEC smoothing algorithm is then presented as well as the derivation of formula for recursive error estimation of the smoothed TEC data. A close form of analytical expressions has been developed that integrate ionospheric TEC smoothing with tomographic modeling to allow simultaneous TEC smoothing and model estimation. Based on GPS data from local area and wide area GPS reference networks, the developed model can be used to provide predicted ionospheric corrections for GPS real-time positioning within a GPS reference network.

4.1 Concept of Ionosphere Modeling

Modeling is the creation of a representation of a system of interest. The ionosphere modeling investigated in this thesis is the establishment of a representative formula for the studied regional/global ionospheric electron density field and evaluation of the formula's overall performance.

The ionospheric modeling involves procedures of collecting measurements about ionosphere, data processing and analysis and final result validation. In this research, the measurements about ionosphere is the smoothed total electron content derived from dual-frequency GPS data. The data processing and analysis is completed using specific methods and tools, such as tomographic model and the "IonoTomo" software developed in this research. Final result validation is executed by comparing the modeling results with the truth data. In this thesis, the model's performance is evaluated by comparing the model-produced ionospheric predictions to the ground-observed ionospheric data.

4.2 Overview of 2D Models and Limitations

To date, a variety of two-dimensional (2D) ionospheric models are available and have been used for various applications depending on their accuracy requirements. A good summary of ionospheric models can be found in El-Arini et al. (1995). These models could in general be categorized as two types: grid-based models and non-grid-based models (El-Arini et al., 1995). Even in the grid-based models, a number of algorithms were developed due to the use of different weighing schemes and have been investigated by many researchers (El-Arini et al., 1993 and 1994; Gao et al., 1994; FAA, 1997; Skone, 1998; Liao and Gao, 2001). As to non-grid-based models, they include the least-squares fit model, spherical harmonic analysis, spherical cap harmonic analysis as well as adjusted spherical harmonic analysis (El-Arini et al., 1995). These non-grid-based models use different function formulations, e.g. polynomial functions (Coster et al., 1992; Komjathy, 1997) and spherical harmonics (Schaer, 1999; Walker, 1989). A common characteristic of these models is that they map the slant ionospheric measurements to a single shell that is located between 250 km and 400 km in altitude above the Earth. The hypothesis behind these models is that all the ionospheric electron concentration is concentrated in a single shell and the ionospheric delay occurs in that shell. This assumption is largely correct because the F2 region, where the largest electron concentration occurs, is located in the region 250~400 km above the Earth surface. Nevertheless, the ionospheric electrons are also distributed within other layers such as D and E layers. Secondly, the F2 layer physically is not a single shell. The height with peak electron density varies with time and location. Previous research results have indicated that the variation of ionospheric shell height might cause a modeling error of several TECU (Komjathy, 1997).

To have a general understanding of the mechanism behind the ionospheric modeling using GPS data, several typical ionospheric modeling methods are described in the following sections and their characteristics are analyzed.

4.2.1 Broadcast model

The broadcast model currently used by GPS was designed to correct ionospheric refraction delays for single frequency GPS users (Klobuchar, 1986). The broadcast or Klobuchar model uses a half cosine function to represent the diurnal variation of TEC in the single frequency GPS user algorithm. The half cosine is expressed as (Klobuchar, 1975):

$$T_{\text{iono}} = \frac{1}{M(\text{ele})} \left\{ \text{DC} + A \cos \left[2\pi (t - \phi) / P \right] \right\} \quad (4.1)$$

where

DC is the night-time constant offset term, set to 5 ns corresponding to 1.5 m ionospheric delay on L1;

A is the amplitude term;

t is local mean solar time at the subionospheric point;

ϕ is the phase of the maximum vertical ionospheric delay which is empirically set to be at 14:00 hour local mean solar time;

P is the period;

M(ele) is the mapping function which converts the slant ionospheric time delay to the vertical time delay.

Both the amplitude term A and the period P can be calculated with a cubic polynomial in geomagnetic latitude using the eight coefficients broadcast in navigation messages. These eight coefficients describe the worldwide behavior of the Earth's ionosphere. It has been found that the electron density at the peak of the F region could be better modeled by using geomagnetic latitude than geographic latitude (Klobuchar, 1996). The implementation details of this algorithm can be found in Klobuchar (1996).

The Klobuchar model has a low efficiency in correcting ionospheric error for single frequency users. Only about 50% of the total ionosphere errors can be removed using this

model (Klobuchar, 1987). This is because GPS satellite messages can only include eight coefficients to describe the worldwide behavior of the Earth's ionosphere. Furthermore, these coefficients are not updated more than once per day, and even not so often. Finally the simple ionospheric model used limits the obtainable accuracy of the algorithm (Klobuchar, 1996). Although the broadcast model has low accuracy to model the ionospheric delay, it however is frequently used because of its simplicity and easy implementation, particularly for GPS positioning and navigation applications where high positioning precision is not required.

4.2.2 Grid model

The grid model is another popularly studied ionospheric model, e.g. El-Arini et al. (1993 and 1994), Gao et al. (1994), FAA (1997), Skone (1998), Liao (2000), Liao and Gao (2001). The US FAA-developed WAAS also uses the grid model to estimate the ionospheric vertical delays at fixed ionospheric grid points (IGPs) (Skone, 1998; El-Arini et al., 1999; Rho and Langley, 2002). The basic concept of the grid model is that the area being modeled is represented by the grid points. The grid points are spaced 5° by 5° between 55°S and 55°N and larger beyond this region (RTCA, 1998). A proposal has been made to add more IGPs to the grid and would allow 5° by 5° spacing between 60°S and 60°N (El-Arini et al., 1999). The model formula for estimating ionospheric vertical delays at the IGPs is given as (Skone, 1998):

$$\text{TEC}_{rs}(t_j) = \frac{1}{M(\text{ele})} \sum_{i=1}^4 W_i(t_j) \times \text{VTEC}_i(t_j) + B_r + B^s + \varepsilon_{\text{TEC}} \quad (4.2)$$

where

$\text{TEC}_{rs}(t_j)$ is the TEC measurement derived from receiver r and satellite s at time t_j ;

$\text{VTEC}_i(t_j)$ is the values of the vertical TEC (VTEC) delay at the four grid points surrounding the ionospheric pierce point (IPP);

- $W_i(t_j)$ is the weight function that determines the contribution of the ionospheric vertical delay at the corresponding IGP to the ionospheric delay at the IPP;
- $M(\text{ele})$ is the mapping function which projects the ionospheric slant delay at IGPs to the vertical direction with elevation angle ele ;
- B_r is the inter-frequency bias for receiver r ;
- B^s is the inter-frequency bias for satellite s ;
- ϵ_{TEC} is the TEC measurement noise.

Compared to non-grid-based ionospheric models, the grid-based model has larger amount of information that needs to be transmitted to users while non-grid-based models only needs to broadcast the coefficients (El-Arini et al., 1995). More important, the grid-based model needs to select a single ionospheric shell to which the vertical ionospheric delays at the ionospheric grid points. Results by Gao et al. (2002a) showed that grid model results were in agreement with the results from Center for Orbit Determination in Europe (CODE) IGS data analysis center at the level of 2 to 4 TECU during ionospheric very quiet days (Kp index ranging 1 to 2) and at the level of 4 to 7 TECU on days with medium ionospheric activities (Kp index ranging 3 to 4) in regional area GPS networks. This indicated that the modeling accuracy of the grid model would severely be degraded with increased ionospheric activities.

4.2.3 Polynomial function model

Another type of ionosphere model is the polynomial function model. Komjathy (1997) proposed the University of New Brunswick (UNB) ionosphere model which uses the ionospheric measurements from a dual frequency GPS receiver. The model can be written as (Komjathy and Langley, 1996; Komjathy, 1997):

$$\text{TEC}_{rs} = M(\text{ele}) \left[a_{0,r}(t_j) + a_{1,r}(t_j) d\lambda_{rs} + a_{2,r}(t_j) d\phi_{rs} \right] + B_r + B^s \quad (4.3)$$

where

- TEC_{rs} is the ionospheric observations in unit of TECU, made at time t_j by receiver r and satellite s ;
- ele denotes the elevation angle of satellite s viewed by receiver r at the sub-ionospheric point, intersection of the GPS signal ray path from a satellite to a receiver with the thin-shell ionosphere;
- $M(ele)$ is the mapping function projecting the line of sight ionospheric measurement at elevation angle ele to the vertical;
- $a_{0,r}(t_j)$ is the parameter for the spatial linear approximation of TEC in unit of TECU, estimated at each receiver r ;
- $a_{1,r}(t_j)$ is the parameter for the spatial linear approximation of TEC in unit of TECU per degree, estimated at each receiver r ;
- $a_{2,r}(t_j)$ is the parameter for the spatial linear approximation of TEC in unit of TECU per degree, estimated at each receiver r ;
- $d\lambda_{rs}$ is the difference between the longitude of a sub-ionospheric point and the longitude of the mean sun. $d\lambda_{rs} = \lambda_{rs} - \lambda_0$;
- $d\phi_{rs}$ is the difference between the geomagnetic latitude of a sub-ionospheric point and the geomagnetic latitude of the station r . $d\phi_{rs} = \phi_{rs} - \phi_0$;
- B_{r_i} is the receiver inter-frequency bias;
- B^{s_i} is the satellite inter-frequency bias.

A distinct characteristic of this model is that three ionospheric parameters and a receiver inter-frequency bias parameter are linked to each station so that the latitudinal and longitudinal gradients can be estimated for each station. After the estimation of the parameters associated with each station, an interpolation is necessary in order to estimate the ionospheric delay at each regularly spaced grid point, e.g. 5° by 5° for global ionosphere TEC maps (Komjathy, 1997). The users inside the 5° by 5° grid points, an

interpolation has to be performed to obtain the ionospheric corrections at user location using the TEC values at grid points derived from previous interpolation. Therefore two interpolations are involved when the users need to estimate ionospheric corrections, which is one more than the grid-based model. The double interpolations might bring more interpolation uncertainties into the user ionospheric corrections than one time interpolation. This model was tested during a medium solar activity period in 1993 and the comparisons showed that the standard deviation was about 9 TECU with TOPEX/Poseidon (T/P)-derived TEC data on a global scale. The tests conducted during low solar activity in 1995 indicated a standard deviation about 5 TECU between the UNB TEC results and T/P data (Komjathy, 1997).

In addition to aforementioned limitations associated with each ionospheric model discussed, a common hypothesis made by these models is that all the ionospheric delay occurs in an ionospheric shell at a selected height above the Earth. An assumption of a single thin ionosphere shell with a fixed altitude between 250 and 450 km above the Earth's surface has been used in all the two-dimensional models. Typically they select a height value of 350 km as the altitude of the ionosphere shell assumed with maximum electron density. This assumption is not necessarily in agreement with real physical conditions of ionosphere and any discrepancy will result in additional ionospheric modeling errors. Komjathy (1997) studied the effect of a fixed ionospheric shell height on the final modeling results and concluded that taking the temporal and spatial variation of the ionospheric shell height into account can change the TEC estimate by up to 1 TECU for mid-latitude conditions at low solar activity levels. During periods of higher solar activity, the effect of the variation of ionospheric shell height is expected to increase (Komjathy, 1997). Next, based on the single shell concept, all the ionospheric delay measurements are mapped to that single spherical plane. This means those ionospheric models are essentially two-dimensional (2D) in nature. The variation of ionospheric vertical profile is reflected only at the altitude in accordance with the height of single

layer model. In order to characterize the vertical profile variations at different altitudes, multiple-layer model should be developed.

4.3 Overview of Other Models Based on Tomography and Limitations

Due to the limitations of the single layer models as discussed above, using tomographic technique method to model ionosphere has started to receive more attentions in the GPS community (Hansen et al., 1997; Hansen, 1998; Hernández-Pajares et al., 1999 and 2000; Colombo et al., 2000 and 2002; Liu and Gao, 2001a and 2001b). Although ionosphere tomographic modeling has been investigated since the early 1990 (Raymund et al., 1990 and 1994; Raymund, 1995; Howe, 1997; Howe et al., 1998), the early investigations have been conducted based on longitudinally aligned data such as Navy Navigation Satellite System (NNSS) data rather than network-based GPS data (Raymund et al., 1994; Raymund, 1995) or simulated ionospheric data (Raymund et al., 1990; Howe, 1997; Howe et al., 1998). The problem associated with the use of NNSS data is that only a relative TEC can be observed, that is, the TEC observed at each station is offset by an unknown constant (Leitinger et al., 1975). In addition, the measurement distribution of longitudinally aligned stations is fundamentally different from that of GPS network of stations. The consequence of the former is that the TEC observation distribution is restricted to longitudinal alignment. This will result in numerical difficulties in the inversion of the tomographic model. Moreover, the tomographic modeling results obtained with longitudinally aligned stations like NNSS data were actually longitudinal slice of the ionosphere field. The investigation of integrating tomographic technique with GPS data has not been conducted until in recent years (Hansen et al., 1997; Hansen, 1998; Hernández-Pajares et al., 1999 and 2000; Colombo et al., 2000 and 2002; Liu and Gao, 2001a and 2001b). Generally, the tomographic models could be categorized as two groups: function-based models such as Howe (1997), Hansen et al. (1997), Hansen (1998), Howe et al. (1998), Liu and Gao (2001a and 2001b) and voxel-based models such

as Raymund et al. (1990 and 1994); Hernández-Pajares et al. (1999 and 2000) and Colombo et al. (2000 and 2002). The function-based models usually use a series of functions to represent the ionospheric electron density in the space while for the voxel-based models, the ionosphere is divided into many small voxels and the ionospheric electron density is assumed to be homogeneous in each voxel.

Hansen et al. (1997) and Hansen (1998) are among the earliest publications that applied the function-based tomographic technique into ionospheric modeling for wide area augmentation system (WAAS) with GPS observations. However, no explicit analytical tomographic formulas were provided in previous publications. A stochastic inversion method was employed to estimate ionospheric parameters (Hansen et al., 1997). Although the inversion is processed epoch by epoch, it inverses all the observations from all the GPS stations together at each epoch. If the number of GPS stations in GPS network is not large, which implies the number of GPS observations from the network is not large, the computational burden of the inversion of all observations is acceptable. However, when the number of GPS stations increases, e.g. for a global GPS network or a GPS network with dense GPS station distribution, the inversion of all the GPS measurements together could become a heavy computational burden or even a serious problem for the implementation. For real-time implementation, more efficient estimation method should be used. The coefficients and inter-frequency biases were determined using a batch process with 60 hours of data as indicated in Hansen (1998). This processing method therefore would require extensive computational resources and large amount of GPS data and very long processing time. So it is not feasible to use this processing method in real-time ionospheric modeling. The ionospheric coefficients were also treated as stationary in the solar-magnetic frame, namely, the ionospheric coefficients were assumed not changing over time except noise (Hansen, 1998). The ionospheric accuracy, after removal of the inter-frequency biases, was reported to have a standard deviation of 1.69 m, equivalent to 10.4 TECU on L1 frequency (Hansen, 1998). The free electron density in a solar-magnetic frame, however, still has variations of

approximately $\pm 5\%$ during low geomagnetic activities and $\pm 10\%$ during high geomagnetic activities within a day (Colombo et al., 2000; Hernández-Pajares et al., 2000). Additional error would be introduced if the variations were not appropriately modeled to take the ionospheric change over time into account. Moreover, the empirical orthogonal functions used in previous study (Hansen et al., 1997) only described the ionospheric region from 80 to 580 km, which is inadequate since the ionosphere usually extends to altitude above 1000 km. Furthermore, data sets employed by Hansen et al. (1997) and Hansen (1998) were both collected from WAAS networks and the modeling was only conducted with respect to the WAAS network. No GPS data set from smaller network such as local area GPS networks was analyzed. Currently there are far more small GPS networks (local area or regional area networks) than large networks like WAAS. At present time, only U.S. WAAS is in operation and several other similar systems like European EGNOS and Japanese MSAS are under development (Doherty et al., 2002). Therefore there is a need to analyze the performance of tomographic modeling in both small and large networks. The voxel-based tomographic modeling using GPS network with a separation of several hundreds of kilometers was reported in Colombo et al. (1999), Hernández-Pajares et al. (2000) and Colombo et al. (2000). The data sets analyzed in Hansen et al. (1997) were from two particular days with very low geomagnetic activities (K_p index values 1~2 for both days) and the data sets analyzed in Hansen (1998) were also collected during very low geomagnetic activities (K_p index values 1~3 during observations). Voxel-based tomographic modeling during ionospheric conditions $K_p=6$ was documented in Hernández-Pajares et al. (2000) and Colombo et al. (2000). However, the ionosphere tomographic modeling (for both function-based and voxel-based modeling) during periods with extremely high geomagnetic activities ($K_p=8\sim 9$) remains a challenging task and has not been reported so far. Previous investigations have applied ionospheric corrections with a five second latency to correct ionospheric errors at the user stations (e.g. Hansen et al., 1997; Hansen, 1998). No attempts have been made to generate predicted ionospheric corrections to correct the ionospheric errors at the user stations. The data transmission, data processing and

correction broadcast must take some time before ionospheric corrections are received at the user ends. Ionospheric modeling using data from a network of GPS reference stations usually consists of three major steps: a) data acquisition at the GPS reference stations equipped with dual-frequency GPS receivers; b) transmission of data from reference stations to data analysis center; c) ionospheric modeling and broadcast to GPS users (Loh et al., 1995). To complete the above three tasks from GPS data acquisition to the receipt of the ionospheric corrections by GPS users, a certain amount of time is required dependent on a variety of factors such as data transmission mode, the power of the computing facilities, the complexity of the ionospheric model, the number of GPS stations in the network as well as the size of the network. Jackson et al. (2002) showed that using VSAT technology to transmit 1 Hz raw GPS data will have an average latency of about 1.2~1.7 seconds. If including the time needed for modeling computation at the data analysis center and for data broadcasting to users, the total latency will be even greater. To eliminate the effect of such latency on real-time positioning, the ionosphere tomographic model should be able to predict TEC corrections with sufficient accuracy so that the GPS users could use them to mitigate ionospheric effects in real-time. In WAAS, the ionospheric grid update interval is typically set to 5 minutes and this is also the maximum update interval (El-Arini et al., 1999). Following this specification, a 5-minute prediction interval is necessary. In order to provide service for other ionosphere-related applications where a longer prediction interval is needed, prediction intervals such as 10-minute and 30-minute should also be investigated.

Recently, ionosphere tomographic modeling based on voxel concept using GPS observations has also been investigated (Hernández-Pajares et al., 1999 and 2000; Colombo et al., 1999, 2000 and 2002). For tropospheric modeling, the voxel-based tomographic techniques have also been used (Flores et al., 2000; Skone and Shrestha, 2003; Nicholson et al., 2003). In the voxel-based tomographic model, the ionosphere is divided into many small voxels and the electron density in each voxel is considered being uniformly distributed at any time. The calculation of the total electron content is done by

the summation of the value for each voxel, which is the result of the distance of signal path that passes through a given voxel timing the density of that voxel. The work proposed in Skone and Shrestha (2003) however can be regarded as a combination of function-based and voxel-based tomographic model because the horizontal troposphere is expressed by a low-order polynomial in latitude and longitude while the vertical is divided into different layers. In Hernández-Pajares et al. (2000) and Colombo et al. (2000), the voxel-based tomographic model can be described by:

$$\lambda_1 \Phi_1 - \lambda_2 \Phi_2 = \alpha \sum_{i=1}^I \sum_{j=1}^J \sum_{k=1}^K (N_e)_{i,j,k} ds_{i,j,k} + b \quad (4.4)$$

where

- λ_1 is the wavelength of the L1 carrier phase; $\lambda_1 = c/f_1 \approx 0.19 \text{ m}$;
- Φ_1 is the carrier phase measurement on L1 frequency;
- λ_2 is the wavelength of the L2 carrier phase; $\lambda_2 = c/f_2 \approx 0.24 \text{ m}$;
- Φ_2 is the carrier phase measurement on L2 frequency;
- α is a constant coefficient, $\alpha = 1.05 \times 10^{-17} \text{ m}/(\text{e1}/\text{m}^2)$;
- i, j, k is the indices for each voxel corresponding to solar longitude, geodetic latitude and height; Their maximum values are I, J, K , respectively, which determines the number of voxels in the ionosphere;
- $(N_e)_{i,j,k}$ is the free electron density for each voxel;
- $ds_{i,j,k}$ is the length of the GPS signal ray path crossing each voxel;
- b is the alignment term that includes L1 and L2 carrier phase integer ambiguities and inter-frequency biases, which is constant in a given satellite-receiver pair in continuous tracking.

The detailed expression for carrier phase measurements Φ_1 and Φ_2 will be given in the next section. An issue associated with the voxel-based tomographic method is that in ionospheric modeling for wide area GPS networks, the numerical computation cost is

high and the difficulty of broadcasting ionospheric model coefficients will be a concern even if the required spatial resolution is not high. Usually two layers in ionosphere are used and the voxel size is defined as $3^{\circ} \times 5^{\circ}$ (Hernández-Pajares et al., 1999). In Flores et al. (2000), a $4 \times 4 \times 40$ voxel grid were defined over a region of 400 km^2 and 15 km in height to model the troposphere. There are totally 640 voxels to be estimated for such a small region. To cover a large region like North America, the total voxel number will exceed several thousands. The computational burden due to a huge number of parameters to be estimated will be very high and the implementation in a real-time mode will be difficult. For example, in the data analysis presented in Chapter 6, the latitude coverage of the GPS network is from 34.3°N to 64.9°N , with a latitudinal span of 30.6° . The longitude coverage is from -52.7°W to -152.5°W , with a longitudinal span of 99.8° . If the voxel size is defined as $3^{\circ} \times 5^{\circ}$ and the ionosphere is divided into two layers as suggested in Hernández-Pajares et al. (1999), then it has $10 \times 20 \times 2 = 200$ voxels in total, which has not yet included the inter-frequency bias parameters. To consider inter-frequency biases, the number of parameters will exceed 200. If higher resolution with a voxel size such as $3^{\circ} \times 3^{\circ}$ horizontally and three layers vertically is required, the number of voxels will dramatically increase to $10 \times 33 \times 3 = 990$ in total. This implies that 990 ionospheric parameters need to be estimated in the ionospheric modeling even if the inter-frequency bias parameters are not included. Estimating such a large number of parameters is computationally expensive for real-time ionospheric modeling. Considering each receiver at a single epoch can averagely observe 10 satellites, 22 stations in GPS network (consider the wide area GPS network described in Chapter 6) can approximately observe 220 satellites in total at a single epoch. Even if the model estimation can be sequentially performed on an epoch-by-epoch basis, the geometry matrix itself has a size of $220 \times 200 = 44000$ or $220 \times 990 = 217800$ elements, either of which is a huge matrix that requires a large amount of computer memories. If the model is not estimated in an epoch-by-epoch basis, the computational burden will be further increased. The large number of ionospheric parameters in the voxel-based model will also make it difficult to broadcast them to users in real time. Furthermore, if these ionospheric parameters are broadcast to

single-frequency GPS users for correcting ionospheric error in their real-time applications, the computational burden at the user ends is also significant because the users must calculate a geometry matrix of 10×200 or 10×990 size (assume that a GPS user observes 10 satellites) and multiply this matrix with the ionospheric parameter vector of size 200×1 or 990×1 . Therefore, the tomographic modeling using the voxel-based concept has computational difficulties for GPS real-time applications.

4.4 Development of the Ionosphere Tomographic Modeling Method

To overcome the limitations associated with previous investigations using function-based tomographic model and voxel-based tomographic models as discussed above, in this research, first the smoothing algorithm using carrier phase measurement and code pseudorange measurements is derived along with its error estimation formula, which allows a recursive computation of the error budget of the smoothed TEC data. The use of smoothed TEC measurements is a first step that ensures high quality of input data for the tomographic model. Then a close form analytical expression that links the TEC observations smoothing and function-based tomographic modeling is developed in this research, which allows the smoothing of TEC measurements and the estimation of tomographic model to be carried out simultaneously, which is crucial for real-time implementation of the tomographic modeling. This newly derived analytical expression is the first one that combines the function-based tomographic modeling and TEC smoothing in a single equation. The modeling system is integrated with Kalman filtering for real-time tomographic modeling and TEC prediction, by performing the computation in a sequential way on both epoch by epoch and station by station basis. This means the GPS observations are processed sequentially epoch by epoch while at each epoch the data are also processed sequentially station by station. This processing method overcomes the inefficiency of the ionospheric parameter estimation methods used in previous research (Hansen et al., 1997; Hansen, 1998).

The ionosphere in the function-based tomographic model to be developed will be represented by spherical harmonic functions (SHF) and empirical orthogonal functions (EOF). The model will be constructed on the basis of integrating function-based tomographic technique with the Kalman filter to sequentially estimate ionosphere in a real-time mode. Different from previous 2D ionospheric models where the variable to be modeled is the total electron content, the variable to be modeled in this tomographic model is the electron density function. The electron density function is a more fundamental variable than the total electron content for the description of the ionospheric property. With the electron density function, TEC can be readily derived. The electron density function explicitly describes the spatial distribution of the electrons in the ionosphere, with which other ionospheric quantity can be derived, such as electron density gradient. The function-based tomographic model also has an advantage of modeling the ionosphere in multiple layers rather than in single layer mode as the 2D models do. In comparison with the voxel-based model, the model proposed in this research requires much smaller number of parameters to characterize the ionosphere. The analysis for a wide area GPS network presented in Chapter 6 shows that using 84 ionospheric parameters can represent the ionosphere very well. It will however require 200~990 parameters to represent the same network using the voxel-based model, 2.38~11.78 times more than the function-based modeling. Apparently the reduced number of parameters will be significantly beneficial for real-time applications. First, the broadcast of ionospheric parameters will become easier since the volume of parameters is much smaller. Second, the computational burden and time cost at GPS user end is also dramatically reduced. The ionospheric modeling using the SHF and EOF method is therefore more suitable for real-time applications.

In this research, the estimation of inter-frequency biases will be based on 24 hours of GPS observations so that the data volume will be significantly smaller compared to previous work using 60 hours of GPS data. Owing to the use of Kalman filtering, the estimation procedure can dramatically reduce the computational resource demand and the

data processing time compared to previous work using a batch process. Also, a pseudo TEC observation is introduced to establish a reference for the estimation of inter-frequency biases. The ionospheric coefficients are also allowed to vary with time by using a first-order Gauss-Markov process and the ionospheric TEC prediction results presented in Chapters 5 and 6 will show that the adoption of this process produces prediction data with good accuracies. The empirical orthogonal functions have been extended to describe the ionosphere to an altitude of 1000 km, which is more appropriate than using a height of 580 km in previous research. Considering the fact that no literature has been reported as to the modeling of ionosphere over local area GPS networks (baseline length about 30~50 km) using tomographic method, a local area GPS network will be analyzed in addition to the analysis of a wide area GPS network. To the author's knowledge, it is the first time that the function-based tomographic model is applied for ionospheric modeling based on data from a local area GPS network. Nowadays, numerous local area GPS networks have been established (Hu et al., 2002; Nicholson et al., 2003) which have properties and characteristics different from wide area GPS networks, such as small network coverage, small ionospheric gradient and dense TEC measurements.

In this research, the data set from the wide area GPS network was observed under extremely high level of ionospheric activity ($K_p=8\sim 9$). No investigation under such a high level of ionospheric activities ($K_p=8\sim 9$) has been documented and the most severe ionospheric condition that has been considered so far was $K_p=6$ for voxel-based ionosphere tomographic modeling (Hernández-Pajares et al., 2000, Colombo et al., 2000). It is thus important to investigate the performance of the function-based tomographic model under extremely high level of ionospheric activity ($K_p=8\sim 9$) using GPS measurements from a wide area GPS network. The performance analysis under both benign and highly severe ionospheric conditions would give a more complete evaluation of the capability of the tomographic modeling method developed in this research. Three

different prediction intervals are tested in this research and they are 5-minute, 10-minute and 30-minute.

Tomography is a two-step process. First, integral measurements are made of the medium of interest, ideally along many paths at many different viewing angles. Second, these integral measurements are inverted to obtain an estimate of the field (Howe et al., 1998; Liu and Gao, 2001a). The TEC measurements derived from GPS dual frequency observations meet the characteristics of tomography very well. The TEC measurements derived from dual-frequency GPS measurements are the integral result of electron density of our interested medium, namely ionosphere. Moreover, the TEC measurements are obtained from many different viewing angles because the GPS signals from a number of satellites penetrate ionosphere from different paths, as shown in Figure 4.1 where the dual-frequency GPS receivers on the ground can make a large number of observations about the ionosphere at different viewing angles. From the GPS observations, the TEC measurements can be subsequently derived. Given in Figure 4.1 is an example which illustrates the ionospheric TEC observations using a GPS network. It shows that a large number of TEC measurements are available for ionospheric modeling. Since a single GPS receiver can usually observe typically 8~10 satellites, which means that 8~10 TEC measurements of different elevation angles can be derived at a single GPS station, a great number of TEC measurements can be obtained at different viewing angles at any single epoch for a GPS network with tens to hundreds of GPS stations. Once the ionospheric TEC measurements are obtained, an inversion of those measurements may lead to estimating the ionospheric electron density function.

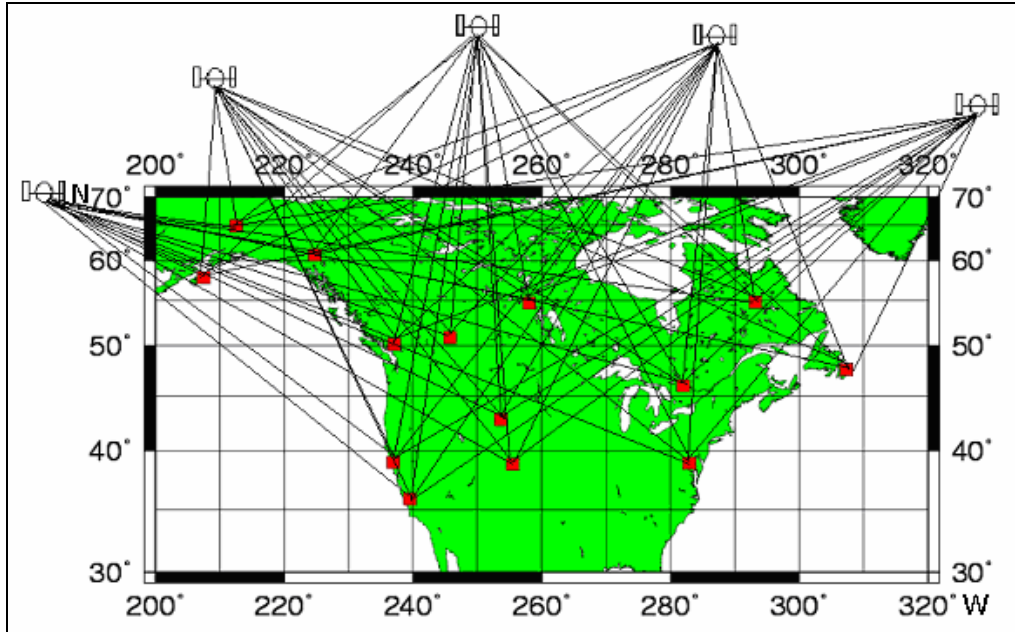


Figure 4.1 Illustration of Ionospheric TEC Observation in GPS Network

In the remainder of the section, the GPS observation equations for code pseudorange and carrier phase measurements are first described. Based on GPS observations, the detailed mathematical derivations of the TEC smoothing algorithm and formula for recursive estimation of the smoothed TEC error are then presented. Next, the close form expression that links the function-based ionospheric tomographic model and the smoothed TEC data is developed. Finally, the formulas for predicting ionospheric TEC data using the constructed tomographic model and the quantitative indicators for evaluating the accuracies of the TEC predictions are developed.

4.4.1 TEC observations

The equations for GPS code pseudorange measurement at L1 and L2 frequencies can be written as (Wells et al., 1987).

$$P_{i,1}^p = \rho_i^p + c(dt^p - dT_i) + d_{orb}^p + I_{i,1}^p + T_{i,1}^p + B_{i,1} + B_1^p + M_{i,1}^p + \varepsilon_{i,P_1} \quad (4.5)$$

$$P_{i,2}^p = \rho_i^p + c(dt^p - dT_i) + d_{orb}^p + \gamma_{i,1}^p + T_{i,2}^p + B_{i,2} + B_2^p + M_{i,2}^p + \varepsilon_{i,P_2} \quad (4.6)$$

where

$P_{i,1}^p$ is the code pseudorange measurement on L1 frequency. The subscript i denotes the receiver ID and the superscript p denotes satellite ID;

$P_{i,2}^p$ is the code pseudorange measurement on L2 frequency;

ρ_i^p is the geometrical distance between receiver i and satellite p ;

c is the speed of light in vacuum;

dt^p is the satellite p clock error with respect to GPS time;

dT_i is the GPS receiver i clock error with respect to GPS time;

d_{orb}^p is the satellite p orbit error;

$I_{i,1}^p$ is the ionospheric refraction delay at L1 frequency for satellite p and receiver i ;

γ is the squared L1 and L2 frequency ratio; $\mathbf{g} = \left(\frac{f_1}{f_2} \right)^2 = \left(\frac{1575.42}{1227.6} \right)^2 = \left(\frac{77}{60} \right)^2$;

$T_{i,1}^p$ is the tropospheric refraction delay for satellite p and receiver i at L1 frequency;

$T_{i,2}^p$ is the tropospheric refraction delay for satellite p and receiver i at L2 frequency;

$B_{i,1}$ is the receiver i instrumental delay on $P_{i,1}^p$ code pseudorange measurement;

$B_{i,2}$ is the receiver i instrumental delay on $P_{i,2}^p$ code pseudorange measurement;

B_1^p is the satellite p instrumental delay on $P_{i,1}^p$ code pseudorange measurement;

B_2^p is the satellite p instrumental delay on $P_{i,2}^p$ code pseudorange measurement;

$M_{i,1}^p$ is the multipath effect for satellite p and receiver i on $P_{i,1}^p$ code pseudorange measurement;

$M_{i,2}^p$ is the multipath effect for satellite p and receiver i on $P_{i,2}^p$ code pseudorange measurement;

ϵ_{i,P_1} is the receiver i measurement noise for $P_{i,1}^p$ code pseudorange measurement;

ϵ_{i,P_2} is the receiver i measurement noise for $P_{i,2}^p$ code pseudorange measurement.

The carrier phase measurements at frequencies L1 and L2 can be written as:

$$\lambda_1 \Phi_{i,1}^p = \rho_i^p + c(dt^p - dT_i) + d_{orb}^p - I_{i,1}^p + T_{i,1}^p + \lambda_1 N_{i,1}^p + b_{i,1} + b_1^p + m_{i,1}^p + \varepsilon_{i,\Phi_1} \quad (4.7)$$

$$\lambda_2 \Phi_{i,2}^p = \rho_i^p + c(dt^p - dT_i) + d_{orb}^p - \gamma I_{i,1}^p + T_{i,2}^p + \lambda_2 N_{i,2}^p + b_{i,2} + b_2^p + m_{i,2}^p + \varepsilon_{i,\Phi_2} \quad (4.8)$$

where some variables are defined above and the others are defined as following:

$\Phi_{i,1}^p$ is the carrier phase measurement on L1 frequency. Subscript i denotes the receiver ID and superscript p denotes satellite ID;

$\Phi_{i,2}^p$ is the carrier phase measurement on L2 frequency;

λ_1 is the wavelength of the L1 carrier phase; $\lambda_1 = c/f_1 \approx 0.19$ m;

λ_2 is the wavelength of the L2 carrier phase; $\lambda_2 = c/f_2 \approx 0.24$ m;

$N_{i,1}^p$ is the ambiguity for satellite p and receiver i on L1 carrier phase;

$N_{i,2}^p$ is the ambiguity for satellite p and receiver i on L2 carrier phase;

$b_{i,1}$ is the receiver i instrumental delay on $\Phi_{i,1}^p$ carrier phase measurement;

$b_{i,2}$ is the receiver i instrumental delay on $\Phi_{i,2}^p$ carrier phase measurement;

b_1^p is the satellite p instrumental delay on $\Phi_{i,1}^p$ carrier phase measurement;

b_2^p is the satellite p instrumental delay on $\Phi_{i,2}^p$ carrier phase measurement;

$m_{i,1}^p$ is the multipath effect for satellite p and receiver i on $\Phi_{i,1}^p$ carrier phase measurement;

$m_{i,2}^p$ is the multipath effect for satellite p and receiver i on $\Phi_{i,2}^p$ carrier phase measurement;

ε_{i,Φ_1} is the receiver i measurement noise for $\Phi_{i,1}^p$ carrier phase measurement;

ε_{i,Φ_2} is the receiver i measurement noise for $\Phi_{i,2}^p$ carrier phase measurement.

It should be noted that for the sake of simplicity, the time tags for the measurements and all the correction items in equations (4.5)~(4.8) are omitted. For the purpose of convenience, the denoted subscript i and superscript p are also omitted in the following derivations, unless explicitly expressed. Differencing equation (4.5) with equation (4.6) as well as equation (4.7) with equation (4.8), the following equations (4.9) and (4.10) can be obtained.

$$P_1 - P_2 = (1 - \gamma)I_1 + (B_{i,1} - B_{i,2}) + (B_1^p - B_2^p) + (M_1 - M_2) + \varepsilon_{P_1, P_2} \quad (4.9)$$

$$\lambda_1 \Phi_1 - \lambda_2 \Phi_2 = -(1 - \gamma)I_1 + (\lambda_1 N_1 - \lambda_2 N_2) + (b_{i,1} - b_{i,2}) + (b_1^p - b_2^p) + (m_1 - m_2) + \varepsilon_{\Phi_1, \Phi_2} \quad (4.10)$$

where ε_{P_1, P_2} is the noise of the code measurement difference and $\varepsilon_{\Phi_1, \Phi_2}$ is the noise of the carrier phase measurement difference. For code measurements, we define $B_i = (B_{i,1} - B_{i,2})$ and $B^p = (B_1^p - B_2^p)$ and for carrier phase measurements, we define $b_i = (b_{i,1} - b_{i,2})$ and $b^p = (b_1^p - b_2^p)$. B_i and B^p represent the receiver's and satellite's differential instrumental delays on code pseudorange measurements between the L1 and L2 frequencies, respectively. b_i and b^p represent the receiver's and satellite's differential instrumental delays on carrier phase measurements between the L1 and L2 frequencies, respectively. They are often referred to as receiver and satellite L1/L2 inter-frequency biases (Gao and Liu, 2002). Thus equations (4.9) and (4.10) can be rewritten as:

$$P_1 - P_2 = (1 - \gamma)I_1 + B_i + B^p + (M_1 - M_2) + \varepsilon_{P_1, P_2} \quad (4.11)$$

$$\lambda_1 \Phi_1 - \lambda_2 \Phi_2 = -(1 - \gamma)I_1 + (\lambda_1 N_1 - \lambda_2 N_2) + b_i + b^p + (m_1 - m_2) + \varepsilon_{\Phi_1, \Phi_2} \quad (4.12)$$

On the right side of equation (4.11), the difference of multipath effects ($M_1 - M_2$) on code pseudorange measurements can be mitigated to the minimum level by careful selection of GPS site and receiver/antenna, e.g. using a narrow correlator receiver with a choke-ring antenna (Lachapelle, 2000). Moreover, the multipath effect can be minimized

by a process called GPS data smoothing over time. The code pseudorange measurement noise $\epsilon_{P_1P_2}$ can also be minimized when high quality GPS receivers are used. Compared to the multipath effects on code pseudorange measurements, the multipath effects on carrier phase measurements are insignificantly small (Langley, 1998b). With the implementation of multipath countermeasures, the multipath effects are neglected in this research. In this case, the equations (4.11) and (4.12) are reduced to the following forms:

$$P_1 - P_2 = (1 - \gamma)I_1 + B_i + B^p + \epsilon_{P_1P_2} \quad (4.13)$$

$$\lambda_1\Phi_1 - \lambda_2\Phi_2 = -(1 - \gamma)I_1 + (\lambda_1N_1 - \lambda_2N_2) + b_i + b^p + \epsilon_{\Phi_1\Phi_2} \quad (4.14)$$

The amount of ionospheric refraction delay on an electromagnetic wave is a function of the operating frequency and the total amount of free electrons along the electromagnetic signal path. In GPS, the ionospheric delay I_1 on L1 frequency can be calculated by (Klobuchar, 1996):

$$I_1 = \frac{40.3\text{TEC}}{f_1^2} \quad (4.15)$$

TEC has a unit of electron / m². The quantity of TEC is usually very large. It can reach as large as 1.0×10^{18} el/m² or even more during active ionosphere period. Even during ionosphere quiet period, the amount of TEC is usually on the order of 1.0×10^{17} el/m². For the purpose of convenience, TEC unit (TECU) is more frequently used in applications. The TEC can be converted into TECU unit by dividing the quantity of TEC by 1.0×10^{16} el/m².

Substituting the ionospheric term I_1 in equation (4.13) by equation (4.15) and reorganizing it, one gets:

$$\text{TEC}_R = \frac{f_1^2[(P_1 - P_2) - B_i - B^p]}{40.3(1 - \gamma)} \quad (4.16)$$

where TEC_R denotes the TEC measurement derived from GPS code pseudorange measurements. Analogously, by inserting the equation (4.15) into (4.14) and rearranging it, the TEC measurement derived from GPS carrier phase measurements, denoted as TEC_ϕ , becomes:

$$TEC_\phi = \frac{f_1^2 [(\lambda_1 \Phi_1 - \lambda_2 \Phi_2) - (\lambda_1 N_1 - \lambda_2 N_2) - b_i - b^p]}{40.3(\gamma - 1)} \quad (4.17)$$

Equation (4.16) indicates that the ionospheric TEC measurements can be directly derived from the GPS code pseudorange observations at frequencies L1 and L2 when the receiver and satellite receiver L1/L2 inter-frequency biases are known. But the receiver and satellite inter-frequency biases would corrupt the direct estimation of TEC measurements from GPS code data if they are not taken into account. The magnitude of satellite inter-frequency bias is usually in the range of several ns (about 30 cm in range per ns) while the receiver inter-frequency bias could be as large as more than 10 ns (Gao et al., 1994). Therefore in precise ionospheric TEC estimation and modeling, the inter-frequency biases must be taken into account and be estimated as unknown parameters of the model. In equation (4.17), it is seen that the TEC measurement can also be directly derived from dual-frequency GPS carrier phase measurements Φ_1 and Φ_2 . Similar to TEC_R , TEC_ϕ has the same problem regarding the inter-frequency biases issue as the code derived TEC_R . Moreover, in the equation (4.17), the two integer ambiguities, N_1 and N_2 , need to be determined. Since the ambiguities are unknown, TEC_ϕ therefore is just a relative value of TEC. Unlike the carrier phase derived TEC_ϕ , the code derived TEC_R has no ambiguities, often referred to as absolute TEC. In this regard, TEC_ϕ is often referred to as relative TEC.

Although the GPS carrier phase measurements produce relative quantity TEC_ϕ , the accuracy is much higher than the absolute value TEC_R because the carrier phase measurements are far more precise than the code pseudorange measurements. Typically

the C/A code measurement has an accuracy (1σ) of 0.2 to 0.3 m and the P2 code measurement has a precision of 0.1~0.2 m. The L1 and L2 carrier phase measurements recorded by the tested receivers were evaluated to demonstrate a precision of 0.02~0.06 cycles, approximately equivalent to 0.004~0.012 m in distance (Gao et al., 2002). Applying the error propagation law to the equations (4.16) and (4.17) and not considering the effects of the inter-frequency biases and ambiguities in the carrier phase measurements since they are regarded constants once determined, we have,

$$\sigma_{\text{TEC}_R} = \frac{f_1^2}{40.3(\gamma-1)} \sqrt{\sigma_{P_1}^2 + \sigma_{P_2}^2} \quad (4.18)$$

$$\sigma_{\text{TEC}_\Phi} = \frac{f_1^2}{40.3(\gamma-1)} \sqrt{\lambda_1^2 \sigma_{\Phi_1}^2 + \lambda_2^2 \sigma_{\Phi_2}^2} \quad (4.19)$$

where σ_{P_1} and σ_{P_2} are the standard deviation of the GPS code pseudorange measurements at L1 and L2 frequencies, respectively, in unit of metres; σ_{Φ_1} and σ_{Φ_2} are the standard deviation of the GPS carrier phase measurements at L1 and L2 frequencies, respectively, in unit of cycle. σ_{TEC_R} and σ_{TEC_Φ} are the standard deviation of the TEC measurements derived from code pseudorange and carrier phase data, respectively, in the unit of TECU. Assuming that $\sigma_{P_1} = \sigma_{P_2} = 0.2$ m, the σ_{TEC_R} computed from equation (4.18) is 2.69 TECU. If it is assumed that $\sigma_{\Phi_1} = \sigma_{\Phi_2} = 0.02$ cycle, then the corresponding σ_{TEC_Φ} is 0.06 TECU. It is clear that the carrier phase derived total electron content TEC_Φ is much more precise than that of the code derived TEC_R . Skone et al. (2002) also confirmed that the code pseudorange derived TEC typically has an accuracy of 1-5 TECU while the carrier phase derived TEC usually better than 0.10 TECU.

4.4.2 TEC smoothed by carrier phase measurements

Combining the individual advantages of the carrier phase derived TEC and code pseudorange derived TEC measurements, an absolute TEC measurement with improved

accuracy can be obtained. The carrier phase derived TEC_{ϕ} measurement has much higher accuracy than TEC_R derived from code pseudorange GPS data, but it is not absolute because of the existence of unknown ambiguities. A method of smoothing the code derived TEC_R by carrier phase derived TEC measurement TEC_{ϕ} is presented below (Mannucci et al., 1993; Skone, 1998).

At epoch n , differencing equations (4.16) and (4.17) results in an offset between the absolute $TEC_{R,n}$ and the relative $TEC_{\phi,n}$, which is denoted as ΔTEC_n .

$$\begin{aligned}
\Delta TEC_n &= TEC_{R,n} - TEC_{\phi,n} \\
&= \frac{f_1^2[(P_1 - P_2) - B_i - B^p]}{40.3(1 - \gamma)} - \frac{f_1^2[(\lambda_1 \Phi_1 - \lambda_2 \Phi_2) - (\lambda_1 N_1 - \lambda_2 N_2) - b_i - b^p]}{40.3(\gamma - 1)} \\
&= \frac{f_1^2[(P_1 - P_2) - B_i - B^p] + f_1^2[(\lambda_1 \Phi_1 - \lambda_2 \Phi_2) - (\lambda_1 N_1 - \lambda_2 N_2) - b_i - b^p]}{40.3(1 - \gamma)} \quad (4.20) \\
&= \frac{f_1^2[(P_1 - P_2) - B_i - B^p + (\lambda_1 \Phi_1 - \lambda_2 \Phi_2) - (\lambda_1 N_1 - \lambda_2 N_2) - b_i - b^p]}{40.3(1 - \gamma)} \\
&= \frac{f_1^2[(P_1 - P_2) - B_i - B^p + (\lambda_1 \Phi_1 - \lambda_2 \Phi_2)]}{40.3(1 - \gamma)} + \frac{f_1^2[-(\lambda_1 N_1 - \lambda_2 N_2) - b_i - b^p]}{40.3(1 - \gamma)}
\end{aligned}$$

At each epoch, a ΔTEC_n can be calculated provided that the GPS code pseudorange and carrier phase observables on both L1 and L2 are available. Theoretically, ΔTEC_n should be constant or very stable over time as long as the carrier phase ambiguities are same because both $TEC_{R,n}$ and $TEC_{\phi,n}$ are the measurements of the same total electron contents over the same location and at the same time. The only difference between $TEC_{R,n}$ and $TEC_{\phi,n}$ is that there are two ambiguities in $TEC_{\phi,n}$, as indicated in equation (4.17). The two ambiguities are constant over time provided that GPS signals are continuously tracked and no cycle slips are present. For each pair of a satellite and a receiver, one ΔTEC_n can be derived at one epoch. A more precise ΔTEC can be

obtained by smoothing it over time. The recursive equation to calculate the ΔTEC_N at epoch N is given below (Skone, 1998).

$$\begin{aligned}\Delta\text{TEC}_N &= \frac{1}{N} \sum_{n=1}^N \Delta\text{TEC}_n = \frac{1}{N} \sum_{n=1}^N (\text{TEC}_{R,n} - \text{TEC}_{\Phi,n}) \\ &= \frac{1}{N} \left[\sum_{n=1}^{N-1} (\text{TEC}_{R,n} - \text{TEC}_{\Phi,n}) + (\text{TEC}_{R,N} - \text{TEC}_{\Phi,N}) \right] \\ &= \frac{1}{N} \left[(N-1) \Delta\text{TEC}_{N-1} + (\text{TEC}_{R,N} - \text{TEC}_{\Phi,N}) \right]\end{aligned}\quad (4.21)$$

The values of satellite and receiver inter-frequency biases are quite stable during a period of a few days (Schaer, 1999). Therefore the smoothed ΔTEC_N should be almost constant over a daily period of time under the condition that either carrier phase L1 or L2 has no cycle slips or cycle slips can be corrected. After the smoothed ΔTEC_N is recursively computed from equation (4.21), the offset between absolute and relative TEC can be added to the relative TEC_{Φ} of equation (4.17). Thus the smoothed absolute TEC_{SM} value is obtained. This process is referred to as carrier phase leveled code pseudorange TEC derivation. The smoothed absolute TEC_{SM} at epoch N is expressed as $\text{TEC}_{\text{SM},N}$ and it can be calculated by:

$$\text{TEC}_{\text{SM},N} = \text{TEC}_{\Phi,N} + \Delta\text{TEC}_N \quad (4.22)$$

where $\text{TEC}_{\Phi,N}$ is the relative total electron content derived from carrier phase measurements at epoch N , as indicated by equation (4.17); ΔTEC_N is the smoothed result at epoch N based on the past N total electron content offsets, which is calculated according to equation (4.21). Inserting equation (4.20) into equation (4.21), it yields:

$$\begin{aligned}
\Delta\text{TEC}_N &= \frac{1}{N} \sum_{n=1}^N \Delta\text{TEC}_n \\
&= \frac{1}{N} \sum_{n=1}^N \left(\frac{f_1^2[(P_1 - P_2) - B_i - B^p + (\lambda_1 \Phi_1 - \lambda_2 \Phi_2)]}{40.3(1-\gamma)} + \frac{f_1^2[-(\lambda_1 N_1 - \lambda_2 N_2) - b_i - b^p]}{40.3(1-\gamma)} \right) \\
&= \frac{1}{N} \sum_{n=1}^N \left(\frac{f_1^2[(P_1 - P_2) - B_i - B^p + (\lambda_1 \Phi_1 - \lambda_2 \Phi_2)]}{40.3(1-\gamma)} \right) \\
&\quad + \frac{1}{N} \sum_{n=1}^N \left(\frac{f_1^2[-(\lambda_1 N_1 - \lambda_2 N_2) - b_i - b^p]}{40.3(1-\gamma)} \right)
\end{aligned} \tag{4.23}$$

In the last term in equation (4.23), the carrier phase measurement ambiguities N_1 and N_2 are constant assuming that cycle slips in measurements are correctly detected and recovered. The receiver and satellite inter-frequency biases b_i and b^p are quite stable over time and they basically maintains constant during one day of time. Thus the last term of equation (4.23) is essentially constant over time if the smoothing period does not exceed one day. Consequently, equation (4.23) is reduced to,

$$\begin{aligned}
\Delta\text{TEC}_N &= \frac{1}{N} \sum_{n=1}^N \left(\frac{f_1^2[(P_1 - P_2) - B_i - B^p + (\lambda_1 \Phi_1 - \lambda_2 \Phi_2)]}{40.3(1-\gamma)} \right) \\
&\quad + \frac{f_1^2[-(\lambda_1 N_1 - \lambda_2 N_2) - b_i - b^p]}{40.3(1-\gamma)}
\end{aligned} \tag{4.24}$$

Integrating equations (4.17) and (4.24), equation (4.22) thus have the following expression:

$$\begin{aligned}
\text{TEC}_{\text{SM},N} &= \text{TEC}_{\Phi,N} + \Delta\text{TEC}_N \\
&= \frac{f_1^2[(\lambda_1 \Phi_1 - \lambda_2 \Phi_2) - (\lambda_1 N_1 - \lambda_2 N_2) - b_i - b^p]}{40.3(\gamma-1)} \\
&\quad + \frac{1}{N} \sum_{n=1}^N \left(\frac{f_1^2[(P_1 - P_2) - B_i - B^p + (\lambda_1 \Phi_1 - \lambda_2 \Phi_2)]}{40.3(1-\gamma)} \right) \\
&\quad + \frac{f_1^2[-(\lambda_1 N_1 - \lambda_2 N_2) - b_i - b^p]}{40.3(1-\gamma)} \\
&= \frac{f_1^2(\lambda_1 \Phi_1 - \lambda_2 \Phi_2)}{40.3(\gamma-1)} + \frac{1}{N} \sum_{n=1}^N \left(\frac{f_1^2[(P_1 - P_2) - B_i - B^p + (\lambda_1 \Phi_1 - \lambda_2 \Phi_2)]}{40.3(1-\gamma)} \right)
\end{aligned} \tag{4.25}$$

In equation (4.25), Φ_1 and Φ_2 are carrier phase measurements observed at each epoch; P_1 and P_2 are code pseudorange measurements observed at each epoch; λ_1 and λ_2 are wavelength of L1 and L2 signals; f_1 is frequency of L1 signal and γ is the squared frequency ratio as defined before. Therefore all the terms in equation (4.25) are measurable observations and constants except the receiver and satellite inter-frequency biases on code pseudorange measurements B_i and B^p . As a matter of fact, B_i and B^p are the unknowns to be estimated within the ionospheric model. Thus the smoothed total electron content $TEC_{SM,N}$ calculated at epoch N using equation (4.25) is absolute and less noisy TEC. In consideration of the fact that B_i and B^p are quite stable over a period of time within one day, they can be treated as constants during the smoothing process. Thus equation (4.25) can be reduced to:

$$\begin{aligned} TEC_{SM,N} &= TEC_{\Phi,N} + \Delta TEC_N \\ &= \frac{f_1^2(\lambda_1\Phi_1 - \lambda_2\Phi_2)}{40.3(\gamma-1)} + \frac{1}{N} \sum_{n=1}^N \left(\frac{f_1^2[(P_1 - P_2) + (\lambda_1\Phi_1 - \lambda_2\Phi_2)]}{40.3(1-\gamma)} \right) + \frac{f_1^2(-B_i - B^p)}{40.3(1-\gamma)} \end{aligned} \quad (4.26)$$

The accuracy of the smoothed $TEC_{SM,N}$ measurement is a function of the number of N . When the number of the smoothing epochs N is larger, the smoothed result should have higher accuracy. In order to derive the accuracy formula for the smoothed TEC measurement $TEC_{SM,N}$, reorganizing equations (4.21) and (4.22) it yields:

$$\begin{aligned} TEC_{SM,N} &= TEC_{\Phi,N} + \frac{1}{N} \sum_{n=1}^N \Delta TEC_n = TEC_{\Phi,N} + \frac{1}{N} (\Delta TEC_1 + \Delta TEC_2 + \dots + \Delta TEC_N) \\ &= TEC_{\Phi,N} + \frac{1}{N} \left[(TEC_{R,1} - TEC_{\Phi,1}) + (TEC_{R,2} - TEC_{\Phi,2}) + \dots + (TEC_{R,N} - TEC_{\Phi,N}) \right] \\ &= \frac{1}{N} (TEC_{R,1} + TEC_{R,2} + \dots + TEC_{R,N}) - \frac{1}{N} (TEC_{\Phi,1} + TEC_{\Phi,2} + \dots + TEC_{\Phi,N-1}) \\ &\quad + \frac{N-1}{N} TEC_{\Phi,N} \end{aligned} \quad (4.27)$$

The standard deviations of each code pseudorange derived TEC measurement $TEC_{R,n}$ ($n = 1, 2, \dots, N$) and the carrier phased derived $TEC_{\phi,n}$ ($n = 1, 2, \dots, N$) have been derived in equations (4.18) and (4.19). Assuming that the code pseudorange derived $TEC_{R,n}$ and carrier phase derived $TEC_{\phi,n}$ are uncorrelated and the GPS derived TEC measurements between two consecutive epochs are uncorrelated, the smoothed TEC measurement $TEC_{SM,N}$ at epoch N can be derived using the error propagation law and it gives:

$$\sigma_{TEC_{SM,N}} = \sqrt{\frac{1}{N^2} (\sigma_{TEC_{R,1}}^2 + \sigma_{TEC_{R,2}}^2 + \dots + \sigma_{TEC_{R,N}}^2) + \frac{1}{N^2} (\sigma_{TEC_{\phi,1}}^2 + \sigma_{TEC_{\phi,2}}^2 + \dots + \sigma_{TEC_{\phi,N-1}}^2) + \frac{(N-1)^2}{N^2} \sigma_{TEC_{\phi,N}}^2} \quad (4.28)$$

In order to derive the recursive expression for estimating the accuracy of the smoothed TEC measurements, let $(N-1)$ substitute the N in equation (4.28) and it yields:

$$\sigma_{TEC_{SM,N-1}} = \sqrt{\frac{1}{(N-1)^2} (\sigma_{TEC_{R,1}}^2 + \sigma_{TEC_{R,2}}^2 + \dots + \sigma_{TEC_{R,N-1}}^2) + \frac{1}{(N-1)^2} (\sigma_{TEC_{\phi,1}}^2 + \sigma_{TEC_{\phi,2}}^2 + \dots + \sigma_{TEC_{\phi,N-2}}^2) + \frac{(N-2)^2}{(N-1)^2} \sigma_{TEC_{\phi,N-1}}^2} \quad (4.29)$$

Reorganizing equations (4.28) and (4.29) and their relationship will be given by:

$$\sigma_{TEC_{SM,N}} = \frac{1}{N} \sqrt{(N-1)^2 \sigma_{TEC_{SM,N-1}}^2 + [1 - (N-2)^2] \sigma_{TEC_{\phi,N-1}}^2 + \sigma_{TEC_{R,N}}^2 + (N-1)^2 \sigma_{TEC_{\phi,N}}^2} \quad (4.30)$$

Equation (4.30) describes the algorithm for recursively computing the standard deviation for the smoothed TEC measurement. It is convenient for the calculation of the standard deviation. The error estimation for the smoothed TEC measurements is useful in the determination of the observation variance-covariance matrix in the Kalman filter to be described in the following section.

4.4.3 Tomographic model development

The total electron content (TEC) represents the total number of electrons in a column along the satellite to receiver signal path with a cross-sectional area of one square metre (Coster et al., 2003). It can be expressed as:

$$\text{TEC}_{\text{SM},\text{N}} = \int_{\text{rx}}^{\text{sv}} N_e(\lambda, \phi, z) ds \quad (4.31)$$

where

$\text{TEC}_{\text{SM},\text{N}}$ is the smoothed total electron content at epoch N obtained from equation (4.26);

$N_e(\lambda, \phi, z)$ denotes the ionospheric electron density function at the position (λ, ϕ, z) ;

(λ, ϕ, z) is the three coordinate components of the spatial position, representing sun-fixed longitude, geomagnetic latitude and altitude, respectively.

"rx" stands for the position of ground GPS receiver;

"sv" stands for the position of space vehicle, namely GPS satellite;

ds is a small distance along the GPS signal path from receiver to satellite.

The ionospheric electron density function $N_e(\lambda, \phi, z)$ can be written as the addition of two parts, $N_0(\lambda, \phi, z)$ and $\delta N_e(\lambda, \phi, z)$. $N_0(\lambda, \phi, z)$ is an approximate value representing the known part of $N_e(\lambda, \phi, z)$ and $\delta N_e(\lambda, \phi, z)$ denotes the correction to the known portion. Equation (4.31) therefore can be written as:

$$\text{TEC}_{\text{SM},\text{N}} = \int_{\text{rx}}^{\text{sv}} [N_0(\lambda, \phi, z) + \delta N_e(\lambda, \phi, z)] ds = \int_{\text{rx}}^{\text{sv}} N_0(\lambda, \phi, z) ds + \int_{\text{rx}}^{\text{sv}} \delta N_e(\lambda, \phi, z) ds \quad (4.32)$$

The approximate value of the deterministic portion $N_0(\lambda, \phi, z)$ can be obtained from historical ionospheric electron density data or from the output of empirical ionospheric models. In case of no information available regarding $N_0(\lambda, \phi, z)$, the easiest way is to

set it to null. The integral of the deterministic part of electron density function along the GPS signal path from satellite to receiver is defined as TEC_0 , namely,

$$TEC_0 = \int_{rx}^{sv} N_0(\lambda, \phi, z) ds \quad (4.33)$$

Since the value of TEC_0 can be calculated according to equation (4.33) and it can be determined before ionospheric modeling. Substituting equation (4.33) into equation (4.32), thus equation (4.32) can be written as:

$$TEC_{SM,N} = TEC_0 + \int_{rx}^{sv} \delta N_e(\lambda, \phi, z) ds \quad (4.34)$$

Defining the difference between total electron content measurement $TEC_{SM,N}$ and its approximate value TEC_0 as δTEC , namely,

$$\delta TEC = TEC_{SM,N} - TEC_0 \quad (4.35)$$

Inserting equation (4.26) into equation (4.35), it yields:

$$\begin{aligned} \delta TEC = & \frac{f_1^2(\lambda_1 \Phi_1 - \lambda_2 \Phi_2)}{40.3(\gamma - 1)} + \frac{1}{N} \sum_{n=1}^N \left(\frac{f_1^2[(P_1 - P_2) + (\lambda_1 \Phi_1 - \lambda_2 \Phi_2)]}{40.3(1 - \gamma)} \right) \\ & + \frac{f_1^2(-B_i - B^p)}{40.3(1 - \gamma)} - TEC_0 \end{aligned} \quad (4.36)$$

Inserting equation (4.34) into equation (4.35), it will yield:

$$\delta TEC = \int_{rx}^{sv} \delta N_e(\lambda, \phi, z) ds \quad (4.37)$$

In ionosphere tomographic modeling, the correction part of electron density $\delta N_e(\lambda, \phi, z)$ is modeled by spherical harmonics functions (SHF) and empirical orthogonal functions (EOF) (Liu and Gao, 2001a and 2001b). The spherical harmonic expansion is used to model the horizontal profile and the empirical orthogonal functions are used for vertical

profile description. The integration of these two sets of functions enables us to depict the ionosphere field in a 3D mode (Liu and Gao, 2001a). Mathematically, the modeling expression can be written as:

$$\delta N_e(\lambda, \phi, z) = \sum_{k=1}^K \sum_{m=-M}^M \sum_{n=|m|}^M [a_{nk}^m \cos(m\lambda) + b_{nk}^m \sin(m\lambda)] \bar{P}_n^m(\cos \phi) Z_k(z) \quad (4.38)$$

where

$\bar{P}_n^m(\cos \phi)$ is the associated Legendre polynomial of order m and degree n ($0 \leq m \leq n$);

$Z_k(z)$ is the empirical orthogonal functions (EOF);

a_{nk}^m is the model's coefficients that need to be estimated;

b_{nk}^m is the model's coefficients that need to be estimated;

K denotes the highest order of empirical orthogonal functions;

M denotes the highest order of spherical harmonics functions.

Other parameters in equation (4.38) have been defined in previous equations. The highest degree of the spherical harmonics functions is governed by the value of M . EOF are derived from empirical data of the ionospheric electron density, which can be obtained from an empirical ionospheric model such as the international reference ionosphere (IRI) model or electron density observations. The empirical data of ionospheric electron densities in the vertical profile are obtained from the international reference ionosphere model (Bilitza, 2001). The IRI model can describe the median values of electron density as a function of height for a given location, time and sunspot number. Given the date, time and location information of the GPS measurements when analyzing the data in Chapters 5 and 6, the vertical ionospheric electron density profile $N(h,t)$ can be calculated from IRI model. Assuming the samples of density profile obtained at different time t_i ($i = 1, 2, \dots, M$) and heights h_j ($j = 1, 2, \dots, N$) are denoted by $N(t_i, h_j)$ ($i = 1, 2, \dots, M; j = 1, 2, \dots, N$), the density profile data matrix can be written as:

$$N(t,h) = \begin{bmatrix} N(t_1, h_1) & N(t_1, h_2) & \cdots & N(t_1, h_N) \\ N(t_2, h_1) & N(t_2, h_2) & \cdots & N(t_2, h_N) \\ \cdots & \cdots & \cdots & \cdots \\ N(t_M, h_1) & N(t_M, h_2) & \cdots & N(t_M, h_N) \end{bmatrix}_{(M \times N)} \quad (4.39)$$

In matrix $N(t,h)$, the row i ($i=1,2,\dots,M$) denotes the electron density values at different heights obtained at the same time t_i ($i=1,2,\dots,M$) and the column j ($j=1,2,\dots,N$) represents a time series of electron density samples at the same height h_j ($j=1,2,\dots,N$). This form of organizing data in a matrix is called *S*-mode analysis (Björnsson and Venegas, 1997). The mean value of each column of matrix $N(t,h)$ is represented by $\bar{N}(h_j)$ ($j=1,2,\dots,N$) and it can be calculated by:

$$\bar{N}(h_j) = \frac{1}{M} \sum_{m=1}^M N(t_m, h_j) \quad (4.40)$$

If each column removes the mean value $\bar{N}(h_j)$, the mean of each column will become zero. The data matrix whose mean values have been removed is denoted as $\tilde{N}(t,h)$. Thus the covariance matrix can be obtained by performing the following matrix operation (Björnsson and Venegas, 1997):

$$S = \tilde{N}^T(t,h)\tilde{N}(t,h) \quad (4.41)$$

where S is the covariance matrix of data set $\tilde{N}(t,h)$. The eigenvectors of matrix S is the empirical orthogonal functions (EOF) that are sought, “empirical” because they arise from data, “orthogonal” because they are uncorrelated over space (Preisendorfer and Mobley, 1988). Using EOF technique, a small number of EOFs can well represented the information originally contained in a large quantity of data (Svensson, 1999). For example, the following Figure 4.2 is one of the electron density profiles obtained from IRI 90 model for March 31, 2001. The electron densities are sampled at four heights, namely 100 km, 400 km, 700 km and 1000 km. Totally four empirical orthogonal functions could be calculated from equation (4.41). However, only three EOFs are used

because the fourth eigenvalue is too small compared to other three eigenvalues. The four eigenvalues in this example are $2.71e+010$, $7.00e+007$, $5.18e+005$ and $2.27e-002$. The fourth value is significantly smaller than others so the fourth EOF is truncated. The eigenvalue gives a measure of the fraction of total variance of the matrix S . The largest eigenvalue corresponds to the largest variance in matrix S which can be numerically calculated by dividing it by the sum of all the eigenvalues. Only the first a few EOFs capture the dynamic behavior of the system and other EOFs that correspond to the smallest eigenvalues are just due to random noise (Björnsson and Venegas, 1997). Three empirical orthogonal functions derived from the electron density profiles using the above method (see equations (4.39)~(4.41)) are depicted in Figure 4.3 to Figure 4.5. The EOF #1 is associated with the largest eigenvalue and the EOF #2 and EOF #3 associated with the second, third largest value, respectively. It can be seen from Figure 4.3 to Figure 4.5 that EOFs use a small number of orthogonal functions to characterize the variability of the time series of empirical data. Because each function is spatially uncorrelated to each other, namely orthogonal to each other, it suggests each function shall look as different as possible from other functions, as shown in Figure 4.3 to Figure 4.5.

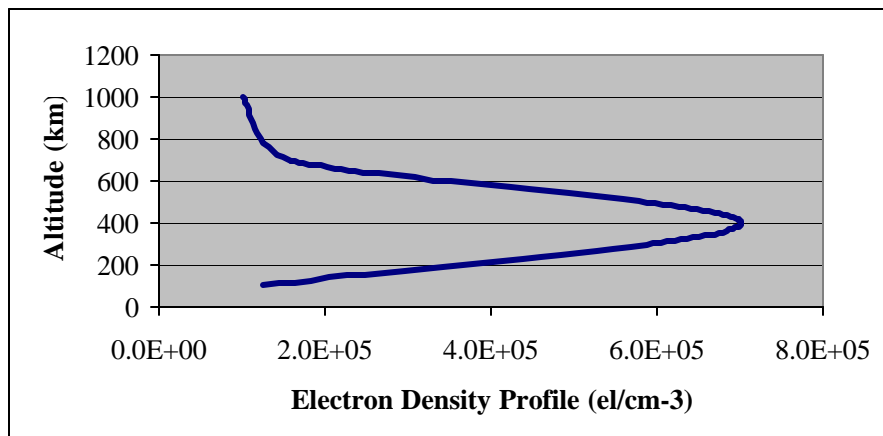


Figure 4.2 Electron Density Profile Obtained from IRI90 Model

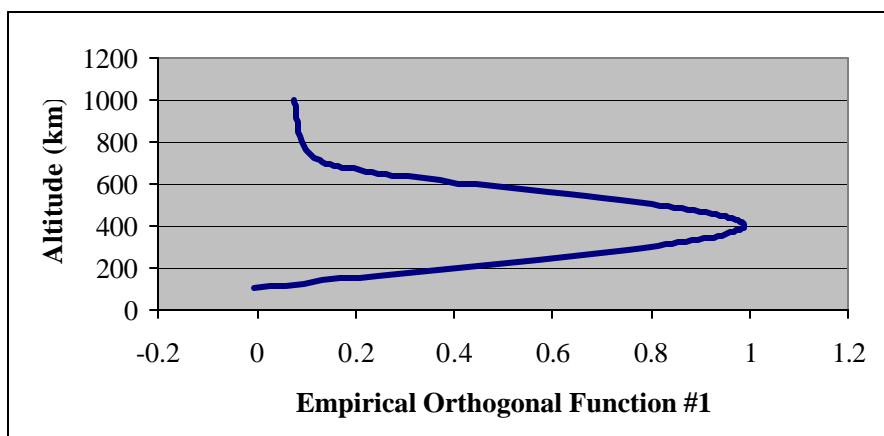


Figure 4.3 EOF #1 Derived from Electron Density Profiles

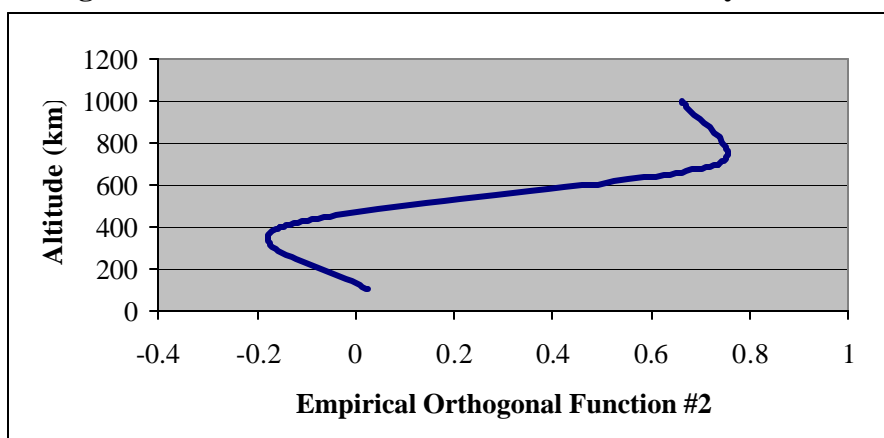


Figure 4.4 EOF #2 Derived from Electron Density Profiles

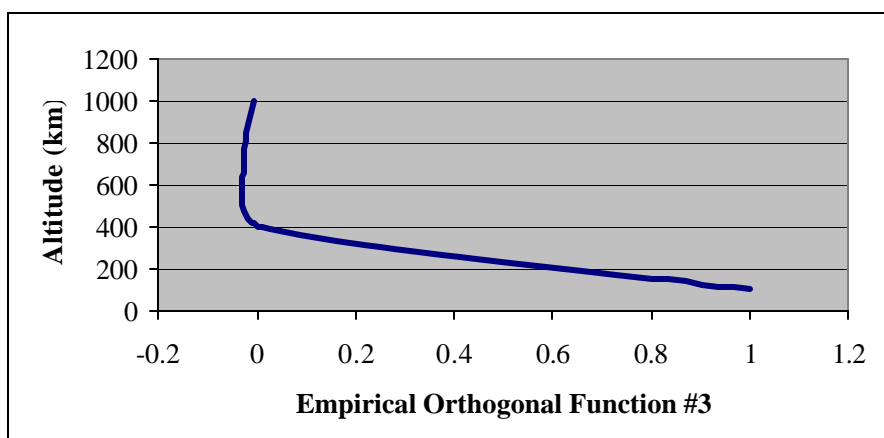


Figure 4.5 EOF #3 Derived from Electron Density Profiles

Combining equations (4.37) and (4.38), it will yield:

$$\begin{aligned}
\delta\text{TEC} &= \int \sum_{rx}^{sv} \sum_{k=1}^K \sum_{m=-M}^M \sum_{n=|m|}^M [a_{nk}^m \cos(m\lambda) + b_{nk}^m \sin(m\lambda)] \bar{P}_n^m(\cos \phi) Z_k(z) ds \\
&= \int \sum_{rx}^{sv} \sum_{k=1}^K \sum_{m=-M}^M \sum_{n=|m|}^M [a_{nk}^m \cos(m\lambda) \bar{P}_n^m(\cos \phi) Z_k(z) + b_{nk}^m \sin(m\lambda) \bar{P}_n^m(\cos \phi) Z_k(z)] ds \\
&= \int \sum_{rx}^{sv} \sum_{k=1}^K \sum_{m=-M}^M \sum_{n=|m|}^M a_{nk}^m \cos(m\lambda) \bar{P}_n^m(\cos \phi) Z_k(z) ds + \int \sum_{rx}^{sv} \sum_{k=1}^K \sum_{m=-M}^M \sum_{n=|m|}^M b_{nk}^m \sin(m\lambda) \bar{P}_n^m(\cos \phi) Z_k(z) ds \quad (4.42) \\
&= \sum_{k=1}^K \sum_{m=-M}^M \sum_{n=|m|}^M \int_{rx}^{sv} a_{nk}^m \cos(m\lambda) \bar{P}_n^m(\cos \phi) Z_k(z) ds + \sum_{k=1}^K \sum_{m=-M}^M \sum_{n=|m|}^M \int_{rx}^{sv} b_{nk}^m \sin(m\lambda) \bar{P}_n^m(\cos \phi) Z_k(z) ds \\
&= \sum_{k=1}^K \sum_{m=-M}^M \sum_{n=|m|}^M a_{nk}^m \int_{rx}^{sv} \cos(m\lambda) \bar{P}_n^m(\cos \phi) Z_k(z) ds + \sum_{k=1}^K \sum_{m=-M}^M \sum_{n=|m|}^M b_{nk}^m \int_{rx}^{sv} \sin(m\lambda) \bar{P}_n^m(\cos \phi) Z_k(z) ds
\end{aligned}$$

As indicated in equation (4.35), δTEC are calculated by differencing the smoothed total electron content measurements with respect to its approximate value. δTEC are the measurement data that will be used as observations in tomographic modeling. Meanwhile, the ionospheric electron density function is modeled using tomographic technique represented by the equation (4.38). The integration and rearrangement of equations (4.36) and (4.42) will result in:

$$\begin{aligned}
\delta\text{TEC} &= \frac{f_1^2(\lambda_1 \Phi_1 - \lambda_2 \Phi_2)}{40.3(\gamma - 1)} + \frac{1}{N} \sum_{n=1}^N \left(\frac{f_1^2[(P_1 - P_2) + (\lambda_1 \Phi_1 - \lambda_2 \Phi_2)]}{40.3(1 - \gamma)} \right) + \\
\frac{f_1^2(-B_i - B^p)}{40.3(1 - \gamma)} - \text{TEC}_0 &= \sum_{k=1}^K \sum_{m=-M}^M \sum_{n=|m|}^M a_{nk}^m \int_{rx}^{sv} \cos(m\lambda) \bar{P}_n^m(\cos \phi) Z_k(z) ds \quad (4.43) \\
+ \sum_{k=1}^K \sum_{m=-M}^M \sum_{n=|m|}^M b_{nk}^m \int_{rx}^{sv} \sin(m\lambda) \bar{P}_n^m(\cos \phi) Z_k(z) ds
\end{aligned}$$

Moving the inter-frequency bias unknowns to the right side of equation (4.43), it yields the fundamental observation equation of ionosphere tomographic modeling:

$$\begin{aligned}
& \frac{f_1^2(\lambda_1\Phi_1 - \lambda_2\Phi_2)}{40.3(\gamma - 1)} + \frac{1}{N} \sum_{n=1}^N \left(\frac{f_1^2[(P_1 - P_2) + (\lambda_1\Phi_1 - \lambda_2\Phi_2)]}{40.3(1 - \gamma)} \right) - \text{TEC}_0 \\
& = \sum_{k=1}^K \sum_{m=-M}^M \sum_{n=|m|}^M a_{nk}^m \int_{rx}^{sv} \cos(m\lambda) \bar{P}_n^m(\cos \phi) Z_k(z) ds \\
& + \sum_{k=1}^K \sum_{m=-M}^M \sum_{n=|m|}^M b_{nk}^m \int_{rx}^{sv} \sin(m\lambda) \bar{P}_n^m(\cos \phi) Z_k(z) ds + \frac{f_1^2}{40.3(1 - \gamma)} B_i + \frac{f_1^2}{40.3(1 - \gamma)} B^p
\end{aligned} \tag{4.44}$$

The first two terms on the left side of equation (4.44) are smoothed total electron content observations for tomographic modeling. The third term terms on the left side of above equation is the approximate value of total electron content and it is calculated based on the historical data or approximate electron density function. The calculation of the first two terms needs use of GPS carrier phase and code pseudorange measurements. The ionospheric model parameters and inter-frequency bias unknowns are on the right side of equation (4.44). Through equation (4.44), the dual frequency GPS observations are linked with the ionospheric model coefficients and receiver and satellite inter-frequency biases. So far a close form analytical expression that describes the relationship between the GPS observations and the ionospheric unknown parameters has been established and this close form expression is the fundamental equation for ionosphere tomographic modeling. In the data analysis presented in Chapters 5 and 6, the highest order of spherical harmonic functions is chosen to 3, namely $M=3$. After extensive calculation and parameterization comparisons, it is found that using the order of spherical harmonic functions as 3 could produce highest tomographic modeling accuracies. For the vertical component in the model, three layers are stratified in the ionosphere. That means the highest order of empirical orthogonal functions is 3 as well, namely $K=3$. The parameterization optimization for tomographic modeling and the method to determine the highest orders for spherical harmonic functions and empirical orthogonal functions can be found in Liu and Gao (2001b).

4.5 Ionosphere Tomographic Model Parameter Estimation

Once the observation equation is established, the next task is to estimate the unknown parameters using an optimal estimator. In this research, the Kalman filter is used to perform the parameter estimation. The reason to use Kalman filter is that one of the objectives of this research is to process the GPS measurements in a real-time mode and through the real-time processing to provide temporally and spatially predicted ionospheric corrections to users for their real-time applications. For ionospheric modeling, the observation data are sequentially recorded and inputted into the tomographic model. The use of Kalman filter is more suitable in the estimation of ionospheric parameters in this research. As indicated above, the unknown vector includes the ionospheric parameters as well as the receiver and satellite differential instrumental biases. The Kalman filter can be described by the following two equations (Brown, 1983):

$$\begin{aligned} x_k &= \Phi_{k,k-1} x_{k-1} + w_{k-1} \\ z_k &= H_k x_k + v_k \end{aligned} \quad (4.45)$$

where

x_k is $(n \times 1)$ system state vector consisting of the unknown parameters at time t_k ;

$\Phi_{k,k-1}$ is $(n \times n)$ transition matrix relating the estimated x_{k-1} and predicted x_k ;

w_{k-1} is $(n \times 1)$ system noise vector assumed to be white uncorrelated sequence with known covariance;

z_k is $(m \times 1)$ measurement vector at time t_k ;

H_k is $(m \times n)$ design matrix describing the relationship between measurement and state vector at time t_k ;

v_k is $(m \times 1)$ measurement error vector assumed to be a white sequence with known covariance.

The first equation in (4.45) is the dynamic equation and the second one is called measurement (observation) equation (Brown, 1983; Schwarz and Wei, 2000). The

dynamic equation describes the state variation over time described by a random process and the measurement equation describes the relationship between the measurements and random process. In this estimation, the state to be estimated is the ionospheric electron density function. More strictly, it is the correction part of the electron density function because the approximate value of electron density function has been assumed known. The measurements employed in the Kalman filter are the smoothed TEC data that are derived from GPS dual-frequency measurements at each receiver. In our estimation, we have 96 ionospheric coefficients including both a_{nk}^m and b_{nk}^m . The determination of the number of coefficients can be calculated by $2K(M+1)^2$. Considering the fact that the computation of the coefficients b_{nk}^m is unnecessary when the order of the associated Legendre polynomial is zero ($m=0$), thus the total number of the coefficients that need to be estimated will be reduced by $K(M+1)$. Consequently the number of actually estimated ionospheric coefficients is equal to $K(M+1)(2M+1) = 84$. Among the 84 parameters, there are $K(M+1)^2 = 48$ a_{nk}^m coefficients and the rest are b_{nk}^m coefficients. The number of b_{nk}^m coefficients is $KM(M+1) = 36$. Considering the estimation of one inter-frequency bias for each satellite and one inter-frequency bias for each receiver, the number of unknown parameters in the system state vector will be $(84 + n_r + n^s)$, where n_r and n^s are the number of receivers used in modeling and the number of satellites tracked by the receivers, respectively. Specifically, the state vector x_k can be written as:

$$x_k = \begin{bmatrix} a_{01}^0 \\ \vdots \\ a_{33}^3 \\ b_{11}^{-1} \\ \vdots \\ b_{33}^3 \\ B_1 \\ \vdots \\ B_{n_r} \\ B^1 \\ \vdots \\ B^{n_s} \end{bmatrix}_{(nx1)} \quad (4.46)$$

The transition matrix $\Phi_{k,k-1}$ is determined by the random process used. In this research, the first order Gauss-Markov process is used to describe the variations of the ionospheric coefficients (Gail et al., 1993). The autocorrelation function of the first order Gauss-Markov process can be described by (Brown, 1983):

$$R_x(\tau) = \sigma^2 e^{-\beta|\tau|} \quad (4.47)$$

where σ and $1/\beta$ are standard deviation of random process noise and correlation time of the process, respectively. The exponential autocorrelation function in equation (4.47) indicates the values of the ionospheric parameters become less and less correlated as the time span increasing. The first order Gauss-Markov process has a relatively simple mathematical description and fits a large number of physical processes (Brown, 1983). The model has also been applied for ionospheric modeling with good performance to represent the variation of the ionospheric variation over time (Skone, 1998). In this research, the correlation time $1/\beta$ is chosen as 60 seconds and the standard deviation σ is 0.7 TECU ($\sigma^2 = 0.5 \text{TECU}^2$) after extensive data analysis and comparison. The standard deviation value is consistent with the one used in Komjathy (1997). The 60 seconds correlation time allows the ionosphere to change with a rapid speed. For inter-

frequency bias states, the correlation time is extended to one-day period (86400 seconds) since the biases are stable over time on a daily even monthly basis (Schaer, 1999). Thus the transition matrix $\Phi_{k,k-1}$ can be written as:

$$\Phi_{k,k-1} = \begin{bmatrix} e^{-\beta \Delta t} & 0 & \dots & 0 \\ 0 & e^{-\beta \Delta t} & \dots & 0 \\ \dots & \dots & \dots & \dots \\ 0 & 0 & \dots & e^{-\beta_n \Delta t} \end{bmatrix}_{(n \times n)} \quad (4.48)$$

where $\Delta t = t_{j+1} - t_j$ is the time interval between two consecutive δTEC measurements. In this thesis research, the interval is 30 seconds because all the GPS data used in the data analysis presented in Chapters 5 and 6 were recorded at a 30-second rate. Equation (4.48) statistically describes how the unknown parameters in the state vector in equation (4.46) vary over time.

The random process noise w_{k-1} and measurement noise v_k are uncorrelated zero-mean random processes with the means:

$$E(w_k) = 0 \quad (4.49)$$

$$E(v_k) = 0 \quad (4.50)$$

and covariance matrices:

$$E[w_k w_j^T] = \begin{cases} Q_k, & k = j \\ 0, & k \neq j \end{cases} \quad (4.51)$$

$$E[v_k v_j^T] = \begin{cases} R_k, & k = j \\ 0, & k \neq j \end{cases} \quad (4.52)$$

$$E[w_k v_j^T] = 0 \quad \text{for all } k \text{ and } j \quad (4.53)$$

Since the ionospheric variation process is modeled as a first order Gauss-Markov process, the corresponding process noise matrix Q_k can be written as in the form of (Skone, 1998):

$$Q_k = \begin{bmatrix} \sigma_1^2(1 - e^{-2\beta_1\Delta t}) & 0 & \dots & 0 \\ 0 & \sigma_2^2(1 - e^{-2\beta_2\Delta t}) & \dots & 0 \\ \dots & \dots & \dots & \dots \\ 0 & 0 & \dots & \sigma_n^2(1 - e^{-2\beta_n\Delta t}) \end{bmatrix}_{(n \times n)} \quad (4.54)$$

The z_k measurement vector consists of the δTEC data as defined in equation (4.36). The measurement vector z_k has the form of:

$$z_k = \begin{bmatrix} \delta\text{TEC}_1 \\ \delta\text{TEC}_2 \\ \vdots \\ \delta\text{TEC}_m \end{bmatrix}_{(m \times 1)} \quad (4.55)$$

where m is the total number of TEC measurements at epoch t_k from all receiver stations. In the estimation of the receiver and satellite inter-frequency biases, a reference has to be introduced because the biases are actually relative values. The IGS data analysis centers usually establish this reference by assuming that the sum of all satellite inter-frequency biases should be equal to zero. In this research, the reference is established by introducing a pseudo TEC observation. This pseudo TEC observation can be an observation of receiver inter-frequency biases or satellite inter-frequency biases. Here the pseudo TEC observation is introduced to let the sum of satellite inter-frequency biases equal zero. This pseudo TEC observation can be written as:

$$\delta\text{TEC}_{m+1} = 0 \quad (4.56)$$

Combining equation (4.56) with equation (4.55), it will yield a measurement vector with one more dimension than the number of the actually observed δTEC measurements:

$$z_k = \begin{bmatrix} \delta\text{TEC}_1 \\ \delta\text{TEC}_2 \\ \vdots \\ \delta\text{TEC}_m \\ 0 \end{bmatrix}_{(m+1) \times 1} \quad (4.57)$$

The design matrix H_k in equation (4.45) describes the relationship between the δTEC data and the unknown parameters, namely the measurement vector z_k and the state vector x_k . The matrix H_k generally has the following form in tomographic modeling, including the pseudo TEC observation:

$$H_k = \begin{bmatrix} h_{11} & h_{12} & \cdots & h_{1,84} & F & 0 & \cdots & 0 & F & 0 & \cdots & 0 \\ h_{21} & h_{22} & \cdots & h_{2,84} & F & 0 & \cdots & 0 & 0 & F & \cdots & 0 \\ \cdots & \cdots & \cdots & \cdots & \cdots & \cdots & \cdots & \cdots & \cdots & \cdots & \cdots & \cdots \\ h_{m,1} & h_{m,2} & \cdots & h_{m,84} & 0 & 0 & \cdots & F & 0 & 0 & \cdots & F \\ 0 & 0 & \cdots & 0 & 0 & 0 & \cdots & 0 & 1 & 1 & \cdots & 1 \end{bmatrix}_{(m+1) \times n} \quad (4.58)$$

$\underbrace{\hspace{10em}}_{(m+1) \times 84} \quad \underbrace{\hspace{10em}}_{(m+1) \times n_r} \quad \underbrace{\hspace{10em}}_{(m+1) \times n^s}$

where F is defined as:

$$F = \frac{f_1^2}{40.3(1 - \gamma)} \quad (4.59)$$

In H_k matrix described in equation (4.58), the elements in the last row are corresponding to the pseudo TEC observation defined in equation (4.56) by making the sum of all satellite inter-frequency biases equal to zero. In H_k , the first sub-matrix is the design matrix for the coefficients of the tomographic model and the second sub-matrix is for the receiver inter-frequency biases and the last sub-matrix is for satellite inter-frequency biases. As mentioned before, 84 ionospheric coefficients are used to characterize the ionospheric electron density. Therefore the size of the first sub-matrix is $(m + 1) \times 84$. As indicated in equation (4.46), n_r and n^s represent the number of receivers and the number

of satellites, respectively. Therefore the sizes of the second and third sub-matrix are $(m+1) \times n_r$ and $(m+1) \times n^s$, respectively. As discussed before, there are 48 a_{nk}^m parameters and 36 b_{nk}^m parameters. Thus the first 48 elements $h_{i,j}$ ($i = 1, 2, \dots, m; j = 1, 2, \dots, 48$) in the first sub-matrix of equation (4.58) correspond to the design matrix for the a_{nk}^m parameters and the elements $h_{i,l}$ ($i = 1, 2, \dots, m; l = 49, 50, \dots, 84$) correspond to the design matrix for b_{nk}^m parameters. Referring to equation (4.43), the calculation of the elements $h_{i,j}$ and $h_{i,l}$ can use the following formulas:

$$h_{i,j} = \int_{rx}^{sv} \cos(m\lambda) \bar{P}_n^m(\cos \phi) Z_k(z) dz \quad (4.60)$$

$$h_{i,l} = \int_{rx}^{sv} \sin(m\lambda) \bar{P}_n^m(\cos \phi) Z_k(z) dz \quad (4.61)$$

For the measurement noise matrix R_k in equation (4.52), it has the following expression considering the measurements are assumed to be uncorrelated:

$$R_k = \begin{bmatrix} r_{11} & 0 & \dots & 0 & 0 \\ 0 & r_{22} & \dots & 0 & 0 \\ \dots & \dots & \dots & \dots & \dots \\ 0 & 0 & \dots & r_{mm} & 0 \\ 0 & 0 & \dots & 0 & \varepsilon \end{bmatrix}_{(m+1) \times (m+1)} \quad (4.62)$$

The elements in equation (4.62) represent the variance-covariance of the observed TEC measurements. In this research, the TEC measurements are assumed to be uncorrelated and their covariance is zero. The variance values of the δTEC measurements derived from GPS dual-frequency data can be evaluated using equation (4.29) or (4.30). In the last row, ε represents the variance value of the pseudo TEC observation. A very small value should be assigned to it in order to make the constraint condition on the satellite inter-frequency biases.

The estimation of the state vector can be performed by recursively incorporating new δTEC measurements into the Kalman filter to update the system state vector x_k at each epoch. In the ionospheric modeling, GPS receivers continuously observe GPS satellite dual-frequency signals. Hence the smoothed TEC data can be continuously derived from GPS measurements. Subsequently, the continuous δTEC measurements are obtained from equation (4.36). Once the δTEC measurements become available at each epoch, the Kalman filter can perform a recursive calculation to update the state vector. First it needs to compute the gain matrix K_k using the covariance information of the measurements and the priori covariance information about the state vector. The gain matrix K_k can be calculated by:

$$K_k = P_k^- H_k^T (H_k P_k^- H_k^T + R_k)^{-1} \quad (4.63)$$

where P_k^- is the a priori covariance information about the a priori estimate of the state vector. Based on the gain matrix and the new δTEC measurements, the updated estimate of state vector \hat{x}_k can be obtained by:

$$\hat{x}_k = \hat{x}_k^- + K_k (z_k - H_k \hat{x}_k^-) \quad (4.64)$$

where \hat{x}_k^- is the a priori estimate of the state vector from previous estimation at last epoch. The corresponding covariance of the updated state vector \hat{x}_k can be calculated by:

$$P_k = (I - K_k H_k) P_k^- \quad (4.65)$$

After the estimation is completed using the δTEC measurements at each epoch, the Kalman filter performs a prediction of the state vector for next epoch. The predicted state vector \hat{x}_{k+1}^- can be written as:

$$\hat{x}_{k+1}^- = \Phi_{k+1,k} \hat{x}_k \quad (4.66)$$

and the covariance matrix corresponding to the predicted state vector \hat{x}_{k+1}^- can be written as:

$$P_{k+1}^- = \Phi_{k+1,k} P_k \Phi_{k+1,k}^T + Q_k \quad (4.67)$$

Combining equations (4.63)~(4.67), the ionospheric coefficients as well as the inter-frequency biases can be recursively estimated in the Kalman filter using the continuously tracked GPS measurements.

4.6 Ionospheric TEC Prediction and Evaluation

The ionospheric modeling using GPS observations is still a post-mission processing of GPS data although the modeling can be implemented in near real-time (NRT) mode and the latency of availability of modeling result may be just a few minutes, depending on the amount of GPS data, the complexity of the model and the power of the computational facility. In the data analysis presented in Chapter 6, the computation time for each session modeling (containing 15 minutes of GPS data from 21 GPS stations for simultaneous TEC smoothing and tomographic model construction as well as TEC prediction for the future 5 minutes at one GPS station) is 4~5 minutes, which is based on a PC computer of Pentium III 550 MHz with 256 MB RAM. If more powerful computer is used, the data processing time shall be reduced accordingly. That is to say, even if the GPS data are collected in real-time, the ionospheric modeling results still have a latency of several minutes (in this research). In real-time applications, such as GPS real-time kinematic (RTK) positioning and WAAS system, real-time ionospheric correction data are required. In this case, the ionospheric model must perform a prediction of the ionosphere and broadcast the predicted ionospheric corrections to users in order to support the real-time applications.

Once the ionosphere tomographic model is established as shown by equation (4.43) and the parameters are estimated by Kalman filter, the parameters can be further utilized to perform the ionospheric prediction. In this research, the ionospheric model is first constructed using 15 minutes of smoothed TEC observations from GPS stations. Then the model performs a prediction for the future 5 minutes, 10 minutes or 30 minutes,

depending on the prediction interval used in the data analysis. For instance, the dual-frequency GPS measurements collected during 00:00:00 to 00:15:00 UTC are used to form smoothed TEC data and construct ionospheric model, then the model is used to perform prediction for the epoch 00:20:00 UTC. The period between the last observed epoch and the predicted epoch is 5-minute. The predictions are assumed to be effective for 5-minute during the period 00:15:00 to 00:20:00 UTC. Therefore it is referred to as 5-minute prediction. If the prediction interval is 30-minute, then the effective period of the predictions is from 00:15:00 to 00:45:00 UTC.

What is actually predicted is the ionospheric coefficients. The predicted coefficients can be used to calculate the TEC at GPS user station in the GPS network. According to the model presented above, the computation of ionospheric δTEC data is the multiplication of the vector of the tomographic model coefficients that describe the ionosphere and the geometry matrix accounting for the TEC's geometrical dependence on the locations of both satellites and receivers. In the ionospheric prediction, the vector of tomographic model coefficients is broadcast to ionospheric users via a given communication channel, e.g. via radio or internet for the GPS RTK users or the geostationary satellites for the WAAS users. The ionosphere model users receive the model coefficients and can calculate the ionospheric TEC for real-time positioning and navigation applications given the coefficient vector and their geometry matrix. The determination of the geometry matrix relies on the locations of the GPS satellites and users' receivers. The satellite positions can be calculated in real-time from the broadcast navigation message or forecast precise orbit data provided by IGS. Thus the geometry can be readily calculated according to equation (4.58) once the satellite positions and the approximate user locations are known. Suppose that the geometry matrix for ionospheric prediction is denoted as G^P and the predicted state vector from Kalman filter is denoted as x^P , then predicted ionospheric δTEC , expressed as δd^P , can be calculated as:

$$\delta d^P = G^P x^P \quad (4.68)$$

Remember, the quantity δd^P computed from equation (4.68) is not the total electron content but only a part of it. In order to obtain the predicted total electron content, the predicted δd^P must add another part that is calculated from approximate value of electron density function $N_0(\lambda, \phi, z)$. The predicted total electron content, denoted as d^P , is calculated with:

$$d^P = \delta d^P + \int_{rx}^{sv} N_0(\lambda, \phi, z) ds \quad (4.69)$$

In equation (4.69), the second term in right side is the known approximate total electron content calculated based on approximate electron density function along the GPS signal path from predicted satellite and receiver. In order to evaluate the accuracy of the predicted ionospheric data d^P , three different accuracy indicators are proposed to conduct a systematic assessment. The three methods are described in the following section while the assessment results will be presented in Chapters 5 and 6.

4.6.1 Evaluation indicator one: vertical TEC error

In order to evaluate the accuracy of the TEC predictions, the predicted TEC data are compared with the TEC data observed at GPS stations equipped with dual-frequency GPS receivers. While the tomographic model is performing 5-minute, 10-minute or 30-minute TEC predictions at GPS user stations, the tested GPS stations are actually still continuously observing GPS satellites. The observed dual-frequency GPS measurements then could be used to derive smoothed ionospheric TEC with equation (4.26). These smoothed TEC data directly derived from GPS measurements are used as known references. Therefore the model prediction accuracy could be evaluated by comparing the model-predicted TEC data with the GPS-measured TEC data. In the analysis, the difference between the predicted and the observed TEC is defined as the prediction error as follows:

$$\Delta d = d^P - d^O \quad (4.70)$$

where d^o is the observed TEC data inferred from GPS observations and d^p is the predicted TEC data; Δd is the disagreement between the two sets of TEC data. Note that the predicted TEC data d^p contain the effect of satellite and receiver inter-frequency biases because the unknown parameter vector x^p consists of both ionospheric model coefficients and biases. The TEC observations d^o inferred from GPS data automatically include the effect of inter-frequency biases. The estimated inter-frequency biases have an accuracy about 0.1 ns, equivalent to 3 cm in distance or about 0.18 TECU on L1 frequency. The subtraction of d^o and d^p will almost eliminate the effect of the inter-frequency biases although the estimated biases have a one σ error about 0.18 TECU. The residual of 0.18 TECU is negligible compared to the modeling error of the tomographic model itself which is at the order of several TECU. The result of the subtraction will be the discrepancy between the predicted TEC and observed TEC. This discrepancy results from the imperfection of the ionospheric model and is called ionospheric modeling error. The ionospheric model error arises from multiple factors such as data used to derive empirical orthogonal functions, the choice of parameters used in Kalman filter, the density and distribution of TEC measurements. The magnitude of Δd indicates the accuracy of the ionospheric model predictions. For each pair of receiver and satellite, one Δd can be calculated. If each element of the slant Δd vector is further mapped to zenith direction in order to eliminate its dependence on elevation angle, the vertical TEC error can be obtained.

$$\Delta d_i^y = M(\text{ele}_i)(d_i^p - d_i^o) = M(\text{ele}_i) \Delta d_i \quad (4.71)$$

where

Δd_i^y is the vertical TEC error for the i -th element in the predicted TEC vector;

$M(\text{ele}_i)$ is the mapping function that projects slant TEC to vertical TEC;

ele_i is the elevation angle for the i -th element in the predicted TEC vector;

d_i^p is the i -th element in the predicted TEC vector;

d_i^o is the i -th element in the observed TEC vector;

Δd_i is the slant TEC error for the i -th element in the predicted TEC vector;

In equation (4.71), the mapping function $M(\text{ele}_i)$ is defined as (Mannucci et al., 1993):

$$M(\text{ele}_i) = \left[1 - \left[\frac{\cos(\text{ele}_i)}{1 + \frac{h}{R_E}} \right]^2 \right]^{\frac{1}{2}} \quad (4.72)$$

where

ele_i is the elevation angle;

h is the ionosphere shell height;

R_E is the Earth's radius.

For all the vertical TEC errors, an RMS value can be calculated using:

$$\Delta d_{\text{rms}}^v = \sqrt{\frac{\sum_{i=1}^N (\Delta d_i^v)^2}{N}} \quad (4.73)$$

The RMS of vertical TEC prediction errors is an indicator of the “absolute” magnitude of the TEC prediction errors and the vertical TEC values is better suited for comparative work (Gail et al., 1993). The following indicator, the relative error, provides an assessment of relative prediction error.

4.6.2 Evaluation indicator two: relative error

The relative error is defined as the ratio of the “absolute” TEC prediction error with respect to the TEC observation. The relative error for each element in the predicted TEC vector is defined as:

$$\text{R.E.}_i = \left| \Delta d_i / d_i^o \right| \times 100\% \quad (4.74)$$

For all the elements in the predicted TEC vector, a mean relative error can be calculated by averaging all the $R.E._i$ obtained from equation (4.70). The relative error indicates the percentage of ionospheric errors in the TEC prediction data with respect to the observed TEC data. For a good ionospheric model, this relative error should be as small as possible. Another definition of relative error, the ratio between RMS value and mean TEC value, is used and a daily relative error ranging about 13~22% is reported (Hernández-Pajares, 2003). In this research, the relative error is defined as equation (4.74) because RMS is a statistic value for a series of TEC predictions and it could not reflect the error of each individual TEC prediction. The relative error defined in equation (4.74) represents the relative error of each predicted TEC.

4.6.3 Evaluation indicator three: recovering efficiency

The third indicator of evaluating the prediction performance is to use recovering efficiency to describe the model's prediction accuracies. The calculation of recovering efficiency is realized by employing three different types of ionospheric models in a GPS single point positioning determination. The three ionospheric models are dual-frequency model, ionospheric tomographic model and zero-model. The dual-frequency model represents the best scenario in ionospheric error correction because it employs the observed dual-frequency GPS data to correct the ionospheric error in GPS positioning. Zero-model represents the worst scenario in ionospheric error correction because no ionospheric corrections are made when using this model in GPS positioning. Tomographic model uses the predicted ionospheric data to correct ionospheric error in GPS positioning. Its performance depends on the quality of the constructed model and it will be evaluated through a comparison with respect to dual-frequency model and zero-model. The dual-frequency model is considered as the most effective and precise way to correct the ionospheric error while the zero-model is the least effective way for ionospheric correction. The performance of the tomographic model should be at some point between the dual-frequency model and the zero-model. If the tomographic model

has a good ionospheric predicting capability, its performance should be closer to that of dual-frequency model rather than closer to zero-model.

If the three different models are employed into a GPS single point positioning test and the computation conditions are kept exactly the same except the use of different ionospheric correction models, the errors in final positioning solutions should reflect the performance of these ionospheric models. In the following, the single point positioning RMS errors corresponding to the three ionospheric models are denoted by SPP_{rms_dual} , SPP_{rms_tomo} and SPP_{rms_zero} , respectively. The recovering efficiency is defined as:

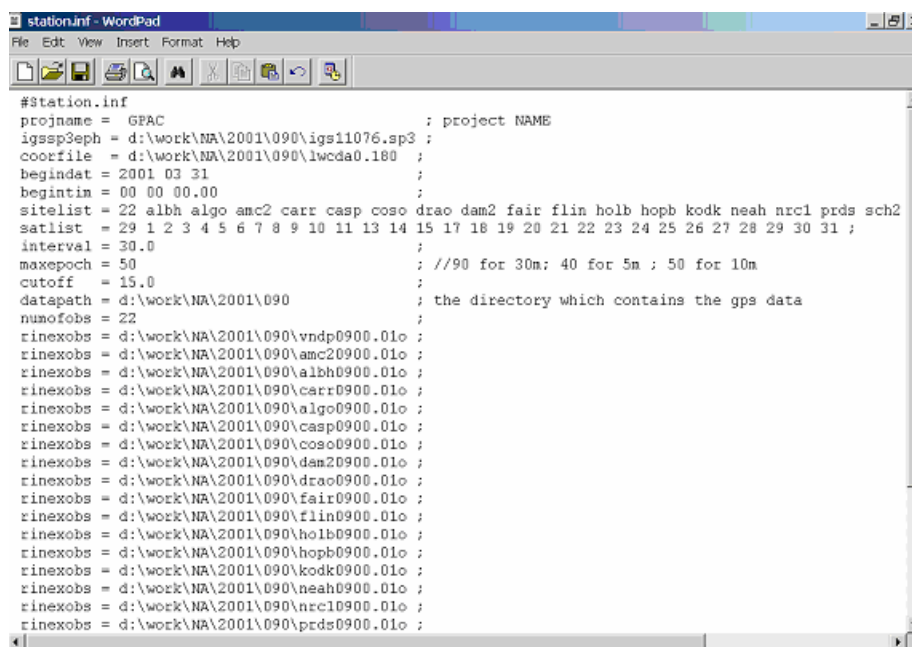
$$Recov = \frac{SPP_{rms_zero} - SPP_{rms_tomo}}{SPP_{rms_zero} - SPP_{rms_dual}} \quad (4.75)$$

If the tomographic model has better capability to predict ionospheric TEC, the positioning solutions from tomographic model should be closer to those of dual-frequency model. Correspondingly the recovering efficiency becomes higher and its maximum value should be 1.

4.7 Software Development and Implementation

A software package that is namely “IonoTomo” has been developed in C++ language to implement the ionospheric tomography modeling method. The major functions of the software include TEC computation using phase smoothed code measurements and error estimation, tomographic model construction, receiver and satellite inter-frequency bias estimation, epoch-by-epoch parameter estimation using Kalman filter, prediction of ionospheric TEC, and accuracy evaluation of the predicted TEC data. The “IonoTomo” software can be compiled and run in Microsoft® Windows environments. Currently it is compiled and run on a Microsoft® Windows 2000 platform on a PC Pentium III 550 MHz with 256 MB RAM. The data processing in Chapter 5 shows that using 15 minutes of TEC observations from 5 GPS stations to construct the ionospheric model and predict

for 5 minutes of TEC data at one GPS station will take approximately one minute while the data processing in Chapter 6 shows that using 15 minutes of TEC observations from 21 GPS stations to construct ionospheric model and predict for 5 minutes of TEC data at one GPS station will take approximately 4-5 minutes to complete. In the future, if the computational facility is updated and the computer source codes are further optimized, the above processing time can be further reduced. The “IonoTomo” software is designed to be easy use. All the configuration parameters are stored in a file, which includes the information such as project name, observation date of GPS data, names and paths of GPS observation files, name and path of precise orbit file (orbit data provided by IGS in SP3 format), the list of GPS stations, the used satellites (user can select to block some particular satellites), the number of epochs for ionospheric modeling and predicting in each session, the start date and time of modeling, data processing interval, data editing cutoff angle, etc. An example of the configuration file is illustrated in Figure 4.6.



```

#Station.inf
projname = GPAC ; project NAME
igssp3eph = d:\work\NA\2001\090\igs11076.sp3 ;
coordfile = d:\work\NA\2001\090\lwcda0.180 ;
begindat = 2001 03 31 ;
begintim = 00 00 00.00 ;
sitelist = 22 albh algo amc2 carr casp coso drao dam2 fair flin holb hopb kodk neah nrc1 prds sch2
satlist = 29 1 2 3 4 5 6 7 8 9 10 11 13 14 15 17 18 19 20 21 22 23 24 25 26 27 28 29 30 31 ;
interval = 30.0 ;
maxepoch = 50 ; //90 for 30m; 40 for 5m ; 50 for 10m
cutoff = 15.0 ;
datapath = d:\work\NA\2001\090 ; the directory which contains the gps data
numofobs = 22
rinexobs = d:\work\NA\2001\090\vndp0900.01o ;
rinexobs = d:\work\NA\2001\090\amc20900.01o ;
rinexobs = d:\work\NA\2001\090\albh0900.01o ;
rinexobs = d:\work\NA\2001\090\carr0900.01o ;
rinexobs = d:\work\NA\2001\090\algo0900.01o ;
rinexobs = d:\work\NA\2001\090\casp0900.01o ;
rinexobs = d:\work\NA\2001\090\coso0900.01o ;
rinexobs = d:\work\NA\2001\090\dam20900.01o ;
rinexobs = d:\work\NA\2001\090\drao0900.01o ;
rinexobs = d:\work\NA\2001\090\fair0900.01o ;
rinexobs = d:\work\NA\2001\090\flin0900.01o ;
rinexobs = d:\work\NA\2001\090\holb0900.01o ;
rinexobs = d:\work\NA\2001\090\hopb0900.01o ;
rinexobs = d:\work\NA\2001\090\kodk0900.01o ;
rinexobs = d:\work\NA\2001\090\neah0900.01o ;
rinexobs = d:\work\NA\2001\090\nrc10900.01o ;
rinexobs = d:\work\NA\2001\090\prds0900.01o ;

```

Figure 4.6 Configuration File Used in IonoTomo

Another necessary file in the modeling contains the known coordinates of the GPS stations, which are used in the calculation of the geometry matrix during the modeling. All these information can be easily obtained and edited before the data processing. Once

they are configured, the software can be run and the predicted TEC data for each session are stored in a single file. Each row of the result file includes the epoch number, the GPS time and UTC time of that prediction, the PRN of predicted satellite, the serial number and the name of predicted GPS station, the observed TEC data, predicted TEC data, the difference between the prediction and TEC observations, the coordinates of the predicted GPS station and the predicted satellite, etc. The users can easily use the TEC predictions in the files for their own applications. An example of the ionospheric TEC prediction result file is given in Figure 4.7.

Epoch	GPS Time	UTC Time	PRN	Serial	Station Name	Observed TEC	Predicted TEC	Difference
33	561420.00	{11:57:00.0}	28	08	d:\work\NA\2001\090\dcao0900.01o	-30.89	-28.65	-2.23
33	561420.00	{11:57:00.0}	08	08	d:\work\NA\2001\090\dcao0900.01o	-16.22	-17.14	0.91
33	561420.00	{11:57:00.0}	10	08	d:\work\NA\2001\090\dcao0900.01o	1.37	-6.22	7.59
34	561450.00	{11:57:30.0}	03	08	d:\work\NA\2001\090\dcao0900.01o	-15.40	-10.61	-4.79
34	561450.00	{11:57:30.0}	19	08	d:\work\NA\2001\090\dcao0900.01o	-14.88	-16.33	1.45
34	561450.00	{11:57:30.0}	31	08	d:\work\NA\2001\090\dcao0900.01o	-7.89	-13.64	5.75
34	561450.00	{11:57:30.0}	01	08	d:\work\NA\2001\090\dcao0900.01o	-18.71	-13.37	-5.34
34	561450.00	{11:57:30.0}	27	08	d:\work\NA\2001\090\dcao0900.01o	-22.49	-21.82	-0.67
34	561450.00	{11:57:30.0}	13	08	d:\work\NA\2001\090\dcao0900.01o	-26.15	-27.33	1.18
34	561450.00	{11:57:30.0}	28	08	d:\work\NA\2001\090\dcao0900.01o	-30.51	-28.60	-1.91
34	561450.00	{11:57:30.0}	08	08	d:\work\NA\2001\090\dcao0900.01o	-16.66	-17.24	0.58
34	561450.00	{11:57:30.0}	10	08	d:\work\NA\2001\090\dcao0900.01o	1.26	-6.18	7.44
35	561480.00	{11:58:00.0}	03	08	d:\work\NA\2001\090\dcao0900.01o	-14.73	-10.61	-4.12
35	561480.00	{11:58:00.0}	19	08	d:\work\NA\2001\090\dcao0900.01o	-14.70	-16.34	1.65
35	561480.00	{11:58:00.0}	31	08	d:\work\NA\2001\090\dcao0900.01o	-8.09	-13.68	5.60
35	561480.00	{11:58:00.0}	01	08	d:\work\NA\2001\090\dcao0900.01o	-18.88	-13.77	-5.12
35	561480.00	{11:58:00.0}	27	08	d:\work\NA\2001\090\dcao0900.01o	-21.76	-21.85	0.09
35	561480.00	{11:58:00.0}	13	08	d:\work\NA\2001\090\dcao0900.01o	-26.30	-27.35	1.05
35	561480.00	{11:58:00.0}	28	08	d:\work\NA\2001\090\dcao0900.01o	-29.87	-28.54	-1.32
35	561480.00	{11:58:00.0}	08	08	d:\work\NA\2001\090\dcao0900.01o	-16.47	-17.35	0.87
36	561510.00	{11:58:30.0}	03	08	d:\work\NA\2001\090\dcao0900.01o	-14.43	-10.60	-3.83
36	561510.00	{11:58:30.0}	19	08	d:\work\NA\2001\090\dcao0900.01o	-14.52	-16.36	1.84
36	561510.00	{11:58:30.0}	31	08	d:\work\NA\2001\090\dcao0900.01o	-8.30	-13.72	5.42
36	561510.00	{11:58:30.0}	01	08	d:\work\NA\2001\090\dcao0900.01o	-18.83	-14.18	-4.65

Figure 4.7 Ionospheric TEC Prediction Results from IonoTomo

In the current version of “IonoTomo”, it can perform real-time ionospheric modeling and ionospheric TEC prediction with local area GPS network and wide area GPS network. The use of the “IonoTomo” is straightforward. Once the observations from GPS reference network are collected, they are converted into RINEX format. The coordinates of the GPS reference stations are collected as well and stored to a coordinate file. A satellite orbit file is needed for the computation of GPS satellite coordinates, which is available from IGS public data center. After these files are prepared, then other

parameters controlling the data editing such as elevation cutoff angle, number of epoch for modeling and predicting in each session, the modeling start date and time, etc, can be configured. After that, the “IonoTomo” software can be run and a result file containing the TEC prediction results for each session could be obtained shortly. In the data analysis, the “IonoTomo” is executed two rounds to get the tomographic TEC prediction results for users. In the first round of execution, the data set with entire day observations is processed to estimate the satellite and receiver inter-frequency biases. After the first round of computation, the estimated inter-frequency biases are used as known values in the second round of computation. In the second round of computation, only the estimation of ionospheric parameters is performed in each computation session. This processing procedure has two advantages. First, the inter-frequency biases can be estimated with a good accuracy while using an entire day of GPS measurements. Second, during the ionospheric modeling within each session, the total number of estimated unknown parameters is reduced and this is helpful for real-time ionospheric modeling estimation. In this research, each computation session uses 15 minutes of GPS observations to estimate ionospheric model. After the processing in each session is completed, the model will perform an ionospheric prediction at specified prediction intervals like 5-minute, 10-minute or 30-minute. Once the prediction is done, the 15-minute time window of the computation session moves forward with the same amount of the prediction interval and starts the ionospheric modeling for next session.

4.8 Advantages of Tomographic Modeling

Compared to other ionospheric 2D ionospheric models, the function-based tomographic modeling system developed in this study has several unique features. First of all, it has the capability to model the ionosphere in multiple layers. This is an improvement over the single-layer ionospheric models where only a single ionospheric shell is used. In the tomographic model, the empirical orthogonal functions are used to characterize the vertical ionospheric profile. The number of layers used in the tomographic model is governed by the order of the empirical orthogonal functions. Secondly, the variable that

is modeled in ionosphere tomographic modeling is the electron density function. This characteristic is essentially to some degree associated with the first characteristic of tomographic model presented above. This is another distinct difference of tomographic model from the 2D models. In the GPS-derived 2D ionospheric models, the variable is usually total electron content (TEC). Based on the electron density function estimated from the tomographic model, other variables including the TEC used by 2D models can be directly derived. Therefore, the tomographic modeling provides more fundamental information about the ionosphere than other the 2D ionospheric models. Thirdly, in its first time, the close form of analytical expression that establishes the link between ionospheric TEC smoothing and function-based ionosphere tomographic modeling is derived. This analytical expression allows the ionospheric smoothing and tomographic modeling to execute in parallel and thus it is very suitable for real-time ionospheric modeling. Fourthly, the function-based tomographic model is integrated with the Kalman filter, which allows the modeling to be operated in real-time process. Furthermore, the ionospheric modeling system developed in this research has the capability to generate both TEC predictions at various prediction intervals. These ionospheric predictions with different prediction intervals can meet the various application requirements by GPS users or other ionospheric users. Finally, compared to the voxel-based tomographic model, the function-based tomographic model has significantly less number of ionospheric parameters. The computational burden at both the data analysis center and user end is much less than that for voxel-based model.

4.9 Applications of Ionosphere Tomographic Modeling

The tomographic technique is particularly useful in modeling ionosphere for regions that is highly structured. In addition to the ionospheric correction for GPS positioning and navigation, the tomographic model can also be used in many HF/VHF/UHF radio applications. Information about the ionosphere can be used to locate the source of radio transmissions that have been reflected from the ionosphere. The tomographic model can be used in VHF/UHF (30-3000MHz) range for applications such as tracking of satellites,

orbiting debris, ballistic projectiles, satellite geolocation of transmitters, ionospheric corrections to (single-frequency) satellite navigation systems.

4.9.1 Single frequency GPS receiver positioning and navigation

As stated before, the ionospheric range delay error is the biggest error source in GPS positioning and navigation after SA was turned off. The ionospheric error must be compensated in order to achieve high positioning precision. Single-frequency GPS users must depend on a given ionospheric model to correct the ionospheric error. The precision of ionospheric model largely determines the obtainable positioning accuracy of single-frequency users. Therefore, the ionospheric correction model for single-frequency users must be as precise as possible in order to obtain higher positioning accuracies. The tomographic model is able to model the ionosphere in multiple layers and can provide high modeling precision for the GPS users. In the correction for single-frequency users, the users first calculate the geometry matrix and then determine the ionospheric TEC correction values by a production of geometry matrix and ionospheric estimated parameters, as indicated in equation (4.68). The correction values are added to the background TEC values and the total TEC values are obtained as indicated by equation (4.69). The total TEC values can further translate into range corrections by using equation (4.14). The range corrections are added to the GPS measurements and thus more precise positioning solutions can be obtained by using the corrected measurements. Chapters 5 and 6 will illustrate the positioning accuracy improvement by using the tomographic model.

4.9.2 Other space-based Earth observation systems (EOS)

Besides the employment of the tomographic modeling results to single-frequency GPS positioning and navigation, the tomographic model is also useful for other space-based Earth observation systems (EOS). In radar altimetry applications, precise ionosphere models (better than 4 TECU) are required to investigate the basin-scale (10 000 km) ocean features with single frequency altimetry data (Giannini and Kilgus, 1997). In the

application of Very Long Baseline Interferometry (VLBI) technique to precisely determine the distances of baselines, the ionospheric errors must be corrected using a model when the VLBI is operating at a single frequency. Ros et al. (1999) successfully used the GPS data to determine ionosphere corrections for a VLBI experiment.

4.9.3 Radio frequency selection

The ionospheric information is also important for radio frequency selections. For successful communications between any two specified locations at any given time of the day, a maximum usable frequency (MUF), lowest usable frequency (LUF) and an optimum working frequency have to be determined. The determination of useable frequency boundaries, MUF and LUF, depends on the refraction properties of the ionosphere, absorption considerations, and the amount of atmospheric noise present. Therefore the information on the ionospheric conditions is crucial for scheduling the MUF and LUF for the radio communications.

4.9.4 Space weather research

Space weather research is a subject related to the observation and forecasting of solar activities. This includes the solar wind, the magnetosphere and the ionosphere. All of them have the potential to affect the near Earth environment. A burst of plasma ejected from the Sun, such as a flare, a coronal mass ejection (CME) can cause significant increase of high energy particles to the magnetosphere and consequently geomagnetic storms occur. A direct result of the geomagnetic storms is the change in the electron density of the ionosphere. The ionosphere is an important component of space weather and it has direct impact on GPS signals. Since variations in the behavior of the ionosphere is a good measurable indicator of changing space weather, studying and modeling the ionosphere will help understand and study the space weather. Space weather impact on GPS users are primarily caused by disturbances in the ionosphere and plasmasphere, which in return causes range delay or even loss of signal lock (Coster et al., 2003). On the other hand, the GPS can be used as a probe tool to measure the

ionospheric range and further infer the ionospheric properties which can be used to monitor space weather events (Coster et al., 2003). Through the study of ionospheric responses to geomagnetic and solar activities, it will be beneficial for better understanding of the interrelationship among the components and the interaction mechanism of the space weather.

CHAPTER 5

IONOSPHERE TOMOGRAPHIC MODELING OVER A LOCAL AREA GPS REFERENCE NETWORK

In Chapter 4, the methodologies of an ionosphere tomographic modeling system have been developed. In order to verify the feasibility of the tomographic modeling method and demonstrate the capability of this tomographic model, data collected from a local area GPS reference network will be used to construct the ionospheric model using the proposed tomographic method and the obtained results will be described in this chapter. Since the performance of ionospheric modeling varies under different modeling environments with the use of different modeling schemes, the modeling scheme optimization issue should be addressed in the data analysis. In ionospheric modeling, the selection of the elevation cutoff angle and the prediction interval will have impacts on the modeling results and their effects will be investigated. The purpose of optimization is to achieve the best modeling accuracy by using the proposed ionosphere tomographic modeling approach. In this chapter, various modeling strategies will be tested so that the optimal scheme can be selected. The modeling scheme optimization is used to a) investigate and understand the magnitudes and patterns of the influences of various parameters on the ionosphere tomographic modeling results. The parameters that will have major impacts on the final modeling results including elevation cutoff angle used in the data edition and analysis, prediction interval used for ionospheric TEC predictions, the selection of highest orders of spherical harmonic functions and empirical orthogonal functions used in the modeling, the temporal length of GPS data set in each modeling session. b) provide general parameterization guidance for future local area GPS network ionospheric modeling studies. Extensive data analysis presented below will show the results corresponding to different parameterization schemes, like different elevation cutoff angles and prediction intervals. Through the data analysis result, it can be learnt

that what level of accuracy can be achieved when using a given type of parameterization scheme. On the contrary, it also can be learnt which parameterization scheme can be used to achieve a given modeling accuracy. To assess the performances of the proposed ionosphere tomographic modeling method, the ionospheric TEC prediction accuracies are also analyzed and quantified using the indicators developed in Chapter 4.

5.1 Tomographic Modeling with A Local Area GPS Network

A local area GPS Network is referred to here as a GPS network that consists of multiple reference GPS stations, ranging from tens of station to even over hundreds of stations, spatially separated in short distances, typically several tens of kilometres. The reason to conduct a performance analysis over a local area GPS network is that many such networks are currently operational around the world and are providing many valuable services to users such as precise GPS positioning and deformation monitoring etc. The Southern California Integrated GPS Network (SCIGN) is a typical example whose average baseline length between reference stations is about 35 km. The Singapore Integrated Multiple Reference Station Network (SIMRSN) and the GPS Earth Observation Network (GEONET) in Japan are another two examples with an average baseline length of about 20 km (Hu et al., 2002). The Southern Alberta GPS network deployed by The University of Calgary has station separation of 30 to 100 km (Nicholson et al., 2003). Precise ionosphere modeling over local areas becomes increasingly important as more and more local area GPS networks become operational and many of them have been established as a municipal infrastructure to support precise positioning and other value-added applications and services. Since the density of the GPS stations within a local area GPS network is usually much higher than that of a wide area GPS network whose reference stations are usually separated from several hundred up to more than one thousand kilometres, more data are therefore available to model the ionospheric conditions over a local area GPS network.

5.2 Data Description

Six GPS reference stations from the Southern California Integrated GPS Network (SCIGN) are selected to form a local area network with an average baseline length of 35 km. The GPS stations of SCIGN are distributed throughout southern California but with much higher density over the greater Los Angeles metropolitan region. The major purpose of SCIGN is to provide geophysical and seismological evidence for possible prediction and detection of the earthquakes and better understanding of the crustal movements in that area. The GPS station distribution is depicted in Figure 5.1. The geographical locations and monumental names of the six stations are provided in Table 5.1. It can be seen from Figure 5.1 and Table 5.1 that the network is a typical local area GPS network.

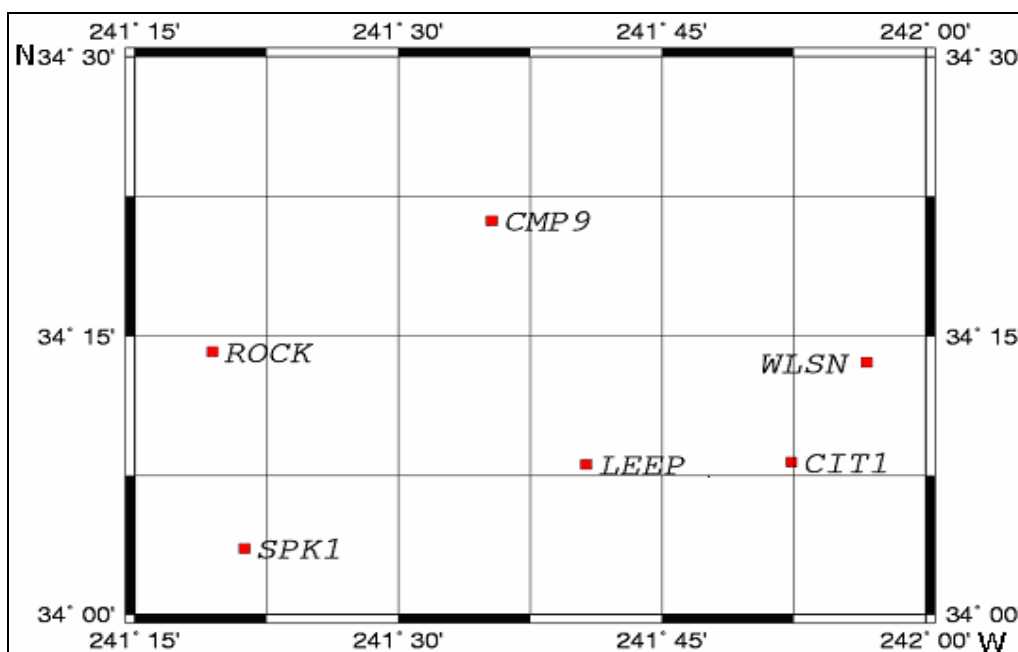


Figure 5.1 GPS Station Distribution of the Local Area GPS Network

Table 5.1 GPS Station Coordinates of the Local Area GPS Network

Station	Location	Latitude (deg)	Longitude (deg)	Height (m)
WLSN	Mt. Wilson, CA	34.2261	-118.0559	1705.3
CMP9	Sylmar, CA	34.3532	-118.4114	138.2
CIT1	Pasadena, CA	34.1367	-118.1273	215.4
LEEP	Hollywood, CA	34.1346	-118.3217	485.3
ROCK	Simi Valley, CA	34.2357	-118.6764	553.6
SPK1	Saddle Peak, CA	34.0593	-118.6461	440.2

All six GPS stations are equipped with dual-frequency GPS receivers which allow the derivation of TEC data at each station directly using dual-frequency observations. The GPS receiver and antenna types at each station are given in Table 5.2.

Table 5.2 GPS Receiver and Antenna Types

Station	Receiver Type	Antenna Type
WLSN	ASHTECH Z-XII3 S/N: LP03089	AOAD/M_T S/N: 416
CMP9	ASHTECH Z-XII3 S/N: LP02745	ASH700936A_M S/N: 11490
CIT1	ASHTECH Z-XII3 S/N: LP02915	AOAD/M_T S/N: 161
LEEP	ASHTECH Z-XII3 S/N: LP03196	ASH700936A_M S/N: 11475
ROCK	ASHTECH Z-XII3 S/N: LP03116	ASH700936A_M S/N: 11479
SPK1	ASHTECH Z-XII3 S/N: LP03261	AOAD/M_T S/N: 204

A summary of the baseline length between each pair of GPS stations is given in Table 5.3. The longest baseline in this network is between WLSN and SPK1 with a baseline length of 57.525 km while the shortest baseline is from WLSN to CIT1 with a length of 11.997 km. The average baseline length of the network is 34.682 km.

The GPS data set used in this study was observed on May 15, 2000, namely day of year (DOY) 136. The geomagnetic activities on that day are represented by a set of Kp index

values shown in Figure 5.2. Kp index is a global measurement of geomagnetic field disturbance (Coster et al., 2003). From Figure 5.2, we see that Kp ranges from 4.3 to 2.3. Value of 4 indicates moderately disturbed ionospheric conditions. On that day, most values are below 4 so May 15, 2000 was basically a day with quiet geomagnetic activities.

Table 5.3 Baseline Lengths in the Local Area GPS Network (km)

Station	WLSN	CMP9	CIT1	LEEP	ROCK	SPK1
WLSN	0.000	35.651	11.997	26.555	57.107	57.525
CMP9	35.651	0.000	35.536	25.629	27.642	39.140
CIT1	11.997	35.536	0.000	17.936	51.686	48.650
LEEP	26.555	25.629	17.936	0.000	34.447	31.090
ROCK	57.107	27.642	51.686	34.447	0.000	19.644
SPK1	57.525	39.140	48.650	31.090	19.644	0.000

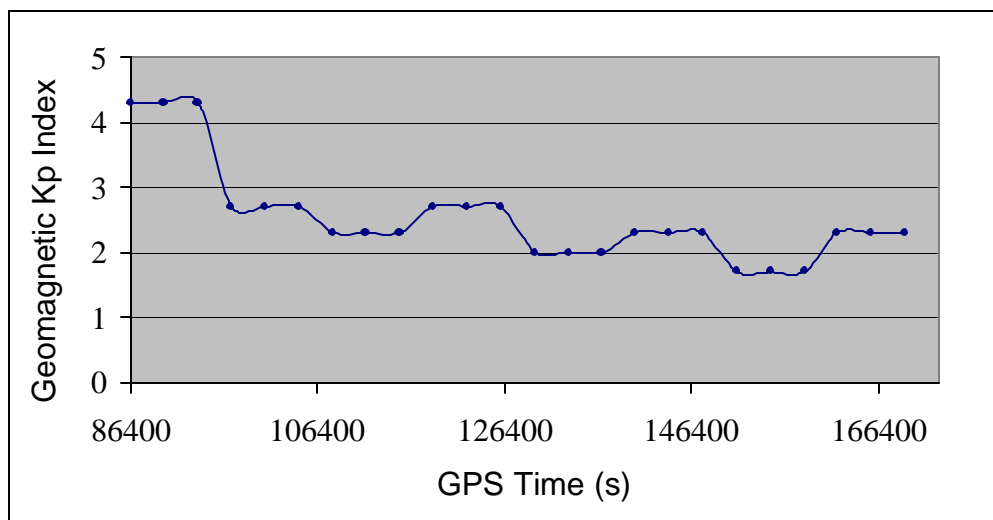


Figure 5.2 Geomagnetic Kp Index Values on May 15, 2000

5.3 Data Analysis Strategy

The implementation of the proposed ionospheric modeling approach consists of two steps. Firstly, two types of TEC measurements, absolute TEC and relative TEC, are

derived from dual-frequency GPS code pseudorange and carrier phase measurements, respectively. The code-derived absolute TEC measurements are smoothed by the phase-derived relative TEC with the smoothing algorithm described in Chapter 4. These TEC measurements contain ionospheric electron density information about the region above the GPS network and they are used as the input data for the tomographic model. Based on the tomographic modeling method developed in Chapter 4, a model can then be constructed using these TEC data. Once the model is constructed, the model can be employed to carry out TEC predictions over a given interval.

5.4 Impacts of Various Parameters

5.4.1 Prediction interval

The ionosphere prediction interval is crucial to GPS positioning and navigation users and also to space weather researchers. For the purpose of GPS positioning and navigation, a 5-min prediction interval usually is sufficient. In this study, the standard prediction period is 5-min, which is also compatible with the WAAS specification on the ionospheric grid update interval (El-Arini et al., 1999). For other ionosphere-related researches such as long-term radio-service planning, however, a longer prediction interval is desired. Recently, ionospheric TEC prediction for 1-hour, 1-day and even 7-day period using neural network method based on 7 years of Faraday-rotation measurements from geostationary satellites was conducted (Xenos et al., 2003). Compared to neural network training using extensive historical data, the TEC prediction presented in this chapter and Chapter 6 is more straightforward and easier to conduct. Although currently 1-hour or longer prediction is not conducted in this research, it will be the direction of endeavor for future research. To test the performance of the ionospheric model with longer prediction intervals, two prediction intervals, 10-min and 30-min, are also used. It is expected that the 30-min TEC prediction data can be useful for ionosphere-related researches and applications, e.g. radio frequency scheduling. The predicted ionospheric TEC data are to

be assessed through a comparison to the observed TEC data. The resultant differences indicate the actual performance of the obtained ionosphere tomographic model.

5.4.2 Elevation cutoff angle

The research results in Liu and Gao (2002) indicate that the elevation cutoff angle used in the data modeling has an impact on prediction accuracy. In this study, the effects of GPS data elevation cutoff angle on ionosphere prediction are investigated through extensive data analysis. Several data analysis schemes have been proposed and are described below.

To investigate the impact of elevation cutoff angle on the model's performance, three elevation cutoff angles, e.g. low elevation angle 15° , medium elevation angle 20° and high elevation angle 25° , are tested using the same data set. For each elevation cutoff angle, the interval of TEC prediction varies from 5-min, 10-min to 30-min. For these different prediction intervals, the corresponding TEC prediction accuracies of the tomographic model can be assessed. The nine analysis schemes that have been employed in the data analysis are given in Table 5.4.

Table 5.4 Data Analysis Schemes

Category	Scheme type	Elevation cutoff (deg)	Prediction interval (min)
Low elevation angle 15°	Scheme 1	15	05
	Scheme 2	15	10
	Scheme 3	15	30
Medium elevation angle 20°	Scheme 4	20	05
	Scheme 5	20	10
	Scheme 6	20	30
High elevation angle 25°	Scheme 7	25	05
	Scheme 8	25	10
	Scheme 9	25	30

5.5 Data Analysis and Results

The data analysis results from different analysis schemes are presented below. At each GPS station, the difference between the predicted TEC and observed TEC is referred to as the ionospheric model's prediction error. As already discussed in Chapter 4, the relative error of each predicted TEC can be calculated when it is compared to the observed TEC derived from dual-frequency GPS data. The mean relative error can be further calculated for each GPS station based on the relative errors of all predicted TEC at that station. The slant TEC errors are dependent on the elevation angle of each slant TEC. To eliminate the dependence of the prediction error on elevation angle, the slant TEC errors are mapped to the zenith direction. As a result, the vertical TEC prediction errors can be determined. In a similar way, the statistics of the vertical TEC prediction errors for each station can be obtained.

5.5.1 Results of low elevation cutoff angle (15°)

5.5.1.1 Results of Scheme 1 (15° , 5 min)

In this scheme, the elevation cutoff angle is selected to be 15° and the prediction interval is 5-min. The predicted TEC and observed TEC for three stations, namely SPK1, LEEP and CIT1, are displayed below. The comparison results at other stations are similar. For the same reason, at each selected GPS station, only the TEC data for satellite PRN 02 are depicted although usually over 25 satellites are observed at a GPS station. The reason of selecting this satellite is that it has the largest amount of TEC data available at all three stations SPK1, LEEP and CIT1. As mentioned before, the TEC showed in the following figures are slant TEC values if they are not specifically stated to be vertical TEC.

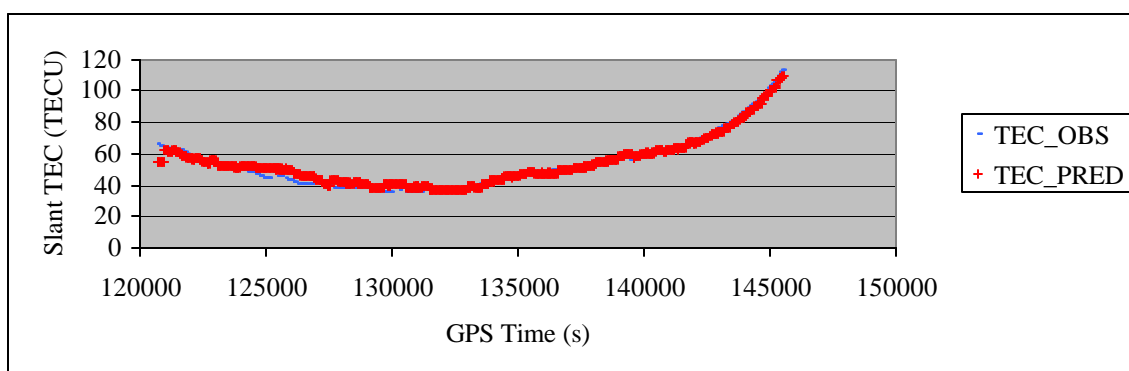


Figure 5.3 Comparison of Observed and Predicted TEC for PRN 02 at SPK1 Station on DOY 136 at 15° Cutoff and 5-min Prediction Interval
(VTEC RMS= 2.355 TECU, Relative Error = 5.29%)

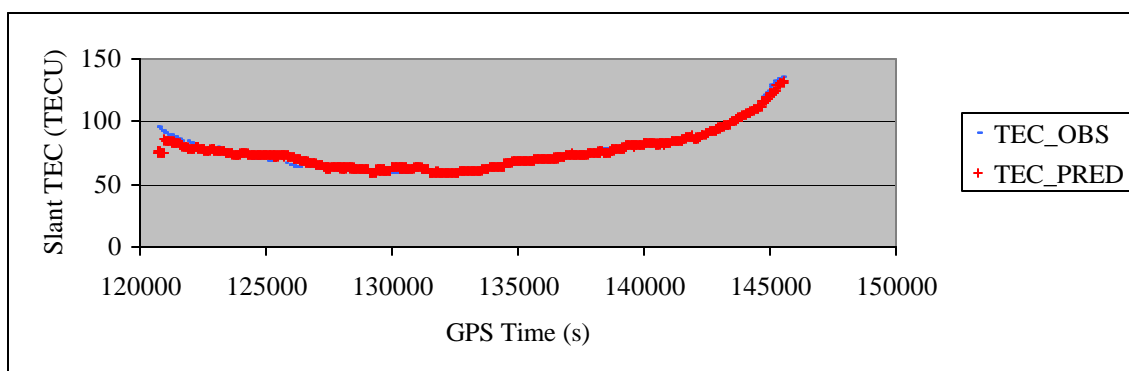


Figure 5.4 Comparison of Observed and Predicted TEC for PRN 02 at LEEP Station on DOY 136 at 15° Cutoff and 5-min Prediction Interval
(VTEC RMS= 2.433 TECU, Relative Error = 3.61%)

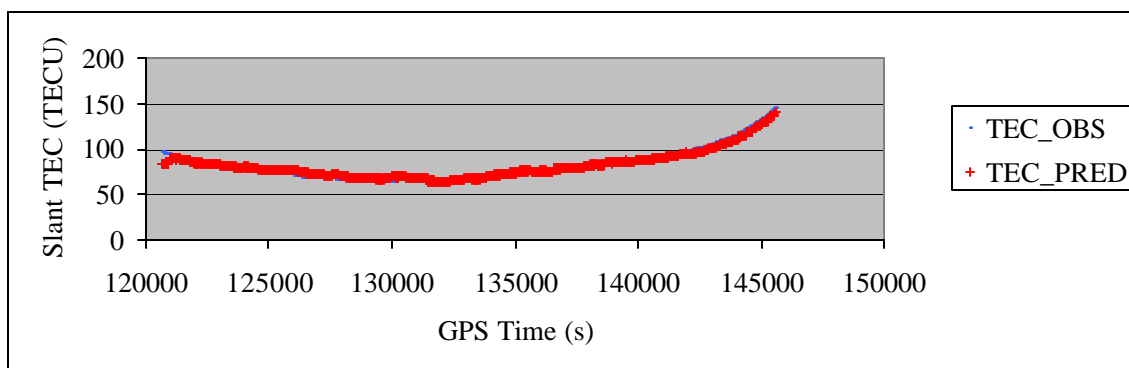


Figure 5.5 Comparison of Observed and Predicted TEC for PRN 02 at CIT1 Station on DOY 136 at 15° Cutoff and 5-min Prediction Interval
(VTEC RMS= 2.608 TECU, Relative Error = 3.63%)

Shown in Figure 5.3 to Figure 5.5 are the predicted and observed TEC data for SPK1, LEEP and CIT1 stations where the observed TEC data are represented by the blue “dash” symbol and the predicted TEC data are symbolized by the red “plus”.

It can be seen that the predicted TEC data agree very well with the observed TEC data except for a few epochs at the beginning of the modeling. The large disagreements at the initial epochs are due to the fact that the satellite is still rising with low elevation angle close to the cutoff angle 15° . At the end of the modeling, the disagreements between them become larger at the last a few epochs. This is because the satellite is going to set to below 15° . However the disagreements when the satellite is setting are not as large as when it is rising. If the disagreements between the predicted TEC and observed TEC are projected to the vertical direction, the vertical TEC prediction errors are obtained. The RMS values for the vertical TEC prediction errors for each figure as well as the relative errors are given in the parentheses in the figure’s caption.

Table 5.5 Error Statistics for 5-min VTEC Prediction with Cutoff 15° on DOY 136

STATION	VTEC Error RMS (TECU)	Relative Error (%)
CMP9	2.904	4.48%
CIT1	2.742	3.44%
LEEP	2.955	4.25%
ROCK	2.818	4.31%
SPK1	2.735	5.88%
WLSN	2.851	3.94%
Mean	2.834	4.38%

For all six GPS stations, the statistics for the vertical TEC prediction errors are summarized in Table 5.5. The last row is the mean value for all stations. It indicates that the VTEC prediction RMS errors are less than 3.0 TECU and the relative errors are less than 6.0% at all stations. The maximum VTEC prediction error is 2.955 TECU at LEEP station while the smallest one is 2.735 TECU at SPK1 station. The mean VTEC prediction RMS error for the entire network is 2.834 TECU and the mean relative error is 4.38%. It means that the predicted ionospheric TEC data account for 95.62% of the

observed TEC and the unaccounted part is 4.38% due to the modeling error. From Table 5.5, it can be noticed that the station with the largest relative error does not mean it has the biggest VTEC prediction RMS error. This is because the relative error is a relative quantitative indicator of the modeling error while the VTEC prediction RMS error is an absolute quantitative indicator. Once the TEC prediction error is given, the relative error depends on the value of the observed TEC data. If the observed TEC has a large value, then the relative error will become small. But the absolute error is not affected by the magnitude of the observed TEC. Even if all the stations are observing the same satellite, the observed TEC values at each station to that satellite are still different because the signals are passing through different ionospheric regions with different elevation angles.

To perform an independent assessment of the model prediction accuracy, a station in the network, namely LEEP, will be excluded from ionospheric modeling. In other words, only GPS data from the other 5 stations are used in each session of ionospheric modeling. This excluded station would be used as a reference station with which the 5-min TEC predictions are compared. In each session, the receiver and satellite biases are no longer estimated because they have been obtained from the first round of calculation using 24-hour GPS data, as described in Section 4.7. They are used as known values in the model construction for each session. In the modeling, the receiver and satellite biases in TEC measurements are all removed. As equations (4.61) and (4.62) indicate, once the tomographic model was constructed in each session, then users could determine their TEC at their locations in a prediction mode. Here the user is the excluded GPS station. According to equations (4.61) and (4.62), once the geometry matrix for the user is calculated, the computation of TEC correction for the user is straightforward. The calculation of the geometry matrix needs only the user's coordinates and GPS satellite's positions. After the calculation of TEC predictions at the user station, the biases for that particular user receiver and observed satellites are added to the predicted TEC because in the observed TEC data the receiver and satellite biases are automatically included. Once the predicted TEC data at the user station were calculated, a comparison was made

between the measured and predicted TEC values. The measured TEC data were smoothed and derived from dual-frequency GPS observations that were collected at the user station using equation (4.25). In the following, the TEC predictions and comparison results for the test station LEEP are presented. As before, the satellites with largest amount of TEC observations are presented to illustrate the comparison of predicted and observed TEC data. Shown in Figure 5.6 and Figure 5.7 are the TEC comparison results for PRN 19 and PRN 02.

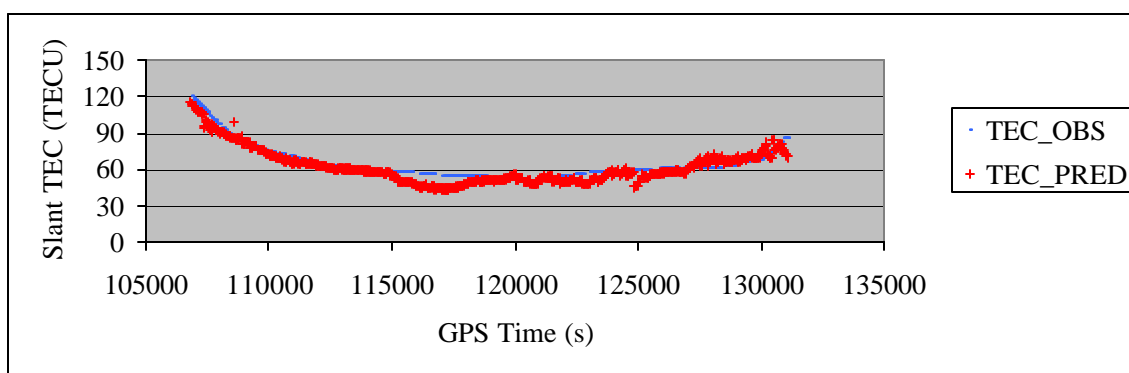


Figure 5.6 Comparison of Observed and Predicted TEC for PRN 19 at LEEP Station on DOY 136 at 15° Cutoff and 5-min Prediction Interval
(VTEC RMS= 3.765 TECU, Relative Error = 6.07%)

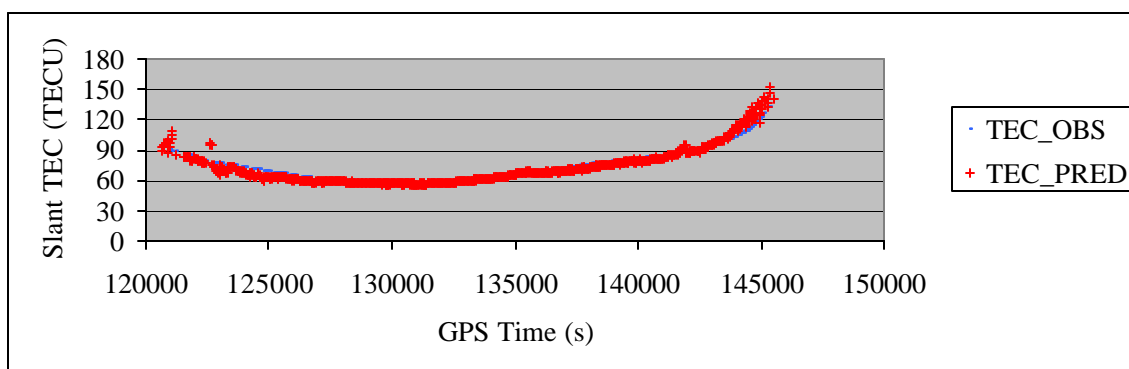


Figure 5.7 Comparison of Observed and Predicted TEC for PRN 02 at LEEP Station on DOY 136 at 15° Cutoff and 5-min Prediction Interval
(VTEC RMS= 2.275 TECU, Relative Error = 3.25%)

Figure 5.6 and Figure 5.7 show that the predicted TEC data at the test station have a good agreement with the observed TEC data. The predicted TEC have basically captured the

trend of ionospheric change over time. The vertical RMS errors for PRN 19 and PRN 02 are 3.765 TECU and 2.275 TECU, respectively. The relative errors for these two satellites are 6.07% and 3.25%, respectively. If all satellites are taken into account, the vertical RMS error is 3.466 TECU and the relative error is 4.77% for the LEEP station. Compared to previous results when the LEEP station was included in ionospheric modeling (see Table 5.5), the prediction error at LEEP station is 0.511 TECU greater in VTEC predictions and 0.42% greater in the relative error. This slight increase of the ionospheric prediction error might be caused by the fact that less GPS measurements are now available for the ionospheric modeling due to the exclusion of the LEEP station. In this case, about 16.67% GPS measurements are reduced on average after one station is excluded. An increase of prediction errors should also be expected due to the elimination of possible correlations between the ionospheric modeling and TEC predictions but it would provide a more realistic estimate about the prediction accuracy obtainable at the user station.

5.5.1.2 Results of Scheme 2 (15°, 10 min)

Shown in Figure 5.8 to Figure 5.10 are the predicted and observed TEC values using 15° cutoff elevation angle and 10 minutes of prediction interval. It can be seen that the predicted TEC data are overall in a good agreement with the observed TEC. It is noticed that the large discrepancies at the beginning of the session experienced by Scheme 1 disappear in this scheme. The reason is that this scheme has employed 10 minutes as the prediction interval but Scheme 1 used 5 minutes. In Scheme 1, each prediction session contained 5-min data and the entire data set (24-hour) was divided into 288 sessions. In Scheme 2, the prediction session period is 10-min and the entire data set is divided into 144 sessions. That means the beginning time of each session in Scheme 2 is different from that of each session in Scheme 1. In the ionospheric modeling, one strategy that has been adopted is that the data from a satellite that did not appear in the ionospheric modeling would not be used for ionospheric prediction. In Scheme 2, when PRN 02 satellite started to rise during the prediction period, it did not appear in the modeling

period. As a result, its TEC was not predicted in the session when it first appeared. That is why the epochs at the beginning time did not show large discrepancies as the Scheme 1 results did.

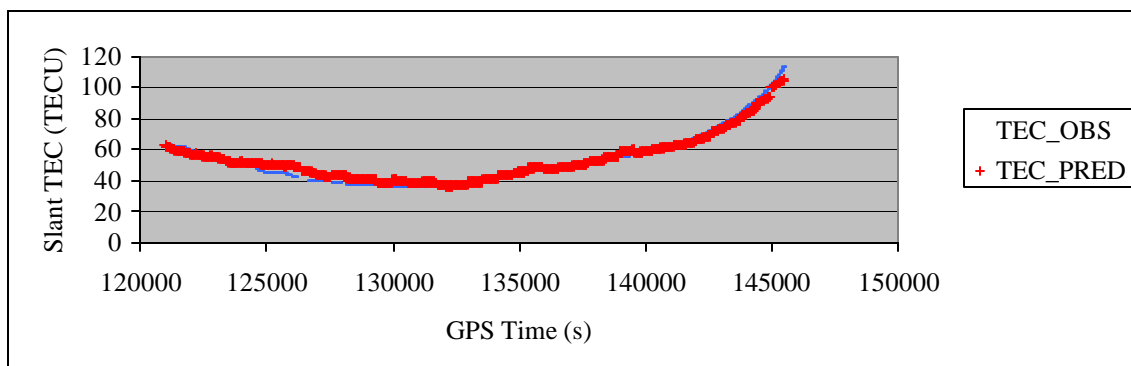


Figure 5.8 Comparison of Observed and Predicted TEC for PRN 02 at SPK1 Station on DOY 136 at 15° Cutoff and 10-min Prediction Interval
(VTEC RMS= 2.450 TECU, Relative Error = 5.51%)

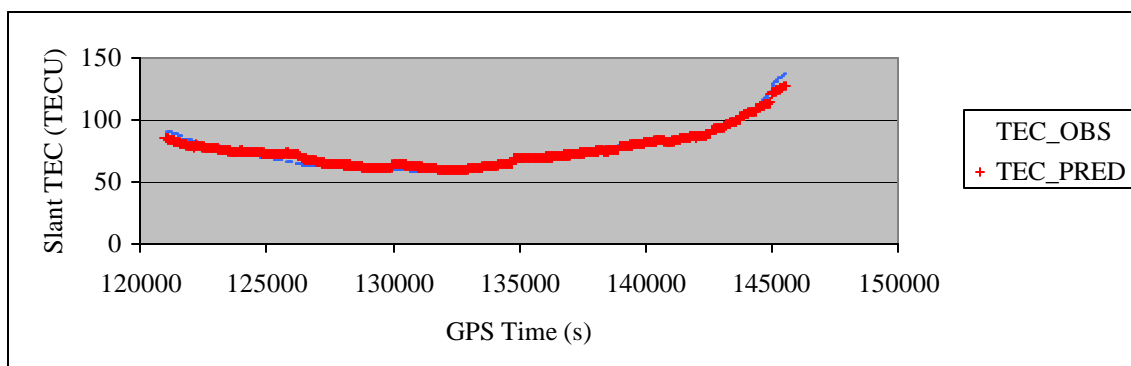


Figure 5.9 Comparison of Observed and Predicted TEC for PRN 02 at LEEP Station on DOY 136 at 15° Cutoff and 10-min Prediction Interval
(VTEC RMS= 2.413 TECU, Relative Error = 3.51%)

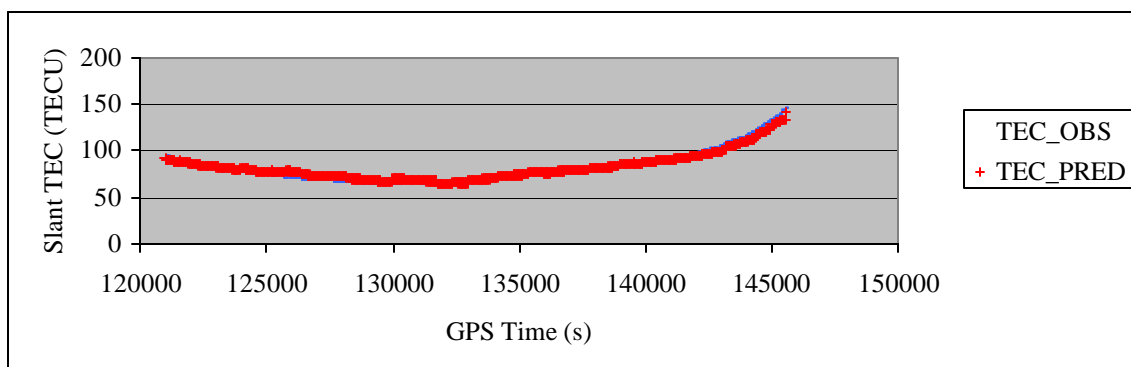


Figure 5.10 Comparison of Observed and Predicted TEC for PRN 02 at CIT1 Station on DOY 136 at 15° Cutoff and 10-min Prediction Interval
(VTEC RMS= 2.801 TECU, Relative Error = 3.81%)

Table 5.6 Error Statistics for 10-min VTEC Prediction with Cutoff 15° on DOY 136

STATION	VTEC Error RMS (TECU)	Relative Error (%)
CMP9	2.956	4.62%
CIT1	2.804	3.61%
LEEP	2.995	4.39%
ROCK	2.887	4.50%
SPK1	2.787	6.16%
WLSN	2.880	4.01%
Mean	2.885	4.55%

As summarized in Table 5.6, the biggest VTEC prediction error among the six stations is 2.995 TECU at LEEP station and the largest relative error is 6.16% at SPK1 station. The six GPS stations have a mean VTEC prediction RMS error of 2.885 TECU, which is slightly larger than the value of 2.834 TECU obtained from Scheme 1. The mean relative error in Scheme 2 is 4.55%, which is also slightly larger than the value of 4.38% in Scheme 1. That is because in Scheme 2 the prediction interval is 10-min while in Scheme 1 it is 5-min. Note that an increased prediction interval would introduce larger prediction errors. It can be seen that the prediction error does not degrade much compared to the Scheme 1 even if the prediction interval has doubled compared to Scheme 1.

To have an independent assessment of the accuracy obtainable at the user stations, the LEEP station will be excluded from the network for ionospheric modeling and used as an independent GPS user station to assess the TEC prediction accuracy. Similar to Scheme 1, the obtained model is used to predict 10-min ionospheric TEC for LEEP station. The predicted TEC and observed TEC are compared. The comparison results for PRN 19 and PRN 02 are presented in Figure 5.11 and Figure 5.12, which show that PRN 19 has larger prediction error than PRN 02.

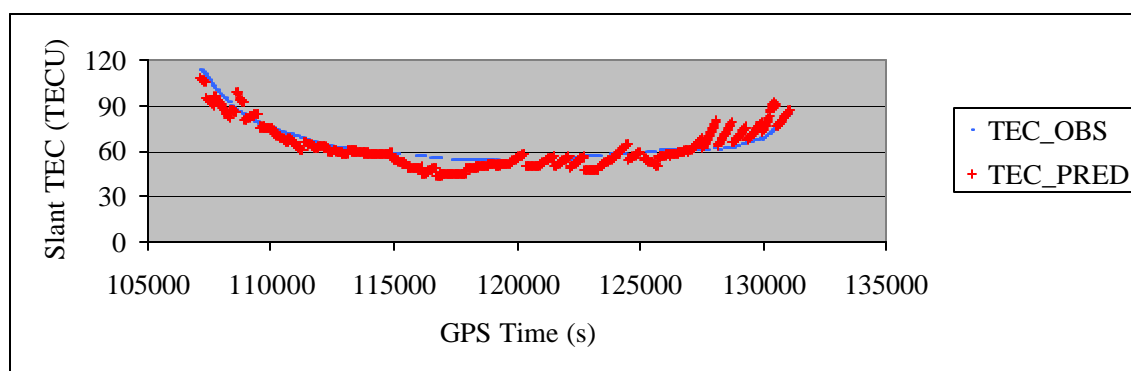


Figure 5.11 Comparison of Observed and Predicted TEC for PRN 19 at LEEP Station on DOY 136 at 15° Cutoff and 10-min Prediction Interval
(VTEC RMS= 4.070 TECU, Relative Error = 7.01%)

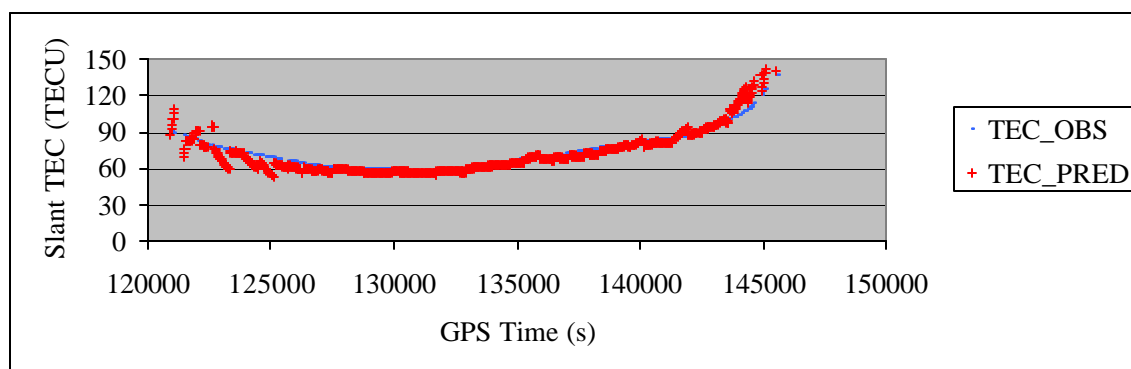


Figure 5.12 Comparison of Observed and Predicted TEC for PRN 02 at LEEP Station on DOY 136 at 15° Cutoff and 10-min Prediction Interval
(VTEC RMS= 2.887 TECU, Relative Error = 4.07%)

The VTEC RMS error for PRN 19 is 4.070 TECU and the VTEC RMS error for PRN 02 is 2.887 TECU, which is 1.183 TECU better than PRN 19. For all the satellites tracked by

LEEP station, the vertical RMS error is 4.278 TECU and the relative error is 6.04%. Compared to the prediction results for 5-min case, the 10-min predictions are 0.812 TECU larger in vertical TEC and 1.27% higher in the relative error. When compared to the results in Table 5.6 where the data from LEEP were included for ionosphere modeling, the prediction accuracy has been degraded by about 1.283 TECU in VTEC RMS error and 1.65% in the relative error.

5.5.1.3 Results of Scheme 3 (15°, 30 min)

Presented in Figure 5.13 to Figure 5.15 are the predicted versus observed TEC data using 15° cutoff angle and 30-min prediction interval. Such a prolonged prediction interval might not be helpful to GPS positioning and navigation where high rate predictions (usually 5-min) is required. However, the 30-min prediction is helpful to other ionosphere-related studies, like long-term radio signal plan. GPS derived TEC data are incorporated with Standard Plasmasphere-Ionosphere Model (SPIM) to investigate global and regional ionosphere structure (Gulyaeva, 2001). Long-term prediction of ionospheric TEC is an important need for communication practice, management and optimization of high-frequency radio, remote sensing systems and evaluation of ionosphere-plasmasphere models (Stankov et al., 2001). The 30-min ionospheric TEC predictions are expected to be useful for other disciplines where TEC predictions are required.

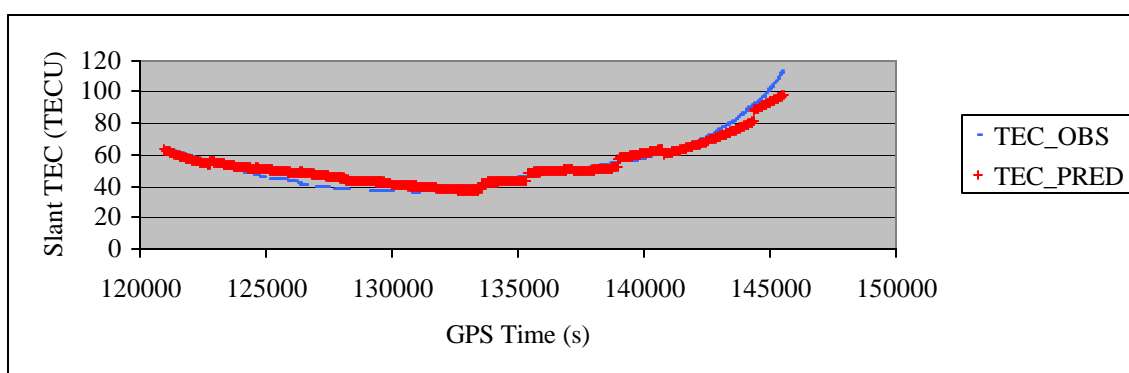


Figure 5.13 Comparison of Observed and Predicted TEC for PRN 02 at SPK1 Station on DOY 136 at 15° Cutoff and 30-min Prediction Interval (VTEC RMS= 3.345 TECU, Relative Error = 7.69%)

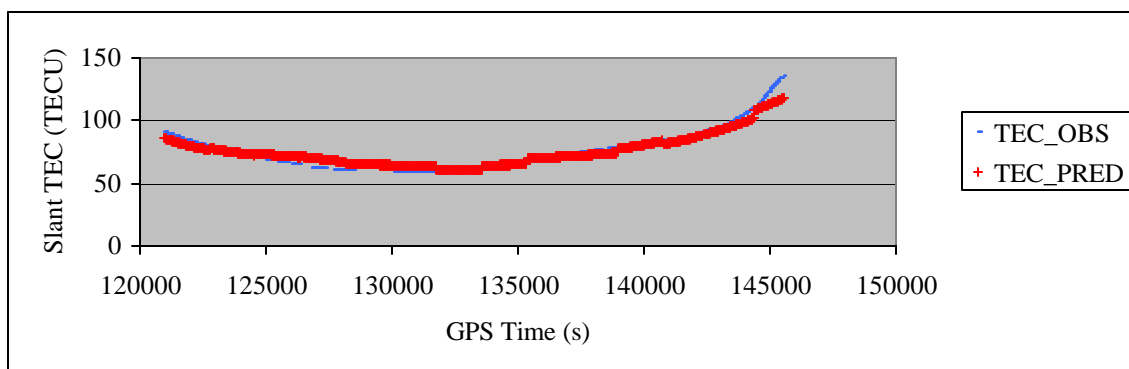


Figure 5.14 Comparison of Observed and Predicted TEC for PRN 02 at LEEP Station on DOY 136 at 15° Cutoff and 30-min Prediction Interval
(VTEC RMS= 3.263 TECU, Relative Error = 4.79%)

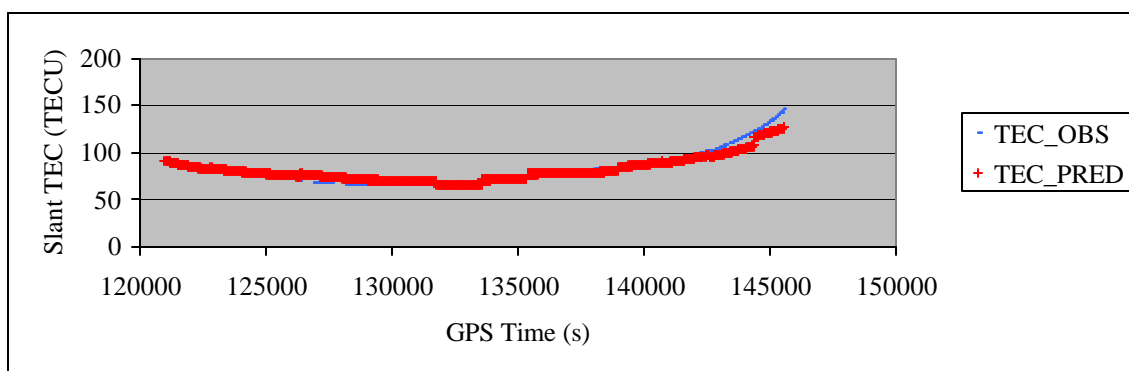


Figure 5.15 Comparison of Observed and Predicted TEC for PRN 02 at CIT1 Station on DOY 136 at 15° Cutoff and 30-min Prediction Interval
(VTEC RMS= 3.563 TECU, Relative Error = 4.93%)

The results shown above indicate that the predicted TEC data basically agree with the observed TEC well except the rear portion of each figure when the satellite PRN 02 was beginning to set. As shown in Table 5.7, the VTEC prediction accuracies at all stations are better than 4.0 TECU, ranging from 3.496~3.695 TECU. The mean network RMS error is 3.591 TECU, which is larger than the mean value 2.885 TECU from Scheme 2 where a 10-min interval was used. The relative errors on all stations are less than 9.0%. Five of the six stations have relative errors at or better than a level of 6.0%. The mean relative error for the network is 6.00%, which is also degraded from the value of 4.55% in Scheme 2. In Scheme 3, all the conditions are identical to Scheme 2 except that

different prediction intervals are used. A degradation in the prediction accuracy should be reasonable since the prediction interval has increased from 10-min to 30-min.

Table 5.7 Error Statistics for 30-min VTEC Prediction with Cutoff 15° on DOY 136

STATION	VTEC Error RMS (TECU)	Relative Error (%)
CMP9	3.695	6.05%
CIT1	3.516	4.86%
LEEP	3.679	5.78%
ROCK	3.657	5.93%
SPK1	3.502	8.17%
WLSN	3.496	5.19%
Mean	3.591	6.00%

Similar to the analysis that has been conducted for 5-min and 10-min predictions, the LEEP will be excluded from the ionospheric modeling computations and serves as independent user station to evaluate the TEC prediction accuracy. What is different is that the prediction interval is now 30-min, which is much longer than the interval of Schemes 1 and 2.

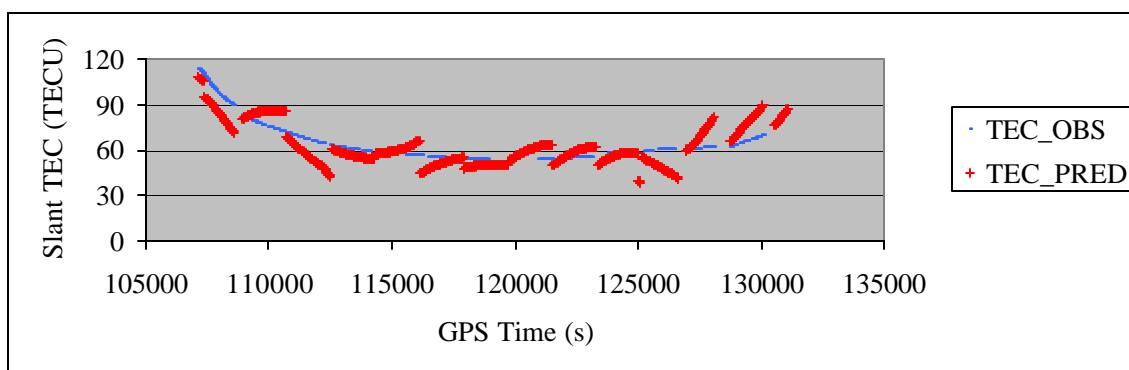


Figure 5.16 Comparison of Observed and Predicted TEC for PRN 19 at LEEP Station on DOY 136 at 15° Cutoff and 30-min Prediction Interval (VTEC RMS= 5.760 TECU, Relative Error = 10.37%)

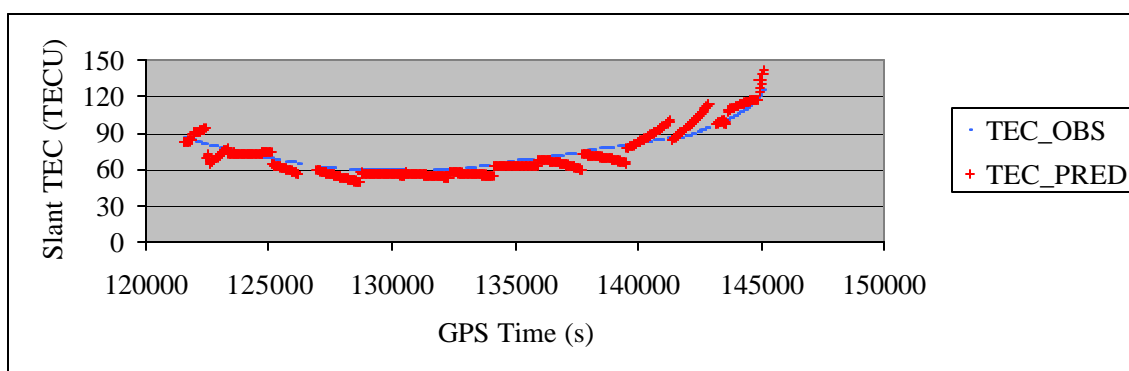


Figure 5.17 Comparison of Observed and Predicted TEC for PRN 02 at LEEP Station on DOY 136 at 15° Cutoff and 30-min Prediction Interval
(VTEC RMS= 4.500 TECU, Relative Error = 6.83%)

Figure 5.16 and Figure 5.17 depict the comparison results for satellite PRN 19 and PRN 02, which are the two satellites with the largest amount of TEC observations at LEEP station. It is apparent that the 30-min predictions are worse than 5-min predictions or 10-min ones, particularly for satellite PRN 19, where the predictions have larger errors than PRN 02. The vertical TEC prediction errors and the relative errors for PRN 19 and PRN 02 are given in the captions of the two figures. Compared to the 5-min case, the vertical TEC RMS error in the 30-min case is 1.995 TECU larger for PRN 19 satellite and is 2.225 TECU larger for PRN 02. The relative error in this scheme has also experienced a degradation compared to the 5-min case. The relative error is 4.3% larger than the 5-min case for PRN 19 and 3.58% larger than the 5-min case for PRN 02. If the prediction accuracies are examined for all the satellites, it shows that the vertical TEC RMS error for LEEP station is 5.908 TECU and the relative error is 8.70%, which are 2.422 TECU larger and 3.93% higher than the 5-min prediction scheme. The prediction results with and without the inclusion of the data from LEEP for ionospheric modeling are also compared. The comparison shows that the prediction error of the latter is 2.229 TECU greater in the VTEC RMS and 2.92% higher in the relative error than that of the former. For 30-min predictions, it can be seen that the reduced amount of GPS measurements has a more significant impact on the prediction accuracy at LEEP station compared to 5-min

and 10-min predictions. The accuracy difference in vertical TEC could be as large as 2.229 TECU.

5.5.2 Results of medium elevation cutoff angle (20°)

5.5.2.1 Results of Scheme 4 (20°, 5 min)

Figure 5.18 to Figure 5.20 present the comparison results of the predicted TEC data with the observed TEC data using 20° cutoff elevation angle and 5-min prediction interval.

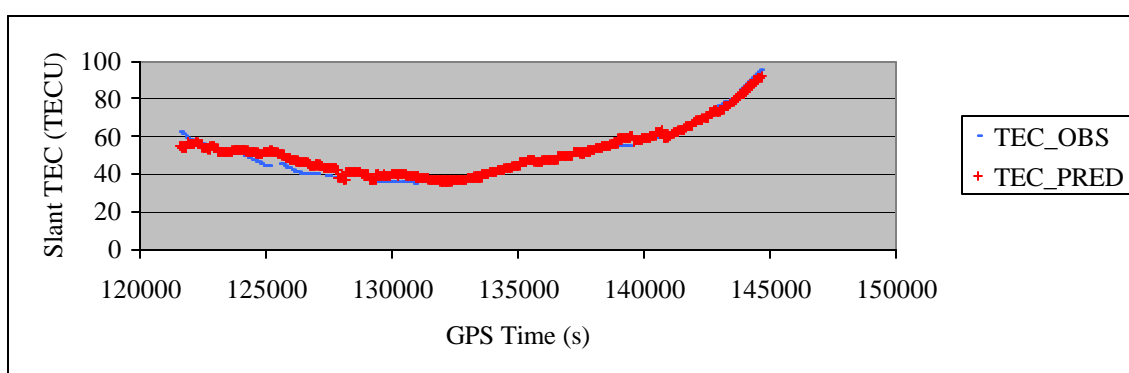


Figure 5.18 Comparison of Observed and Predicted TEC for PRN 02 at SPK1 Station on DOY 136 at 20° Cutoff and 5-min Prediction Interval
(VTEC RMS= 2.420 TECU, Relative Error = 5.24%)

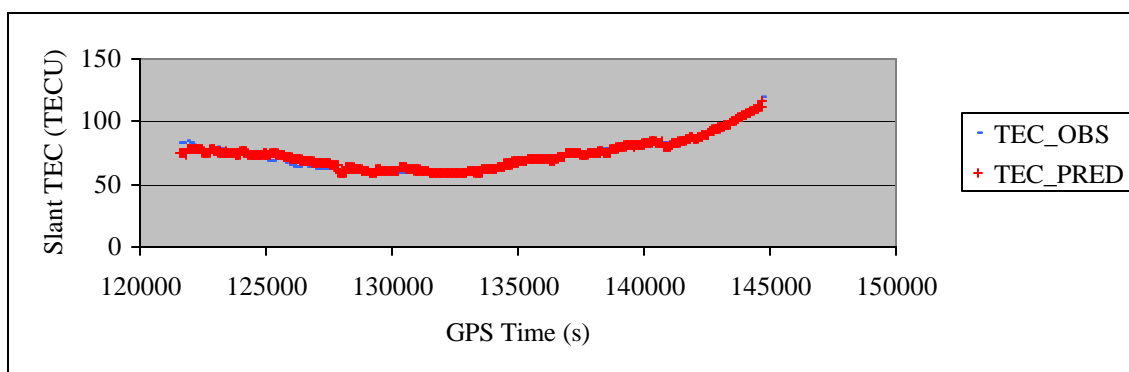


Figure 5.19 Comparison of Observed and Predicted TEC for PRN 02 at LEEP Station on DOY 136 at 20° Cutoff and 5-min Prediction Interval
(VTEC RMS= 2.364 TECU, Relative Error = 3.55%)

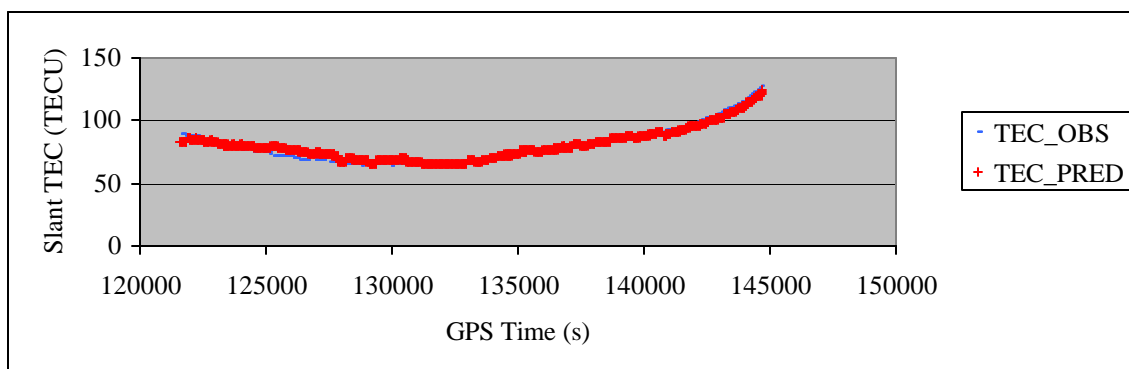


Figure 5.20 Comparison of Observed and Predicted TEC for PRN 02 at CIT1 Station on DOY 136 at 20° Cutoff and 5-min Prediction Interval
(VTEC RMS= 2.512 TECU, Relative Error = 3.46%)

The goal of this scheme is to study the effect of elevation cutoff on the prediction accuracy when it increases from 15° to 20°. The results of this scheme will compare to the results obtained from Scheme 1 because they have the same prediction interval but different elevation angles. It can be seen from the figures that the predicted TEC data agree with the observed TEC very well except over the starting portion of each figure when the satellite PRN 02 was rising to be marginally over 20°. It can be seen in Table 5.8 that at all stations the VTEC prediction accuracies are better than 3.0 TECU. The relative errors to all stations show a result of less than 6.0%. As shown in Table 5.8, the VTEC prediction RMS error at each station ranges from 2.742 TECU to 2.956 TECU. The network mean VTEC RMS error is 2.819 TECU, which is slightly smaller than the 2.834 TECU in Scheme 1 where 15° cutoff elevation angle was used. The mean relative error for the network is 4.26%, which is also a little less than the 4.38% shown in Table 5.5 for Scheme 1. The comparison of Table 5.5 and Table 5.8 shows that the ionosphere tomographic modeling using a cutoff elevation angle of 20° produces slightly higher prediction accuracies than using 15° when the prediction interval is 5-min. This probably is the result of a tradeoff between the amount of TEC observations and the level of noise in TEC observations. While using 15° cutoff angle, there will be more TEC data used in both ionospheric modeling and predictions than the 20° case. However, the noise level of TEC data using 20° is lower than those data using 15° because a smaller variance is given

to GPS measurements of higher elevation angle in consideration of the fact that higher elevation angle measurements are less susceptible to multipath effects.

Table 5.8 Error Statistics for 5-min VTEC Prediction with Cutoff 20° on DOY 136

STATION	VTEC Error RMS (TECU)	Relative Error (%)
CMP9	2.847	4.27%
CIT1	2.751	3.37%
LEEP	2.956	4.14%
ROCK	2.811	4.21%
SPK1	2.742	5.82%
WLSN	2.808	3.75%
Mean	2.819	4.26%

5.5.2.2 Results of Scheme 5 (20°, 10 min)

Figure 5.21 to Figure 5.23 depict the comparison results of the predicted TEC data with the observed TEC data employing 20° elevation cutoff and 10-min prediction interval. The goal of this scheme is to study the effect of elevation cutoff on the prediction accuracy when it rises from 15° to 20° and the effect of increasing the prediction interval from 5-min to 10-min. The results will compare to those in Scheme 2 and Scheme 4 because this scheme has the same prediction interval but different cutoff elevation angles as Scheme 2 and same elevation cutoff but different prediction intervals as Scheme 4.

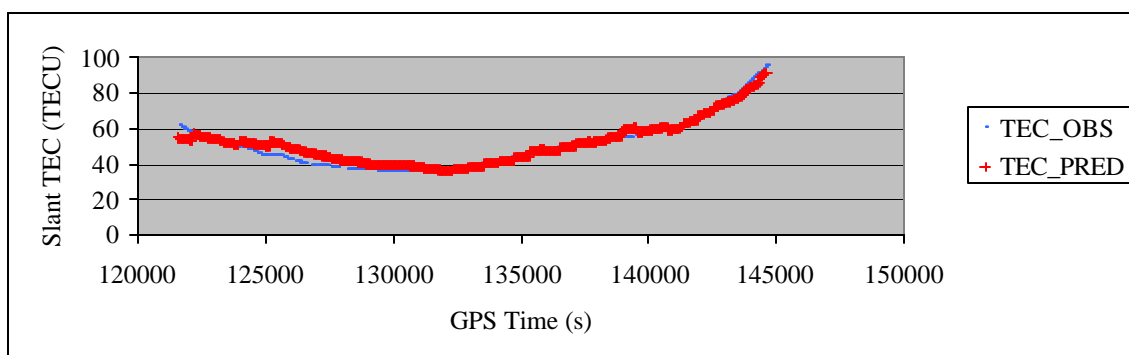


Figure 5.21 Comparison of Observed and Predicted TEC for PRN 02 at SPK1 Station on DOY 136 at 20° Cutoff and 10-min Prediction Interval (VTEC RMS= 2.600 TECU, Relative Error = 5.83%)

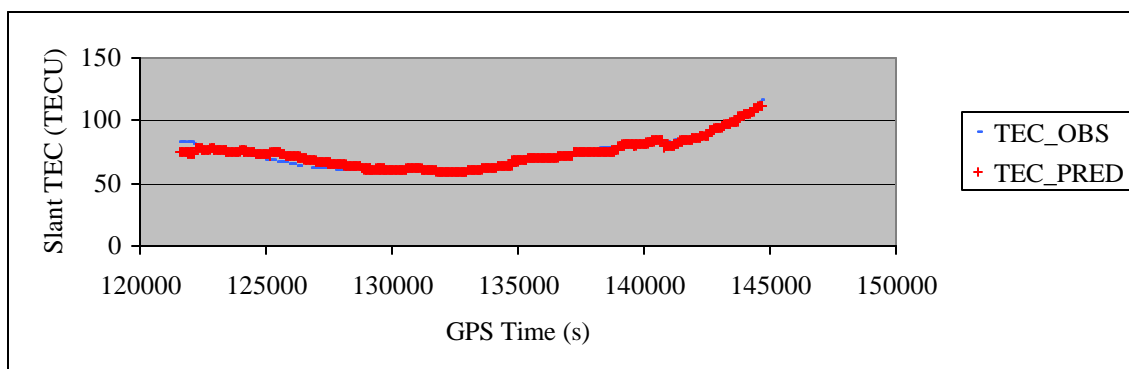


Figure 5.22 Comparison of Observed and Predicted TEC for PRN 02 at LEEP Station on DOY 136 at 20° Cutoff and 10-min Prediction Interval
(VTEC RMS= 2.480 TECU, Relative Error = 3.71%)

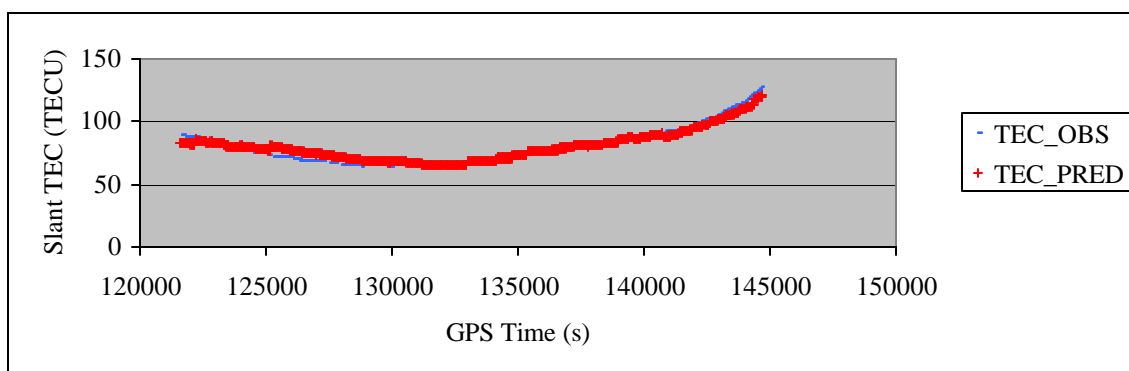


Figure 5.23 Comparison of Observed and Predicted TEC for PRN 02 at CIT1 Station on DOY 136 at 20° Cutoff and 10-min Prediction Interval
(VTEC RMS= 2.773 TECU, Relative Error = 3.86%)

Table 5.9 Error Statistics for 10-min VTEC Prediction with Cutoff 20° on DOY 136

STATION	VTEC Error RMS (TECU)	Relative Error (%)
CMP9	2.904	4.45%
CIT1	2.782	3.55%
LEEP	2.972	4.26%
ROCK	2.874	4.41%
SPK1	2.777	6.10%
WLSN	2.837	3.87%
Mean	2.858	4.44%

Figure 5.21 to Figure 5.23 show that both the predicted TEC data and the observed TEC agree with each other very well at most times. As shown in Table 5.9, the VTEC prediction RMS error at each station varies from 2.777 to 2.972 TECU with a mean value of 2.858 TECU. The relative error varies from 3.55% to 6.10% with a mean value of 4.44%. Both the mean RMS error 2.858 TECU and mean relative error 4.44% in Scheme 5 (20° , 10-min) are smaller than the mean values, 2.885 TECU and 4.55%, of Scheme 2 (15° , 10-min). This confirms that the ionosphere tomographic modeling using a cutoff elevation angle of 20° would produce slightly better prediction accuracies than using the 15° when the prediction interval is 10-min. This conclusion is consistent with the conclusion obtained in Scheme 4 for the 5-min case. When comparing the results of this scheme summarized in Table 5.9 with those of Scheme 4 (20° , 5-min) given in Table 5.8, it can be easily found that the 5-min prediction has smaller errors than the 10-min prediction. The mean VTEC RMS error and mean relative error of Scheme 4 is 2.819 TECU and 4.26%, respectively. In Scheme 5, they are 2.858 TECU and 4.44%, respectively.

5.5.2.3 Results of Scheme 6 (20° , 30 min)

The comparison results for Scheme 6 (20° , 30-min) are shown in Figure 5.24 to Figure 5.26. The results of this scheme will be compared with those from Scheme 3 (15° , 30-min) to assess the effect of different cutoff elevation angles on the ionospheric modeling accuracy when the prediction interval is set to 30-min.

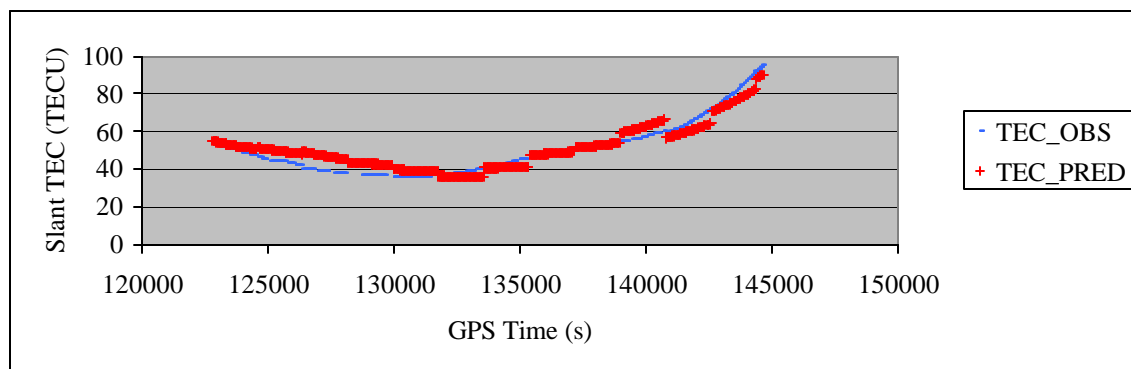


Figure 5.24 Comparison of Observed and Predicted TEC for PRN 02 at SPK1 Station on DOY 136 at 20° Cutoff and 30-min Prediction Interval
(VTEC RMS= 3.648 TECU, Relative Error = 8.67%)

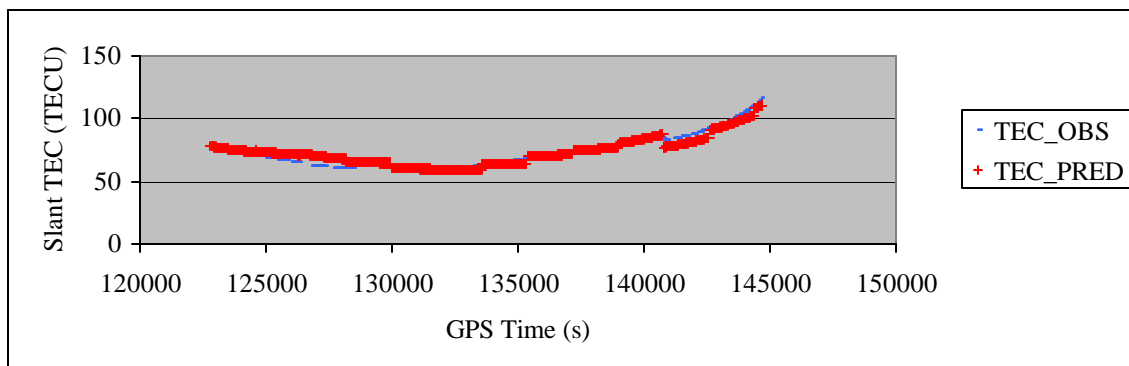


Figure 5.25 Comparison of Observed and Predicted TEC for PRN 02 at LEEP Station on DOY 136 at 20° Cutoff and 30-min Prediction Interval
(VTEC RMS= 3.223 TECU, Relative Error = 4.77%)

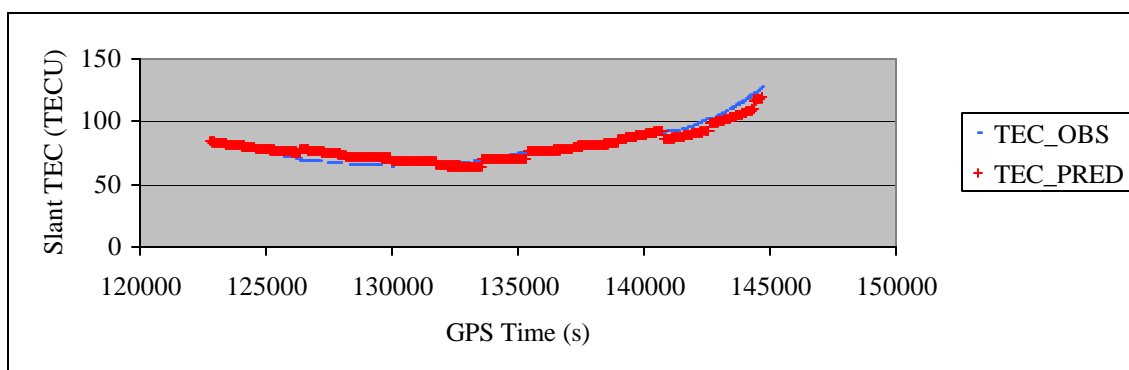


Figure 5.26 Comparison of Observed and Predicted TEC for PRN 02 at CIT1 Station on DOY 136 at 20° Cutoff and 30-min Prediction Interval
(VTEC RMS= 3.707 TECU, Relative Error = 5.31%)

Comparing the VTEC RMS errors and relative errors in Figure 5.24 to Figure 5.26 from this scheme with those in Figure 5.13 to Figure 5.15 from Scheme 3, it is found that the VTEC RMS errors as well as the relative error at both SPK1 and CIT1 stations in this scheme are larger than its counterparts in Scheme 3. The LEEP station is an exception whose RMS error and relative error in Scheme 6 is smaller than those in Scheme 3. But if we examine the VTEC RMS errors and relative errors for all the observed satellites at each GPS station, it can be found that the RMS values in Table 5.10 are generally larger

than those in Table 5.7 by 0.128 TECU. The mean relative error of this scheme (20°, 30-min) is also slightly larger than that of Scheme 3 (15°, 30-min) by about 0.05%. The results indicate that when performing lengthy period of prediction (e.g. 30-min), the selection of 15° is slightly superior to the use of 20°.

Table 5.10 Error Statistics for 30-min VTEC Prediction with Cutoff 20° on DOY 136

STATION	VTEC Error RMS (TECU)	Relative Error (%)
CMP9	3.764	6.04%
CIT1	3.630	4.89%
LEEP	3.822	5.75%
ROCK	3.792	5.98%
SPK1	3.625	8.31%
WLSN	3.680	5.32%
Mean	3.719	6.05%

Although the results show that the prediction errors of this scheme (20°, 30-min) are slightly larger than those of Scheme 3 (15°, 30-min), the vertical TEC prediction errors at all the stations are still smaller than 4.0 TECU. Table 5.10 demonstrates that five out of the six stations have relative errors at the level of about 6.0%. The SPK1 station has relatively larger error of about 8.31%.

5.5.3 Results of high elevation cutoff angle (25°)

5.5.3.1 Results of Scheme 7 (25°, 5 min)

Figure 5.27 to Figure 5.29 illustrate the TEC comparison results for Scheme 7 (25°, 5-min). It could be seen that the predicted and observed TEC shown in Figure 5.27 to Figure 5.29 have a good agreement with each other. The RMS values of VTEC prediction error for these three figures are 2.383, 2.263 and 2.598 TECU, respectively. These values indicate that the disagreements between those two sets of TEC data are small. When taking a look at the VTEC prediction errors for all the observed satellites at each station summarized in Table 5.11, it indicates that the mean VTEC RMS error is 2.723 TECU and the mean relative error is 4.10%. When comparing the results of Scheme 7 (25°, 5-

min) to the results of Scheme 1 (15° , 5-min), it can be found that an increase of elevation cutoff angle from 15° to 25° may reduce the VTEC prediction errors by 0.111 TECU and the relative error by 0.28%. Furthermore, the results of this scheme are slightly better than those from Scheme 4 (20° , 5-min) by 0.096 TECU in VTEC prediction error and by 0.16% in relative error when the cutoff angle increases from 20° to 25° . The comparison between Scheme 7, Scheme 1 and Scheme 4 concludes that within a local area GPS reference network, the short-term (5-min) ionospheric TEC prediction based on the ionosphere tomographic model could produce the optimal modeling accuracies when the elevation cutoff angle is chosen to be 25° . This is because a smaller variance is given to GPS measurements of 25° elevation angle in the modeling and also because the amount of GPS data reduced by raising cutoff angle from 15° , 20° to 25° is not significant. When the elevation cutoff angle is set higher than 25° , the usable GPS data may significantly reduce because of the rejection of a large amount of GPS measurements whose elevation angles are below the cutoff. A further increase of the cutoff elevation angle from 25° will also be detrimental to the application of TEC corrections to GPS positioning and navigation since adequate GPS measurements are crucial for the derivation of accurate and reliable positioning solutions. If the GPS users employ data only above the cutoff angle higher than 25° , the usable GPS data in positioning will be significantly reduced and the positioning accuracy and reliability will be affected. The cutoff angle is usually chosen between 15° and 25° in applications. If a higher elevation cutoff angle is used, the ionospheric modeling is constructed based on the GPS data above that cutoff angle. The TEC prediction for the GPS satellites below that cutoff angle therefore might have larger disagreements with the observed TEC data because the ionospheric field coefficients are estimated using data only from high elevation satellites. Although the predicted TEC data for low elevation can still be used to correct the ionospheric errors, they however contain much larger uncertainties and the residual ionospheric errors after the model correction would still remain large. The GPS positioning and navigation solutions with those TEC prediction data may suffer a degraded accuracy due to large ionospheric residual errors.

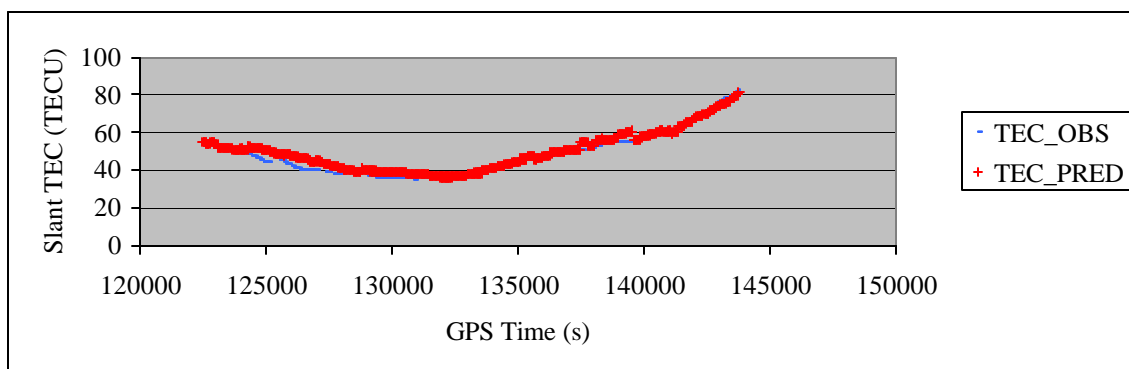


Figure 5.27 Comparison of Observed and Predicted TEC for PRN 02 at SPK1 Station on DOY 136 at 25° Cutoff and 5-min Prediction Interval
(VTEC RMS= 2.383 TECU, Relative Error = 5.24%)

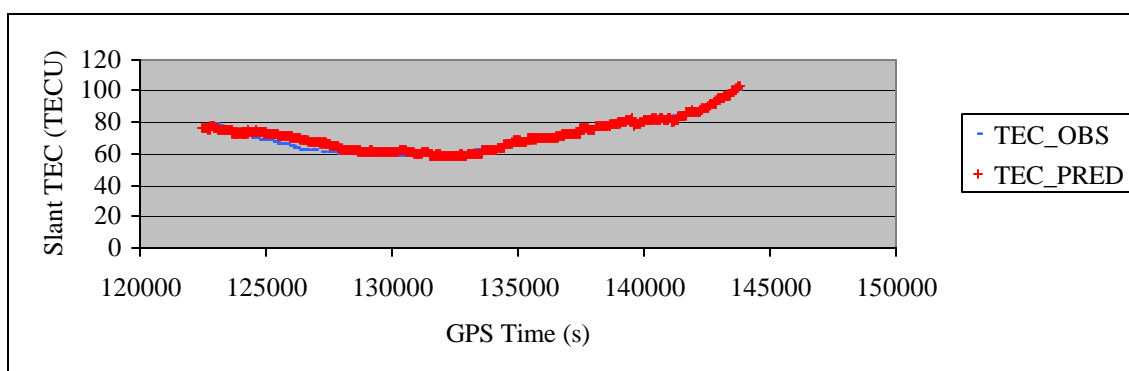


Figure 5.28 Comparison of Observed and Predicted TEC for PRN 02 at LEEP Station on DOY 136 at 25° Cutoff and 5-min Prediction Interval
(VTEC RMS= 2.263 TECU, Relative Error = 3.32%)

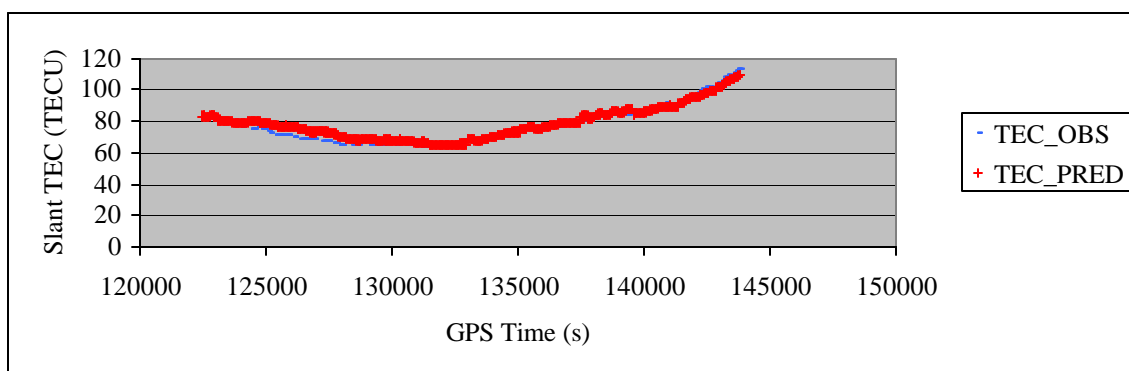


Figure 5.29 Comparison of Observed and Predicted TEC for PRN 02 at CIT1 Station on DOY 136 at 25° Cutoff and 5-min Prediction Interval
(VTEC RMS= 2.598 TECU, Relative Error = 3.55%)

Table 5.11 Error Statistics for 5-min VTEC Prediction with Cutoff 25° on DOY 136

STATION	VTEC Error RMS (TECU)	Relative Error (%)
CMP9	2.740	4.07%
CIT1	2.662	3.27%
LEEP	2.816	3.91%
ROCK	2.735	4.05%
SPK1	2.655	5.70%
WLSN	2.728	3.62%
Mean	2.723	4.10%

With results in Table 5.11, it can be found that all the GPS stations have a VTEC prediction error less than 3.0 TECU and the relative errors for all the stations are about 4.0% except the SPK1 station with a larger value of 5.70%. It shows that the modeling accuracies at all the stations are quite similar to each other. The results imply that the ionosphere electron density within that local area region is quite homogeneously distributed. This is because all the GPS data are collected from a typical local area network with limited geographical coverage.

5.5.3.2 Results of Scheme 8 (25°, 10 min)

Figure 5.30 to Figure 5.32 illustrate the TEC comparison results for Scheme 8 (25°, 10-min). The predicted and observed TEC given in Figure 5.30 to Figure 5.32 show a consistent agreement with each other. This can be seen from the RMS values of VTEC prediction error for these three figures, 2.517 TECU, 2.356 TECU and 2.743 TECU, respectively. The relative error corresponding to these figures are 5.58%, 3.37% and 3.77%, respectively. When looking at the VTEC prediction errors for all the observed satellites at each station summarized in Table 5.12, it indicates that the mean VTEC RMS error is 2.859 TECU and the mean relative error is 4.38%. Comparing the results of Scheme 8 (25°, 10-min) to the results of Scheme 2 (15°, 10-min), it can be found that an increase of elevation cutoff angle from 15° to 25° may reduce the VTEC prediction errors by 0.026 TECU and the relative error by 0.17%. Furthermore, the results of this scheme are almost the same as those from the Scheme 5 (20°, 10-min). The VTEC prediction

error in Scheme 5 is 2.858 TECU and the prediction error for Scheme 8 is 2.859 TECU. The relative error for Scheme 5 is 4.44% while it is 4.38% for Scheme 8. The differences are 0.001 TECU in VTEC prediction error and 0.06% in relative error. It can be seen that when performing medium-term (10-min) ionospheric TEC prediction within a local area GPS reference network, the employment of 20° or 25° as cutoff angle does not show much impact on the final TEC prediction accuracies.

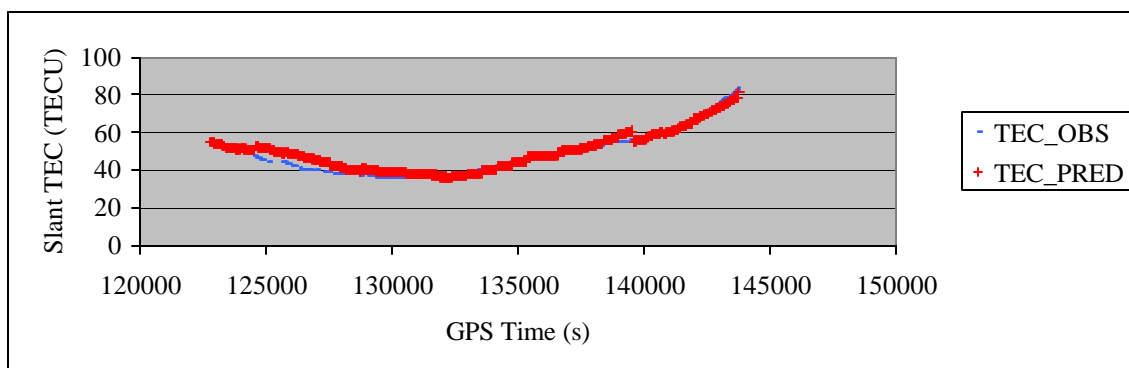


Figure 5.30 Comparison of Observed and Predicted TEC for PRN 02 at SPK1 Station on DOY 136 at 25° Cutoff and 10-min Prediction Interval
(VTEC RMS= 2.517 TECU, Relative Error = 5.58%)

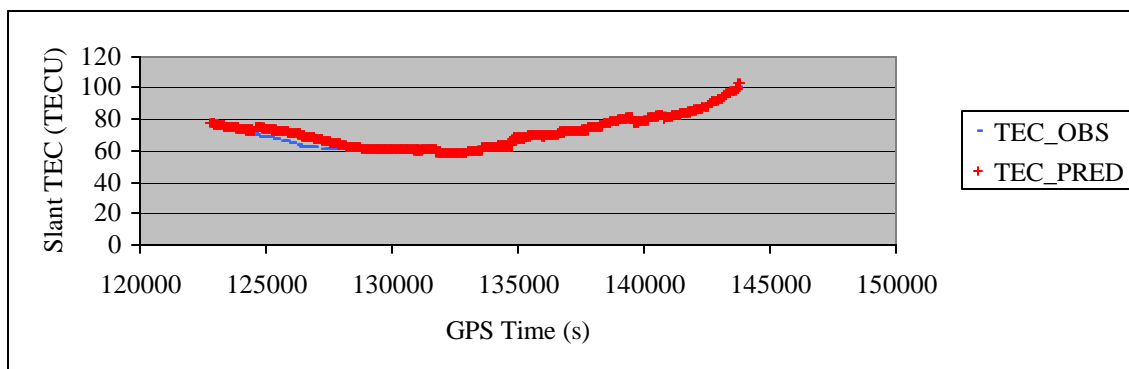


Figure 5.31 Comparison of Observed and Predicted TEC for PRN 02 at LEEP Station on DOY 136 at 25° Cutoff and 10-min Prediction Interval
(VTEC RMS= 2.356 TECU, Relative Error = 3.37%)

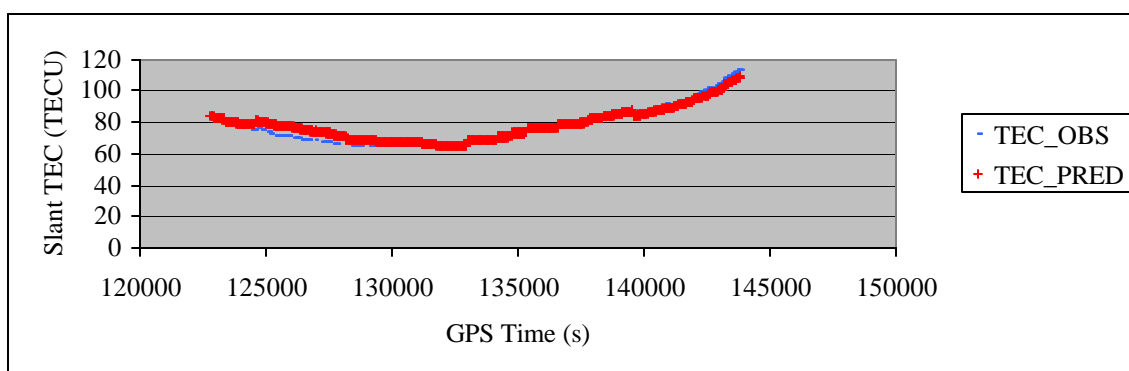


Figure 5.32 Comparison of Observed and Predicted TEC for PRN 02 at CIT1 Station on DOY 136 at 25° Cutoff and 10-min Prediction Interval (VTEC RMS= 2.743 TECU, Relative Error = 3.77%)

Table 5.12 Error Statistics for 10-min VTEC Prediction with Cutoff 25° on DOY 136

STATION	VTEC Error RMS (TECU)	Relative Error (%)
CMP9	2.846	4.31%
CIT1	2.813	3.54%
LEEP	2.961	4.14%
ROCK	2.873	4.32%
SPK1	2.804	6.12%
WLSN	2.859	3.84%
Mean	2.859	4.38%

Examining the VTEC prediction error and relative error in Table 5.12, it shows that the VTEC prediction accuracies at all the six stations are better than 3.0 TECU. The relative errors at all the stations are less than 5.0% except SPK1 which has a relative error 6.12%. The mean relative error is 4.38%, which implies that 10-min TEC predictions can recover about 95.62% of the total ionospheric TEC.

5.5.3.3 Results of Scheme 9 (25°, 30 min)

Figure 5.33 to Figure 5.35 illustrate the TEC comparison results for Scheme 9 (25°, 30-min). The predicted and observed TEC in Figure 5.33 to Figure 5.35 show a good agreement with each other in most portions of the entire period. During some periods such as 124560 ~128130 s, the two sets of TEC data have relatively large disagreements.

When inspecting the reason for that large disagreement, it is found that it is caused by the abnormal performance of GPS satellite PRN 18. As the PRN 18 satellite appeared above the cut-off elevation, all the predictions for PRN 18 at all the GPS stations are very poor, experiencing large disagreements with the observed TEC data. The performance of all other 25 satellites has also been examined and their TEC predictions did not show large disagreements compared to the observed TEC data. The poor quality of the dual-frequency data from PRN 18 which has caused the TEC data derived from this satellite to contain large uncertainties. Those poor TEC data have further affected the modeling construction and the estimation of the ionospheric field coefficients. As a result, the TEC predictions during that period show relatively large disagreements with respect to the observed TEC data.

The vertical TEC prediction errors shown in the Figure 5.33, Figure 5.34 and Figure 5.35 are 3.762 TECU, 3.442 TECU and 3.778 TECU, respectively. The RMS errors for all the observed satellites at the six stations are summarized in Table 5.13. The mean VTEC prediction error is 3.789 TECU and the mean relative error is 5.82%. The RMS value of this scheme (25°, 30-min) is larger than the RMS of Scheme 3 (15°, 30-min) by 0.198 TECU. Compared to Scheme 6 (20°, 30-min), the RMS value of this scheme is larger than that of Scheme 6 by 0.070 TECU. The comparison of the VTEC prediction RMS errors from three modeling schemes shows that in local area GPS reference network based modeling, the selection of 15° as elevation cutoff angle will produce slightly better TEC prediction results when performing long-term (30-min) TEC prediction.

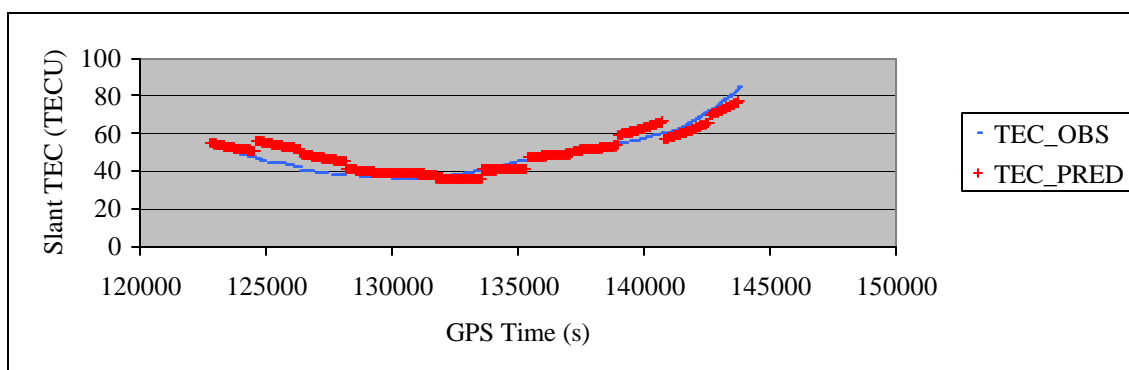


Figure 5.33 Comparison of Observed and Predicted TEC for PRN 02 at SPK1 Station on DOY 136 at 25° Cutoff and 30-min Prediction Interval
(VTEC RMS= 3.762 TECU, Relative Error = 8.63%)

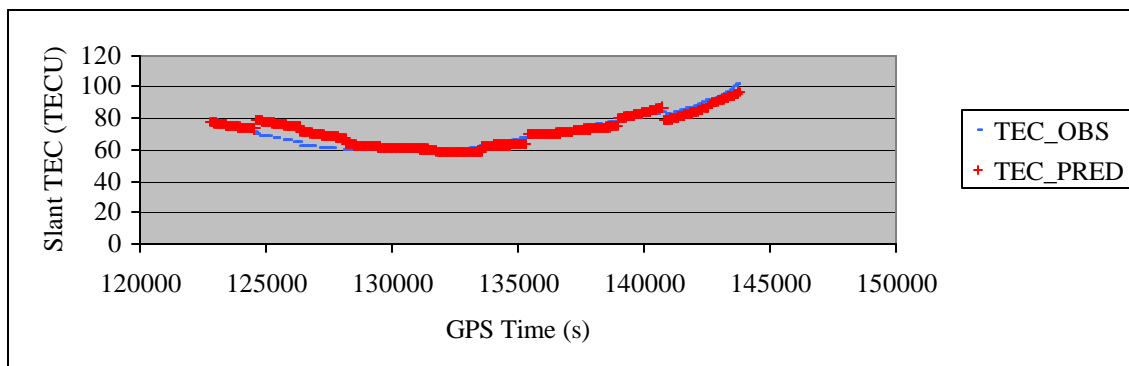


Figure 5.34 Comparison of Observed and Predicted TEC for PRN 02 at LEEP Station on DOY 136 at 25° Cutoff and 30-min Prediction Interval
(VTEC RMS= 3.442 TECU, Relative Error = 5.04%)

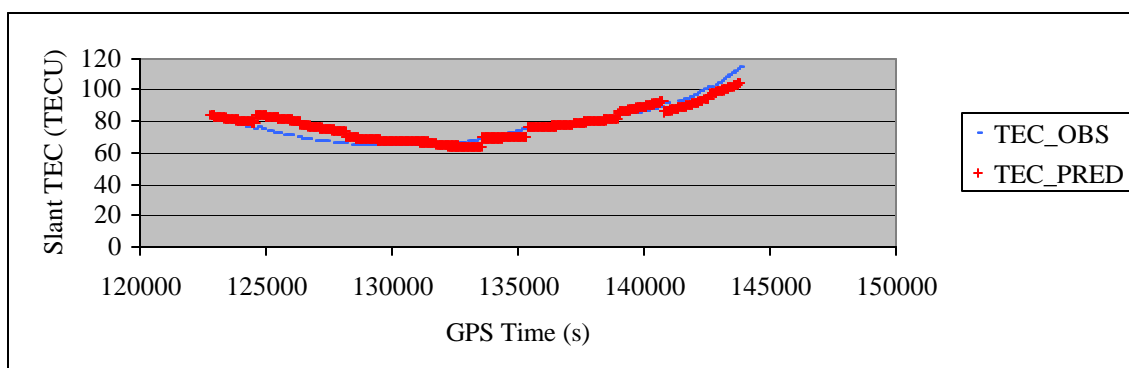


Figure 5.35 Comparison of Observed and Predicted TEC for PRN 02 at CIT1 Station on DOY 136 at 25° Cutoff and 30-min Prediction Interval
(VTEC RMS= 3.778 TECU, Relative Error = 5.34%)

It can be seen in Table 5.13 that the accuracy of VTEC prediction for each station is better than 4.0 TECU. The slant TEC prediction relative errors are smaller than 6.0% at five stations except that SPK1 station has a slightly larger relative error over 8.0%. This is because the magnitudes of the observed TEC data at SPK1 station are comparatively small. Comparing the values of observed TEC data in Figure 5.33, Figure 5.34 and Figure 5.35, it can be seen that in Figure 5.33, the minimum observed TEC data are at the level of 40 TECU while in both Figure 5.34 and Figure 5.35, the minimum observed TEC data

have quantities over 60 TECU. Therefore the relative error at SPK1 station is slightly larger than other stations.

Table 5.13 Error Statistics for 30-min VTEC Prediction with Cutoff 25° on DOY 136

STATION	VTEC Error RMS (TECU)	Relative Error (%)
CMP9	3.765	5.69%
CIT1	3.763	4.75%
LEEP	3.881	5.51%
ROCK	3.866	5.78%
SPK1	3.717	8.09%
WLSN	3.743	5.11%
Mean	3.789	5.82%

5.6 Application of Predicted Ionospheric TEC Corrections to SPP

Through extensive result comparisons among different modeling schemes, the above section has systematically shown that the predicted TEC data have a good agreement with the observed TEC data. This can be seen from the TEC comparisons and statistics of the VTEC prediction errors and relative errors of each modeling scheme in the above section. In addition to the accuracy evaluation with respect to the observed TEC data, the ionospheric tomography model is also assessed via its application to a single point positioning (SPP) system. A software package $P^3\text{TM}$ developed at The University of Calgary will be used to facilitate the positioning test using data from a single receiver and ionospheric corrections from the tomographic model. The $P^3\text{TM}$ software package can process code and/or carrier phase measurements from a single-frequency or dual-frequency GPS receiver. In this study, only the C/A code measurements are processed although the data sets contain dual-frequency observations. The purpose of selecting only C/A code measurements is to assess how well the ionosphere tomographic model can serve as a correction algorithm to eliminate ionospheric refraction errors to support single-frequency GPS users. One main goal of this ionosphere tomographic model

developed in this thesis is to apply this modeling method to generate ionospheric corrections for single-frequency GPS users.

In order to compare the performance of the predicted TEC data, two other different ionospheric models are also implemented in SPP. They are called zero-model (the worst scenario, i.e., no ionospheric correction is made) and dual-frequency model (the best scenario, i.e., using dual-frequency GPS data to remove ionospheric errors). Since no ionospheric corrections are made, the purpose of using zero-model is to illustrate the total effect of ionospheric errors on point positioning solutions. The use of dual-frequency model is to assess how much the positioning accuracy can be improved after the ionospheric errors are removed. In this test, only the ionospheric correction models are different in different testing cases while all other conditions and parameters maintain exactly the same. Through a comparison of the positional solutions from the use of different ionospheric models, their performances can be assessed.

The C/A data from a single GPS receiver are processed on an epoch-by-epoch basis in the data analysis. The position solutions computed by the SPP at each epoch are compared to the known coordinates and their differences are calculated. The root-mean-squares (RMS) is computed based on the epoch-by-epoch differences of the coordinates. Once the RMS values corresponding to three ionospheric models are obtained, the recovering efficiency of the tomographic model can be calculated with equation (4.38).

To avoid too lengthy presentation of the results, in the following, the TEC predictions using an elevation angle cutoff 15° are applied for SPP position determination to demonstrate the performance of the model.

5.6.1 SPP results using 5-min TEC predictions

Shown in Figure 5.36 to Figure 5.38 are the C/A code pseudorange positioning errors at the stations SPK1, LEEP and CIT1 on an epoch-by-epoch basis using three different

ionospheric correction models, respectively. In the figures, the positioning error corresponding to the ionospheric zero-model is represented by the dark blue diamonds. The positioning error of the tomographic model is denoted by the pink squares and the results of dual-frequency model are denoted by the yellow triangles. The TEC predictions used here are the results of Scheme 1 in the previous section and the prediction interval is 5-min. The positioning error at each epoch is calculated by differencing the SPP solution with respect to its known coordinates. It can be seen in the three figures that the positioning errors corresponding to the zero-model are significantly larger than those that have used the tomographic model and dual-frequency model. When comparing the performances of the tomographic model and the dual-frequency model, it can be seen that the use of these two models have produced positioning errors with similar sizes. At most epochs the positioning errors of these two models are very close to each other. Only at very few epochs the positioning errors using the tomographic model are larger than those using the dual-frequency model. That is to say, the performances of the developed ionospheric tomographic model is very close to the performance using the dual-frequency model in terms of their capability to correct ionospheric errors for GPS positioning and navigation.

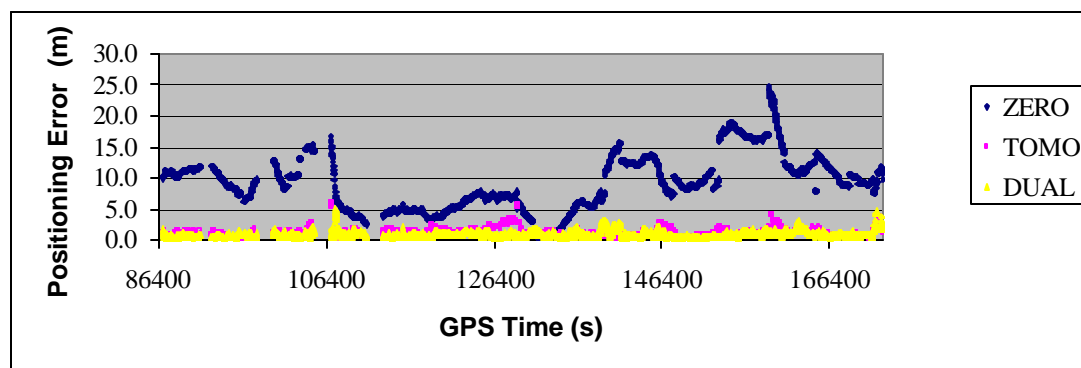


Figure 5.36 Positioning Error at SPK1 Station Using Three Ionospheric Models, Tomographic Correction Predicted at 15° and 5-min Interval

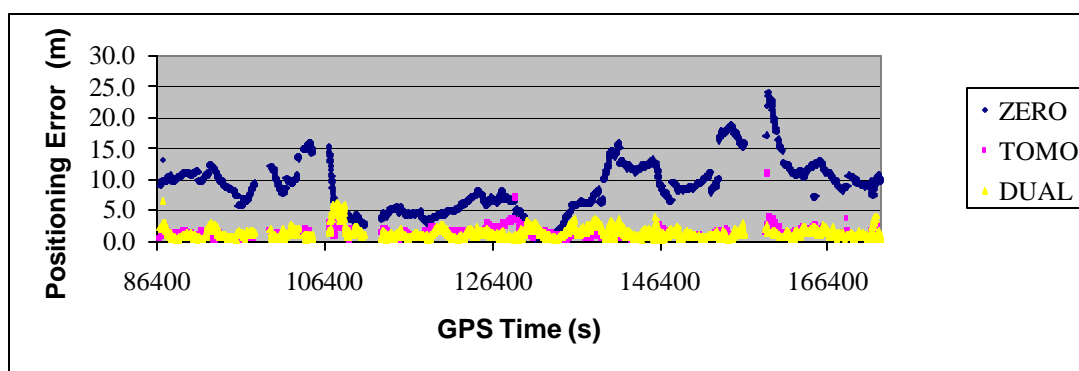


Figure 5.37 Positioning Error at LEEP Station Using Three Ionospheric Models, Tomographic Correction Predicted at 15° and 5-min Interval

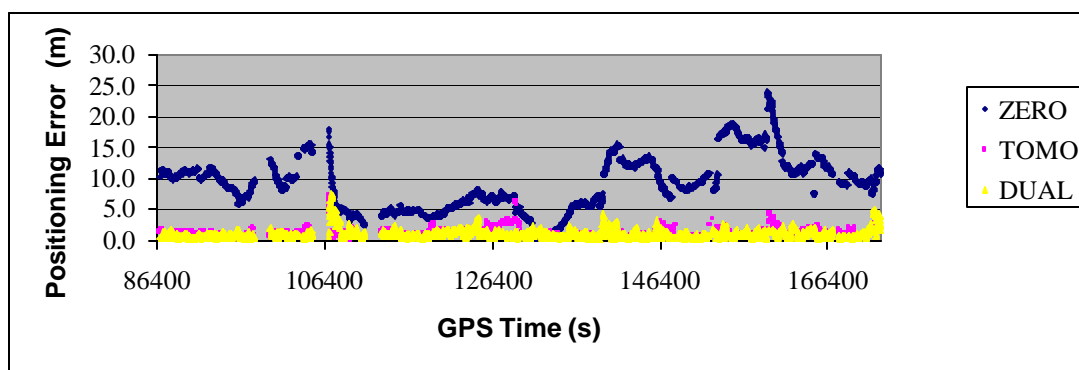


Figure 5.38 Positioning Error at CIT1 Station Using Three Ionospheric Models, Tomographic Correction Predicted at 15° and 5-min Interval

Table 5.14 summarizes the positioning RMS errors in latitude, longitude and height component as well as the total positioning errors for all the six GPS stations. From the results corresponding to the zero-model, it is found that the ionospheric error in GPS single station positioning primarily affect the positioning accuracy in height component. The horizontal part, including the latitude and longitude components, has much smaller positioning errors than the height component. Without any ionospheric corrections, namely using zero-model, the positioning error in latitude component is at the order of 2.1 m and it is about 1.0 m in the longitude component. However in the height component, the positioning error is significantly increased to about 9.5 m. This is mainly due to the better horizontal geometry than the vertical one during the positioning. In

terms of the ionospheric effect on horizontal positioning, the ionospheric errors have more influences in the latitude component than the longitude component.

Table 5.14 Single-frequency Single Point Positioning RMS Error at 6 Stations Using Tomographic Corrections Predicted at 15° and 5-min Interval (m)

Station	Component	Zero Model	Tomographic Model	Dual-frequency Model
CMP9	Latitude	2.060	0.688	0.565
	Longitude	1.011	0.497	0.603
	Height	9.323	1.265	1.526
	3D	9.601	1.524	1.736
CIT1	Latitude	2.197	0.661	0.411
	Longitude	0.915	0.399	0.381
	Height	9.690	1.163	1.161
	3D	9.978	1.396	1.290
LEEP	Latitude	2.189	0.681	0.571
	Longitude	0.956	0.440	0.513
	Height	9.203	1.238	1.403
	3D	9.508	1.480	1.599
ROCK	Latitude	2.063	0.685	0.538
	Longitude	0.960	0.390	0.471
	Height	9.276	1.237	1.303
	3D	9.551	1.467	1.486
SPK1	Latitude	2.136	0.596	0.404
	Longitude	0.901	0.407	0.348
	Height	9.785	1.159	0.918
	3D	10.056	1.365	1.062
WLSN	Latitude	2.051	0.818	0.617
	Longitude	0.949	0.497	0.528
	Height	9.347	1.656	1.669
	3D	9.617	1.912	1.856

Examining the average positioning errors shown in Table 5.14 corresponding to three different ionospheric models, we can find that the solutions of the zero-model have the worst accuracies and the positioning errors are in the range of 9.5 m to 10.0 m. When the dual-frequency model is applied in the SPP, the positioning accuracy has been significantly increased to the level of 1.0 m to 1.8 m. If the 5-min TEC predictions from the tomographic model are used, the positioning accuracy has also significantly improved

over the zero-model. According to the results from all six stations, the positioning accuracies for the tomographic model are in the range of 1.4 m to 1.9 m, which are very comparable to the accuracies using the dual-frequency model.

During the SPP data processing, all conditions are identical except the use of different ionospheric correction models. Table 5.14 indicates that the positioning accuracies vary with the use of different models. The variation of the positioning accuracies should attribute to the difference in performance provided by different ionospheric models. The model with best performance should have the highest capacity to correct the ionospheric errors and therefore the positioning solutions of that model should be the most accurate. The zero-model has least correction capability and consequently its positioning errors are the largest. The dual-frequency model is the most effective method to correct ionospheric errors and the remaining residuals after the application of dual-frequency model are negligible. Therefore, the positioning solutions of dual-frequency model are not affected by ionospheric errors. Taking SPK1 station as an example, the positioning error of zero-model is 10.056 m and the error of dual-frequency model is 1.062 m. Thus the contribution of ionospheric errors to the positioning solutions is 8.994 m. When using the tomographic model to correct the ionospheric errors, the positioning accuracy at SPK1 station improves from 10.056 m to 1.365 m, with an accuracy gain 8.691 m over the zero-model. That is to say the tomographic model correct 8.691 m of ionospheric effects in the positioning solutions. This correction accounts for 96.63% of the total ionospheric effect 8.994 m. In other words, the 5-min TEC predictions from the ionospheric tomographic model have an efficiency of correcting 96.63% ionospheric errors in the GPS single point positioning. The remaining 3.37% errors are uncorrectable by the TEC predictions due to the uncertainties in the predictions. For CIT1 station, the predicted TEC data correct 98.78% ionospheric errors in GPS positioning and the tomographic model efficiency at WLSN is 99.28%. At other three stations, ROCK, LEEP and CMP9, the positioning accuracies corresponding to tomographic model even outperform those from dual-frequency model. That is possible from a statistical point of view because the dual-

frequency model uses code pseudorange measurements without carrier phase smoothing to calculate ionospheric corrections. While in the tomographic modeling the TEC data are smoothed by carrier phase measurements thus the predicted TEC data have the effects of carrier phase smoothing. Overall, the positioning error statistics of all six GPS stations shown in Table 5.14 indicate that the employment of TEC predictions generated from the tomographic model can effectively correct the ionospheric errors in GPS positioning and that the correcting efficiency is comparable to the dual-frequency model. Table 5.15 summarizes the ionospheric model's recovering efficiency at each station.

Table 5.15 Ionospheric Recovering Efficiency of 5-min TEC Predictions

Station	Recovering Efficiency (%)	Residual Error (%)
CMP9	100.00%	0.00%
CIT1	98.78%	1.22%
LEEP	100.00%	0.00%
ROCK	100.00%	0.00%
SPK1	96.63%	3.37%
WLSN	99.28%	0.72%
Mean	99.12%	0.88%

In the following, the performance of the ionospheric predictions is assessed with respect to single point positioning at an independent user station. For that purpose, LEEP station is excluded from the ionospheric modeling so the measured TEC data from LEEP can be used as an independent reference to assess the accuracy of the predicted TEC data generated from the tomographic model. The single point positioning results using three types of ionospheric models are presented in Figure 5.39. It shows that the tomographic model can significantly reduce the positioning error from a level of 10.0~20.0 m to a level of several metres. The positioning solutions at each epoch using different ionospheric models are compared to the known coordinates of LEEP station. The positioning RMS is 9.375 m using the zero-model but it is significantly reduced to 2.689 m when using the tomographic model. The RMS value is 1.606 m when using the dual-frequency model. The recovering efficiency calculated from equation (4.75) is 86.06%. Compared to the results with LEEP station included for tomographic modeling, the

recovering efficiency has been degraded by 13.94%. This is consistent with the slight degradation of the VTEC prediction accuracy of the TEC predictions at LEEP station when excluding its data from ionospheric modeling, as shown in Section 5.5.1.1.

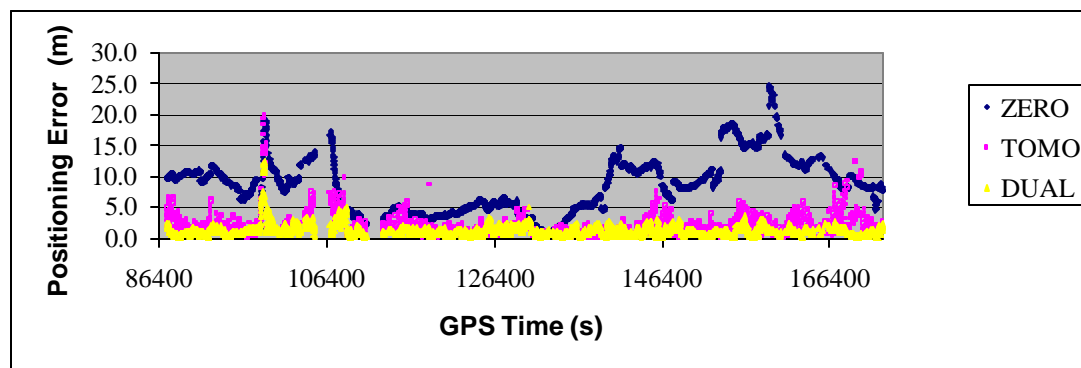


Figure 5.39 Positioning Error at LEEP Station Using Three Ionospheric Models, Tomographic Correction Predicted at 15° and 5-min Interval

5.6.2 SPP results using 10-min TEC predictions

In this section, the point positioning is performed using the TEC predictions from Scheme 2 (15°, 10-min). Figure 5.40 to Figure 5.42 show the epoch-by-epoch single receiver positioning errors for SPK1, LEEP and CIT1 stations, respectively. The goal of this analysis is to see the efficiency of the medium-term (10-min) TEC predictions in correcting ionospheric errors for GPS positioning and navigation. The results in the figures show that even if the prediction interval is increased from 5-min to 10-min, the predicted TEC data still have a good capability to correct the ionospheric errors. The positioning errors of using tomographic model are significantly smaller than those using the zero-model. The performance of the tomographic model is basically comparable to that of the dual-frequency model when examining the positioning errors at the three stations.

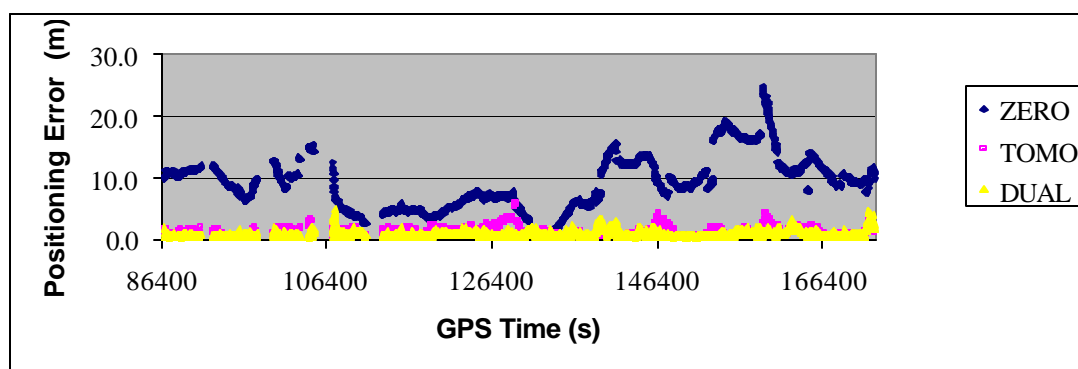


Figure 5.40 Positioning Error at SPK1 Station Using Three Ionospheric Models, Tomographic Correction Predicted at 15° and 10-min Interval

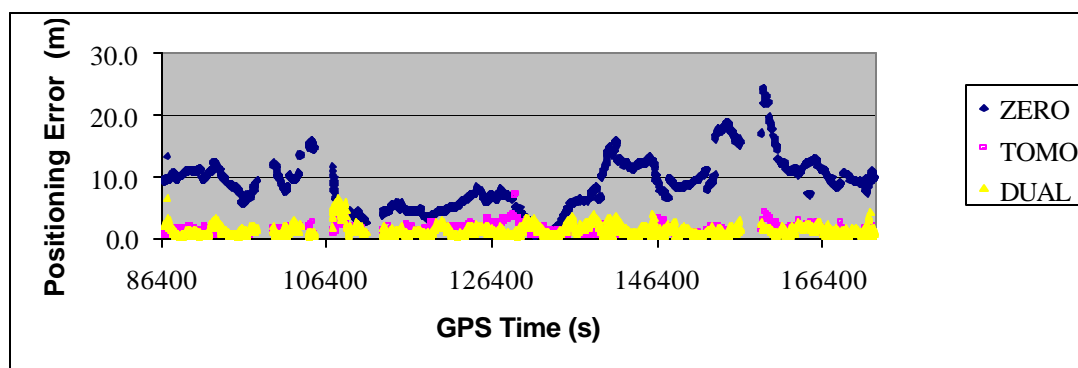


Figure 5.41 Positioning Error at LEEP Station Using Three Ionospheric Models, Tomographic Correction Predicted at 15° and 10-min Interval

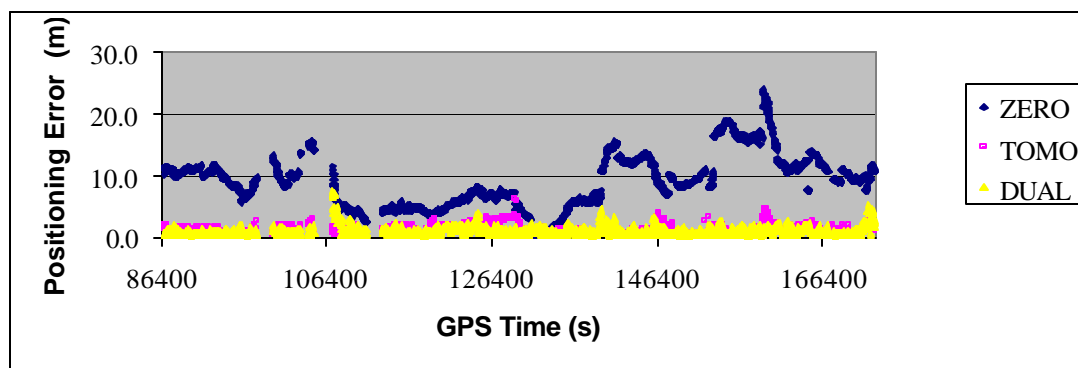


Figure 5.42 Positioning Error at CIT1 Station Using Three Ionospheric Models, Tomographic Correction Predicted at 15° and 10-min Interval

Table 5.16 gives a summary of the RMS errors of each component and the total positioning RMS errors for all the six stations.

Table 5.16 Single-frequency Single Point Positioning RMS Error at 6 Stations Using Tomographic Corrections Predicted at 15° and 10-min Interval (m)

Station	Component	Zero Model	Tomographic Model	Dual-frequency Model
CMP9	Latitude	2.065	0.710	0.566
	Longitude	1.007	0.505	0.602
	Height	9.298	1.326	1.495
	3D	9.578	1.587	1.708
CIT1	Latitude	2.196	0.705	0.410
	Longitude	0.916	0.421	0.380
	Height	9.658	1.193	1.128
	3D	9.946	1.448	1.259
LEEP	Latitude	2.196	0.714	0.569
	Longitude	0.958	0.422	0.511
	Height	9.176	1.285	1.404
	3D	9.484	1.530	1.599
ROCK	Latitude	2.065	0.702	0.538
	Longitude	0.959	0.416	0.472
	Height	9.247	1.319	1.300
	3D	9.523	1.551	1.484
SPK1	Latitude	2.143	0.628	0.404
	Longitude	0.903	0.413	0.350
	Height	9.742	1.200	0.917
	3D	10.015	1.416	1.061
WLSN	Latitude	2.051	0.862	0.601
	Longitude	0.947	0.501	0.528
	Height	9.337	1.697	1.602
	3D	9.606	1.968	1.790

Comparing to the zero-model, it can be seen that after applying the 10-min TEC predictions to SPP the ionospheric errors can be effectively corrected and the positioning accuracies are significantly improved from 9~10 m level to better than 2 m. Using the method proposed in the above section, the ionospheric correcting efficiency of the tomographic model at each station can be calculated. For CIT1 station, the efficiency is 97.82% that is slightly lower than the efficiency 98.78% when using 5-min TEC predictions. The tomographic model has an efficiency of 99.17% at ROCK station. The 5-min TEC predictions have a performance even better than dual-frequency model as shown before. At SPK1 and WLSN stations, the efficiencies are 96.04% and 97.72%,

respectively. The efficiencies of using 10-min predictions at both SPK1 and WLSN stations are smaller than the 5-min predictions (96.63% at SPK1 and 99.28% at WLSN). The slight degradation in the ionospheric correcting efficiency attributes to the increasing prediction uncertainties while the prediction interval is increased.

Summarized in Table 5.17 is the recovering efficiency of 10-min ionospheric TEC data predicted by the ionospheric model to correct the ionospheric error for GPS single station point positioning.

Table 5.17 Ionospheric Recovering Efficiency of 10-min TEC Predictions

Station	Recovering Efficiency (%)	Residual Error (%)
CMP9	100.00%	0.00%
CIT1	97.82%	2.18%
LEEP	100.00%	0.00%
ROCK	99.17%	0.83%
SPK1	96.04%	3.96%
WLSN	97.72%	2.28%
Mean	98.46%	1.54%

Shown in Figure 5.45 are the single point positioning results at LEEP station using different ionospheric models. Note that the model predicted TEC data are obtained using other five stations not including LEEP. The results show that the application of TEC predictions from the tomographic model can significantly improve the positioning accuracy for single-frequency users. The positioning accuracy is 9.134 m using the zero-model, 3.283 m using the tomographic model, 1.612 m using the dual-frequency model. The recovering efficiency is 77.79%. Compared to the results with a 5-min prediction interval, the recovering efficiency with longer prediction interval (10-min here) has a degradation of 8.27% when using the model predicted TEC corrections. Compared to the recovering efficiency where LEEP station is included in tomographic modeling, it has a degradation of about 22.21%.

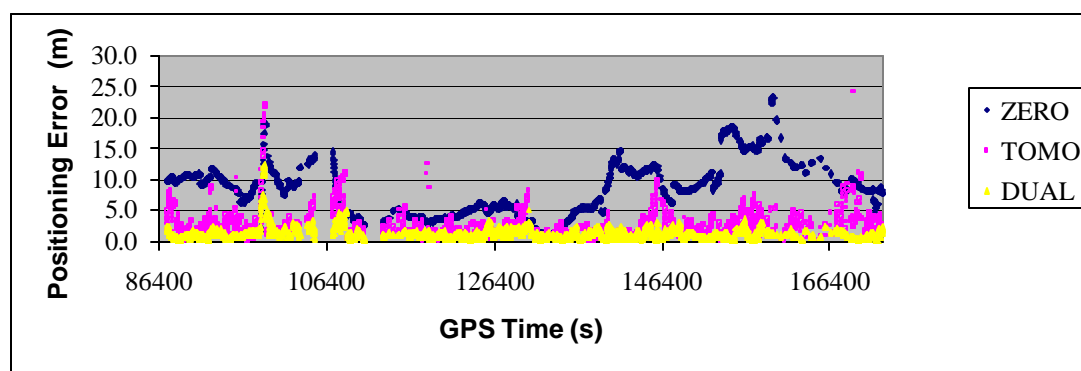


Figure 5.43 Positioning Error at LEEP Station Using Three Ionospheric Models, Tomographic Correction Predicted at 15° and 10-min Interval

5.6.3 SPP results using 30-min TEC predictions

In order to examine the performance of TEC data predicted with 30-min interval in correcting ionospheric errors for GPS positioning, the following results are obtained. Figure 5.44 to Figure 5.46 show the single receiver single epoch positioning error for SPK1, LEEP and CIT1 stations, respectively. In each figure, three different ionospheric models are employed to make a comparison of their performances in correcting the ionospheric errors. It is clearly seen that the dual-frequency model has the best correction capability among the three models. The positioning error corresponding to the dual-frequency model is the smallest. Although the positioning solutions using the 30-min TEC predictions from the tomographic model are not as good as the results of the dual-frequency model, they still make a big improvement over the zero-model. The detailed statistics for all the six stations can be found in Table 5.18.

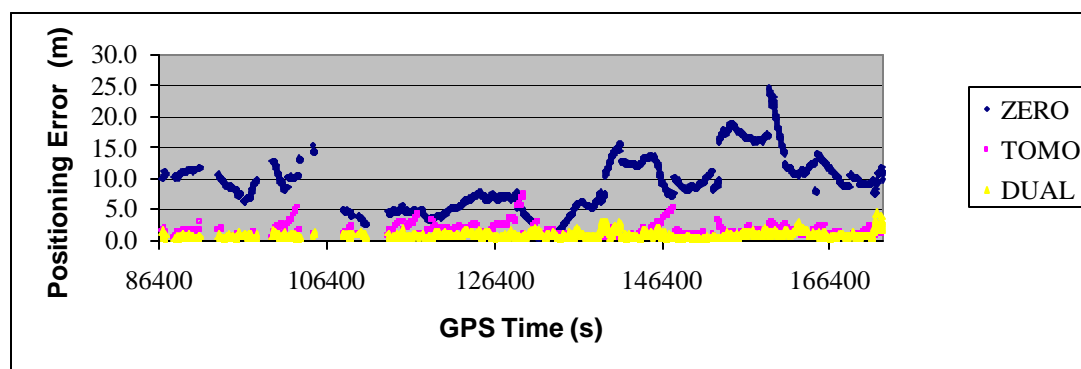


Figure 5.44 Positioning Error at SPK1 Station Using Three Ionospheric Models, Tomographic Correction Predicted at 15° and 30-min Interval

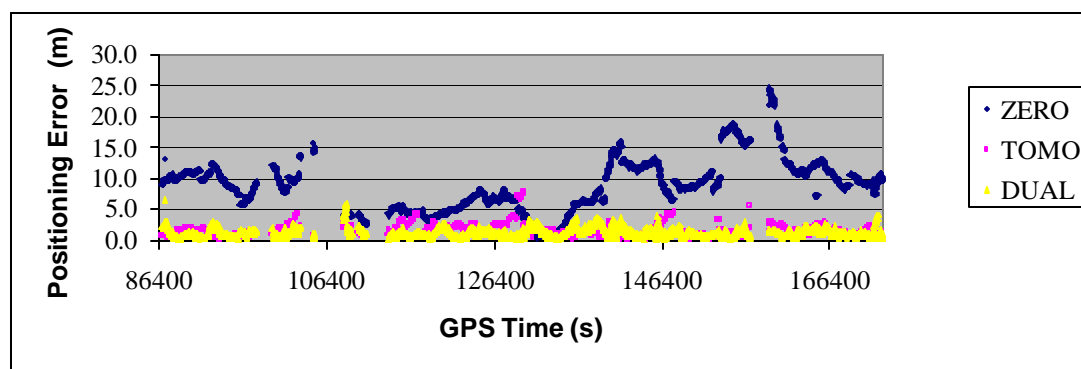


Figure 5.45 Positioning Error at LEEP Station Using Three Ionospheric Models, Tomographic Correction Predicted at 15° and 30-min Interval

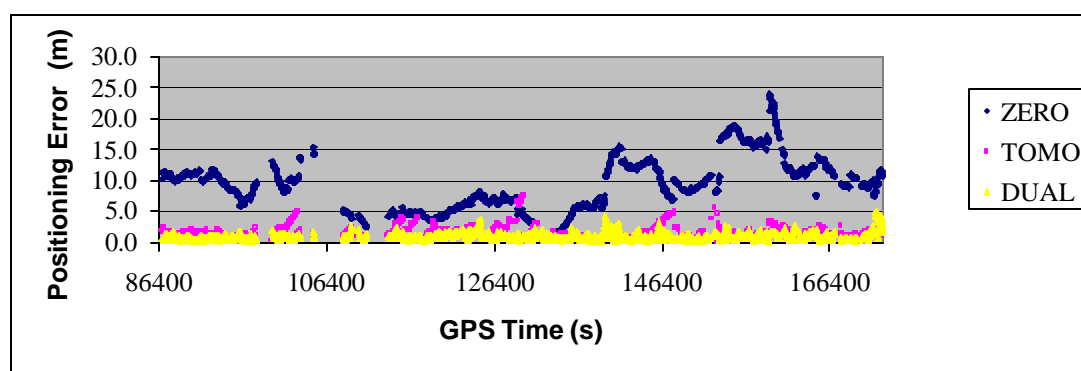


Figure 5.46 Positioning Error at CIT1 Station Using Three Ionospheric Models, Tomographic Correction Predicted at 15° and 30-min Interval

Table 5.18 gives the statistics of the positioning errors in different coordinate components and the three-dimensional positioning errors for all the six stations. Table 5.18 shows the accuracy improvement using the 30-min TEC predictions over using the zero-model. The three-dimensional positioning errors are significantly decreased from 9.5~10 m to 1.9~2.0 m after the employment of the tomographic model. This improvement confirms the excellent performance of the tomographic model in correcting ionospheric errors. When compared to the ideal situation with the use of the dual-frequency model, the accuracy difference between the solutions of the dual-frequency model and the tomographic model is only about 0.5~0.9 m. the efficiency of the tomographic model at

each station can also be assessed from the positioning errors using different ionospheric models.

Table 5.18 Single-frequency Single Point Positioning RMS Error at 6 Stations Using Tomographic Corrections Predicted at 15° and 30-min Interval (m)

Station	Component	Zero Model	Tomographic Model	Dual-frequency Model
CMP9	Latitude	2.056	0.948	0.554
	Longitude	0.987	0.594	0.598
	Height	9.488	1.743	1.428
	3D	9.758	2.071	1.645
CIT1	Latitude	2.181	0.885	0.394
	Longitude	0.919	0.534	0.379
	Height	9.684	1.608	1.027
	3D	9.969	1.911	1.163
LEEP	Latitude	2.193	0.882	0.548
	Longitude	0.954	0.516	0.509
	Height	9.245	1.623	1.286
	3D	9.549	1.918	1.488
ROCK	Latitude	2.058	0.847	0.526
	Longitude	0.954	0.535	0.465
	Height	9.239	1.769	1.279
	3D	9.513	2.033	1.459
SPK1	Latitude	2.152	0.827	0.397
	Longitude	0.914	0.480	0.353
	Height	9.772	1.652	0.894
	3D	10.048	1.909	1.040
WLSN	Latitude	2.061	1.015	0.585
	Longitude	0.931	0.547	0.520
	Height	9.330	2.035	1.451
	3D	9.600	2.339	1.649

The efficiency of the tomographic model in correcting ionospheric errors for GPS positioning at each GPS station is shown in Table 5.19. It shows the accuracy improvement using the 30-min TEC predictions over using the zero-model. The three-dimensional positioning errors are significantly decreased from 9.5~10 m to 1.9~2.0 m after the employment of the tomographic model. This improvement confirms the excellent performance of the tomographic model in correcting ionospheric errors. When

compared to the ideal situation with the use of the dual-frequency model, the accuracy difference between the solutions of the dual-frequency model and the tomographic model is only about 0.5~0.9 m. the efficiency of the tomographic model at each station can also be assessed from the positioning errors using different ionospheric models. Table 5.19 shows that the predicted ionospheric TEC data can averagely recover over 92% ionospheric errors in point positioning. The irrecoverable ionospheric residual is less than 8%.

Table 5.19 Ionospheric Recovering Efficiency of 30-min TEC Predictions

Station	Recovering Efficiency (%)	Residual Error (%)
CMP9	94.75%	5.25%
CIT1	91.50%	8.50%
LEEP	94.66%	5.34%
ROCK	92.87%	7.13%
SPK1	90.35%	9.65%
WLSN	91.32%	8.68%
Mean	92.58%	7.42%

Similar to Sections 5.6.1 and 5.6.2, the TEC prediction data at LEEP station obtained from excluding LEEP station from ionospheric modeling are incorporated to the single point positioning program and the results are compared to those obtained from the other two ionospheric models. The positioning results are given in Figure 5.47. It shows that the use of 30-min TEC predictions generated from the tomographic model can improve the positioning accuracy using a single-frequency receiver when compared to the zero-model. The improvement is however not as significant as the 5-min or 10-min TEC predictions. As shown in Figure 5.47 there are no solutions for some epochs. This is because some measurements have been rejected due to large residuals, resulting in inadequate number of satellites necessary for a position fix. The positioning accuracy is 8.685 m using the zero-model and is 4.402 m using the tomographic model. Using the dual-frequency model, the positioning accuracy is 1.490 m. The recovering efficiency is 59.53%. It can be seen in Figure 5.47 that at some epochs, the positioning errors using the tomographic model are even greater than those using the zero model. The degraded

positioning accuracies at these epochs are due to large TEC correction errors for some satellites. As shown in Figure 5.16, the TEC prediction errors could be as high as 10~20 TECU at some epochs and it probably contributes to the degraded positioning accuracies with tomographic model.

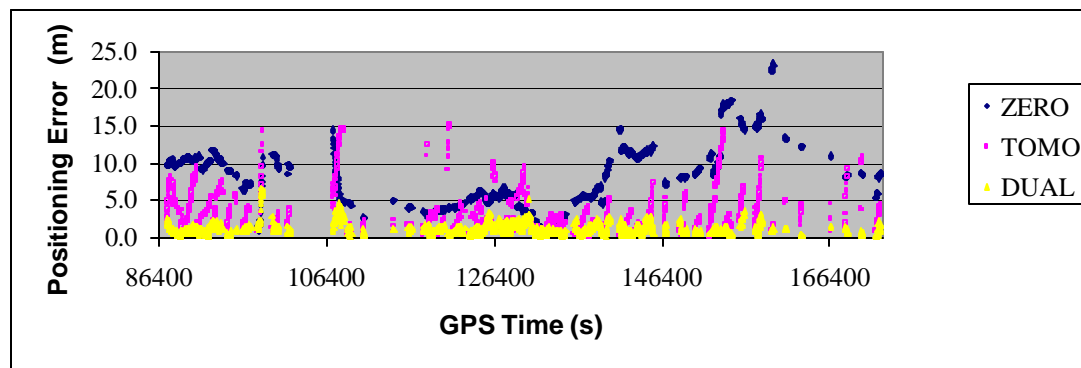


Figure 5.47 Positioning Error at LEEP Station Using Three Ionospheric Models, Tomographic Correction Predicted at 15° and 30-min Interval

CHAPTER 6

IONOSPHERE TOMOGRAPHIC MODELING OVER A WIDE AREA GPS REFERENCE NETWORK

In Chapter 5, the methodologies of ionosphere tomographic modeling are implemented with a local area GPS reference network. To demonstrate the capability of this method to model ionosphere over wide area GPS reference networks, this chapter analyzes a data set observed over a wide area GPS reference network and uses the proposed tomographic technique to construct the ionospheric model. Similar to Chapter 5, the ionospheric TEC prediction tests are carried out to evaluate the tomographic model's performance over large-scale GPS networks. To assess the model's performance during periods of active ionosphere, a data set acquired on March 30-31, 2001 was used. On March 31, 2001, geomagnetic storm occurred, prior to which two coronal mass ejections and one an X-class solar flare had occurred two days earlier (Coster et al., 2003).

The purpose of this data analysis is to 1) test the model's feasibility to Wide Area GPS reference networks; 2) test the model's performances under different ionospheric conditions, including both quiet and disturbed conditions; 3) find an optimal modeling scheme for wide area GPS network based ionospheric modeling, applicable to other similar wide area networks. In this chapter, the modeling performances over a wide area GPS network with various modeling schemes will be analyzed. The modeling results using different schemes are compared to identify an optimal parameterization scheme. The significance of this study is firstly to test the capability of the ionospheric tomography model over wide area GPS reference network; and secondly, to investigate and understand the magnitudes and patterns of the influences of various factors on the ionosphere tomographic modeling results; and finally, to provide general

parameterization guidance for other wide area GPS reference networks using ionosphere tomographic modeling method.

6.1 Data Description

The dataset used in this study is collected from a wide area GPS network consisting of 22 GPS stations. This wide area network covers most of the North America continent. The network stretches from 34.3°N to 64.9°N in latitude and from -52.7°W to -152.5°W in longitude. The geographical locations and monumental names of the stations are listed in Table 6.1. The GPS station distribution is depicted in Figure 6.1. It shows that the network is a typical wide area GPS network.

Table 6.1 Coordinates of GPS Station in Wide Area GPS Reference Network

Station	Latitude (°)	Longitude (°)	Height (m)
ALBH	48.3898	-123.4880	31.7625
ALGO	45.9558	-78.0714	200.906
AMC2	38.8031	-104.5250	1911.413
CARR	35.8883	-120.4310	479.242
CASP	42.8192	-106.3840	1571.416
COSO	35.9823	-117.8090	1455.453
DAM2	34.3348	-118.3970	583.396
DRAO	49.3226	-119.6250	541.859
FAIR	64.9780	-147.4990	318.999
FLIN	54.7256	-101.9780	311.518
HOLB	50.6404	-128.1350	559.586
HOPB	38.9952	-123.0750	353.306
KODK	57.7351	-152.5010	37.864
NEAH	48.2979	-124.6250	459.931
NRC1	45.4542	-75.6238	82.493
PRDS	50.8714	-114.2940	1247.980
SCH2	54.8321	-66.8326	498.231
STJO	47.5952	-52.6777	152.841
USNO	38.9190	-77.0662	48.888
VNDP	34.5563	-120.6160	-11.515
WHIT	60.7505	-135.2220	1427.380
WSLR	50.1265	-122.9210	909.258

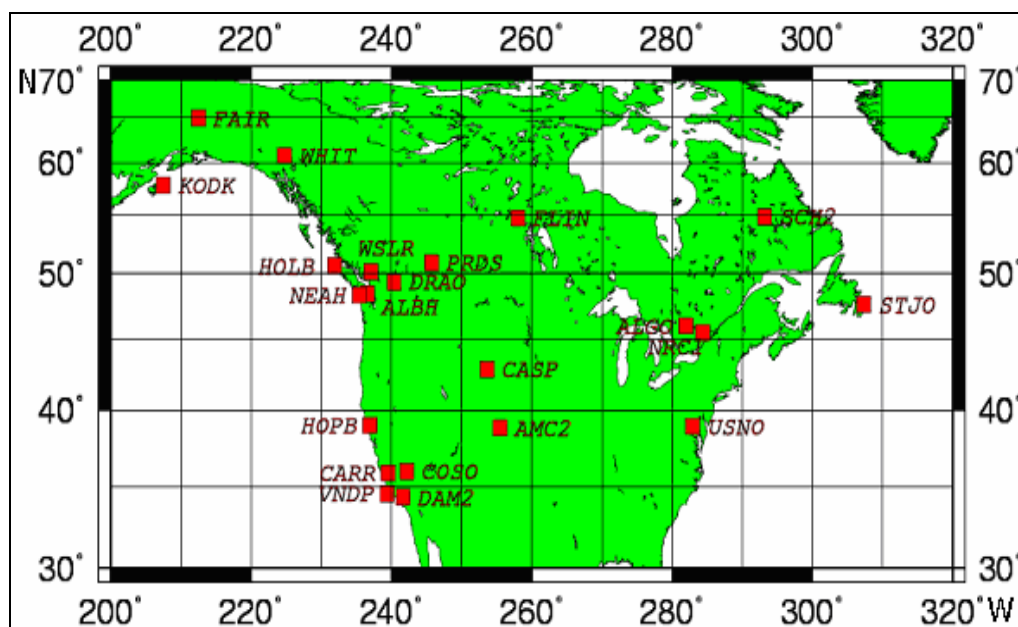


Figure 6.1 GPS Station Distribution within Wide Area GPS Reference Network

The number of reference stations and the density used in this analysis is very close to that of the WAAS Reference Stations (WRS) in FAA's Phase I WAAS (Loh et al., 1995). In this study, three intervals, 5-min, 10-min and 30-min, are used for TEC prediction. The 5-min prediction interval is the same as the WAAS ionospheric grid update interval (El-Arini et al., 1999). The longer intervals of TEC prediction are aiming at using these predicted TEC data for other ionosphere-related researches.

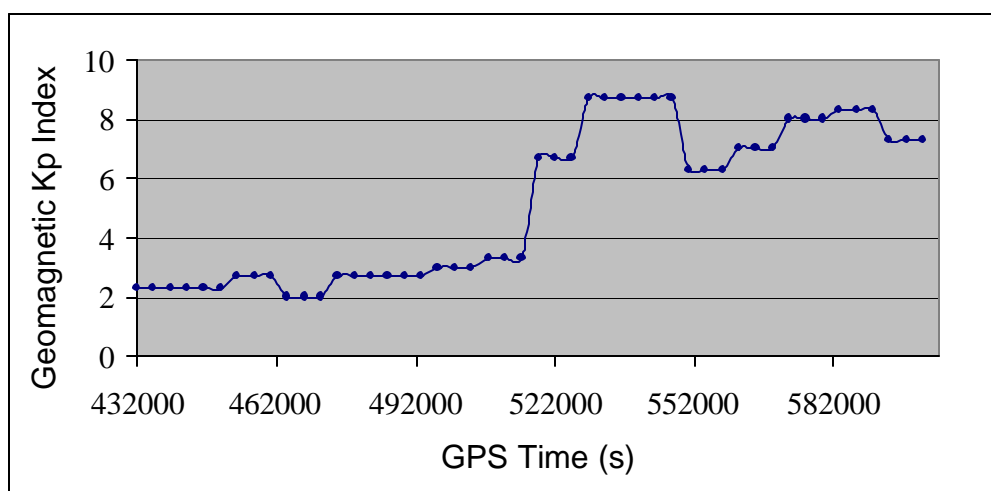


Figure 6.2 Geomagnetic Kp Index Values during March 30-31, 2001

The GPS data used in this study were observed during March 30 to 31, 2001. The Kp variations during the two days are displayed in Figure 6.2. It is seen that on March 31, 2001 between 3:00 and 9:00 UTC, the Kp reached as high as 9. Compared to March 31, the Kp values on March 30 were much smaller. This indicated that March 30, 2001 basically was a geomagnetically quiet day and March 31, 2001 was an ionospherically disturbed day.

The baseline separations between any two GPS stations are given in Table 6.2. The longest baseline in this network is from KODK to STJO with a distance of 5975.2 km. The baseline between ALBH and NEAH is the shortest with a baseline length of 84.9 km. There are totally 231 baselines within this wide area network. The mean baseline length among the entire network is 2497.9 km. From Figure 6.1 and Table 6.2, it can be concluded that the network used in this ionospheric modeling analysis is a typical wide area GPS network.

Table 6.2 Baseline Distances between GPS Stations in GPS Network (km)

	ALBH	ALGO	AMC2	CARR	CASP	COSO	DAM2	DRAO	FAIR	FLIN	HOLB	HOPB	KODK	NEAH	NRC1	PRDS	SCH2	STJO	USNO	VNDP	WHIT	WSLR
ALBH	0	3362.9	1850.7	1408.3	1463.6	1451.8	1612.8	301.8	2318.4	1636.6	419.2	1043.2	2171.3	84.9	3553.1	718.3	3819.1	4955.6	3769	1550.8	1562.2	197.5
ALGO	3362.9	0	2293.8	3639.5	2258.9	3439.7	3576.4	3074.7	4475.8	1940	3628.4	3676.3	4888.2	3444.4	198.6	2687.9	1265.1	1931.8	785.5	3727.6	3924.3	3287.9
AMC2	1850.7	2293.8	0	1441.2	472.8	1214.5	1333.1	1671.9	3945.4	1774.9	2259.1	1602.6	3953.1	1920.7	2470.5	1541.2	3287.4	4165.7	2360.9	1507.8	3201.5	1914.1
CARR	1408.3	3639.5	1441.2	0	1428.9	236.8	253.1	1490.5	3648.9	2511.6	1746.5	416.6	3349.2	1418	3820.8	1730.7	4459.1	5421.5	3761.6	148.7	2932.1	1590.5
CASP	1463.6	2258.9	472.8	1428.9	0	1239.2	1402.9	1249.1	3501.8	1360	1860.1	1463.1	3543.1	1540.5	2448.7	1077	3111.4	4094.5	2480.6	1534	2753.6	1499.3
COSO	1451.8	3439.7	1214.5	236.8	1239.2	0	190.5	1486.1	3722.4	2397.8	1821.3	573	3471.5	1474.9	3619.9	1673.5	4295	5241.1	3543.2	300.5	2991.9	1620.5
DAM2	1612.8	3576.4	1333.1	253.1	1402.9	190.5	0	1663.1	3865.8	2582.4	1968.5	664.6	3586.4	1630.3	3753.6	1860.4	4452.7	5377.3	3648.5	205.5	3144.4	1786.9
DRAO	301.8	3074.7	1671.9	1490.5	1249.1	1486.1	1663.1	0	2374	1344.8	627.1	1178.3	2330.1	384.4	3265.7	418.4	3535.8	4677.6	3498.3	1637.7	1603.9	253.9
FAIR	2318.4	4475.8	3945.4	3648.9	3501.8	3722.4	3865.8	2374	0	2698.3	1943.6	3258.8	849.1	2288	4624.3	2453.7	4238.7	5384.5	5113.2	3775.8	780.2	2174.8
FLIN	1636.6	1940	1774.9	2511.6	1360	2397.8	2582.4	1344.8	2698.3	0	1808.7	2344.3	3048.1	1712.1	2121.5	932.4	2226.3	3420.2	2546	2647.3	2055.8	1503.5
HOLB	419.2	3628.4	2259.1	1746.5	1860.1	1821.3	1968.5	627.1	1943.6	1808.7	0	1351.3	1757.1	364	3814.8	974.8	3966.6	5126	4081.7	1881	1207.3	375.1
HOPB	1043.2	3676.3	1602.6	416.6	1463.1	573	664.6	1178.3	3258.8	2344.3	1351.3	0	2945.4	1040	3862.7	1485.1	4395.8	5416.6	3881.8	539.1	2545.9	1235.2
KODK	2171.3	4888.2	3953.1	3349.2	3543.1	3471.5	3586.4	2330.1	849.1	3048.1	1757.1	2945.4	0	2113.8	5050.5	2546	4831.3	5975.2	5452.3	3458.9	1037.1	2088.5
NEAH	84.9	3444.4	1920.7	1418	1540.5	1474.9	1630.3	384.4	2288	1712.1	364	1040	2113.8	0	3634.2	798.8	3892.2	5029	3849.9	1558.1	1538.7	238.3
NRC1	3553.1	198.6	2470.5	3820.8	2448.7	3619.9	3753.6	3265.7	4624.3	2121.5	3814.8	3862.7	5050.5	3634.2	0	2879.2	1213.9	1764.4	735.2	3906.5	4088.7	3477
PRDS	718.3	2687.9	1541.2	1730.7	1077	1673.5	1860.4	418.4	2453.7	932.4	974.8	1485.1	2546	798.8	2879.2	0	3133.2	4286.2	3150.7	1876.5	1694.3	617.2
SCH2	3819.1	1265.1	3287.4	4459.1	3111.4	4295	4452.7	3535.8	4238.7	2226.3	3966.6	4395.8	4831.3	3892.2	1213.9	3133.2	0	1269.2	1921.4	4568.3	3869.4	3689.8
STJO	4955.6	1931.8	4165.7	5421.5	4094.5	5241.1	5377.3	4677.6	5384.5	3420.2	5126	5416.6	5975.2	5029	1764.4	4286.2	1269.2	0	2179.2	5512.3	5057	4843.2
USNO	3769	785.5	2360.9	3761.6	2480.6	3543.2	3648.5	3498.3	5113.2	2546	4081.7	3881.8	5452.3	3849.9	735.2	3150.7	1921.4	2179.2	0	3823.3	4527.4	3729.2
VNDP	1550.8	3727.6	1507.8	148.7	1534	300.5	205.5	1637.7	3775.8	2647.3	1881	539.1	3458.9	1558.1	3906.5	1876.5	4568.3	5512.3	3823.3	0	3065.8	1734.4
WHIT	1562.2	3924.3	3201.5	2932.1	2753.6	2991.9	3144.4	1603.9	780.2	2055.8	1207.3	2545.9	1037.1	1538.7	4088.7	1694.3	3869.4	5057	4527.4	3065.8	0	1408.3
WSLR	197.5	3287.9	1914.1	1590.5	1499.3	1620.5	1786.9	253.9	2174.8	1503.5	375.1	1235.2	2088.5	238.3	3477	617.2	3689.8	4843.2	3729.2	1734.4	1408.3	0

The 22 GPS stations used in this data analysis are all equipped with dual-frequency GPS receivers. The receiver and antenna models for these stations are summarized within Table 6.3.

Table 6.3 GPS Receive and Antenna Types

Station	Receiver Type	Installation Date	Antenna Type	Installation Date
ALBH	AOA BENCHMARK ACT	Mar-15-2000	AOAD/M_T	Jun-07-1995
ALGO	AOA BENCHMARK ACT	Aug-19-1999	AOAD/M_T	Jan-16-1997
AMC2	AOA SNR-12 ACT	Jul-10-2000	AOAD/M_T	Mar-24-1998
CARR	ASHTECH Z-XII3	Mar-06-2001	AOAD/M_T	May-31-1994
CASP	ASHTECH UZ-12	Jun-28-2000	ASH700936E	Apr-01-2000
COSO	ASHTECH Z-XII3	Jul-27-1999	ASH700936D_M	Apr-29-1996
DAM2	ASHTECH Low Power Z-XII	Oct-23-1996	ASHTECH	Oct-23-1996
DRAO	AOA BENCHMARK ACT	Dec-06-2000	AOAD/M_T	Jun-01-1999
FAIR	AOA SNR-8100 ACT	Apr-15-2000	AOAD/M_T	Apr-16-1996
FLIN	AOA BENCHMARK ACT	Jan-13-2001	AOAD/M_T	Sep-21-1999
HOLB	AOA SNR-8000 ACT	Mar-21-2001	AOAD/M_T	May-19-1999
HOPB	ASHTECH Z-XII3	Aug-04-1999	ASH700936C_M	Aug-04-1999
KODK	ASHTECH Z-XII3	Dec-07-1999	ASH701933B_M	Aug-09-2000
NEAH	ASHTECH Z-XII3	Aug-20-1999	ASH700936A_M	Feb-02-1997
NRC1	AOA SNR-12 ACT	Feb-16-2000	AOAD/M_T	Jul-01-1996
PRDS	AOA SNR-12 ACT	Jun-24-1999	AOAD/M_T	Jun-14-1999
SCH2	AOA SNR-12 ACT	Aug-05-1999	AOAD/M_T	Jun-29-1997
STJO	AOA SNR-12 ACT	Aug-06-1999	AOAD/M_T	May-26-2000
USNO	AOA SNR-12 ACT	Jun-29-2000	AOAD/M_T	Nov-12-1998
VNDP	ASHTECH Z-XII3	Jul-09-1999	ASH700936B_M	Nov-09-1995
WHIT	AOA SNR-8000 ACT	Oct-04-2000	AOAD/M_T	Jun-24-1997
WSLR	AOA SNR-8000 ACT	Mar-29-2000	AOAD/M_T	Mar-29-2000

6.2 Data Analysis Strategy

The implementation of the ionospheric tomography model consists of two steps. Firstly, two types of TEC measurements, absolute TEC and relative TEC, are derived from dual-frequency GPS code pseudorange and carrier phase measurements, respectively. The absolute TEC measurements are smoothed by the relative TEC ones using smoothing algorithm as described in Chapter 4. These TEC measurements contain the ionospheric electron density information and they are used as the input data of the tomography model.

Based on the tomography modeling method developed in Chapter 4, a model is constructed using these TEC data. The GPS data observed on DOY 089 and 090 have 24-hour GPS observations. First, the 24-hour GPS data are employed to estimate the satellite and receiver inter-frequency biases. Next, the 24-hour data set is split into many sessions. Each session contains 30 epochs, namely 15-minute, of GPS observations and a model is constructed using each session's GPS data. The advantage of dividing many sessions is that the data processing time for the modeling can be remarkably reduced and it allows the truly real-time ionospheric modeling and prediction. During the modeling, the satellite and receiver inter-frequency biases in ionospheric TEC observations are removed by using the result from the previous estimation using 24-hour GPS data. Once the model is constructed, the model is employed to carry out ionospheric TEC prediction at pre-defined intervals. Please note, the satellite and receiver inter-frequency biases are added back to the predicted TEC data since the observed TEC data used for comparison inherently contain the biases. Similar to Chapter 5, three prediction intervals, 5-min, 10-min and 30-min, are used in the analysis. For example, if the session is constructed with GPS data collected during 00:00:00 to 00:15:00 UTC, then the ionospheric prediction (actually ionospheric parameter prediction) at 5-min interval is performed at the moment at 00:20:00 UTC. The ionospheric parameters are assumed to be effective for the period between 00:15:00 and 00:20:00 UTC. Therefore, it is called 5-min prediction. Similarly, for the 10-min prediction, the ionospheric parameters are predicted for the epoch 00:25:00 UTC and its effective period is assumed to be from 00:15:00 to 00:25:00 UTC. Meanwhile, the model prediction performances are assessed at three different elevation angles, namely low cutoff angle 15° , medium cutoff angle 20° and high cutoff angle 25° . The systematic analysis of the dataset will examine the model's performance under different modeling conditions. The nine analysis schemes employed in this chapter are the same as those provided in Table 5.4 in Chapter 5.

6.3 Data Analysis and Results

The data analysis results from different analysis schemes are presented below. For each analysis scheme, comparisons between the predicted and observed TEC are performed. Although there are a large number of comparisons having been conducted, only a portion of the comparison results will be presented in the following to demonstrate the performance of different schemes.

At each GPS station, the differences between the predicted and observed TEC are referred to as ionospheric model's prediction error. These errors are slant TEC errors, which are dependent on the elevation angle of each slant TEC. The elevation angle of each slant TEC is different since it changes with time due to continuous satellite motion. To eliminate the dependence of the prediction error on elevation angle, the slant TEC errors are mapped to the zenith direction. Thus the vertical TEC prediction errors can be obtained. The comparison between the vertical TEC prediction errors is more convenient than the comparison of slant TEC errors because each slant TEC error may have different elevation angle. Mapping to the vertical direction can eliminate the influence of elevation angles. For each GPS station, the statistics of the vertical TEC prediction errors can be calculated.

As discussed in Chapter 4, the relative error of each predicted TEC can be calculated once the observed TEC are derived from dual-frequency GPS data. The mean relative error can be further calculated for each GPS station based on the relative errors of all predicted TEC at that station.

Although our final goal is to predict the ionospheric TEC data, which can be used to in real time applications, the nuisance parameters satellite and receiver inter-frequency biases have to be estimated in order to estimate their influences. In the modeling, the parameters are estimated first using the whole day data. Then in each session's modeling, the parameters are used as knowns. As a byproduct of the modeling, the following

presents the comparison with Jet Propulsion Laboratory (JPL) results of the satellite inter-frequency biases obtained at elevation cutoff 15° . The inter-frequency biases obtained at elevation cutoff 20° and 25° have similar values as the results obtain at 15° but they are not compared here because the data processing for JPL's results usually uses 15° elevation angle. Figure 6.3 and Figure 6.4 show the comparison of satellite inter-frequency biases obtained from tomographic model with JPL results for DOY 089 and DOY 090, respectively. The RMS error for differences between two sets of biases obtained for DOY 089 is 0.17 ns. For DOY 090, the RMS value calculated with differences of the two sets of bias values is 0.19 ns.

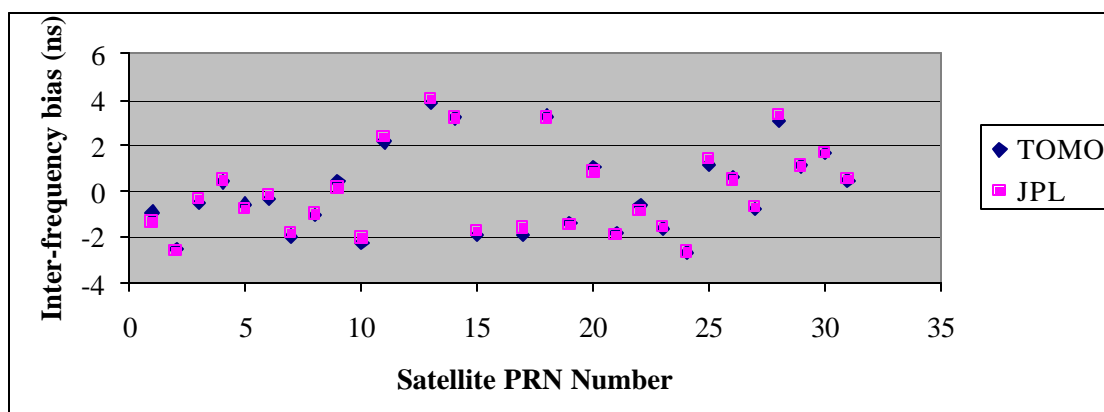


Figure 6.3 Comparison of Satellite Biases on DOY 089

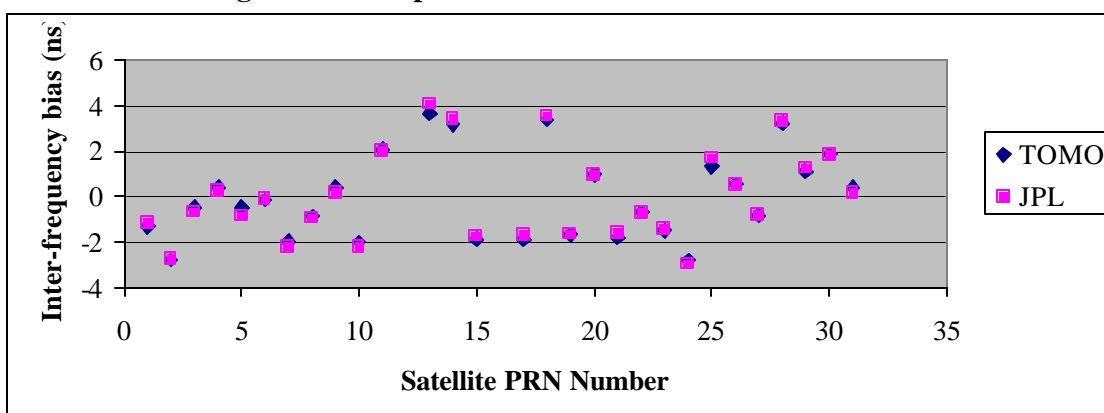


Figure 6.4 Comparison of Satellite Biases on DOY 090

Also the comparison of the GPS receiver inter-frequency biases obtained from DOY 089 and 090 is presented below in Figure 6.5. It shows that the receiver inter-frequency biases are basically quite stable over two days. Their variation of between two days is 0.32 ns.

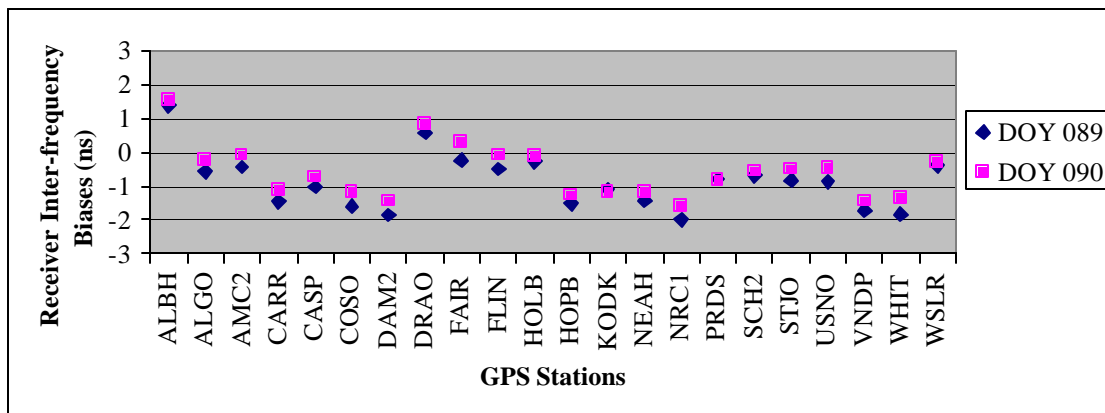


Figure 6.5 Comparison of Receiver Biases for DOY 089 and 090

6.3.1 Results of low elevation cutoff angle (15°)

6.3.1.1 Results of Scheme 1 (15° , 5 min)

In Scheme 1, the elevation cutoff angle is selected to be 15° and the prediction interval is set to 5-min. In the following two subsections, the predicted and observed TEC comparison results for day of year (DOY) 089 (March 30), 2001 and DOY 090 (March 31), 2001 are presented. As mentioned before, on DOY 089 the ionosphere was relatively quiet but on DOY 090 the ionosphere was extremely disturbed. In this wide area GPS network, the total number of GPS stations is 22. The average number of the observed satellites at each station is 27. Therefore there are a great number of TEC pairs within this wide area GPS network. In the following, the TEC pairs between the following six stations located in different latitude regions, namely CARR, COSO, AMC2, CASP, PRDS and FAIR and the following four satellites, namely PRN 02, PRN 03, PRN 04 and PRN 31, are used to form TEC pairs between stations and satellites to illustrate the modeling performance. At CARR and COSO stations, satellite PRN 02 is used to form TEC pairs because the TEC pairs corresponding to this satellite have the largest amount

of data. For the same reason, satellite PRN 03 is used at AMC2 and CASP stations, PRN 31 at PRDS and PRN 04 at FAIR station, respectively.

6.3.1.1.1 Results on ionosphere quiet day DOY 089

Figure 6.6 to Figure 6.11 display the predicted TEC and observed TEC for some stations and satellites. Figure 6.6 and Figure 6.7 show the TEC comparison results for PRN 02 satellite at CARR and COSO stations, respectively. The agreement between the predicted and observed TEC data is quite good except for a few epochs when the satellite was rising. Figure 6.8 and Figure 6.9 illustrate the two sets of TEC data for PRN 03 satellite at AMC2 and CASP stations, respectively. Basically the predicted TEC data are in a good agreement with the observed TEC. The prediction results for other two stations, PRDS and FAIR, are shown in Figure 6.10 and Figure 6.11, respectively. It can be found that at FAIR (the most northern station in the network) the predicted TEC has a relatively large disagreement with the observed TEC, in particular in the first portion of the data (GPS time 457260 s ~ 469560 s). The vertical TEC prediction error for PRN 04 satellite at FAIR station is 5.005 TECU, which is much larger than the VTEC prediction errors at other stations. This might be due to the fact that FAIR station is at the edge of the network and there is less dense ionospheric TEC measurements around it than other non-edge stations. During 457260 s ~ 469560 s as shown in Figure 6.11, it can be seen that the observed TEC data are at the level from a few TECU to less than 20 TECU. The magnitudes of the TEC values are much smaller than that at other stations as shown in Figure 6.6 to Figure 6.10. As mentioned in Chapter 5, the relative error is much dependent on the magnitude of the observed TEC. The small observed TEC in the first portion of Figure 6.11 results in larger relative error at FAIR station than other five stations.

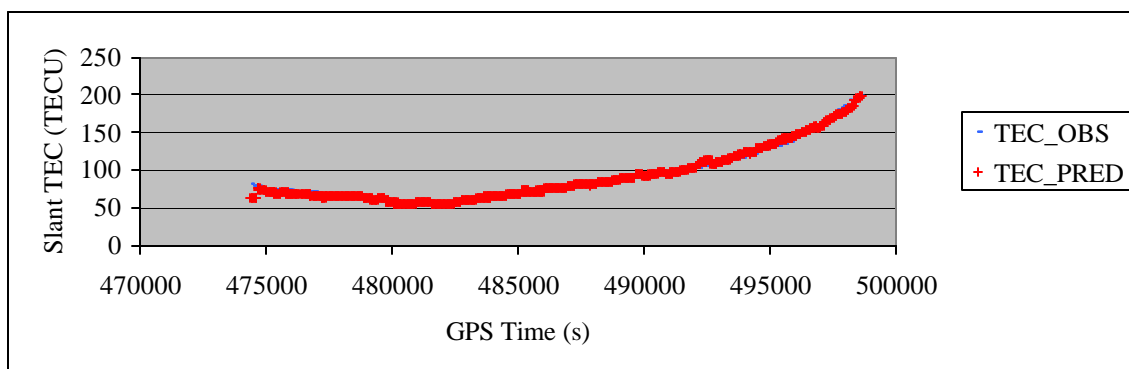


Figure 6.6 Comparison of Observed and Predicted TEC for PRN 02 at CARR Station on DOY 089 at 15° Cutoff and 5-min Prediction Interval
(VTEC RMS= 2.679 TECU, Relative Error = 3.45%)

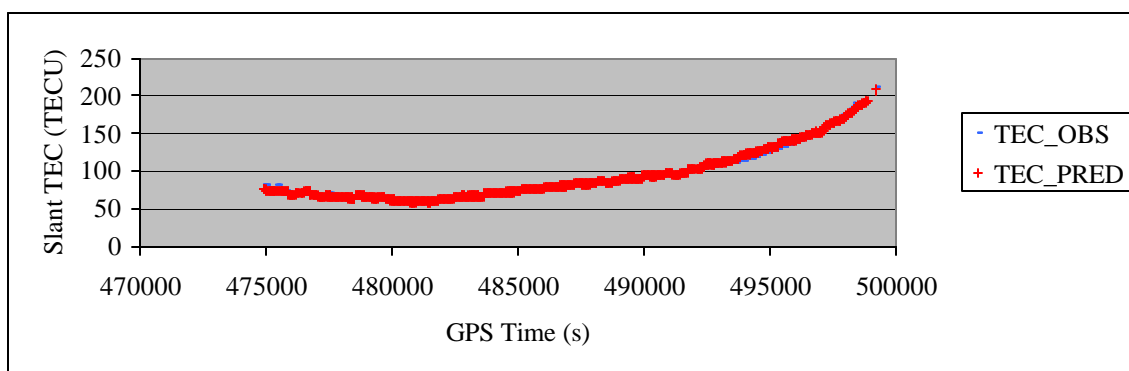


Figure 6.7 Comparison of Observed and Predicted TEC for PRN 02 at COSO Station on DOY 089 at 15° Cutoff and 5-min Prediction Interval
(VTEC RMS= 2.892 TECU, Relative Error = 3.57%)

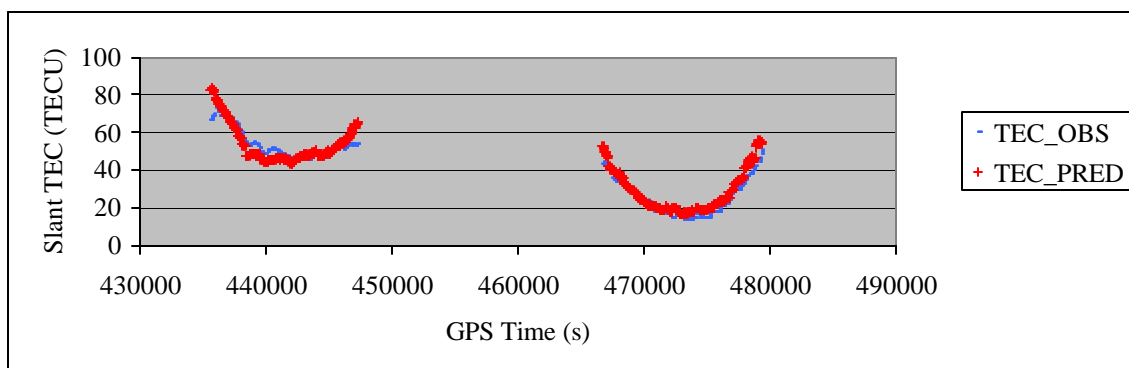


Figure 6.8 Comparison of Observed and Predicted TEC for PRN 03 at AMC2 Station on DOY 089 at 15° Cutoff and 5-min Prediction Interval
(VTEC RMS= 2.292 TECU, Relative Error = 11.80%)

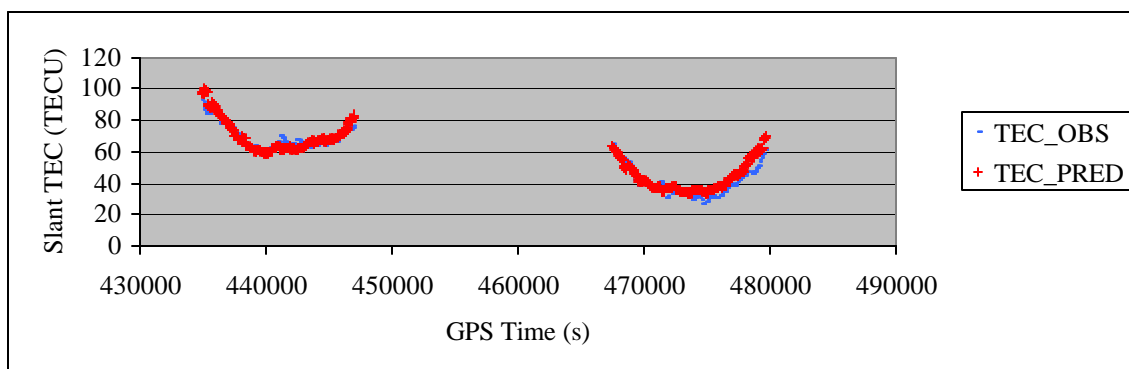


Figure 6.9 Comparison of Observed and Predicted TEC for PRN 03 at CASP Station on DOY 089 at 15° Cutoff and 5-min Prediction Interval
(VTEC RMS= 2.598 TECU, Relative Error = 8.24%)

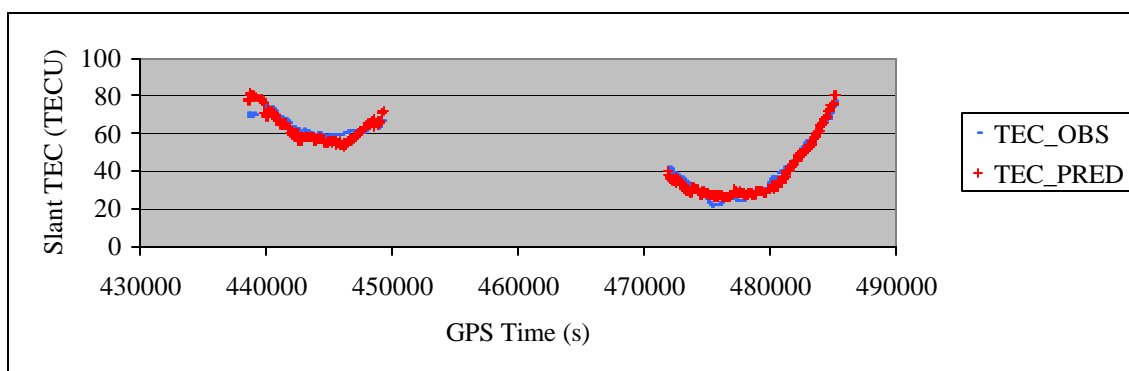


Figure 6.10 Comparison of Observed and Predicted TEC for PRN 31 at PRDS Station on DOY 089 at 15° Cutoff and 5-min Prediction Interval
(VTEC RMS= 2.018 TECU, Relative Error = 7.03%)

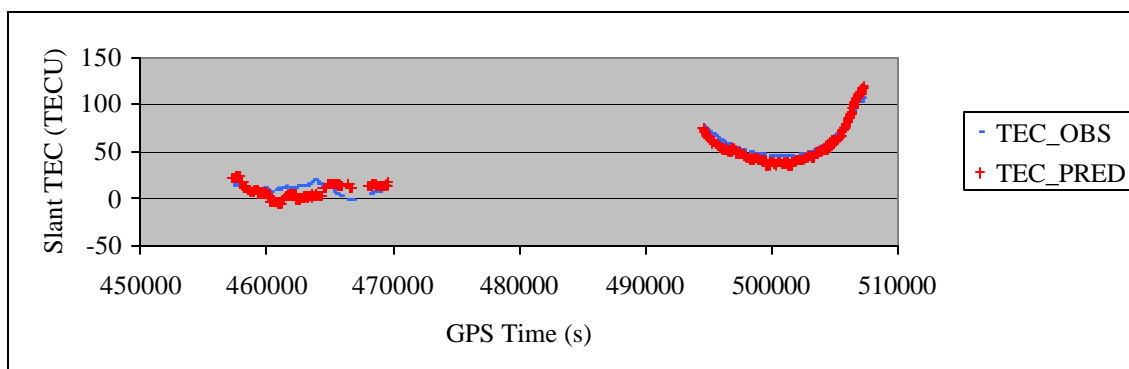


Figure 6.11 Comparison of Observed and Predicted TEC for PRN 04 at FAIR Station on DOY 089 at 15° Cutoff and 5-min Prediction Interval
(VTEC RMS= 5.005 TECU, Relative Error = 61.82%)

Table 6.4 Error Statistics for 5-min VTEC Prediction with Cutoff 15° on DOY 089

STATION	VTEC Error RMS (TECU)	Relative Error (%)
ALBH	3.060	16.63%
ALGO	3.258	20.94%
AMC2	3.067	16.97%
CARR	3.298	4.97%
CASP	3.199	8.34%
COSO	3.141	4.69%
DAM2	3.567	4.61%
DRAO	3.010	21.59%
FAIR	4.702	31.59%
FLIN	3.546	20.53%
HOLB	2.821	18.02%
HOPB	3.129	4.63%
KODK	5.039	8.69%
NEAH	3.137	5.80%
NRC1	3.551	5.10%
PRDS	3.853	10.29%
SCH2	4.571	21.12%
STJO	3.636	13.44%
USNO	3.247	12.34%
VNDP	3.316	4.25%
WHIT	3.861	6.21%
WSLR	2.861	19.80%
Mean	3.494	12.75%

Table 6.4 summarized the vertical TEC prediction errors and relative errors for all 22 GPS stations. It can be seen that most stations have an error at the level of 3.0~4.0 TECU. The mean RMS error for the entire wide area network is 3.494 TECU. As for the relative error in the network, it varies at different stations. Overall, the mean relative error for the network is 12.75%. Table 6.4 illustrates that 10 of 22 stations have a relative error less than 10.0%. Among the 22 stations, 21 of them have a relative error less than or about 20.0%. The FAIR station has the biggest relative error among all stations that is equal to 31.59%.

Besides the above TEC comparisons, another comparison test is conducted at two independent stations whose GPS data are not included in the ionospheric modeling. First, the DRAO station is selected as the test station and the ionospheric model is constructed using only other 21 stations. The ionospheric TEC at DRAO station is predicted in each session. The 5-min predicted and observed TEC for satellite PRN 31 and PRN 03, which have the longest time span of TEC observation at DRAO station, are compared and shown in Figure 6.12 and Figure 6.13, respectively.

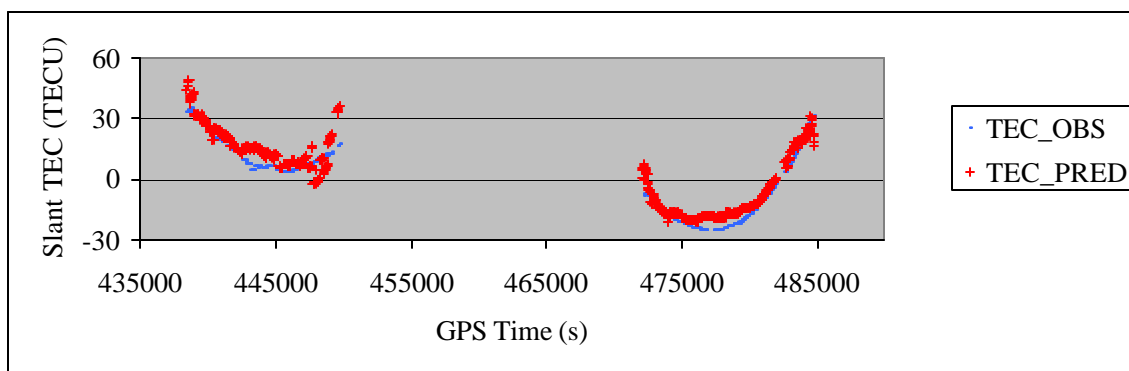


Figure 6.12 Comparison of Observed and Predicted TEC for PRN 31 at DRAO Station on DOY 089 at 15° Cutoff and 5-min Prediction Interval
(VTEC RMS= 3.367 TECU, Relative Error = 47.25%)

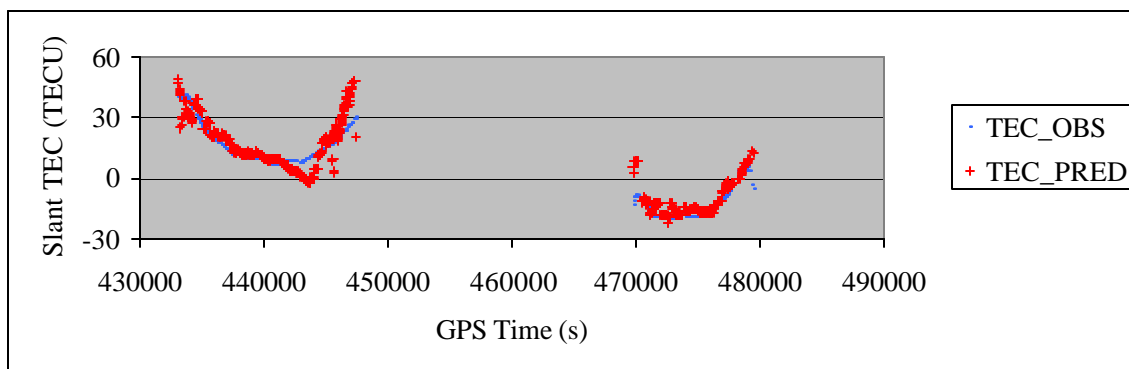


Figure 6.13 Comparison of Observed and Predicted TEC for PRN 03 at DRAO Station on DOY 089 at 15° Cutoff and 5-min Prediction Interval
(VTEC RMS= 3.272 TECU, Relative Error = 36.14%)

The results presented in Figure 6.12 and Figure 6.13 show that the predicted TEC data have a good agreement with the observed TEC data. The vertical RMS errors for the two

satellites are 3.367 TECU and 3.272 TECU, respectively. The relative errors for the satellites however are significant, 47.25% and 36.14%, respectively. This is caused by the extremely high relative errors at some epochs. For instance, during GPS time 443130~444540 s, the observed TEC are very small, having values of only several TECU. But the slant prediction errors are several times larger than the observed slant TEC values. Thus the relative errors at these epochs are several hundred percent. The mean relative error for that satellite therefore becomes large owing to large relative errors at those epochs. If considering the prediction errors for all satellites, the statistic vertical RMS error is 5.007 TECU at DRAO station and its relative error is 34.21%. Compared to the previous prediction results at DRAO station presented in Table 6.4 where the GPS data at DRAO station are included in the ionospheric modeling, the predictions without including DRAO station in ionospheric modeling are 1.997 TECU greater in the vertical TEC RMS error and 12.62% higher in the relative error. As already stated in previous sections, the degradation of the ionospheric prediction accuracy may attribute to the reduced amount of GPS measurements in the ionospheric modeling and the elimination of the correlation between the GPS data used for ionospheric modeling and ionospheric prediction.

Another test is conducted at station DAM2. Similar to the analysis for DRAO station, the prediction results are compared between the predicted and observed TEC and presented in Figure 6.14 and Figure 6.15. The two figures show that the predicted TEC for PRN 02 and PRN 27 have good agreements with observed TEC data except a portion of data during the period of GPS time 466650~470100 s for PRN 27, where the predicted TEC have larger discrepancies with respect to the observed TEC data than other portions. One reason that could be contributing to the large discrepancies is that this satellite is in rising period, during which larger multipath and noise effect on GPS measurements are expected compared to satellites in high elevation. A second reason might be the quality of the GPS measurements acquired during that period of time. An examination of the observed TEC data indicates that the observed TEC changes over time are not as smooth as other periods, which experience some fluctuations. Such an irregular variation was not

present in TEC observations during other time periods. The vertical RMS error is 3.747 TECU for PRN 02 satellite and 4.016 TECU for PRN 27 satellite. The relative errors for the two satellites are 5.02% and 6.44%, respectively. For all tracked satellites at DAM2 station, the vertical TEC RMS error is 5.784 TECU and the relative error is 7.51%. Compared to previous prediction results shown in Table 6.4 at DAM2 station, the prediction error without including DAM2 station in ionospheric modeling is 2.217 TECU higher in the vertical TEC RMS error and 2.90% higher in the relative error than that when DAM2 station was included. The discrepancy in the vertical TEC RMS error is quite comparable to that at DRAO station.

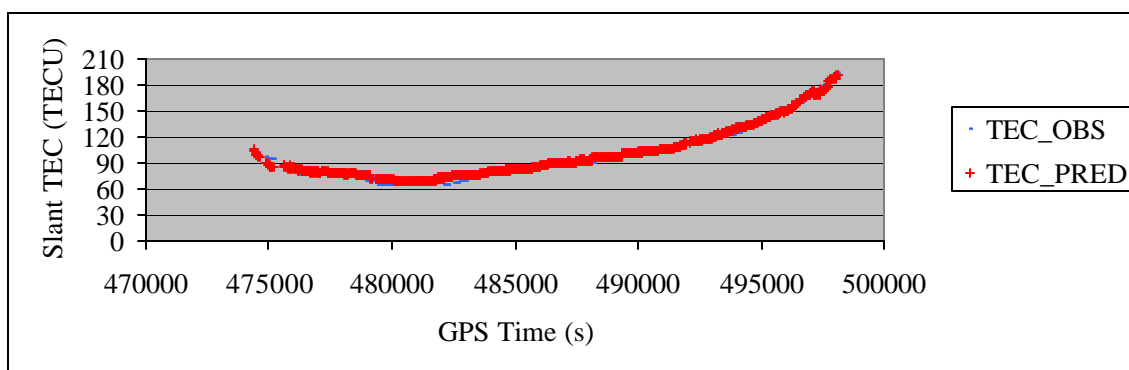


Figure 6.14 Comparison of Observed and Predicted TEC for PRN 02 at DAM2 Station on DOY 089 at 15° Cutoff and 5-min Prediction Interval
(VTEC RMS= 3.747 TECU, Relative Error = 5.02%)

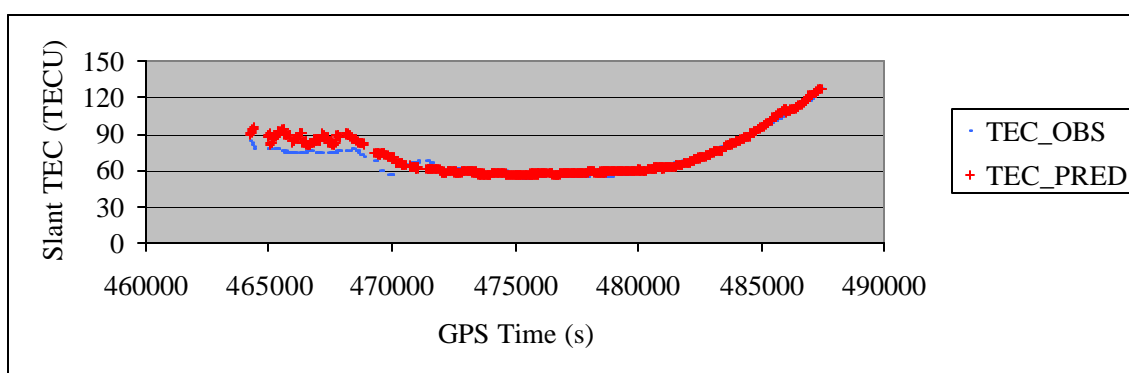


Figure 6.15 Comparison of Observed and Predicted TEC for PRN 27 at DAM2 Station on DOY 089 at 15° Cutoff and 5-min Prediction Interval
(VTEC RMS= 4.016 TECU, Relative Error = 6.44%)

6.3.1.1.2 Results on ionosphere disturbed day DOY 090

The above subsection presents the TEC prediction results obtained on an ionosphere quiet day. The following results are obtained on an ionospherically disturbed day. The TEC data in Figure 6.16 to Figure 6.21 show that the disagreements between the predicted and observed TEC data are larger than those on DOY 089. During the 24-hour period on March 31, 2001, all the Kp index values were larger than the Kp values on March 30, 2001. Therefore, it is possible the prediction errors on March 31, 2001 will demonstrate a larger value than the previous quiet day, in particular during the period from GPS time 529200 s to 550800 s, when the Kp index values reached 9.

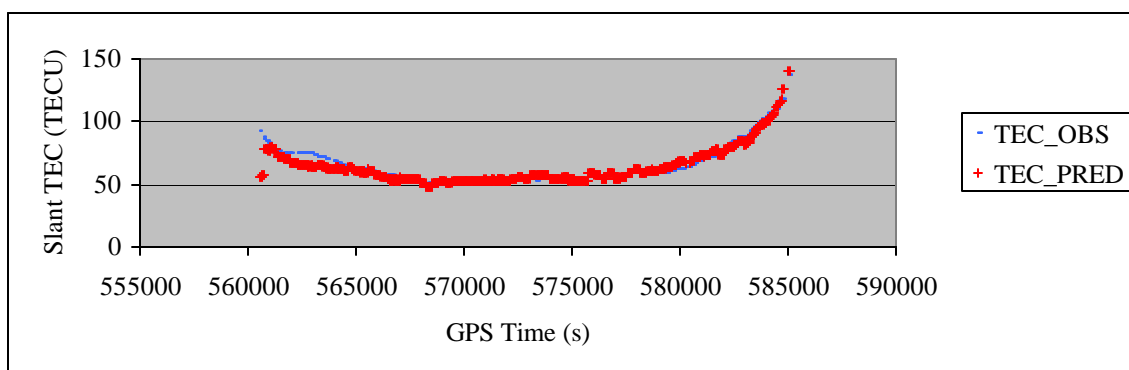


Figure 6.16 Comparison of Observed and Predicted TEC for PRN 02 at CARR Station on DOY 090 at 15° Cutoff and 5-min Prediction Interval
(VTEC RMS= 2.719 TECU, Relative Error = 4.85%)

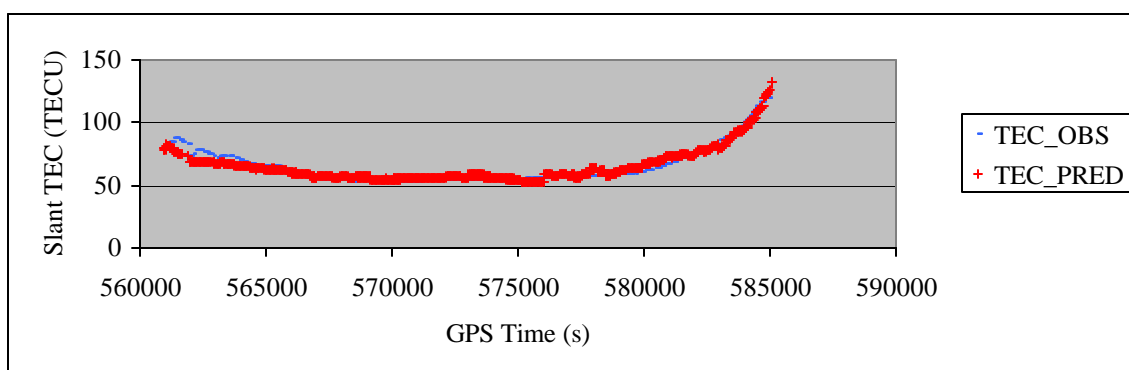


Figure 6.17 Comparison of Observed and Predicted TEC for PRN 02 at COSO Station on DOY 090 at 15° Cutoff and 5-min Prediction Interval
(VTEC RMS= 2.817 TECU, Relative Error = 5.35%)

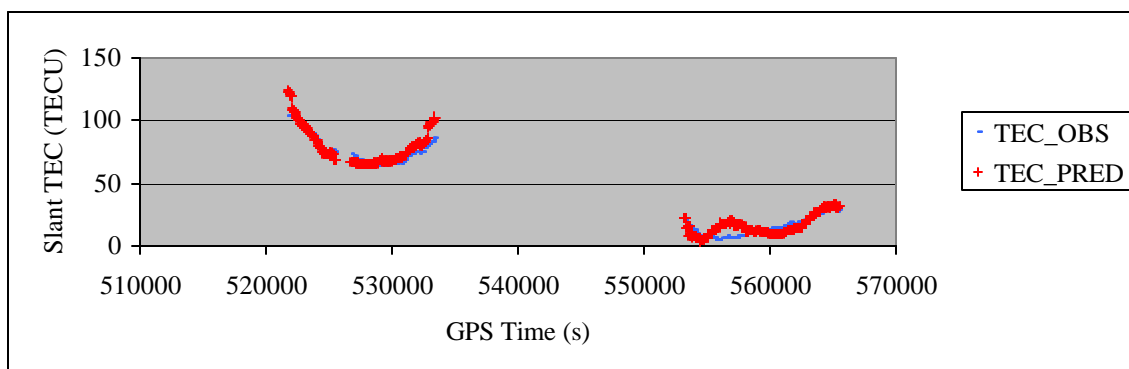


Figure 6.18 Comparison of Observed and Predicted TEC for PRN 03 at AMC2 Station on DOY 090 at 15° Cutoff and 5-min Prediction Interval
(VTEC RMS= 3.209 TECU, Relative Error = 32.88%)

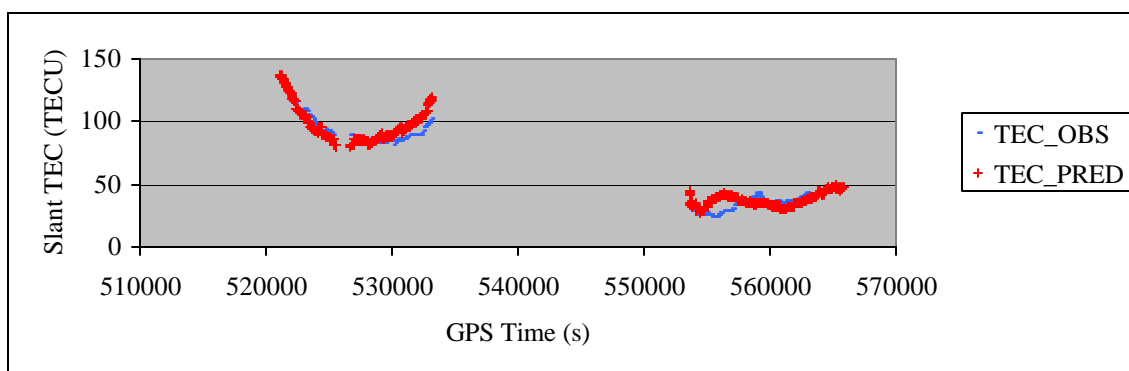


Figure 6.19 Comparison of Observed and Predicted TEC for PRN 03 at CASP Station on DOY 090 at 15° Cutoff and 5-min Prediction Interval
(VTEC RMS= 3.506 TECU, Relative Error = 10.92%)

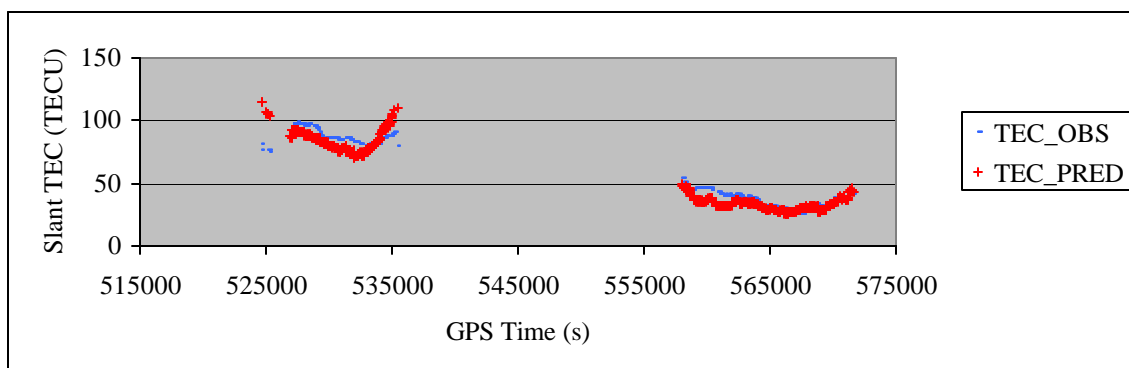


Figure 6.20 Comparison of Observed and Predicted TEC for PRN 31 at PRDS Station on DOY 090 at 15° Cutoff and 5-min Prediction Interval
(VTEC RMS= 3.539 TECU, Relative Error = 9.02%)

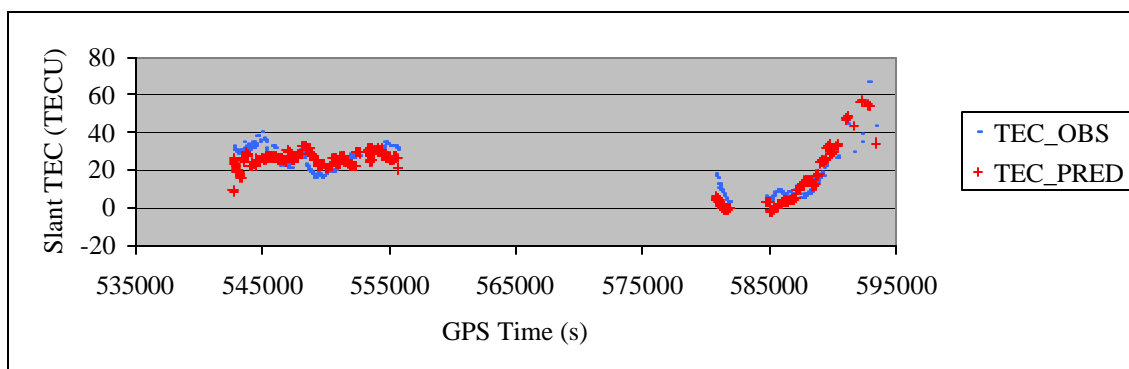


Figure 6.21 Comparison of Observed and Predicted TEC for PRN 04 at FAIR Station on DOY 090 at 15° Cutoff and 5-min Prediction Interval
(VTEC RMS= 3.734 TECU, Relative Error = 34.09%)

Table 6.5 Error Statistics for 5-min VTEC Prediction with Cutoff 15° on DOY 090

STATION	VTEC Error RMS (TECU)	Relative Error (%)
ALBH	4.588	29.17%
ALGO	5.595	29.66%
AMC2	4.692	29.76%
CARR	4.064	7.54%
CASP	5.369	13.78%
COSO	4.194	7.61%
DAM2	4.695	7.21%
DRAO	4.568	51.90%
FAIR	4.513	47.88%
FLIN	6.124	34.29%
HOLB	4.090	23.46%
HOPB	4.019	7.07%
KODK	4.139	7.78%
NEAH	4.597	8.23%
NRC1	5.705	8.12%
PRDS	5.750	13.37%
SCH2	4.512	26.80%
STJO	4.661	31.69%
USNO	5.957	32.31%
VNDP	4.458	6.81%
WHIT	4.169	7.08%
WSLR	4.205	18.39%
Mean	4.757	20.45%

Table 6.5 shows the ionospheric prediction errors for all 22 stations using the Scheme 1 for DOY 090. It can be seen that the prediction RMS errors on DOY 090 are higher than those in the previous day as shown in Table 6.4. In Table 6.4, the VTEC prediction errors range between 3.0~4.0 TECU while in Table 6.5 the VTEC prediction errors vary from 4.0 to 5.0 TECU. Among 22 stations, 16 of them have an RMS error in the range of 4.0~5.0 TECU. The other 6 stations have errors between 5.0~6.0 TECU except FLIN station which is slightly greater than 6.0 TECU. In terms of the mean RMS error, it is 3.494 TECU for the network on the previous ionosphere quiet day. While on the disturbed day, the mean RMS error is 4.757 TECU, which has an increase of 1.263 TECU.

As to relative error, Table 6.5 indicates that 9 out of the 22 stations have a relative error less than 10.0%. Most stations, 17 of 22 stations, have a relative error below 30.0%. The mean relative error on DOY 090 is 20.45% while it is 12.75% on DOY 089. By comparing the two days' results, the ionospheric disturbance effects on ionospheric modeling can be immediately assessed. During time periods with increased ionospheric activities, the ionosphere variations become more unpredictable. Subsequently ionospheric modeling becomes more difficult and the TEC prediction will consequently become less accurate. Note that the ionospheric activities presented on DOY 090 were one of the worst cases in solar maximum years and such a highly disturbed ionospheric condition is actually not frequently met. Overall the modeling results still demonstrate reasonably good accuracy even under such a severe ionospheric environment. The mean relative error is 20.45%, which means that the 79.55% ionospheric effects can be recovered by the TEC prediction data.

Presented in Figure 6.22 to Figure 6.25 are the TEC prediction results where the data from DRAO and DAM2 stations are excluded from ionospheric modeling.

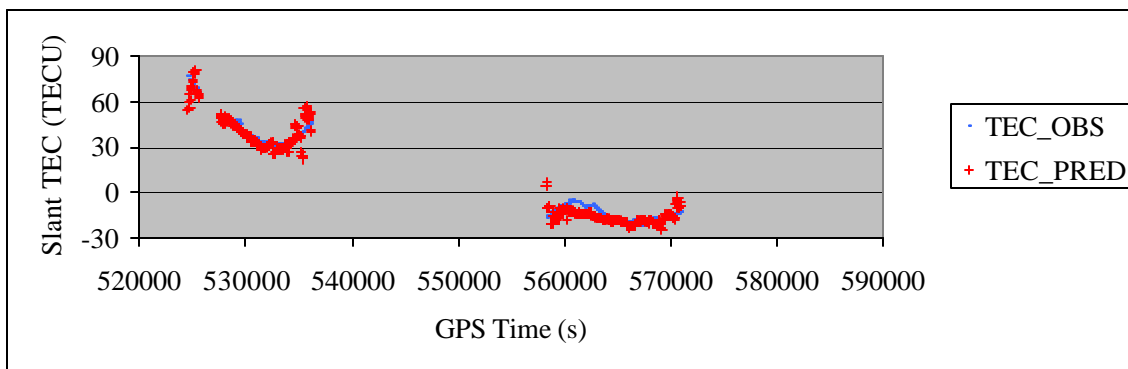


Figure 6.22 Comparison of Observed and Predicted TEC for PRN 31 at DRAO Station on DOY 090 at 15° Cutoff and 5-min Prediction Interval
(VTEC RMS= 2.340 TECU, Relative Error = 20.15%)

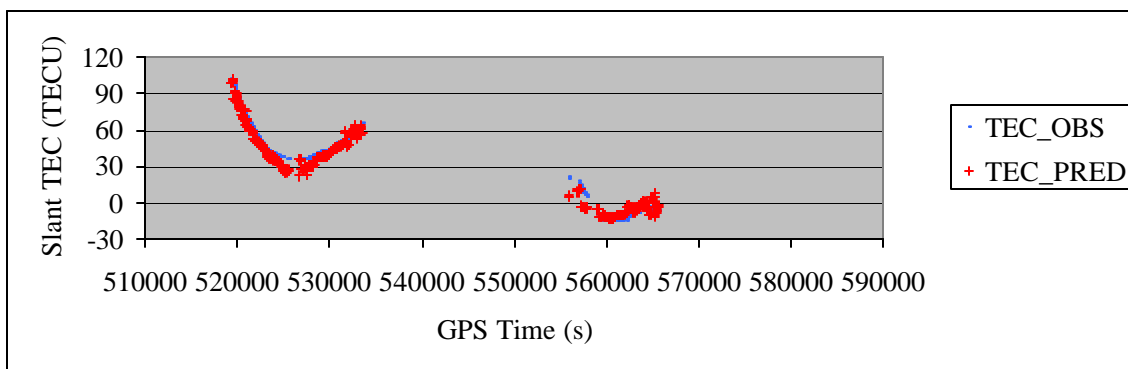


Figure 6.23 Comparison of Observed and Predicted TEC for PRN 03 at DRAO Station on DOY 090 at 15° Cutoff and 5-min Prediction Interval
(VTEC RMS= 3.250 TECU, Relative Error = 25.46%)

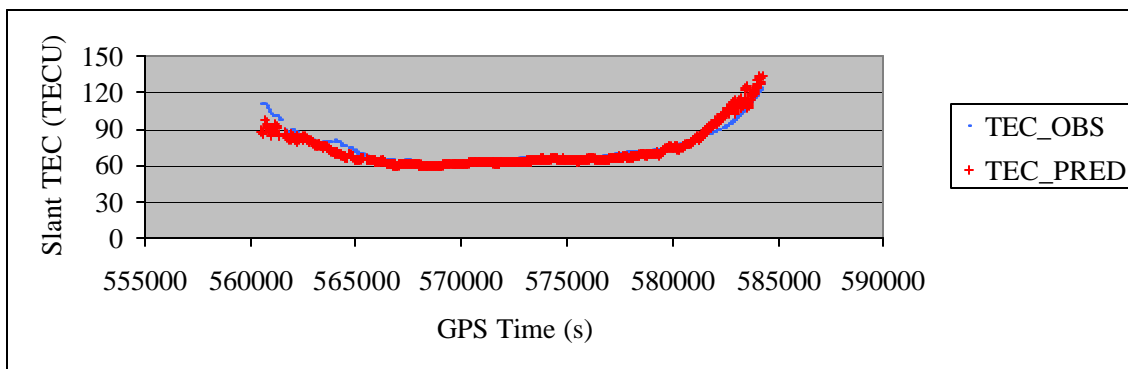


Figure 6.24 Comparison of Observed and Predicted TEC for PRN 02 at DAM2 Station on DOY 090 at 15° Cutoff and 5-min Prediction Interval
(VTEC RMS= 2.783 TECU, Relative Error = 3.75%)

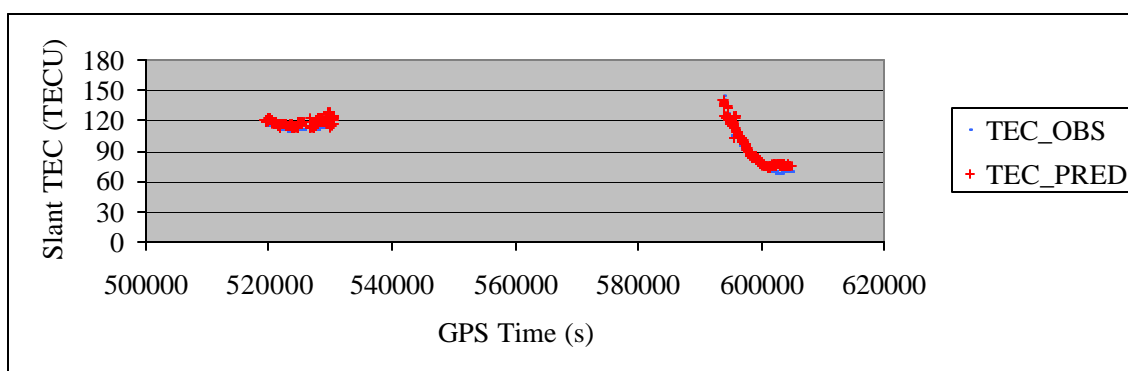


Figure 6.25 Comparison of Observed and Predicted TEC for PRN 17 at DAM2 Station on DOY 090 at 15° Cutoff and 5-min Prediction Interval
(VTEC RMS= 5.273 TECU, Relative Error = 6.90%)

The first test is to exclude GPS station DRAO, a station with a latitude 49.32°N that can be used to analyze the mid-latitude ionospheric activities. The second test is to exclude GPS station DAM2, with a latitude 34.33°N, for the analysis of low-latitude ionospheric activities. The results presented in Figure 6.22 to Figure 6.25 show that the predicted TEC values are in good agreement with the measured ones. At station DRAO, the relative errors for both PRN 31 and PRN 03 are over 20%. This is due to the small values of the TEC observations during GPS time 550000~570000 s. It can be seen that the TEC observations during that particular period are less than 30 TECU and at some epochs they are just several TECU. At those epochs, even a small prediction error will result in a large relative error due to small denominators in the relative error computation. However, the vertical TECU RMS error is not affected by the TEC observations. The RMS errors for both satellites are at the level of 2~3 TECU. Shown in Figure 6.24 and Figure 6.25 are the TEC comparison results for PRN 02 and PRN 17 at DAM2 station, which have the largest amount of TEC data among all the satellites. Figure 6.24 and Figure 6.25 show that the TEC observations are significantly larger than those at DRAO station. For PRN 02, the largest TEC value is about 130 TECU while it is about 150 TECU for PRN 17. Therefore, the relative error at DAM2 station is much smaller, ranging from 3.75%~6.90%. The VTEC RMS error is at the level of 2.8~5.3 TECU.

The above results show the prediction accuracy only for two satellites that have the largest amount of TEC observation data. If the prediction errors for all the satellites are considered, the DRAO station has a VTEC RMS error of 5.238 TECU and DAM2 has a VTEC RMS error of 5.857 TECU. The relative error for all the satellites at DRAO station is 46.30% and it is 8.09% at DAM2 station. Compared to the results shown in Table 6.5, it shows that the TEC predictions at DRAO station have a degradation of 0.670 TECU in VTEC RMS error compared to the predictions at DRAO station whose data are included for ionospheric modeling as summarized in Table 6.5. At DAM2 station, the prediction errors are 1.162 TECU higher in VTEC RMS error and 0.88% higher in the relative error than the case when the DAM2 station is included in the ionospheric modeling, as shown in Table 6.5.

6.3.1.2 Results of Scheme 2 (15°, 10 min)

In this scheme, the elevation cutoff angle used is still 15° but the prediction interval is increased to 10 minutes.

6.3.1.2.1 Results on ionosphere quiet day DOY 089

Shown in Figure 6.26 to Figure 6.31 are the TEC comparison results for DOY 089 at the six selected stations. Similar to the results of DOY 089 in Scheme 1, the two sets of TEC data agree very well at the CARR and COSO stations. The predicted TEC data at AMC2, CASP and PRDS stations appear to follow the TEC change pattern of the observed TEC quite well although the agreements on these three stations are not as good as those at CARR and COSO stations. The TEC predictions at the high latitude station, FAIR, apparently have the largest disagreements with the observed TEC data. Compared to the results of DOY 089 in Scheme 1 shown in Figure 6.6 to Figure 6.11, the VTEC prediction errors become larger than those in Scheme 1. The only exception is the CASP station where the VTEC prediction error is 0.113 TECU which is smaller than the error in Scheme 1. The overall results indicate that with the increase of the prediction interval, the accuracies of the prediction will experience certain degree of degradation.

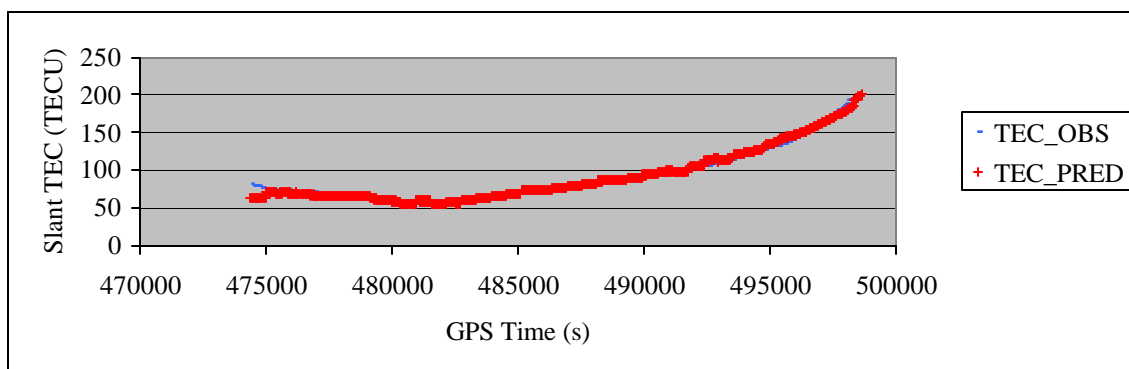


Figure 6.26 Comparison of Observed and Predicted TEC for PRN 02 at CARR Station on DOY 089 at 15° Cutoff and 10-min Prediction Interval
(VTEC RMS= 2.904 TECU, Relative Error = 3.79%)

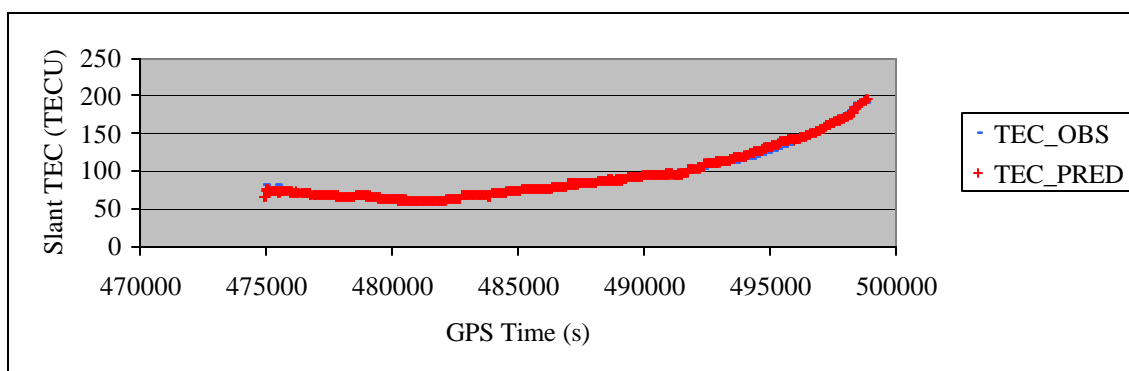


Figure 6.27 Comparison of Observed and Predicted TEC for PRN 02 at COSO Station on DOY 089 at 15° Cutoff and 10-min Prediction Interval
(VTEC RMS= 3.199 TECU, Relative Error = 3.87%)

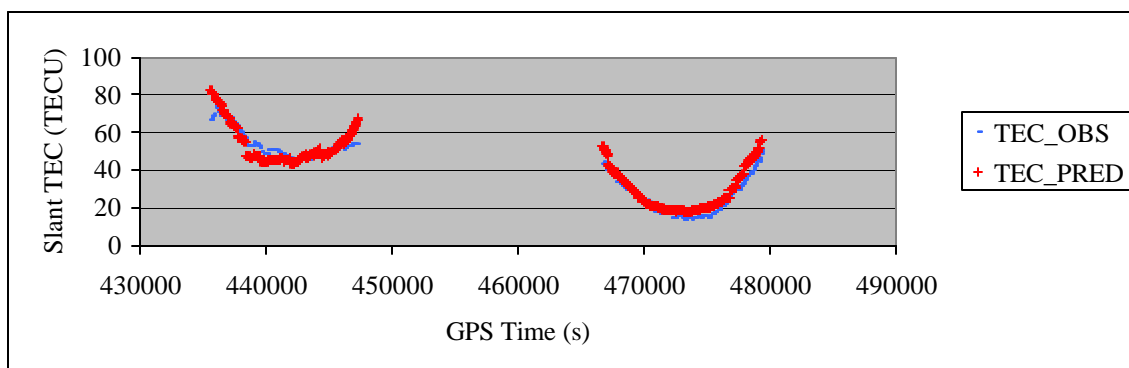


Figure 6.28 Comparison of Observed and Predicted TEC for PRN 03 at AMC2 Station on DOY 089 at 15° Cutoff and 10-min Prediction Interval
(VTEC RMS= 2.379 TECU, Relative Error = 12.45%)

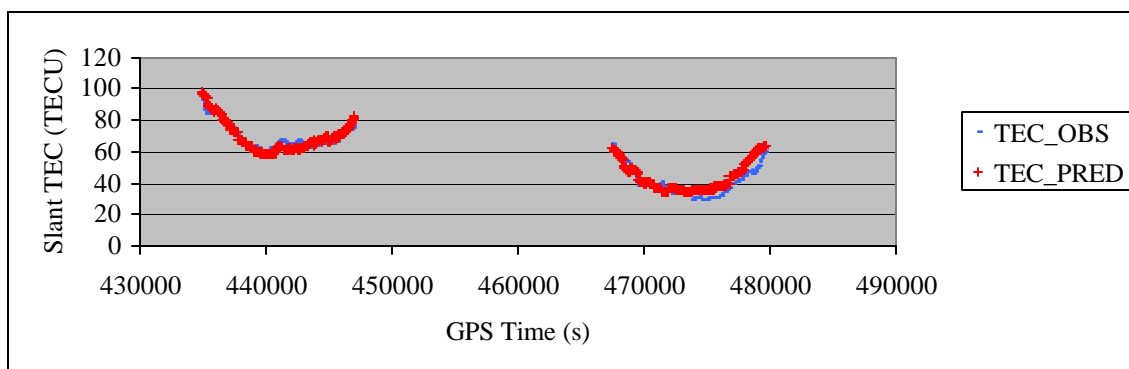


Figure 6.29 Comparison of Observed and Predicted TEC for PRN 03 at CASP Station on DOY 089 at 15° Cutoff and 10-min Prediction Interval
(VTEC RMS= 2.485 TECU, Relative Error = 8.18%)

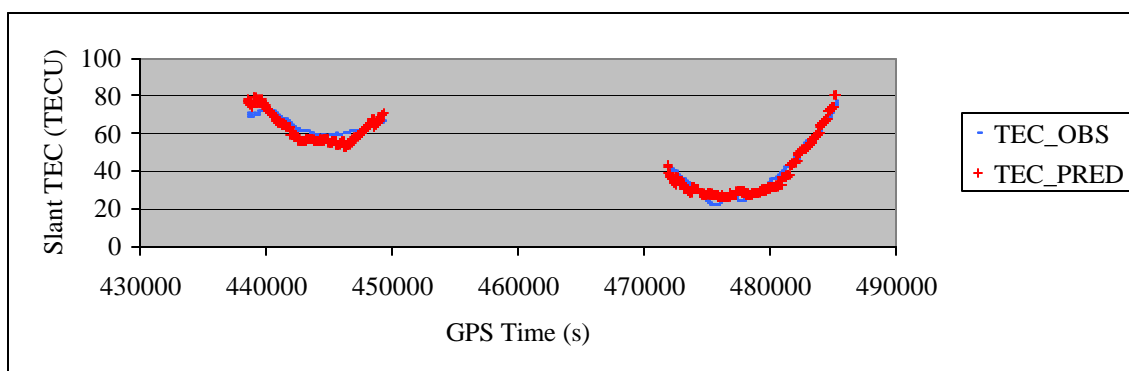


Figure 6.30 Comparison of Observed and Predicted TEC for PRN 31 at PRDS Station on DOY 089 at 15° Cutoff and 10-min Prediction Interval
(VTEC RMS= 2.033 TECU, Relative Error = 6.89%)

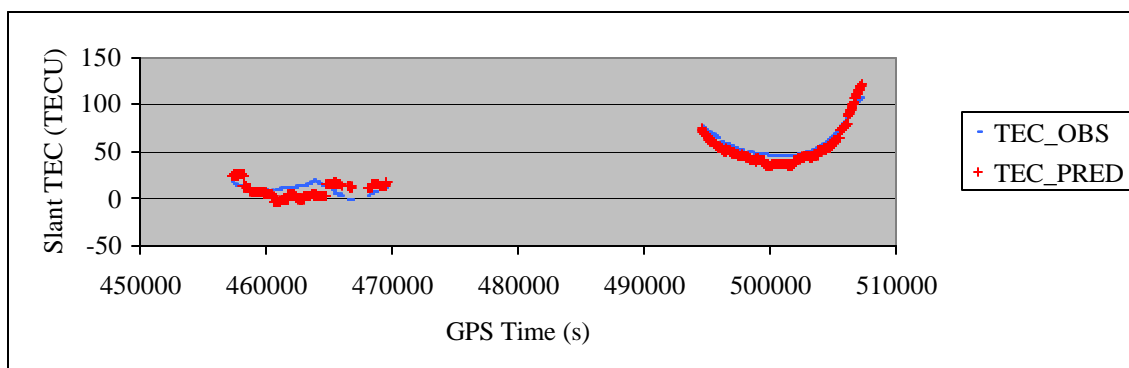


Figure 6.31 Comparison of Observed and Predicted TEC for PRN 04 at FAIR Station on DOY 089 at 15° Cutoff and 10-min Prediction Interval
(VTEC RMS= 5.287 TECU, Relative Error = 64.92%)

Table 6.6 summarizes the VTEC prediction errors and relative errors at all stations for DOY 089 using Scheme 2. It can be seen that the VTEC prediction errors at most stations have an RMS error in the range of 3.0~4.0 TECU. Only three stations have a prediction error larger than 4.0 TECU but the largest error is still less than 5.2 TECU. The relative error changes from station by station, in a range of a few percent to the largest value of 31.51%. Table 6.6 indicates that 10 out of the 22 stations are less than 10.0%. Almost all stations have a relative error less than or just slightly larger than 20.0%. The mean VTEC prediction error of Scheme 2 on DOY 089 is 3.558 TECU, which is 0.064 TECU larger than the mean value on the same day using Scheme 1. The relative error of this scheme is also slightly higher than Scheme 1 by 0.21%.

Table 6.6 Error Statistics for 10-min VTEC Prediction with Cutoff 15° on DOY 089

STATION	VTEC Error RMS (TECU)	Relative Error (%)
ALBH	3.138	16.80%
ALGO	3.260	20.99%
AMC2	3.091	17.00%
CARR	3.374	5.08%
CASP	3.200	8.22%
COSO	3.208	4.77%
DAM2	3.604	4.64%
DRAO	3.079	21.76%
FAIR	4.840	31.51%
FLIN	3.627	20.66%
HOLB	2.911	18.76%
HOPB	3.171	4.75%
KODK	5.170	8.94%
NEAH	3.163	5.82%
NRC1	3.586	5.15%
PRDS	3.861	10.49%
SCH2	4.700	21.67%
STJO	3.706	13.89%
USNO	3.270	12.70%
VNDP	3.374	4.36%
WHIT	4.007	6.50%
WSLR	2.939	20.57%
Mean	3.558	12.96%

Like Scheme 1, ionospheric TEC predictions are also performed at two independent stations DRAO and DAM2, whose data are not included for ionospheric modeling. The first test is performed at DRAO station. The TEC prediction results at DRAO station are obtained from each session's modeling based on GPS measurements from other 21 GPS stations. The comparison of the TEC predictions and observations for two satellites corresponding to the longest signal tracking are presented in Figure 6.32 and Figure 6.33. It can be seen that the 10-min TEC predictions still have a good agreement with the TEC observations. The vertical RMS errors for these two satellites are 3.249 TECU and 3.477 TECU, respectively. The relative errors are at a level of 37%~47% due to larger relative error contributions at some epochs. In Figure 6.33, for example, the observed TEC are at the level of several TECU during GPS time 443160~443700 s and the prediction errors are even larger than the observed TEC at these epochs. Thus the relative errors for these epochs are larger than 100%. The mean relative error for PRN 03 therefore becomes as large as 37.17% due to the contributions from these epochs with large relative errors. The statistic shows that the vertical TEC RMS error for all the satellites at DRAO station is 5.056 TECU and the relative error is 34.84%. The prediction results at DRAO station are compared to those results shown in Table 6.6 where the DRAO station is included in tomographic modeling. It shows that the predictions without including DRAO station are 1.977 TECU larger in the VTEC RMS error and 13.08% higher in the relative error than the results that have included DRAO station during ionospheric modeling. This indicates that the amount of GPS measurements that are available for tomographic modeling has an impact on the ionospheric prediction results and the correlation between the TEC observations used for ionospheric modeling and the data used for ionospheric prediction also has an influence on the prediction accuracy.

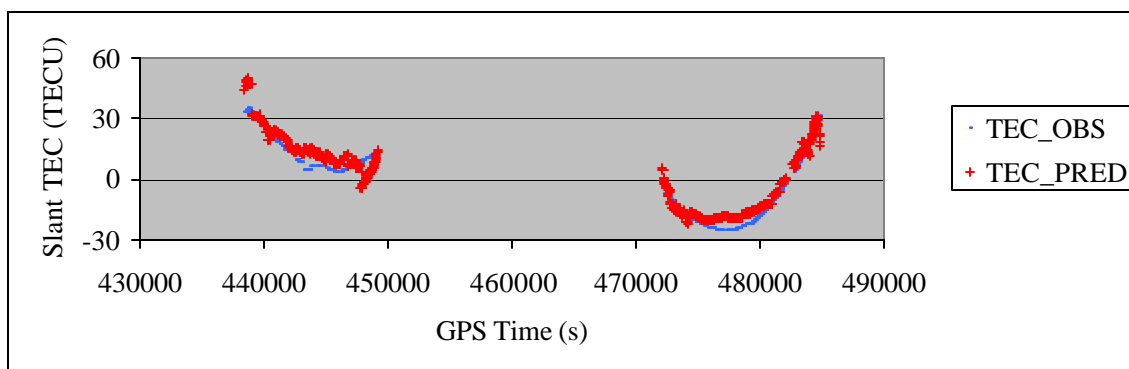


Figure 6.32 Comparison of Observed and Predicted TEC for PRN 31 at DRAO Station on DOY 089 at 15° Cutoff and 10-min Prediction Interval
(VTEC RMS= 3.249 TECU, Relative Error = 47.54%)

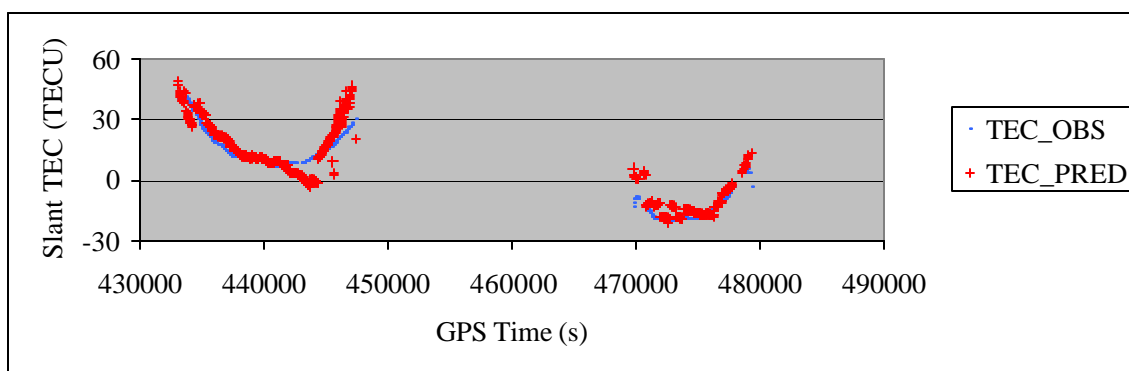


Figure 6.33 Comparison of Observed and Predicted TEC for PRN 03 at DRAO Station on DOY 089 at 15° Cutoff and 10-min Prediction Interval
(VTEC RMS= 3.477 TECU, Relative Error = 37.17%)

Another test to evaluate the TEC prediction performance is performed at DAM2. Again, DAM2 is an excluded station. The comparison results at DAM2 station is illustrated by Figure 6.34 and Figure 6.35 for satellites PRN 02 and PRN 27. The two figures show that the predicted TEC data basically match with the TEC observations very well, except a short portion of data for PRN 27, which is very similar to the 5-min prediction case. For all satellites tracked at DAM2, the vertical RMS error is 5.828 TECU and the relative error is 7.55%. These results are 2.224 TECU and 2.91% higher respectively in terms of VTEC RMS error and relative error than the previous prediction results at DAM2 station

shown in Table 6.6, where the GPS data at DAM2 station are included in tomographic modeling.

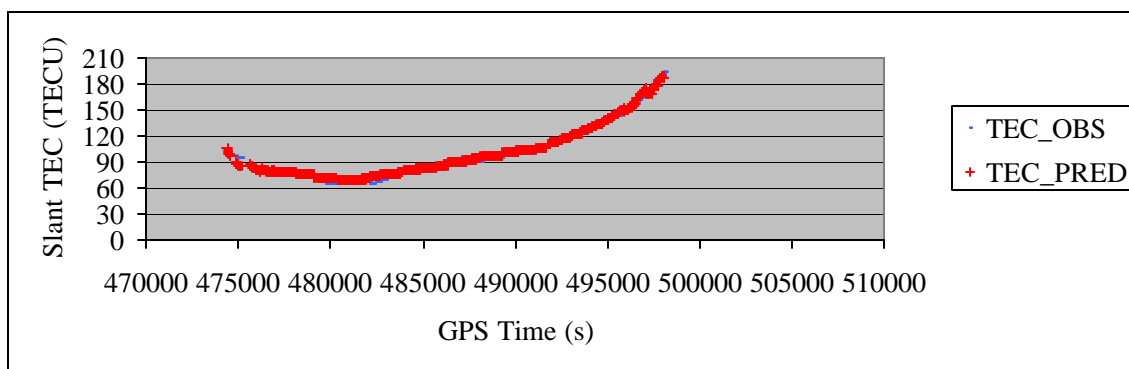


Figure 6.34 Comparison of Observed and Predicted TEC for PRN 02 at DAM2 Station on DOY 089 at 15° Cutoff and 10-min Prediction Interval
(VTEC RMS= 3.525 TECU, Relative Error = 4.66%)

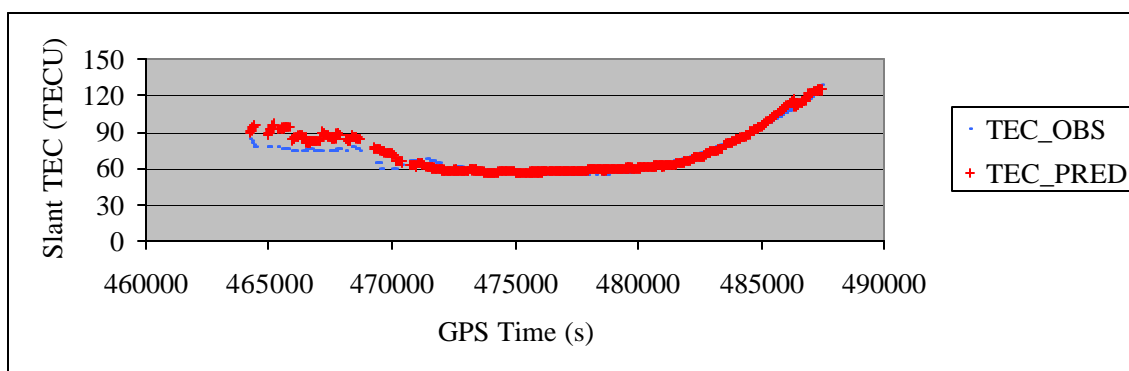


Figure 6.35 Comparison of Observed and Predicted TEC for PRN 27 at DAM2 Station on DOY 089 at 15° Cutoff and 10-min Prediction Interval
(VTEC RMS= 4.025 TECU, Relative Error = 6.59%)

6.3.1.2.2 Results on ionosphere disturbed day DOY 090

The TEC prediction results from Scheme 2 (15°, 10-min) on the ionospherically disturbed day DOY 090 are shown in Figure 6.36 to Figure 6.41. The predicted TEC data and observed TEC data are generally in good agreement with each other. Examining the receiver type used at these stations, it is found that AMC2, PRDS and FAIR stations used AOA Turborogue receivers (with different models SNR-12 and SNR-8100) while CARR, COSO and CASP stations used ASHTECH Z12 receivers. The ASHTECH Z12 are

semicodeless receivers and their tracking performances are superior to that of AOA Turborogue codeless receivers under stormy conditions, in terms of less cycle slips in the carrier phase measurements (Skone, 2001). Less cycle slips in carrier phase measurements implies the smoothed TEC measurements have better accuracies. In the comparison, the observed TEC data are also the smoothed results derived from GPS measurements. This means the observed TEC data at CARR, COSO and CASP station have better quality than those at AMC2, PRDS and FAIR stations. That is why the RMS values and relative errors at AMC2, PRDS and FAIR stations are much higher than other three stations, e.g. AMC2 with a relative error of 31.90% and FAIR having a relative error of 35.59%. Compared to the results of Scheme 1 (15° , 5-min) on the same day DOY 090, the results at four stations in this scheme have a higher VTEC prediction error than those in Scheme 1. The other two stations CARR and AMC2 show slightly better accuracy than Scheme 1 by 0.059 TECU and 0.032 TECU, respectively. This might be due to the effect of different smoothing time windows that have been used in data processing. In this scheme, the prediction interval is longer than Scheme 1 and the TEC smoothing time window is therefore longer than Scheme 1. The smoothing effects might be the reason for slightly better accuracies at CARR and AMC2 stations. But general speaking, the longer prediction interval usually causes larger prediction error in the predicted TEC data.

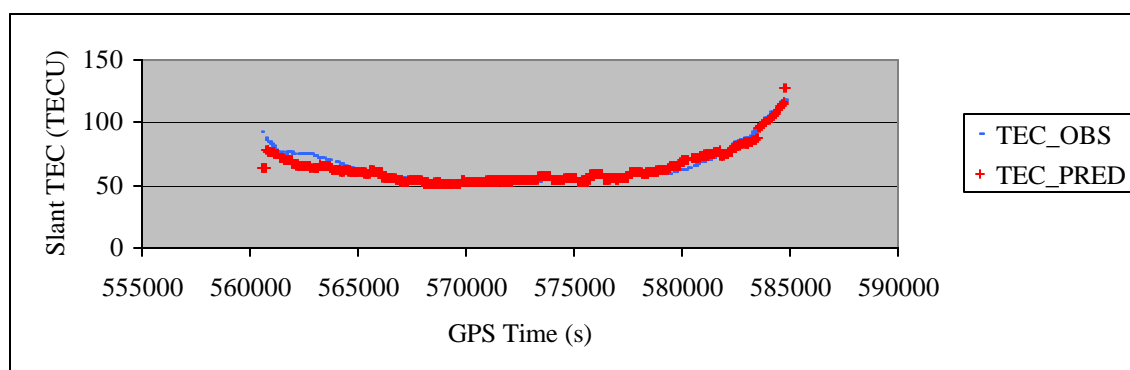


Figure 6.36 Comparison of Observed and Predicted TEC for PRN 02 at CARR Station on DOY 090 at 15° Cutoff and 10-min Prediction Interval
(VTEC RMS= 2.660 TECU, Relative Error = 4.85%)

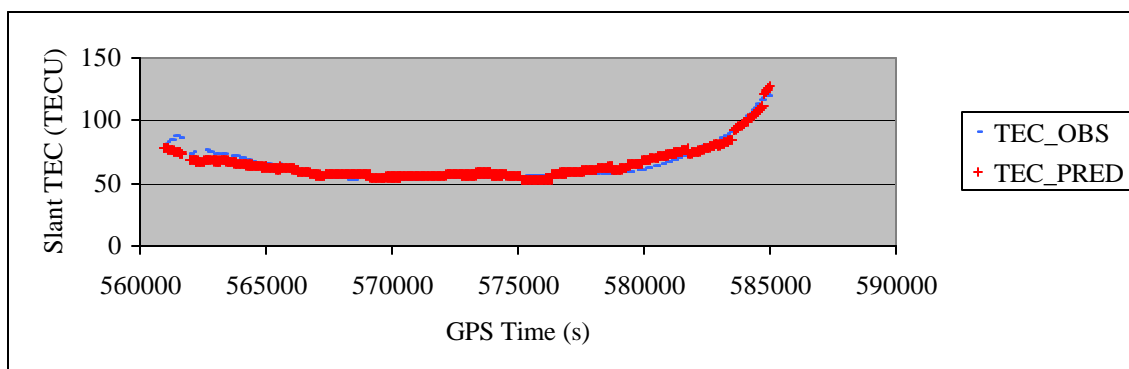


Figure 6.37 Comparison of Observed and Predicted TEC for PRN 02 at COSO Station on DOY 090 at 15° Cutoff and 10-min Prediction Interval
(VTEC RMS= 3.037 TECU, Relative Error = 5.87%)

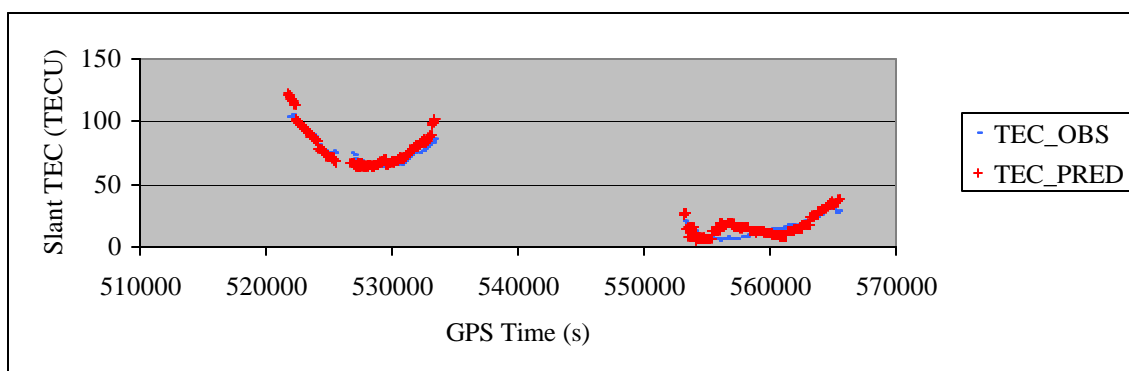


Figure 6.38 Comparison of Observed and Predicted TEC for PRN 03 at AMC2 Station on DOY 090 at 15° Cutoff and 10-min Prediction Interval
(VTEC RMS= 3.177 TECU, Relative Error = 31.90%)

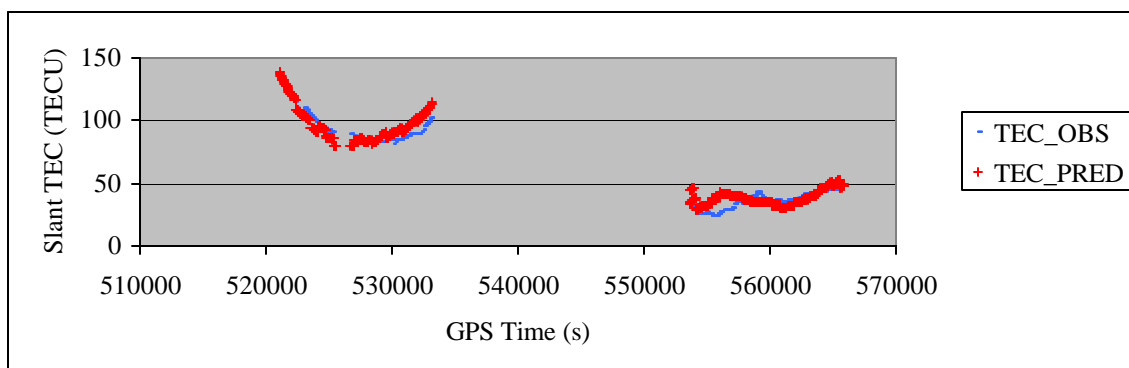


Figure 6.39 Comparison of Observed and Predicted TEC for PRN 03 at CASP Station on DOY 090 at 15° Cutoff and 10-min Prediction Interval
(VTEC RMS= 3.530 TECU, Relative Error = 11.82%)

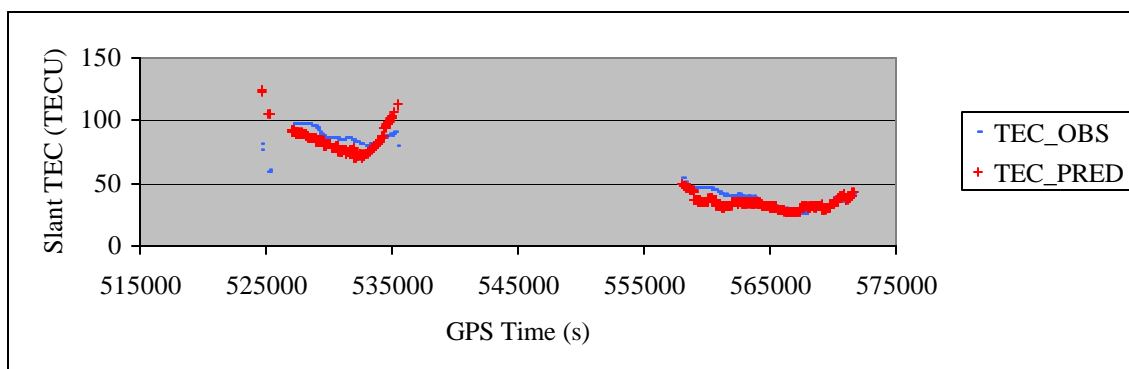


Figure 6.40 Comparison of Observed and Predicted TEC for PRN 31 at PRDS Station on DOY 090 at 15° Cutoff and 10-min Prediction Interval
(VTEC RMS= 3.860 TECU, Relative Error = 9.28%)

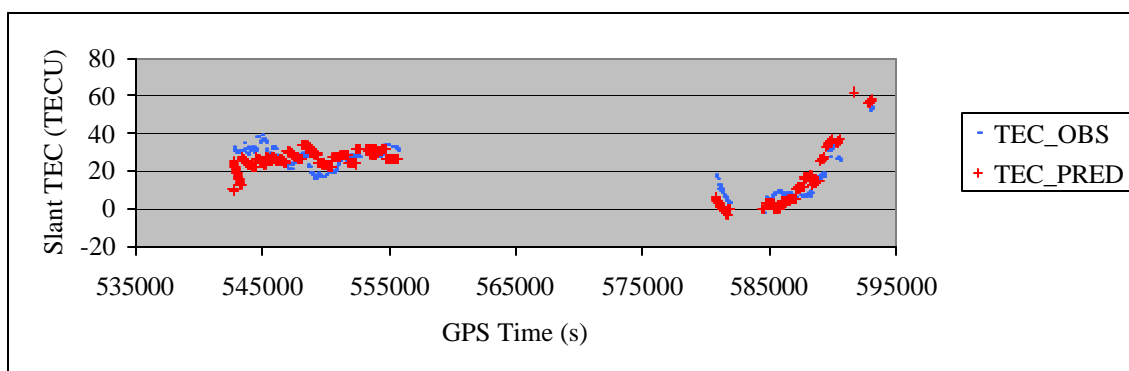


Figure 6.41 Comparison of Observed and Predicted TEC for PRN 04 at FAIR Station on DOY 090 at 15° Cutoff and 10-min Prediction Interval
(VTEC RMS= 4.119 TECU, Relative Error = 35.59%)

Table 6.7 summarizes the VTEC prediction errors and relative errors at all stations in the network. Most stations have a VTEC prediction error between 4.0~5.0 TECU. Table 6.7 shows that 16 out of the 22 stations have a VTEC prediction error less than 5.0 TECU. Only 6 stations have errors larger than 5.0 TECU in their VTEC prediction. The largest error is still bounded below 6.2 TECU. This is quite consistent with the results from Scheme 1 on DOY 090 as shown in Table 6.5. In terms of the mean value of VTEC prediction error, it is 4.874 TECU for this 10-min prediction scheme, which is slightly larger than the mean value 4.757 TECU shown in Table 6.5 for the 5-min scheme. As for relative error, 9 out of the 22 stations have a relative error less than 10.0% and 20 out of

the 22 stations less than or only slightly larger than 30.0%. Only two stations have a relative error around 50.0%. The mean relative error of this scheme is 21.19%, which is also a little higher than 20.45% shown in Table 6.5 for the 5-min prediction scheme. The statistics indicate that the 10-min prediction scheme has experienced a small degradation in VTEC prediction accuracy when compared to the shorter interval (5-min) prediction scheme.

Table 6.7 Error Statistics for 10-min VTEC Prediction with Cutoff 15° on DOY 090

STATION	VTEC Error RMS (TECU)	Relative Error (%)
ALBH	4.702	30.54%
ALGO	5.680	30.58%
AMC2	4.791	30.32%
CARR	4.154	7.69%
CASP	5.434	13.92%
COSO	4.256	7.74%
DAM2	4.745	7.33%
DRAO	4.690	54.28%
FAIR	4.813	50.54%
FLIN	6.111	34.93%
HOLB	4.278	24.56%
HOPB	4.099	7.16%
KODK	4.286	8.01%
NEAH	4.739	8.57%
NRC1	5.772	8.32%
PRDS	5.883	13.85%
SCH2	4.734	28.21%
STJO	4.873	33.36%
USNO	6.000	32.79%
VNDP	4.512	6.90%
WHIT	4.303	7.33%
WSLR	4.365	19.27%
Mean	4.874	21.19%

Similar to ionospheric quiet day DOY 089, the ionospheric predictions are also performed at two independent stations DRAO and DAM2 on the ionospheric disturbed day 090. The TEC prediction and comparison results for satellites PRN 31 and PRN 03 at DRAO station are depicted in Figure 6.42 and Figure 6.43. It shows that under the

ionospheric disturbed condition, the predictions still have good agreements with the TEC observations. The vertical RMS error for PRN 31 and PRN 03 are 2.469 TECU and 3.879 TECU, respectively. Their relative errors are 21.22% and 31.49%, respectively. Including all the tracked satellites, the DRAO station has a vertical TEC prediction RMS error of 5.382 TECU and a relative error of 48.21%. The TEC predictions show a degradation of 0.692 TECU in vertical TEC compared to TEC predictions at DRAO station shown in Table 6.7 whose data are included in ionospheric modeling. For DAM2 station, the TEC predictions for PRN 02 and PRN 17 are illustrated. The results show that their vertical TEC prediction errors are 3.333 TECU and 5.513 TECU, respectively. The relative errors are 4.16% and 7.21%. Including all the satellites, the station's vertical TEC RMS error is 6.067 TECU and its relative error is 8.46%. These two accuracy indicators are also compared to those shown in Table 6.7. The comparison indicates the predictions without the DAM2 station in ionospheric modeling have a greater vertical TEC RMS error by 1.322 TECU and a higher relative error by 1.13% than the predictions in Table 6.7 where the station is included in tomographic modeling.

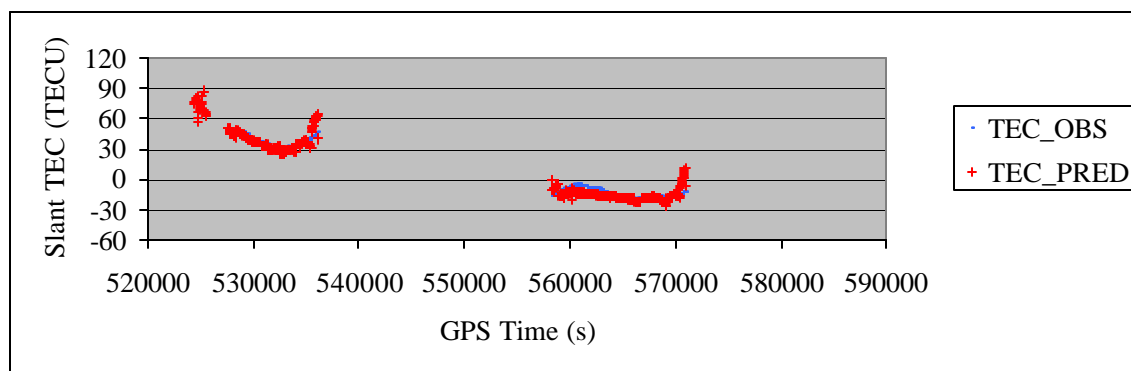


Figure 6.42 Comparison of Observed and Predicted TEC for PRN 31 at DRAO Station on DOY 090 at 15° Cutoff and 10-min Prediction Interval
(VTEC RMS= 2.469 TECU, Relative Error = 21.22%)

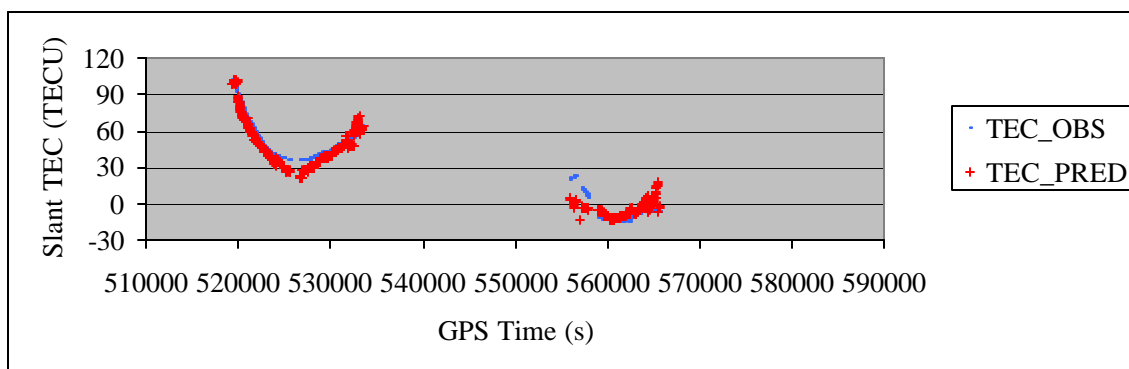


Figure 6.43 Comparison of Observed and Predicted TEC for PRN 03 at DRAO Station on DOY 090 at 15° Cutoff and 10-min Prediction Interval
(VTEC RMS= 3.879 TECU, Relative Error = 31.49%)

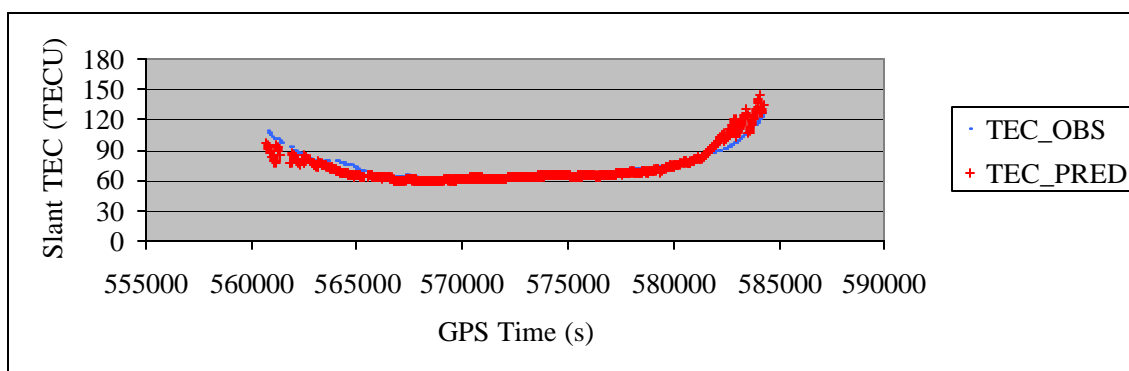


Figure 6.44 Comparison of Observed and Predicted TEC for PRN 02 at DAM2 Station on DOY 090 at 15° Cutoff and 10-min Prediction Interval
(VTEC RMS= 3.333 TECU, Relative Error = 4.16%)

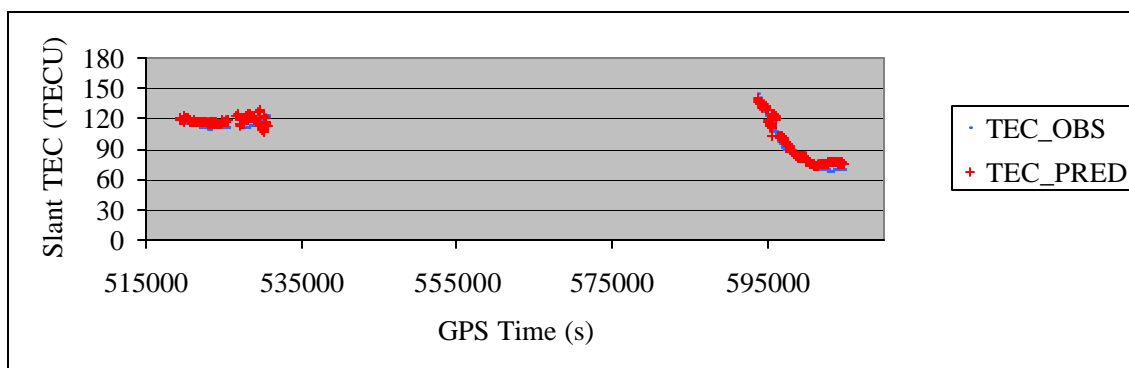


Figure 6.45 Comparison of Observed and Predicted TEC for PRN 17 at DAM2 Station on DOY 090 at 15° Cutoff and 10-min Prediction Interval
(VTEC RMS= 5.513 TECU, Relative Error = 7.21%)

6.3.1.3 Results of Scheme 3 (15°, 30 min)

The following two subsections present the results of Scheme 3 (15°, 30-min) where the elevation cutoff angle is 15° but the TEC prediction interval is increased to 30 minutes. The prolonged TEC prediction interval is useful for potential space weather applications.

6.3.1.3.1 Results on ionosphere quiet day DOY 089

Figure 6.46 to Figure 6.51 show the TEC prediction results for six GPS stations. Similar to previous results, the predicted and the observed TEC data match each other quite well, in particular at the low latitude stations like CARR and COSO. The agreements between the two sets of TEC data at other four stations are not as good as those at CARR and COSO stations, but the predicted TEC at these stations basically follow the ionospheric change trends. When compared to the results of 5-min prediction in Scheme 1 and 10-min prediction in Scheme 2 for DOY 089, it can be found that the VTEC prediction errors shown in Figure 6.46 to Figure 6.51 are 0.5~1.0 TECU larger than those in Scheme 1 and Scheme 2. This is because the prediction interval in this scheme is much longer than Schemes 1 and 2.

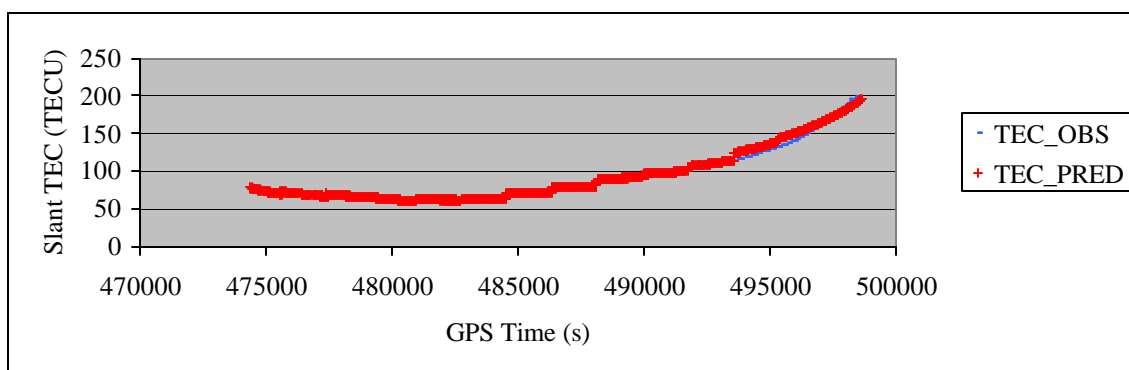


Figure 6.46 Comparison of Observed and Predicted TEC for PRN 02 at CARR Station on DOY 089 at 15° Cutoff and 30-min Prediction Interval
(VTEC RMS= 3.803 TECU, Relative Error = 4.80%)

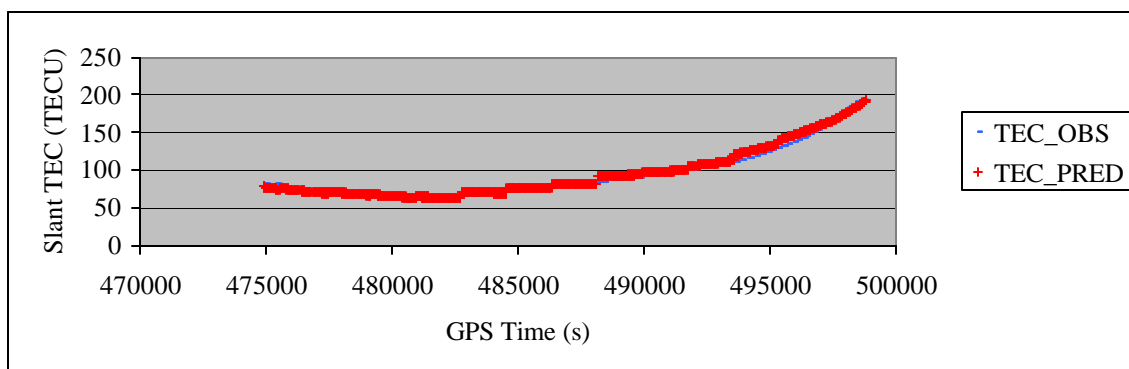


Figure 6.47 Comparison of Observed and Predicted TEC for PRN 02 at COSO Station on DOY 089 at 15° Cutoff and 30-min Prediction Interval
(VTEC RMS= 4.223 TECU, Relative Error = 5.45%)

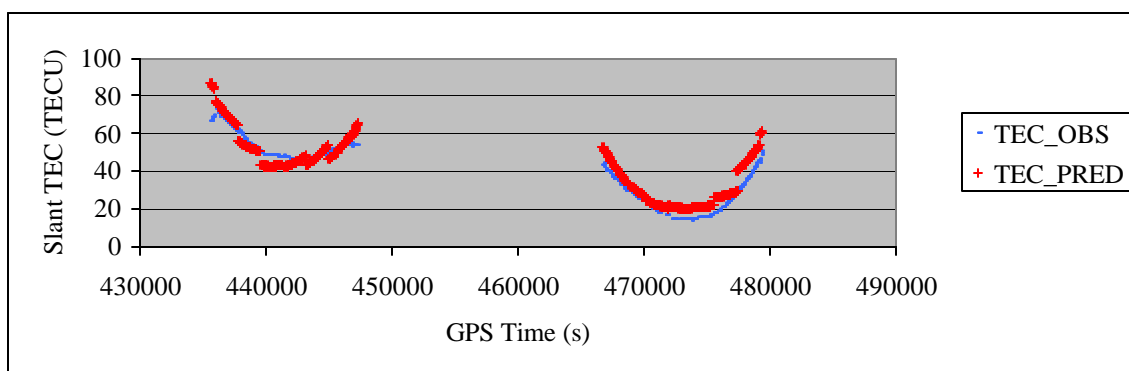


Figure 6.48 Comparison of Observed and Predicted TEC for PRN 03 at AMC2 Station on DOY 089 at 15° Cutoff and 30-min Prediction Interval
(VTEC RMS= 3.137 TECU, Relative Error = 17.49%)

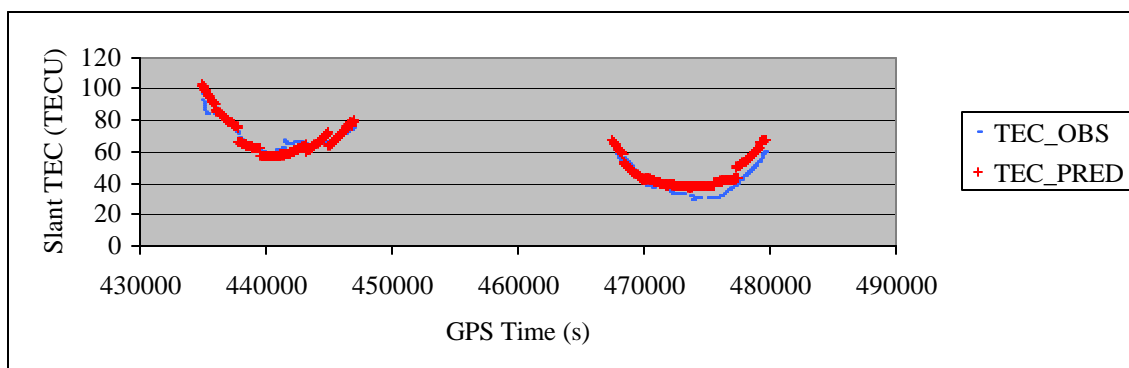


Figure 6.49 Comparison of Observed and Predicted TEC for PRN 03 at CASP Station on DOY 089 at 15° Cutoff and 30-min Prediction Interval
(VTEC RMS= 3.262 TECU, Relative Error = 10.77%)

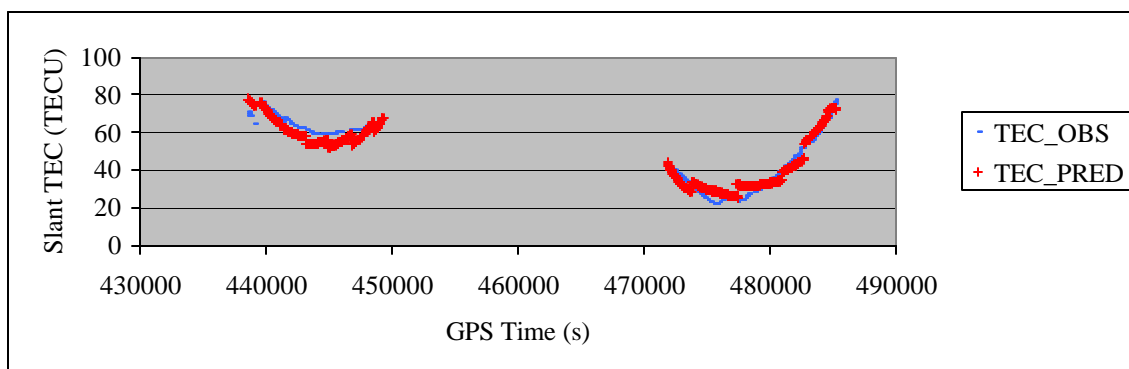


Figure 6.50 Comparison of Observed and Predicted TEC for PRN 31 at PRDS Station on DOY 089 at 15° Cutoff and 30-min Prediction Interval (VTEC RMS= 2.571 TECU, Relative Error = 8.98%)

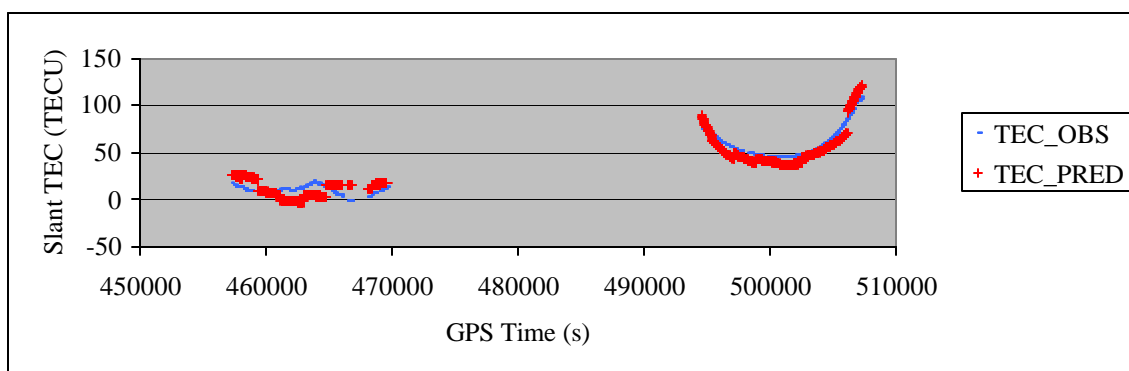


Figure 6.51 Comparison of Observed and Predicted TEC for PRN 04 at FAIR Station on DOY 089 at 15° Cutoff and 30-min Prediction Interval (VTEC RMS= 5.748 TECU, Relative Error = 75.79%)

Table 6.8 gives a summary of the VTEC prediction errors and relative errors with a 30-min prediction interval. It can be seen that most stations have a VTEC prediction errors in the range of 3.0~4.0 TECU. There are only 6 stations with a VTEC prediction error that is well above 4.0 TECU. The VTEC prediction errors at other 16 stations are below or just slightly over 4.0 TECU. Within the network, the mean VTEC prediction error is 4.028 TECU, which is 0.534 TECU larger than that of Scheme 1 (5-min prediction interval) and is 0.470 TECU larger than that of Scheme 2 (10-min prediction interval). Table 6.8 also shows that among the 22 stations, only seven stations have a relative error that is over 20.0%. The other 15 stations have a relative error less than 20.0%. Among the

above 15 stations, ten stations are better than 10.0%. The network's mean relative error is 14.60%, which is also higher than those of Schemes 1 and 2. The mean relative error in this scheme is 14.60% while it is 12.75% and 12.96% in Schemes 1 and 2, respectively. Although a certain amount of degradation in both VTEC prediction error and relative error can be seen when the prediction interval increases from 5-min or 10-min to 30-min, the degradation however is not significant. The results show that the degradation is only about half TECU over the wide area GPS network when the ionospheric activity is relatively quiet.

Table 6.8 Error Statistics for 30-min VTEC Prediction with Cutoff 15° on DOY 089

STATION	VTEC Error RMS (TECU)	Relative Error (%)
ALBH	3.651	19.53%
ALGO	3.945	23.58%
AMC2	3.447	17.80%
CARR	3.776	5.68%
CASP	3.521	8.98%
COSO	3.659	5.54%
DAM2	3.767	4.88%
DRAO	3.637	25.46%
FAIR	5.173	31.48%
FLIN	4.100	22.35%
HOLB	3.504	22.82%
HOPB	3.483	5.17%
KODK	5.387	9.70%
NEAH	3.578	6.83%
NRC1	4.036	5.84%
PRDS	4.345	12.39%
SCH2	5.198	24.70%
STJO	4.669	17.18%
USNO	3.799	14.25%
VNDP	3.704	4.97%
WHIT	4.745	7.76%
WSLR	3.497	24.22%
Mean	4.028	14.60%

Besides the above predictions at stations whose data are used in both ionospheric modeling and prediction, the ionospheric prediction tests below at two stations DRAO

and DAM2 are performed by excluding the test station from ionospheric modeling. The two stations are used for independent comparison. The comparison results of the predicted and observed TEC data for DRAO station are presented in Figure 6.52 and Figure 6.53 while the comparison results for DAM2 station are presented in Figure 6.54 and Figure 6.55. The vertical RMS errors for the PRN 31 and PRN 26 at DRAO station are 2.795 TECU and 2.663 TECU, respectively. Their relative errors are 34.92% and 23.50%. For the satellites PRN 02 and PRN 31 at DAM2 station, the vertical TEC prediction errors are 2.837 TECU and 3.478 TECU, respectively. The relative errors are 3.58% and 6.19% respectively for these two satellites. The results indicate that the predictions agree with the TEC observations. For all satellites tracked by the two stations, the vertical TEC RMS errors are 5.463 TECU at DRAO station and 5.852 TECU at DAM2 station. The relative errors for the two stations are 34.74% for DRAO station and 7.62% for the DAM2 station. In comparison with the prediction results of Table 6.8 where the stations are included in both ionospheric modeling and prediction, it shows that the vertical TEC prediction RMS error of the predictions by excluding DRAO from ionospheric modeling is 1.826 TECU greater than that of the prediction results in Table 6.8 which have included the DRAO station in tomographic modeling. At DAM2 station, a degradation of 2.085 TECU occurs in the vertical TEC prediction RMS error compared to the previous predictions in Table 6.8 for the same station. In terms of relative error, the prediction results at DRAO and DAM2 stations have an error larger by 9.28% and 2.74% than the predictions including the two stations in tomographic modeling.

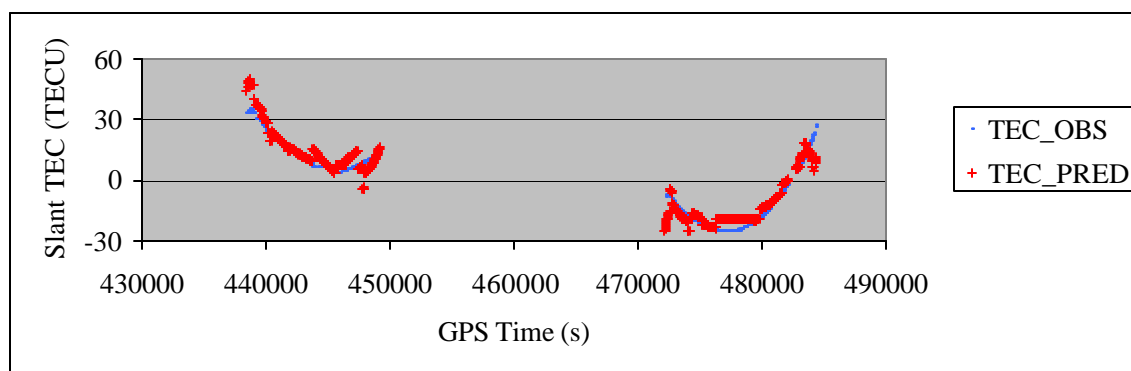


Figure 6.52 Comparison of Observed and Predicted TEC for PRN 31 at DRAO Station on DOY 089 at 15° Cutoff and 30-min Prediction Interval
(VTEC RMS= 2.795 TECU, Relative Error = 34.92%)

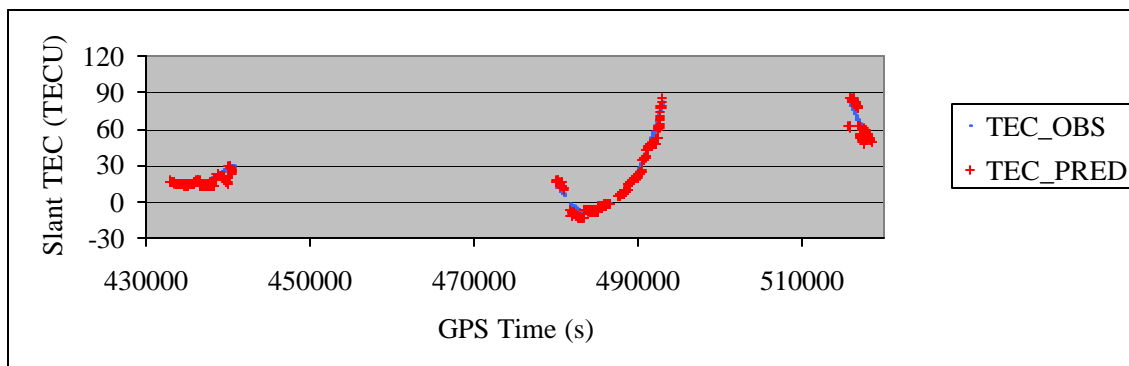


Figure 6.53 Comparison of Observed and Predicted TEC for PRN 26 at DRAO Station on DOY 089 at 15° Cutoff and 30-min Prediction Interval
(VTEC RMS= 2.663 TECU, Relative Error = 23.50%)

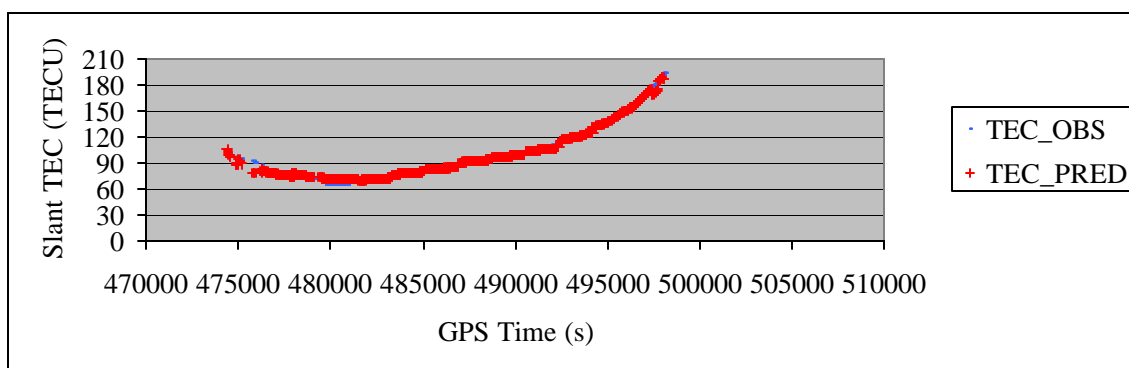


Figure 6.54 Comparison of Observed and Predicted TEC for PRN 02 at DAM2 Station on DOY 089 at 15° Cutoff and 30-min Prediction Interval
(VTEC RMS= 2.837 TECU, Relative Error = 3.58%)

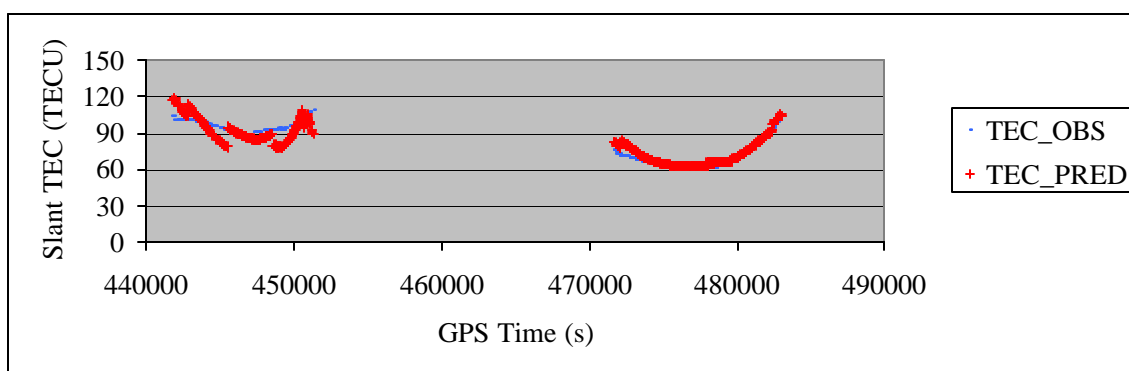


Figure 6.55 Comparison of Observed and Predicted TEC for PRN 31 at DAM2 Station on DOY 089 at 15° Cutoff and 30-min Prediction Interval
(VTEC RMS= 3.478 TECU, Relative Error = 6.19%)

6.3.1.3.2 Results on ionosphere disturbed day DOY 090

Shown in Figure 6.56 to Figure 6.61 are the results from Scheme 3 with an elevation cutoff angle of 15° and a prediction interval of 30-min during ionosphere disturbed DOY 090. The predicted TEC data at all stations generally show larger disagreements with the observed TEC data when compared to DOY 089. These disagreements are particularly visible at the high latitude stations PRDS and FAIR. At the low latitude stations CARR and COSO, the disagreements are also large during the satellite rising period, see the starting portions in Figure 6.56 and Figure 6.57. The VTEC prediction errors shown in the following six figures are generally larger than the errors on DOY 089 by 0.2~0.6 TECU. The difference of the two days' prediction errors at the high latitude site PRDS station could sometimes greater than 2.0 TECU.

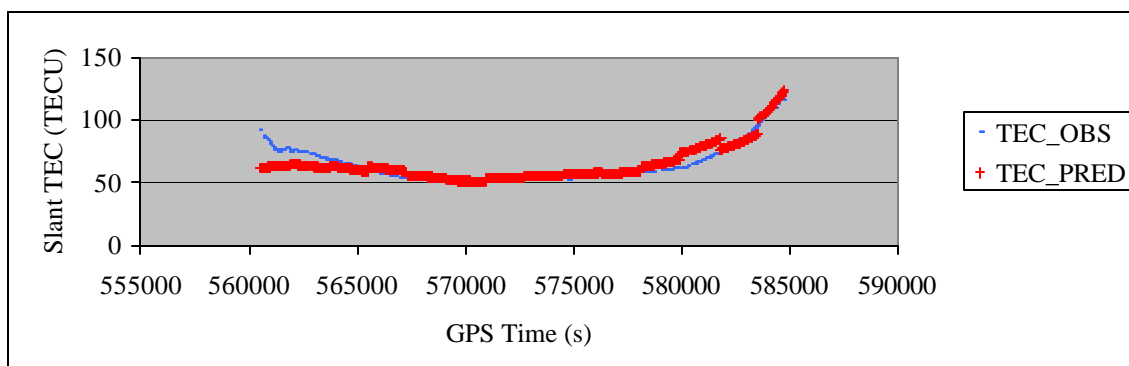


Figure 6.56 Comparison of Observed and Predicted TEC for PRN 02 at CARR Station on DOY 090 at 15° Cutoff and 30-min Prediction Interval
(VTEC RMS= 4.074 TECU, Relative Error = 7.74%)

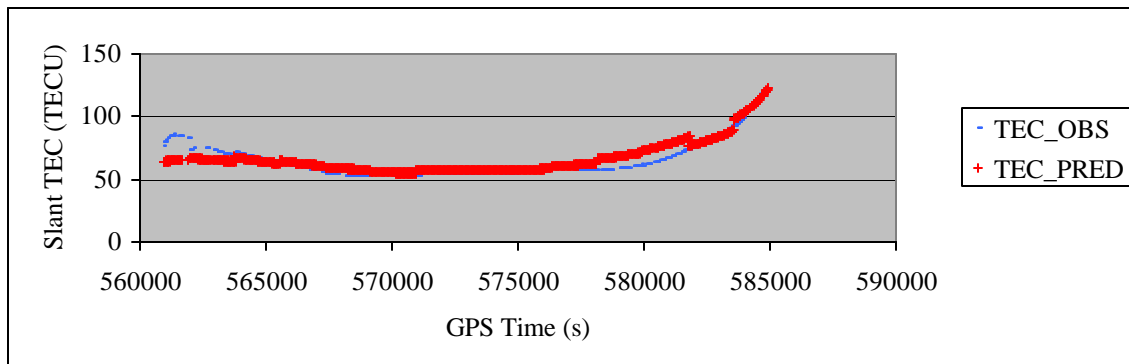


Figure 6.57 Comparison of Observed and Predicted TEC for PRN 02 at COSO Station on DOY 090 at 15° Cutoff and 30-min Prediction Interval
(VTEC RMS= 4.640 TECU, Relative Error = 8.67%)

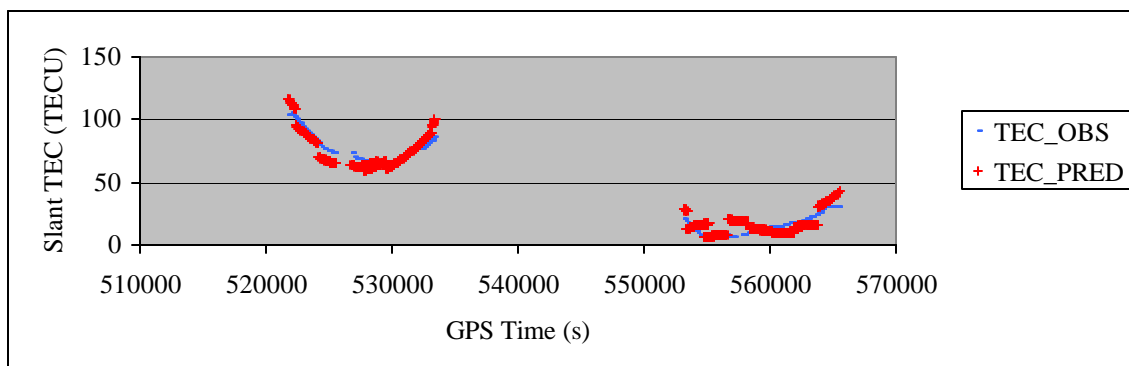


Figure 6.58 Comparison of Observed and Predicted TEC for PRN 03 at AMC2 Station on DOY 090 at 15° Cutoff and 30-min Prediction Interval
(VTEC RMS= 3.515 TECU, Relative Error = 35.73%)

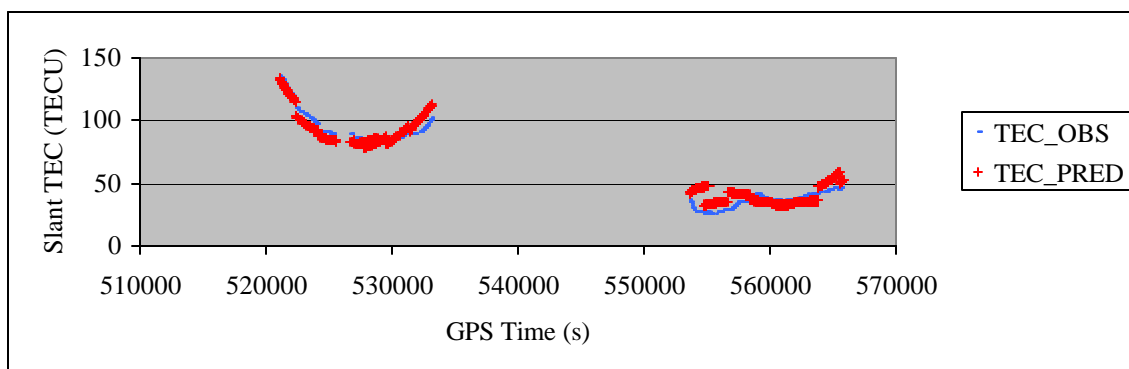


Figure 6.59 Comparison of Observed and Predicted TEC for PRN 03 at CASP Station on DOY 090 at 15° Cutoff and 30-min Prediction Interval
(VTEC RMS= 3.834 TECU, Relative Error = 14.30%)

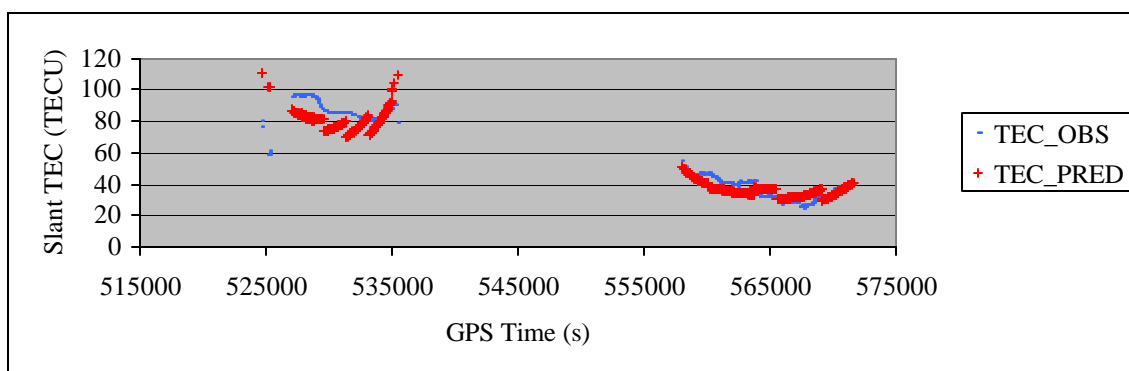


Figure 6.60 Comparison of Observed and Predicted TEC for PRN 31 at PRDS Station on DOY 090 at 15° Cutoff and 30-min Prediction Interval
(VTEC RMS= 4.555 TECU, Relative Error = 11.54%)

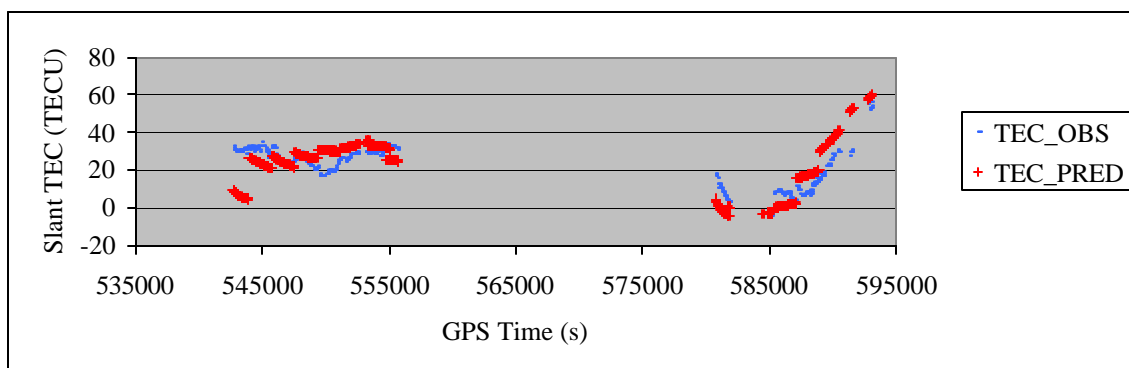


Figure 6.61 Comparison of Observed and Predicted TEC for PRN 04 at FAIR Station on DOY 090 at 15° Cutoff and 30-min Prediction Interval
(VTEC RMS= 5.642 TECU, Relative Error = 48.35%)

Table 6.9 Error Statistics for 30-min VTEC Prediction with Cutoff 15° on DOY 090

STATION	VTEC Error RMS (TECU)	Relative Error (%)
ALBH	5.440	34.86%
ALGO	6.315	35.04%
AMC2	5.561	35.69%
CARR	4.905	9.19%
CASP	6.010	16.56%
COSO	4.928	9.22%
DAM2	5.340	8.33%
DRAO	5.432	65.21%
FAIR	5.740	64.38%
FLIN	6.415	39.81%
HOLB	5.192	30.74%
HOPB	4.818	8.39%
KODK	5.119	9.58%
NEAH	5.496	10.31%
NRC1	6.381	9.62%
PRDS	6.208	16.39%
SCH2	5.461	32.41%
STJO	5.736	38.96%
USNO	6.306	36.19%
VNDP	5.147	8.11%
WHIT	4.921	8.64%
WSLR	5.151	24.44%
Mean	5.546	25.09%

The VTEC prediction errors as well as the relative errors for all 22 stations are presented in Table 6.9. It can be seen that the 30-min TEC prediction RMS errors are in the range between 5.0 TECU and 6.0 TECU. The network mean RMS error is 5.546 TECU, which is apparently larger than the mean RMS value 4.028 TECU obtained on the ionosphere quiet day DOY 089 using the same scheme (15°, 30-min). Compared to errors shown in Table 6.8, the RMS errors in Table 6.9 are generally 1.0~2.0 TECU larger than the results of ionosphere quiet day. Table 6.9 shows that almost all the stations have an RMS error larger than 5.0 TECU while on DOY 089 Table 6.8 shows all the stations except several have an RMS error less than 4.0 TECU. The increase of VTEC prediction RMS error is because of the significant ionosphere disturbance on DOY 090 compared to the relatively

quiet DOY 089. The disturbed ionosphere conditions made it more difficult to model and predict the ionosphere. Nevertheless, the mean RMS error is still as good as 5.546 TECU. The relative errors are quite different from station to station. Table 6.9 indicates 9 out of the 22 stations have a relative error less than 10.0%. At most stations the relative errors are at the level of 30.0%. Just a few stations are significantly over 30.0%. Two stations, DRAO and FAIR, have particularly high relative errors. This may be caused by two reasons. Both stations used AOA TurboRogue GPS receivers and the tracking performance of this type of codeless receiver is significantly degraded in geomagnetic stormy conditions. The poor tracking performance will affect the quality of smoothed TEC data, which are used in modeling and evaluation. Compared to the relative errors of previous quiet day, the relative errors on both stations have a degradation of about 30%. On other stations equipped with AOA TurboRogue receivers, similar large relative errors are found when compared to other stations equipped with ASHTECH receivers. In comparison, Table 6.8 indicates most stations have a relative error at the order of 20.0%. The predictions on DOY 090 have a relative error about 10.0% higher than that from DOY 089 using the same Scheme 3.

Similar to DOY 089, two independent test stations DRAO and DAM2 are used for the further evaluation of the TEC prediction performance. The comparison between the TEC predictions and observations for test station DRAO are presented in Figure 6.62 and Figure 6.63 while the comparison results for station DAM2 are illustrated in Figure 6.64 and Figure 6.65. The figures indicate that the predicted and observed TEC data match with each other quite well even if the prediction interval is extended to 30-min. The vertical TEC RMS errors for the satellites presented below are in the range of 3.158~5.905 TECU and their relative errors are also small, ranging from 4.63% to 35.83%. Taking all the observed satellites into account, the vertical TEC prediction RMS error at DRAO station is 5.785 TECU and the relative error is 51.62%. For station DAM2, the vertical RMS error is 6.656 TECU and the relative error is 9.81%. Like DOY 089, the TEC predictions at DRAO and DAM2 stations are also compared to the previous

predictions at these two stations given in Table 6.9 where the two stations are included in ionospheric modeling. The comparisons indicate that the predictions with the test station excluded from ionospheric modeling have a degradation in vertical TEC RMS by 0.353 TECU at DRAO station and by 1.316 TECU at DAM2 station. As to the relative error, the prediction errors without using the data from DAM2 station in ionospheric modeling are greater by 1.48% than the predictions with DAM2 station included for modeling.

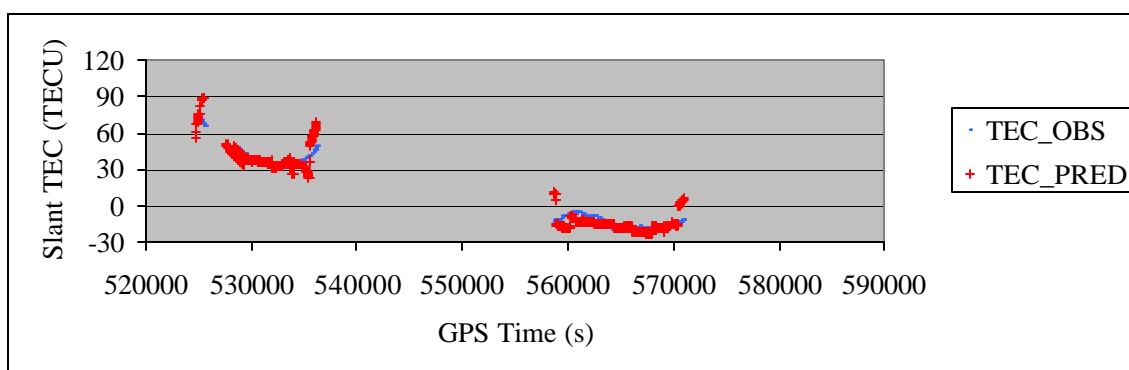


Figure 6.62 Comparison of Observed and Predicted TEC for PRN 31 at DRAO Station on DOY 090 at 15° Cutoff and 30-min Prediction Interval
(VTEC RMS= 3.158 TECU, Relative Error = 23.79%)

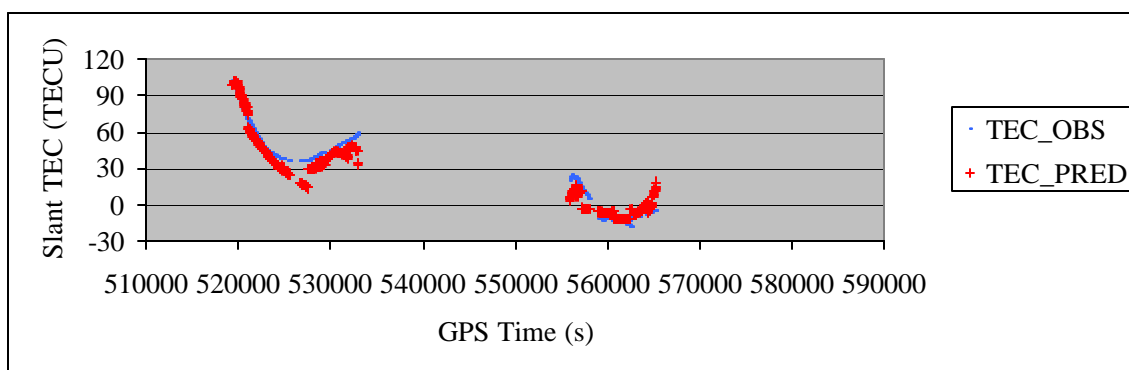


Figure 6.63 Comparison of Observed and Predicted TEC for PRN 03 at DRAO Station on DOY 090 at 15° Cutoff and 30-min Prediction Interval
(VTEC RMS= 5.130 TECU, Relative Error = 35.83%)

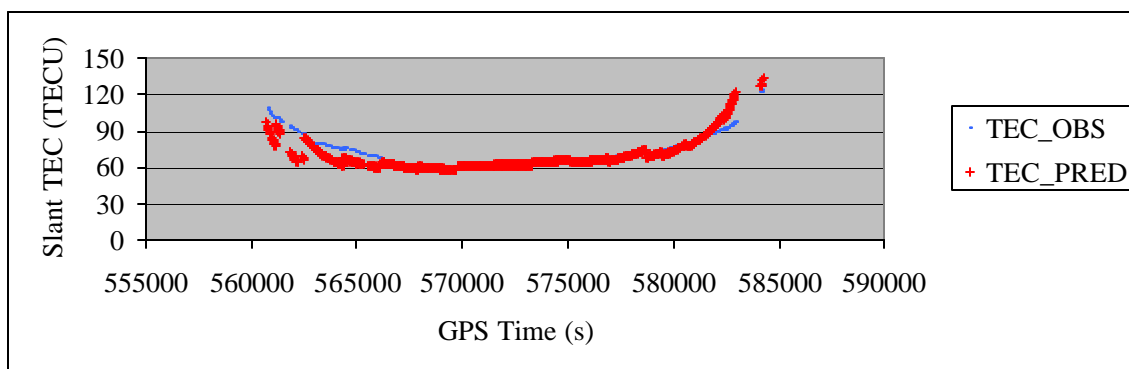


Figure 6.64 Comparison of Observed and Predicted TEC for PRN 02 at DAM2 Station on DOY 090 at 15° Cutoff and 30-min Prediction Interval
(VTEC RMS= 3.691 TECU, Relative Error = 4.63%)

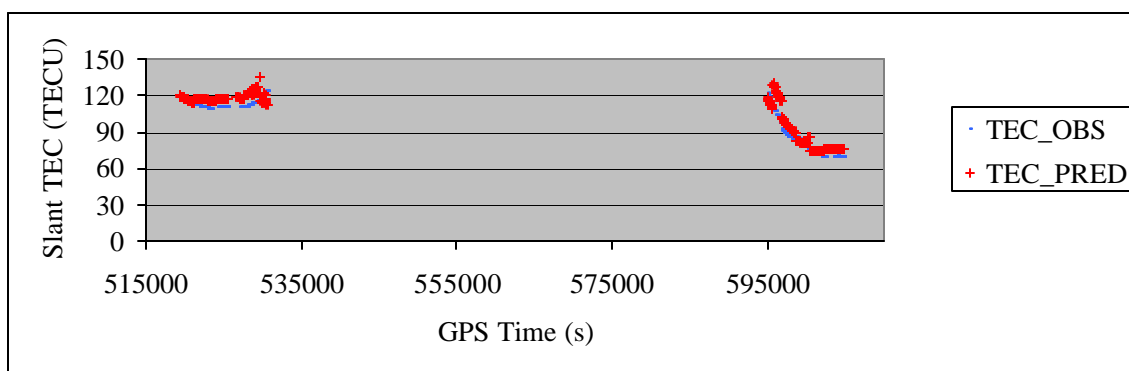


Figure 6.65 Comparison of Observed and Predicted TEC for PRN 17 at DAM2 Station on DOY 090 at 15° Cutoff and 30-min Prediction Interval
(VTEC RMS= 5.905 TECU, Relative Error = 7.90%)

6.3.2 Results of medium elevation cutoff angle (20°)

6.3.2.1 Results of Scheme 4 (20°, 5 min)

In this scheme, the elevation cutoff angle is raised to 20° from 15° and the prediction interval is set to 5-min. The data analysis results for the ionosphere quiet day and disturbed day are presented in the following two subsections.

6.3.2.1.1 Results on ionosphere quiet day DOY 089

Figure 6.66 and Figure 6.67 show the TEC comparisons between CARR and COSO stations. Both figures indicate that the TEC predictions and TEC observations agree with each other very well except a few epochs at the starting portion of each figure. For Figure 6.68 to Figure 6.71, the disagreements between the two sets of TEC data are also small except at the FAIR station where its first part of TEC prediction data has large disagreements. Compared to the VTEC prediction errors shown in Figure 6.6 to Figure 6.11 for Scheme 1 on DOY 089, it can be found the VTEC prediction RMS errors shown in Figure 6.66 to Figure 6.71 are all smaller than those in Scheme 1 except CASP station. At some stations, the improvements are as high as about 0.4 TECU. That is to say in the 5-min TEC predictions under ionosphere quiet environment the rise of the elevation cutoff angle from 15° to 20° will be helpful in enhancing the prediction accuracies. Looking at Table 6.10, it can be seen the mean VTEC prediction RMS error is 3.277 TECU, which is smaller than the mean RMS error 3.494 TECU indicated in Table 6.4 for Scheme 1 on DOY 089. The mean relative error 12.41% in this scheme is also smaller than 12.75% in Scheme 1.

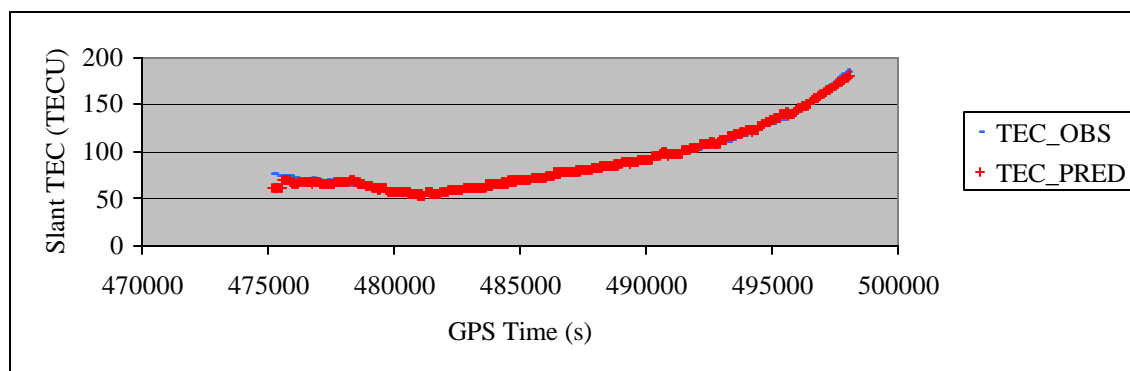


Figure 6.66 Comparison of Observed and Predicted TEC for PRN 02 at CARR Station on DOY 089 at 20° Cutoff and 5-min Prediction Interval
(VTEC RMS= 2.335 TECU, Relative Error = 3.20%)

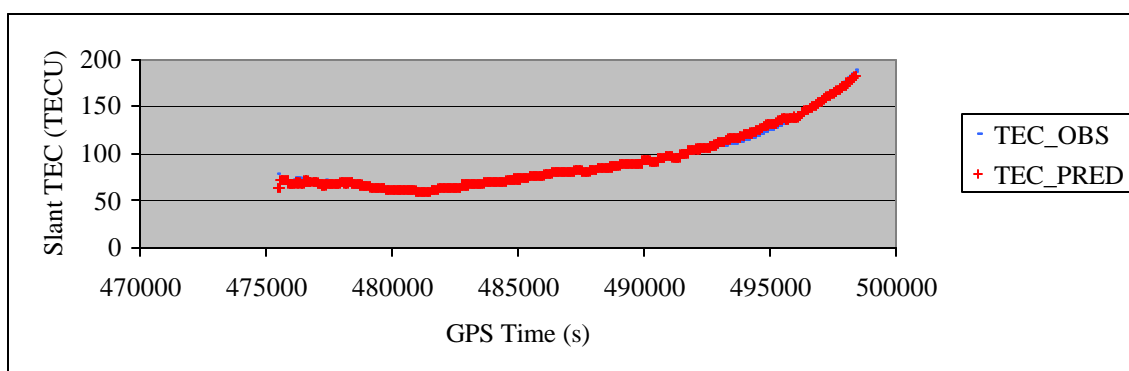


Figure 6.67 Comparison of Observed and Predicted TEC for PRN 02 at COSO Station on DOY 089 at 20° Cutoff and 5-min Prediction Interval
(VTEC RMS= 2.445 TECU, Relative Error = 3.02%)

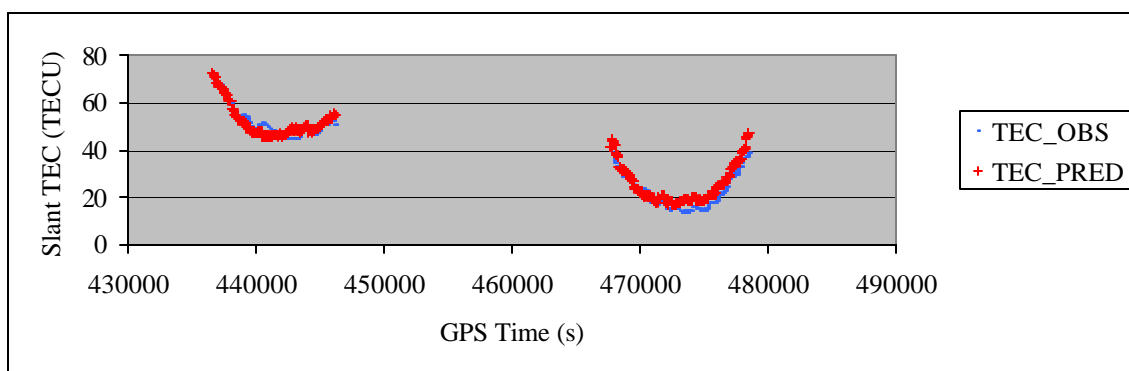


Figure 6.68 Comparison of Observed and Predicted TEC for PRN 03 at AMC2 Station on DOY 089 at 20° Cutoff and 5-min Prediction Interval
(VTEC RMS= 1.971 TECU, Relative Error = 11.24%)

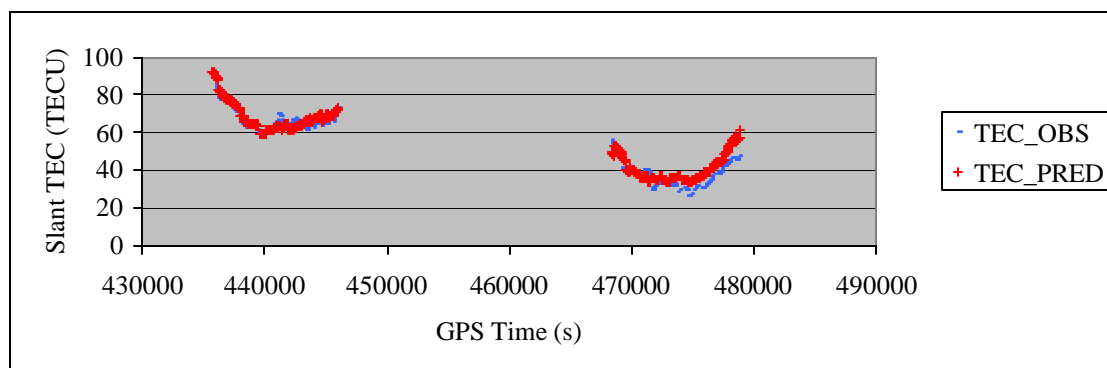


Figure 6.69 Comparison of Observed and Predicted TEC for PRN 03 at CASP Station on DOY 089 at 20° Cutoff and 5-min Prediction Interval
(VTEC RMS= 2.664 TECU, Relative Error = 8.90%)

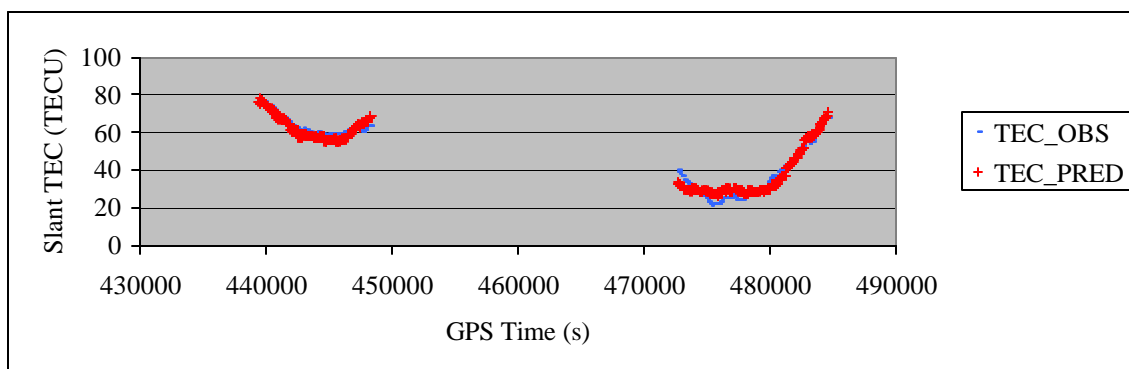


Figure 6.70 Comparison of Observed and Predicted TEC for PRN 31 at PRDS Station on DOY 089 at 20° Cutoff and 5-min Prediction Interval
(VTEC RMS= 2.005 TECU, Relative Error = 7.28%)

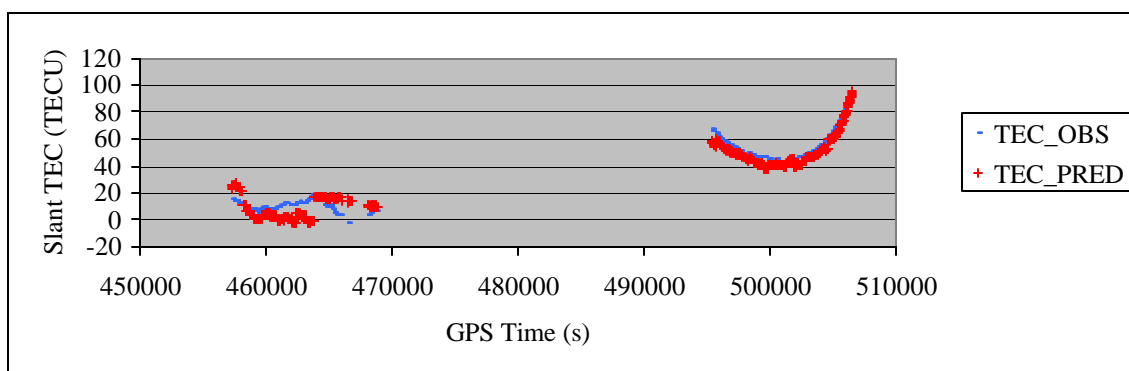


Figure 6.71 Comparison of Observed and Predicted TEC for PRN 04 at FAIR Station on DOY 089 at 20° Cutoff and 5-min Prediction Interval
(VTEC RMS= 4.800 TECU, Relative Error = 63.50%)

Table 6.10 indicates that at most stations the VTEC prediction RMS values are smaller than 3.0 TECU. Only four stations have an RMS value that is much larger than 3.0 TECU. The largest RMS value is still bounded to below 5.0 TECU. The mean value of RMS errors in the network is 3.277 TECU. When looking at the relative errors, it can be seen half of the stations are better than 10.0% and 19 out of the 22 stations are below 20.0%. The mean relative error for this scheme is 12.41%, which is better than the mean relative error shown in Table 6.4 for Scheme 1.

Table 6.10 Error Statistics for 5-min VTEC Prediction with Cutoff 20° on DOY 089

STATION	VTEC Error RMS (TECU)	Relative Error (%)
ALBH	2.975	14.20%
ALGO	2.923	20.52%
AMC2	3.013	17.38%
CARR	3.148	4.77%
CASP	3.092	8.32%
COSO	2.976	4.38%
DAM2	3.333	4.35%
DRAO	2.941	19.86%
FAIR	4.618	33.28%
FLIN	3.468	21.59%
HOLB	2.767	17.55%
HOPB	3.043	4.44%
KODK	4.707	8.14%
NEAH	2.908	5.23%
NRC1	3.113	4.62%
PRDS	3.383	9.52%
SCH2	3.878	19.80%
STJO	3.129	13.40%
USNO	3.045	12.19%
VNDP	3.138	3.99%
WHIT	3.708	5.85%
WSLR	2.791	19.73%
Mean	3.277	12.41%

6.3.2.1.2 Results on ionosphere disturbed day DOY 090

The comparisons of TEC observations and predictions using 20° cutoff angle and 5-min prediction interval for the ionosphere disturbed DOY 090 are presented in Figure 6.72 to Figure 6.77. The six figures show that the predictions agree with the TEC observations very well and their discrepancies are small, especially at the low latitude stations. The comparison of the results in this scheme with those from Scheme 1 on the same day DOY 090 shows that five out of the six stations at this scheme have an improvement in the VTEC prediction accuracy over the Scheme 1. The improvement over Scheme 1 is about 0.1~0.4 TECU. The mean VTEC prediction RMS error shown in Table 6.11 is 4.666

TECU, which is smaller by 0.091 TECU than the mean RMS value of Scheme 1. The mean relative error shown in Table 6.11 is 19.61%, which is also below 20.45% from Scheme 1. The analysis results show that for wide area GPS network based modeling under ionosphere disturbance conditions, the employment of 20° elevation cutoff angle will produce superior performance for short-term (5-min) TEC predictions if using an elevation cut-off angle of 15°.

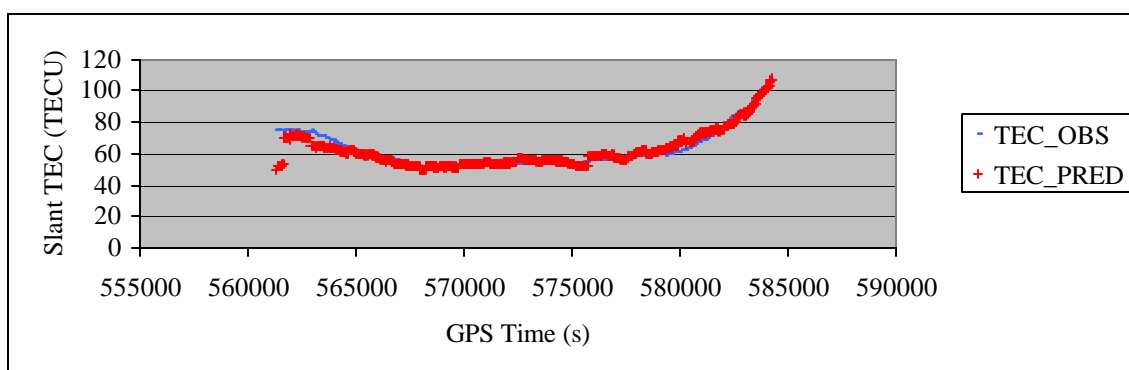


Figure 6.72 Comparison of Observed and Predicted TEC for PRN 02 at CARR Station on DOY 090 at 20° Cutoff and 5-min Prediction Interval
(VTEC RMS= 2.615 TECU, Relative Error = 4.75%)

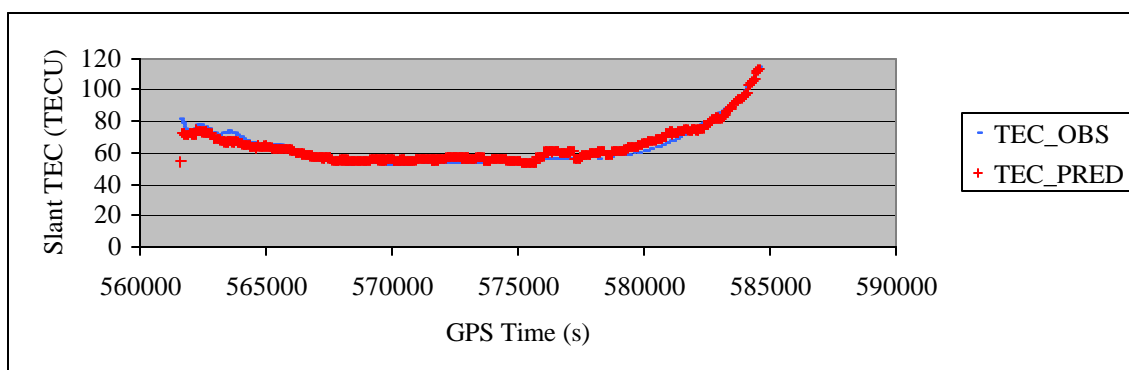


Figure 6.73 Comparison of Observed and Predicted TEC for PRN 02 at COSO Station on DOY 090 at 20° Cutoff and 5-min Prediction Interval
(VTEC RMS= 2.609 TECU, Relative Error = 4.82%)

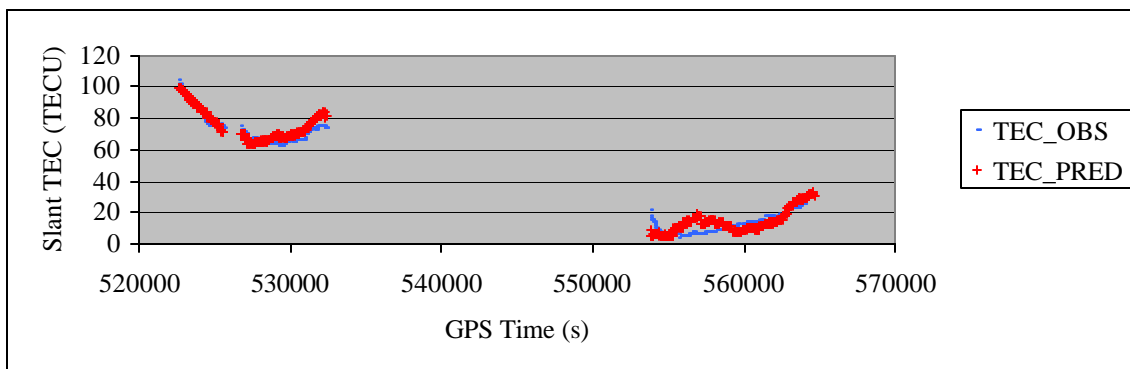


Figure 6.74 Comparison of Observed and Predicted TEC for PRN 03 at AMC2 Station on DOY 090 at 20° Cutoff and 5-min Prediction Interval (VTEC RMS= 2.849 TECU, Relative Error = 31.11%)

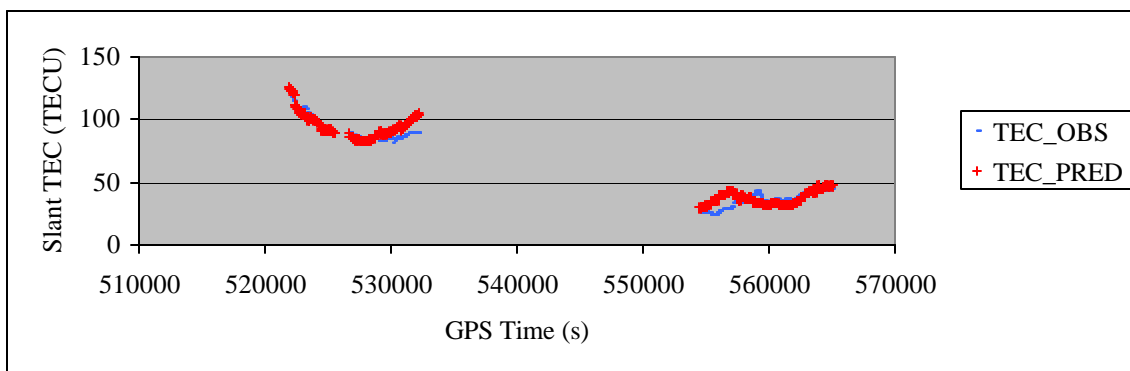


Figure 6.75 Comparison of Observed and Predicted TEC for PRN 03 at CASP Station on DOY 090 at 20° Cutoff and 5-min Prediction Interval (VTEC RMS= 3.431 TECU, Relative Error = 10.78%)

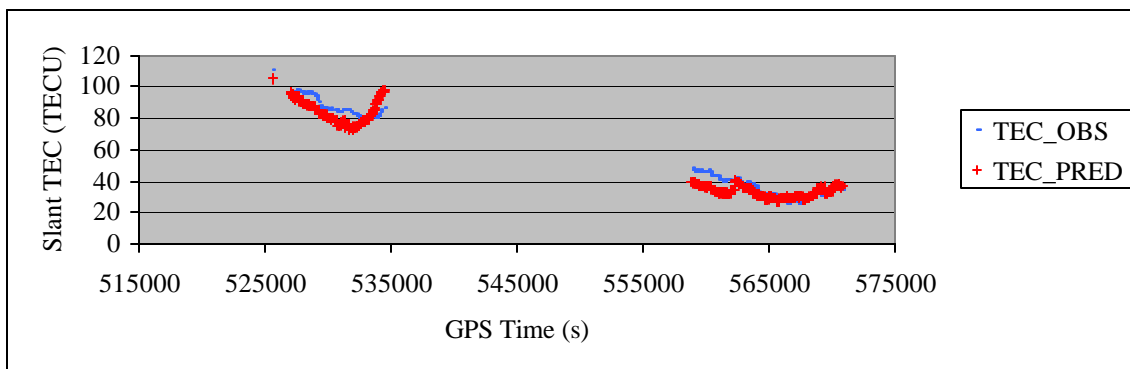


Figure 6.76 Comparison of Observed and Predicted TEC for PRN 31 at PRDS Station on DOY 090 at 20° Cutoff and 5-min Prediction Interval (VTEC RMS= 3.139 TECU, Relative Error = 8.30%)

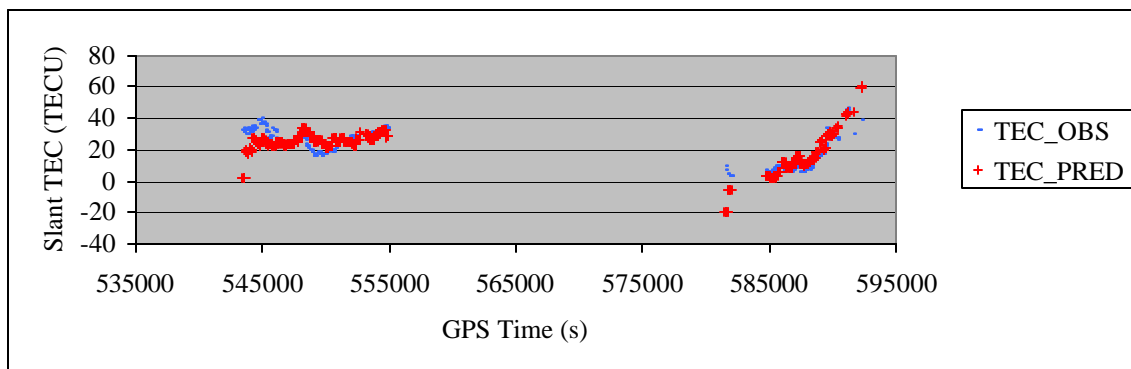


Figure 6.77 Comparison of Observed and Predicted TEC for PRN 04 at FAIR Station on DOY 090 at 20° Cutoff and 5-min Prediction Interval
(VTEC RMS= 4.240 TECU, Relative Error = 38.31%)

Table 6.11 Error Statistics for 5-min VTEC Prediction with Cutoff 20° on DOY 090

STATION	VTEC Error RMS (TECU)	Relative Error (%)
ALBH	4.536	26.45%
ALGO	5.652	29.15%
AMC2	4.604	29.34%
CARR	3.956	7.10%
CASP	5.219	13.50%
COSO	4.000	7.12%
DAM2	4.513	6.85%
DRAO	4.392	48.86%
FAIR	4.269	46.39%
FLIN	6.150	33.35%
HOLB	4.076	22.03%
HOPB	3.929	6.68%
KODK	4.060	7.08%
NEAH	4.458	7.67%
NRC1	5.665	7.73%
PRDS	5.547	12.50%
SCH2	4.246	24.76%
STJO	4.575	31.48%
USNO	6.152	32.33%
VNDP	4.308	6.41%
WHIT	4.189	6.86%
WSLR	4.159	17.71%
Mean	4.666	19.61%

Table 6.11 summarizes the VTEC prediction RMS errors and relative errors for all stations. It shows the VTEC prediction errors are quite homogeneously distributed over the network. Table 6.11 shows that VTEC prediction errors with the 5-min interval vary between 4.0~5.0 TECU during the ionosphere disturbed period. Most stations have an RMS error at the level of 4.0~5.0 TECU. Just a few stations show an error above the average level. The mean RMS error for this scheme is 4.666 TECU. For the relative errors, 9 stations have a relative error less than 10.0% and the relative errors at most stations are less than 30.0%. The mean value of the relative error is 19.61%.

6.3.2.2 Results of Scheme 5 (20°, 10 min)

6.3.2.2.1 Results on ionosphere quiet day DOY 089

Scheme 5 is to show the modeling performance under the condition of using 20° cutoff angle and 10-min prediction interval. Shown in Figure 6.78 to Figure 6.83 are the comparisons of the predicted and observed slant TEC at selected stations. The figures show that the two sets of slant TEC agree quite well at each station. Similar to the previous sections, the agreements at low latitude stations are generally better than at high latitude stations. This can be seen from the results at FAIR station shown in Figure 6.83, especially at the first portion of the data set showing a large disagreement. Compared to Scheme 2 (15°, 10-min) for DOY 089, four stations of this scheme have better VTEC prediction accuracies than the Scheme 2. The largest improvements at the order of 0.6 TECU occur at low latitude stations CARR and COSO. As shown in Table 6.12, the mean VTEC prediction RMS error for the network is 3.357 TECU, which is smaller by 0.201 TECU than the result of Scheme 2 shown in Table 6.6. The mean relative error of this scheme is 12.61%, which is also below the value of 12.96% shown in Table 6.6 for Scheme 2. The results indicate that for wide area network modeling under ionosphere quiet period the use of 20° elevation cutoff angle is superior than the use of 15° over 10-min TEC predictions.

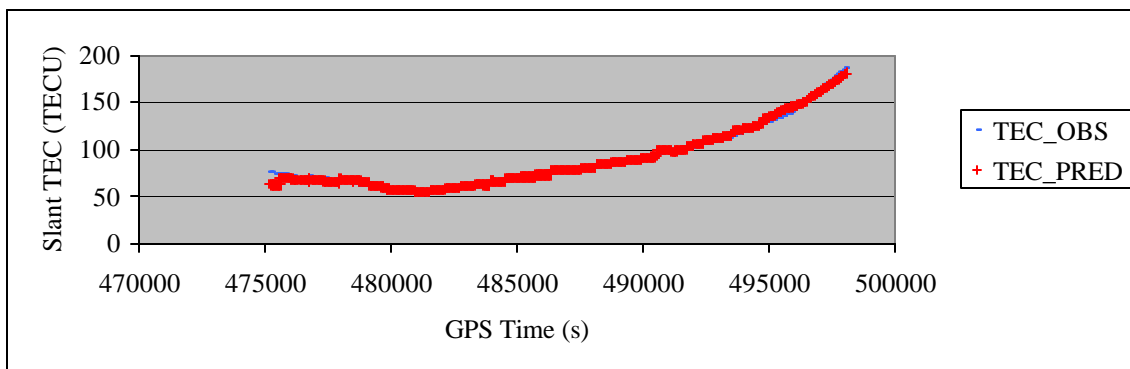


Figure 6.78 Comparison of Observed and Predicted TEC for PRN 02 at CARR Station on DOY 089 at 20° Cutoff and 10-min Prediction Interval (VTEC RMS= 2.386 TECU, Relative Error = 3.13%)

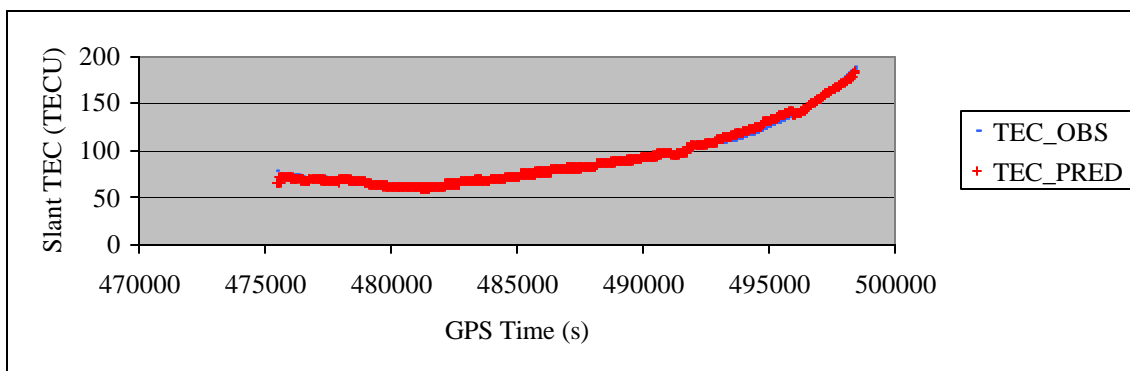


Figure 6.79 Comparison of Observed and Predicted TEC for PRN 02 at COSO Station on DOY 089 at 20° Cutoff and 10-min Prediction Interval (VTEC RMS= 2.611 TECU, Relative Error = 3.22%)

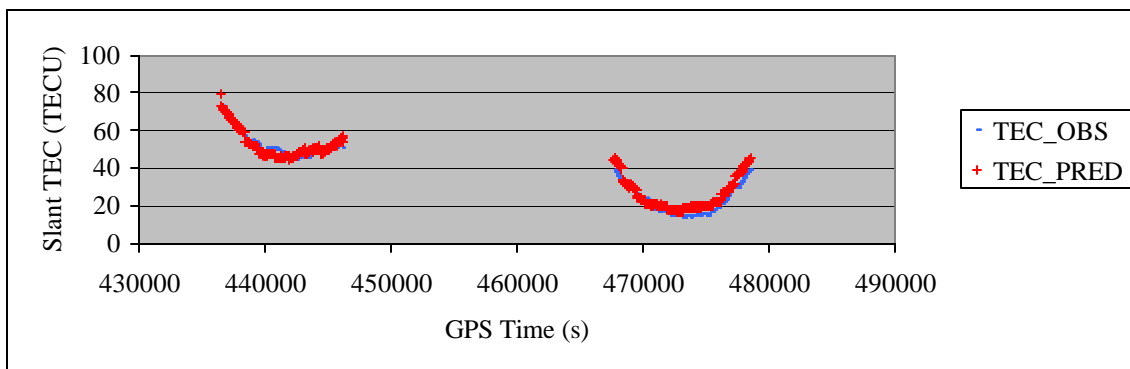


Figure 6.80 Comparison of Observed and Predicted TEC for PRN 03 at AMC2 Station on DOY 089 at 20° Cutoff and 10-min Prediction Interval (VTEC RMS= 2.071 TECU, Relative Error = 11.97%)

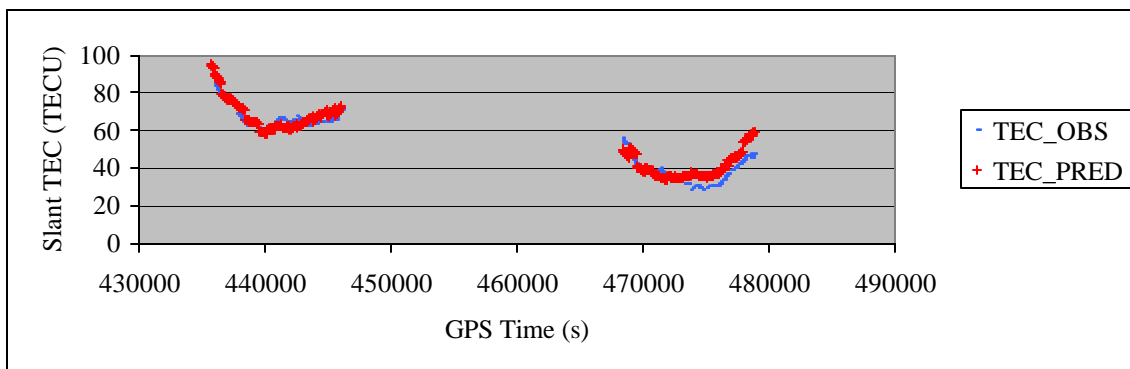


Figure 6.81 Comparison of Observed and Predicted TEC for PRN 03 at CASP Station on DOY 089 at 20° Cutoff and 10-min Prediction Interval (VTEC RMS= 2.778 TECU, Relative Error = 9.30%)

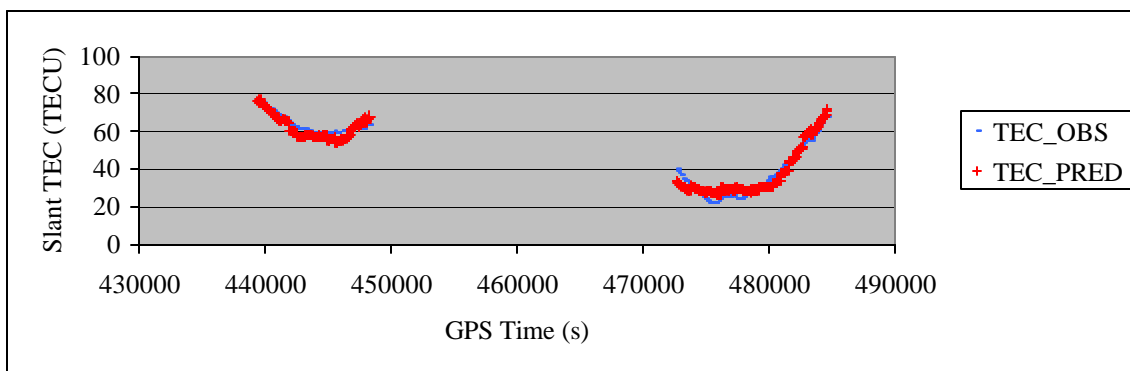


Figure 6.82 Comparison of Observed and Predicted TEC for PRN 31 at PRDS Station on DOY 089 at 20° Cutoff and 10-min Prediction Interval (VTEC RMS= 2.077 TECU, Relative Error = 7.46%)

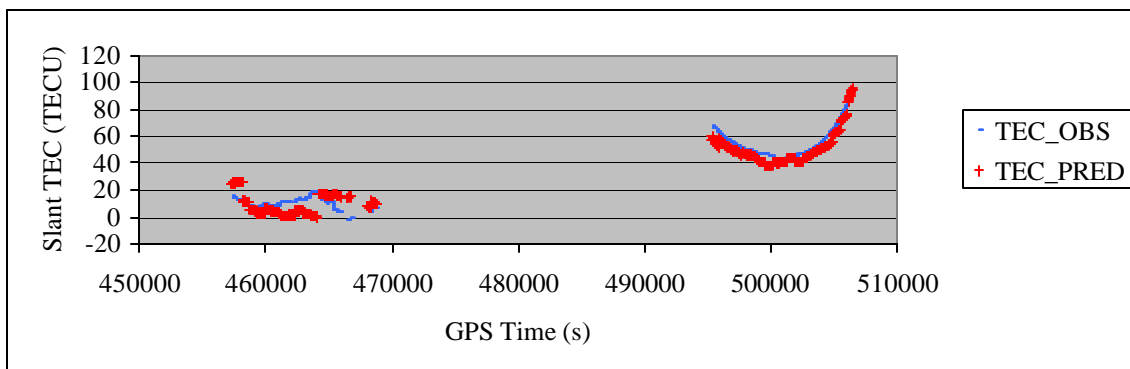


Figure 6.83 Comparison of Observed and Predicted TEC for PRN 04 at FAIR Station on DOY 089 at 20° Cutoff and 10-min Prediction Interval (VTEC RMS= 4.957 TECU, Relative Error = 63.16%)

Table 6.12 Error Statistics for 10-min VTEC Prediction with Cutoff 20° on DOY 089

STATION	VTEC Error RMS (TECU)	Relative Error (%)
ALBH	3.052	14.28%
ALGO	3.030	21.17%
AMC2	3.049	17.49%
CARR	3.216	4.85%
CASP	3.121	8.34%
COSO	3.056	4.44%
DAM2	3.358	4.36%
DRAO	3.036	19.95%
FAIR	4.626	32.38%
FLIN	3.512	21.39%
HOLB	2.867	18.22%
HOPB	3.091	4.50%
KODK	4.841	8.52%
NEAH	2.967	5.35%
NRC1	3.230	4.75%
PRDS	3.456	9.69%
SCH2	4.026	20.43%
STJO	3.266	13.89%
USNO	3.143	12.63%
VNDP	3.182	4.06%
WHIT	3.854	6.14%
WSLR	2.880	20.59%
Mean	3.357	12.61%

Table 6.12 summarizes the VTEC prediction RMS errors and relative errors for all stations. It shows that on this ionosphere quiet day the RMS errors for most stations are at the level of 3.0 TECU. Only four of the 22 stations have a VTEC prediction RMS error at 4.0~5.0 TECU level. The mean RMS error is 3.357 TECU. For the relative error, it can be seen that 11 of the 22 stations have a relative error below 10.0% and that most stations have a relative error better than 20.0%. The mean relative error in the network is 12.61%.

6.3.2.2.2 Results on ionosphere disturbed day DOY 090

Figure 6.84 to Figure 6.89 show the slant TEC results at six stations obtained on DOY 090 for the Scheme 5. It can be found that the discrepancies between the predicted and

observed TEC data at all stations are generally small except at a few epochs. For example at the beginning a few epochs at CARR and COSO stations, the predictions have a large difference from the TEC observations. Also at the high latitude station FAIR, the predictions show large discrepancies from the observations. Comparing the results in Scheme 2 (15°, 10-min) on DOY 090, the mean VTEC prediction RMS of this scheme is 4.811 TECU as shown in Table 6.13, which is smaller than the mean value 4.874 TECU in Scheme 2 as shown in Table 6.7. The mean relative error of this scheme is 20.35%, which is also smaller than 21.19% from Scheme 2. The analysis indicates that for wide area network modeling during ionosphere disturbed periods, the employment of 20° as the elevation cutoff angle can produce higher accuracies for 10-min predictions than using 15°.

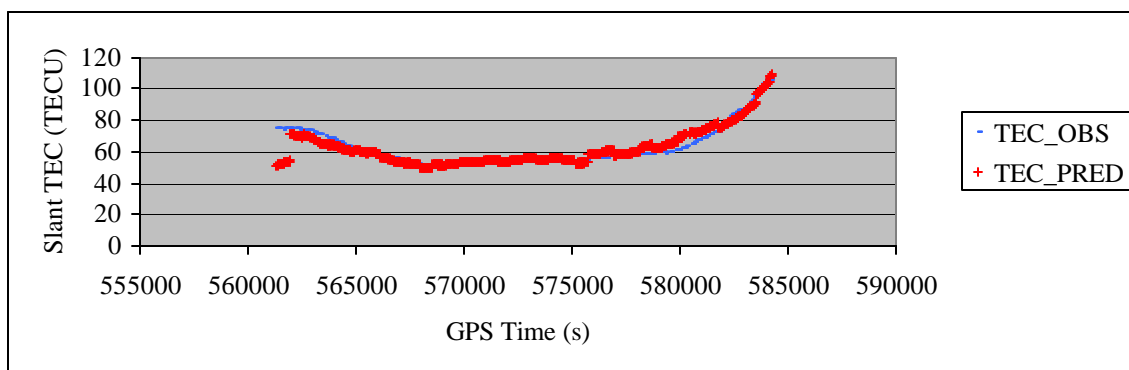


Figure 6.84 Comparison of Observed and Predicted TEC for PRN 02 at CARR Station on DOY 090 at 20° Cutoff and 10-min Prediction Interval
(VTEC RMS= 3.068 TECU, Relative Error = 5.44%)

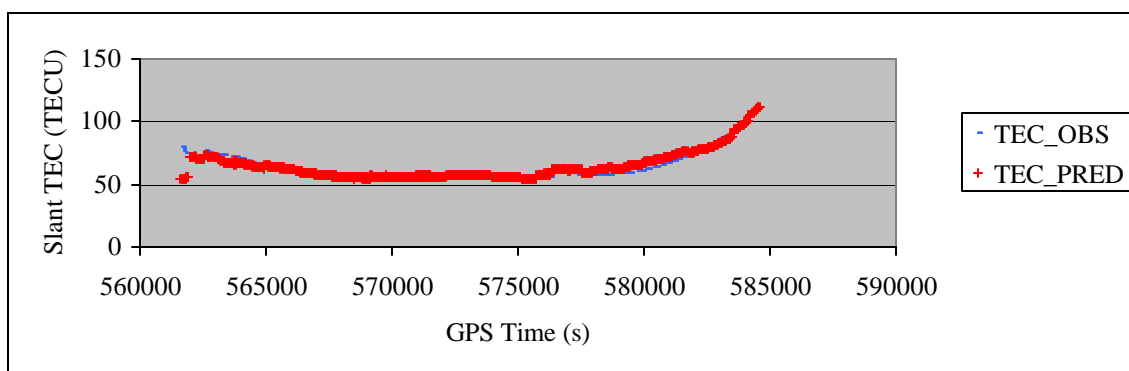


Figure 6.85 Comparison of Observed and Predicted TEC for PRN 02 at COSO Station on DOY 090 at 20° Cutoff and 10-min Prediction Interval
(VTEC RMS= 3.195 TECU, Relative Error = 5.79%)

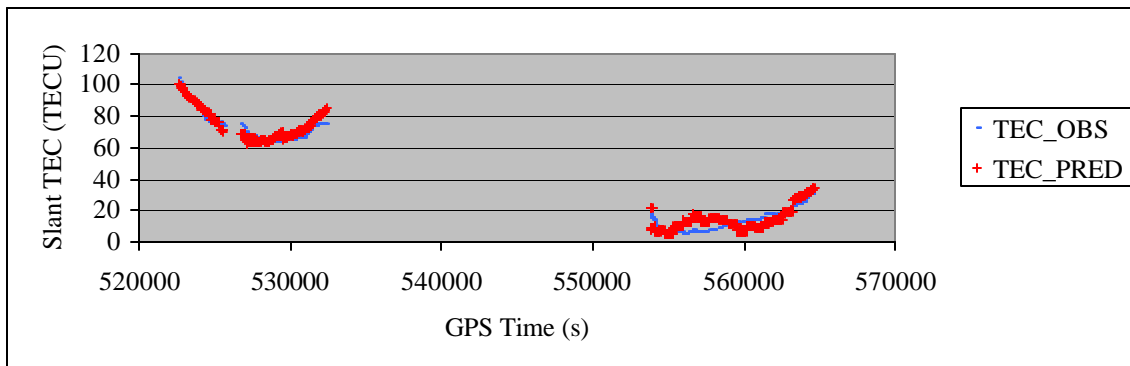


Figure 6.86 Comparison of Observed and Predicted TEC for PRN 03 at AMC2 Station on DOY 090 at 20° Cutoff and 10-min Prediction Interval
(VTEC RMS= 2.756 TECU, Relative Error = 29.09%)

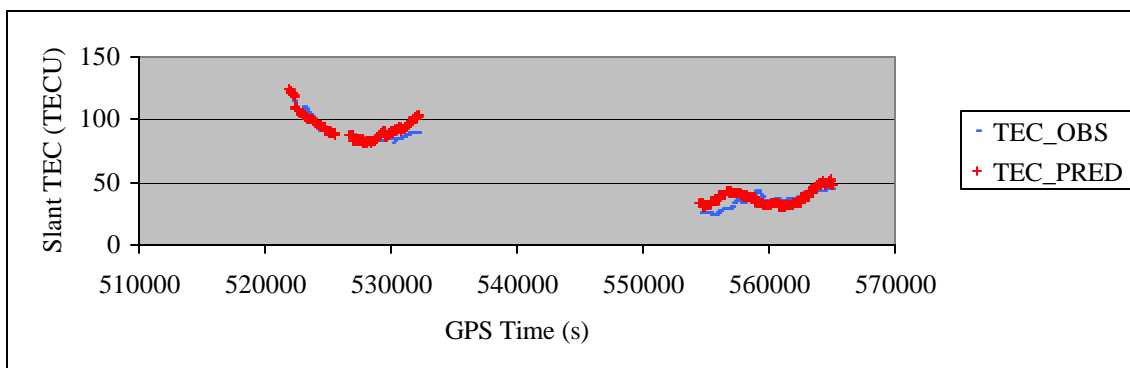


Figure 6.87 Comparison of Observed and Predicted TEC for PRN 03 at CASP Station on DOY 090 at 20° Cutoff and 10-min Prediction Interval
(VTEC RMS= 3.430 TECU, Relative Error = 11.49%)

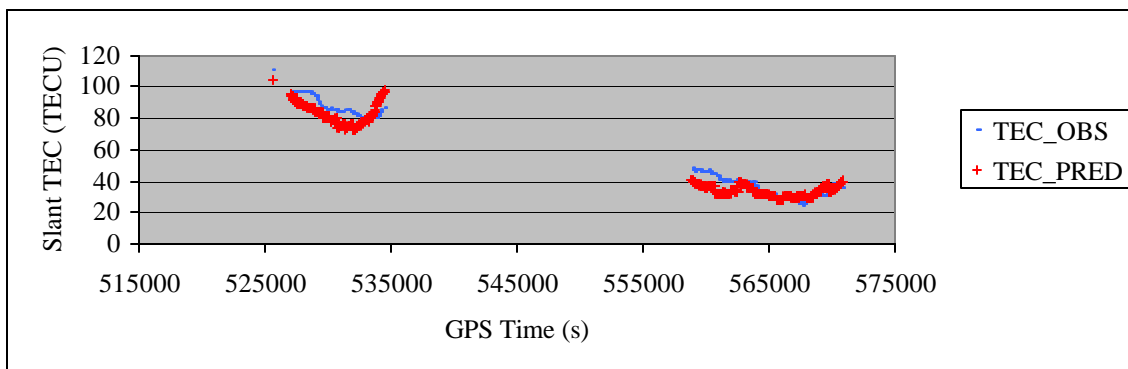


Figure 6.88 Comparison of Observed and Predicted TEC for PRN 31 at PRDS Station on DOY 090 at 20° Cutoff and 10-min Prediction Interval (VTEC RMS= 3.355 TECU, Relative Error = 8.94%)

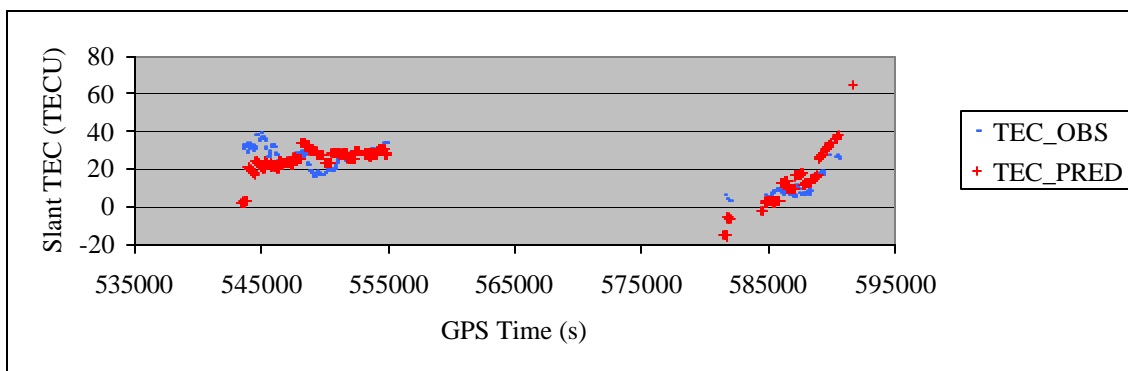


Figure 6.89 Comparison of Observed and Predicted TEC for PRN 04 at FAIR Station on DOY 090 at 20° Cutoff and 10-min Prediction Interval (VTEC RMS= 5.171 TECU, Relative Error = 45.29%)

Table 6.13 summarizes the vertical TEC prediction errors and slant TEC relative errors for all stations in the network. It indicates that at most stations the VTEC prediction RMS errors are between 4.0 TECU and 5.0 TECU. Only six stations have an RMS error larger than 5.0 TECU. All other 16 stations have a VTEC prediction RMS error less than 5.0 TECU. Most stations among the 16 stations are actually at the level of 4.0 TECU. The average RMS error for all stations is 4.811 TECU. In terms of relative error, it varies from station to station because of significant differences for the magnitude of the observed TEC at each station. Table 6.13 shows that 9 of the 22 stations have a relative error smaller than 10.0%. Among those 22 stations, 17 have a relative error less than

30.0%. The left five stations have a relative error larger than other stations. Overall, the mean relative error in the network is 20.35%, which means using the tomographic model 10-min TEC predictions can recover about 79.65% of the ionospheric TEC range delays.

Table 6.13 Error Statistics for 10-min VTEC Prediction with Cutoff 20° on DOY 090

STATION	VTEC Error RMS (TECU)	Relative Error (%)
ALBH	4.728	27.83%
ALGO	5.798	30.13%
AMC2	4.720	29.86%
CARR	4.068	7.34%
CASP	5.319	13.71%
COSO	4.106	7.33%
DAM2	4.639	7.06%
DRAO	4.545	51.19%
FAIR	4.480	48.36%
FLIN	6.176	34.12%
HOLB	4.314	23.45%
HOPB	4.062	6.89%
KODK	4.273	7.49%
NEAH	4.625	8.01%
NRC1	5.750	7.89%
PRDS	5.711	13.15%
SCH2	4.421	26.10%
STJO	4.784	32.81%
USNO	6.207	32.57%
VNDP	4.406	6.53%
WHIT	4.348	7.12%
WSLR	4.370	18.72%
Mean	4.811	20.35%

6.3.2.3 Results of Scheme 6 (20°, 30 min)

6.3.2.3.1 Results on ionosphere quiet day DOY 089

In order to evaluate the model's performance for long-term TEC prediction, Scheme 6 using 20° elevation cutoff angle and 30-min prediction interval is used to both ionosphere quiet and disturbed time periods. Figure 6.90 to Figure 6.95 show the TEC comparison

results on six GPS stations. It can be seen the 30-min TEC predictions basically have a good agreement with the TEC observations at all stations. At the low latitude stations like CARR and COSO, the agreements are better than those from high latitude stations. A comparison to the results from Scheme 3 (15° , 30-min) show that at the two low latitude stations, CARR and COSO, the VTEC prediction errors are smaller than those obtained in Scheme 3 for DOY 089. Although the comparisons of other four figures in this scheme with Scheme 3 have a different situation, the mean VTEC prediction error of this scheme for the entire network shows that the use of 20° as the cutoff angle is slightly better (improved by 0.087 TECU) than the use of 15° when the TEC predictions are performed at 30-min intervals under ionosphere quiet conditions.

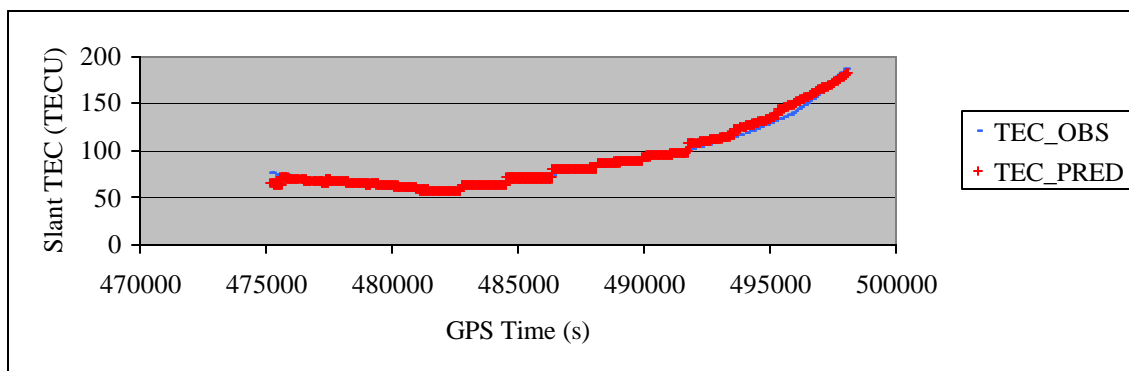


Figure 6.90 Comparison of Observed and Predicted TEC for PRN 02 at CARR Station on DOY 089 at 20° Cutoff and 30-min Prediction Interval
(VTEC RMS= 3.380 TECU, Relative Error = 4.26%)

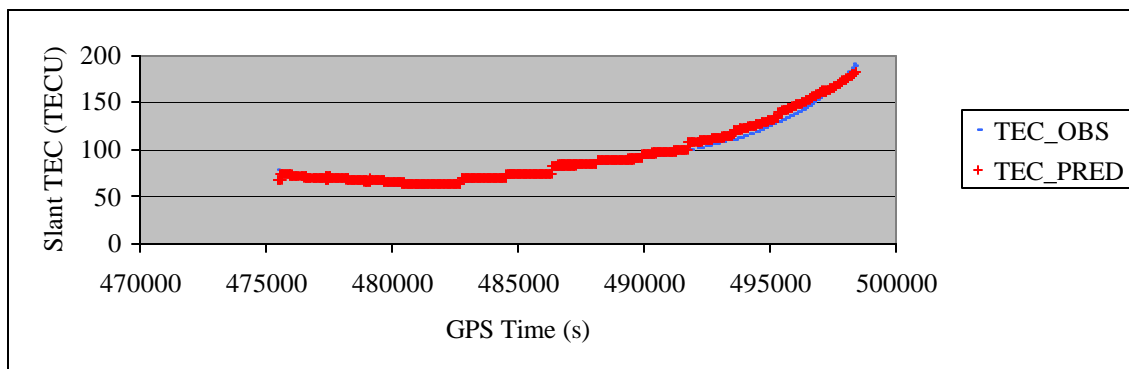


Figure 6.91 Comparison of Observed and Predicted TEC for PRN 02 at COSO Station on DOY 089 at 20° Cutoff and 30-min Prediction Interval
(VTEC RMS= 3.825 TECU, Relative Error = 4.92%)

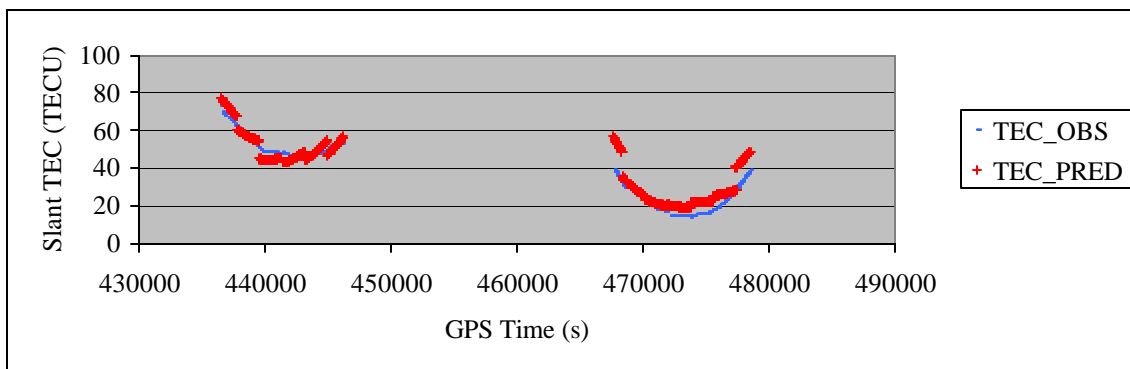


Figure 6.92 Comparison of Observed and Predicted TEC for PRN 03 at AMC2 Station on DOY 089 at 20° Cutoff and 30-min Prediction Interval
(VTEC RMS= 3.215 TECU, Relative Error = 17.65%)

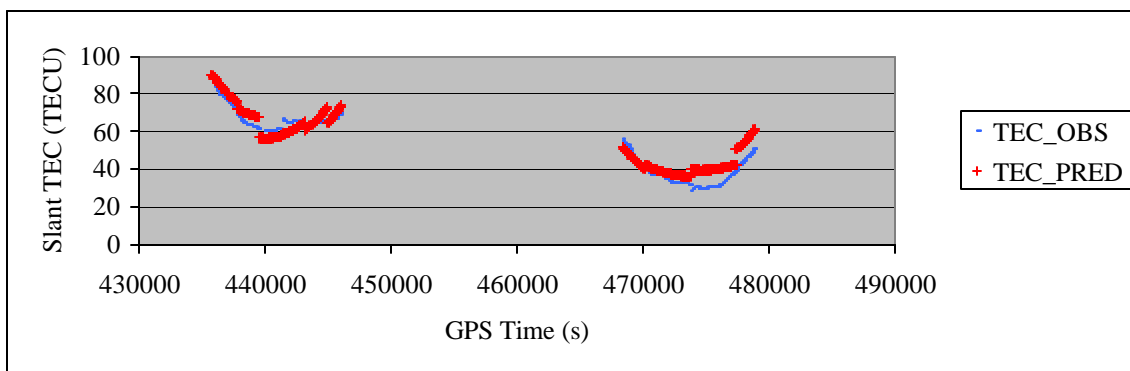


Figure 6.93 Comparison of Observed and Predicted TEC for PRN 03 at CASP Station on DOY 089 at 20° Cutoff and 30-min Prediction Interval
(VTEC RMS= 3.509 TECU, Relative Error = 11.71%)

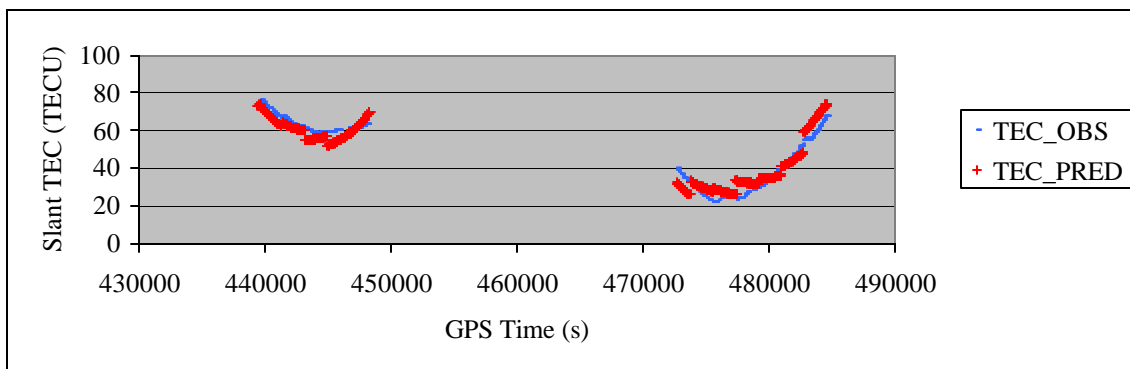


Figure 6.94 Comparison of Observed and Predicted TEC for PRN 31 at PRDS Station on DOY 089 at 20° Cutoff and 30-min Prediction Interval
(VTEC RMS= 2.811 TECU, Relative Error = 10.09%)

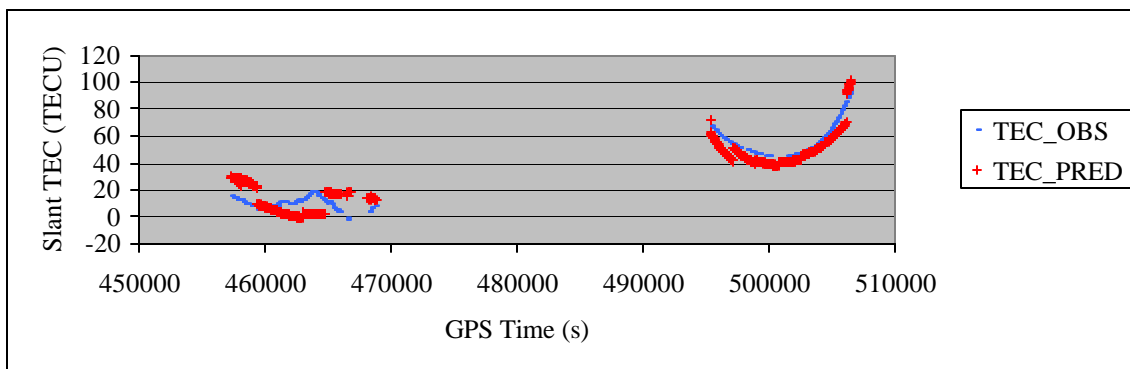


Figure 6.95 Comparison of Observed and Predicted TEC for PRN 04 at FAIR Station on DOY 089 at 20° Cutoff and 30-min Prediction Interval (VTEC RMS= 6.177 TECU, Relative Error = 85.14%)

Table 6.14 Error Statistics for 30-min VTEC Prediction with Cutoff 20° on DOY 089

STATION	VTEC Error RMS (TECU)	Relative Error (%)
ALBH	3.635	17.25%
ALGO	3.736	26.43%
AMC2	3.511	18.58%
CARR	3.775	5.78%
CASP	3.563	9.37%
COSO	3.666	5.39%
DAM2	3.799	4.92%
DRAO	3.727	23.92%
FAIR	4.889	33.19%
FLIN	3.886	22.42%
HOLB	3.636	24.19%
HOPB	3.536	5.13%
KODK	5.082	9.47%
NEAH	3.553	6.63%
NRC1	3.853	5.66%
PRDS	4.210	12.08%
SCH2	4.457	24.93%
STJO	4.427	18.53%
USNO	3.662	13.94%
VNDP	3.775	4.88%
WHIT	4.796	7.76%
WSLR	3.528	26.24%
Mean	3.941	14.85%

Table 6.14 summarizes the vertical TEC prediction RMS errors and relative errors for the Scheme 6 (20°, 30-min) on the ionosphere quiet day. The results show that the RMS errors at most stations are at the level of 3.0~4.0 TECU. The RMS errors at some stations could be at the level of 4.0~5.0 TECU. It shows that only six stations have an RMS error over 4.0 TECU. All other 16 stations have accuracy better than 4.0 TECU. The largest RMS error is 5.082 TECU, slightly over 5.0 TECU. As to the mean RMS error, this scheme has a value of 3.941 TECU. Table 6.14 indicates that 10 of the 22 stations have a relative error less than 10.0% and 15 of the 22 stations have a relative error less than 20.0%. The mean relative error in the network is 14.85%.

6.3.2.3.2 Results on ionosphere disturbed day DOY 090

Presented in Figure 6.96 to Figure 6.101 are the TEC comparison results on ionosphere disturbed day DOY 090 using 20° elevation cutoff with a 30-min prediction interval. The figures show that at the low latitude stations like CARR and COSO, the discrepancies between the TEC predictions and observations are generally in a good agreement. However for the stations with higher latitudes, the disagreements become larger, particularly at FAIR station (the most northern station in the network). Comparing the results with those in Scheme 3 (15°, 30-min) on DOY 090, five stations in Scheme 6 have a larger VTEC prediction error than that in Scheme 3. In terms of the mean VTEC prediction error for the network, the mean value in Scheme 6 is 5.592 TECU, which is also larger than 5.546 TECU from Scheme 3 as shown in Table 6.9. The analysis shows that during ionosphere disturbed period with a 30-min prediction interval in the network, the use of 15° as the elevation cutoff angle would produce a slightly better prediction accuracy than using 20°.

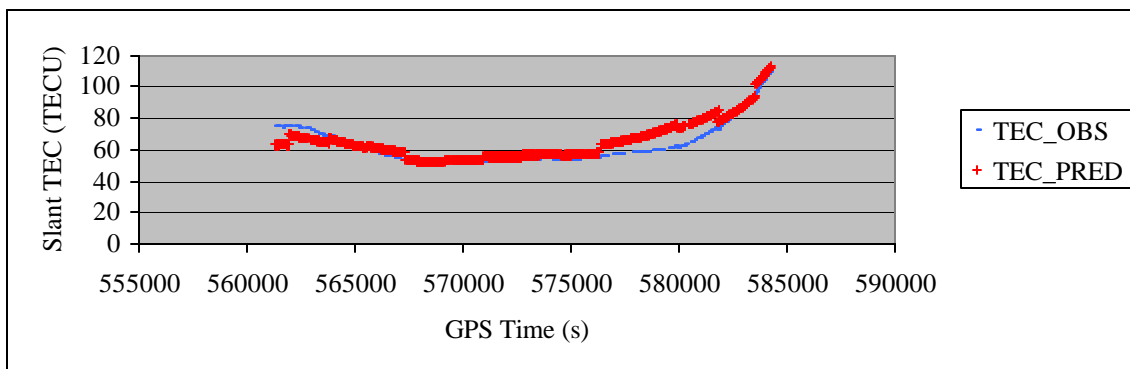


Figure 6.96 Comparison of Observed and Predicted TEC for PRN 02 at CARR Station on DOY 090 at 20° Cutoff and 30-min Prediction Interval (VTEC RMS= 4.743 TECU, Relative Error = 8.52%)

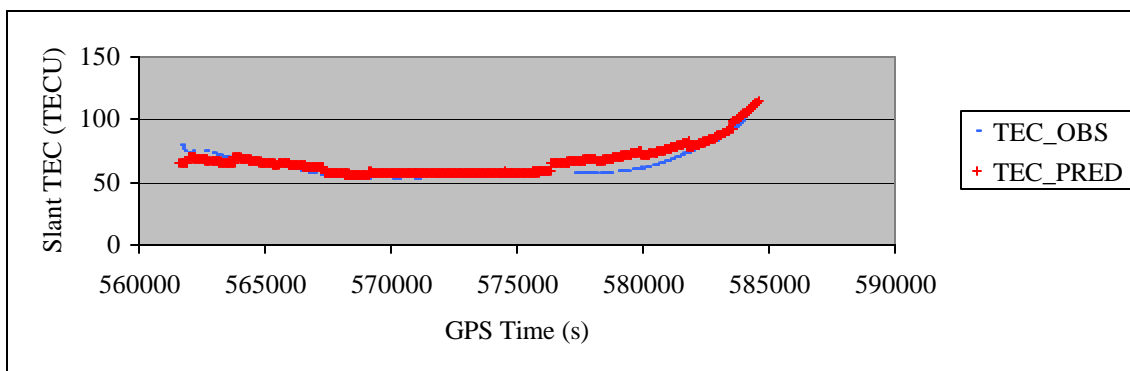


Figure 6.97 Comparison of Observed and Predicted TEC for PRN 02 at COSO Station on DOY 090 at 20° Cutoff and 30-min Prediction Interval (VTEC RMS= 5.175 TECU, Relative Error = 9.40%)

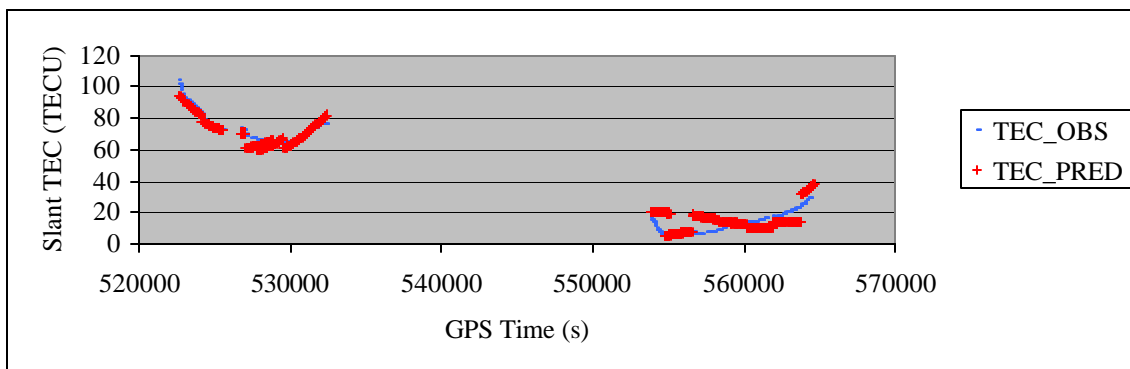


Figure 6.98 Comparison of Observed and Predicted TEC for PRN 03 at AMC2 Station on DOY 090 at 20° Cutoff and 30-min Prediction Interval (VTEC RMS= 3.225 TECU, Relative Error = 37.64%)

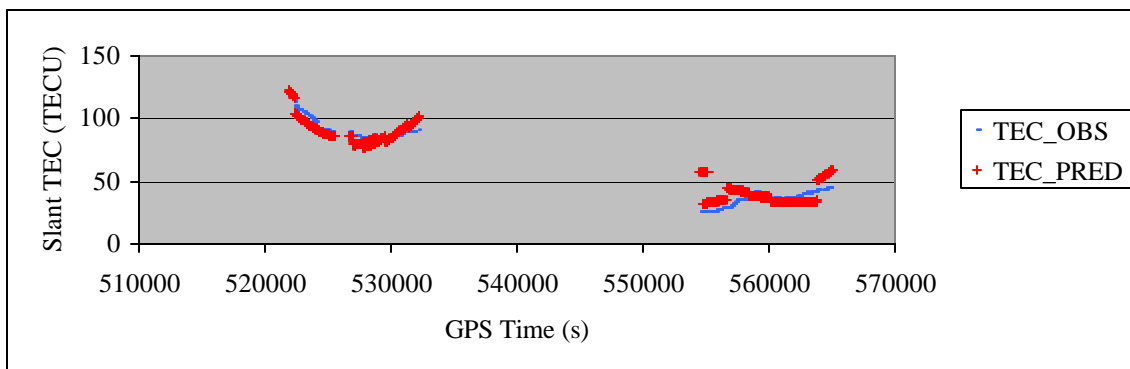


Figure 6.99 Comparison of Observed and Predicted TEC for PRN 03 at CASP Station on DOY 090 at 20° Cutoff and 30-min Prediction Interval (VTEC RMS= 4.353 TECU, Relative Error = 14.96%)

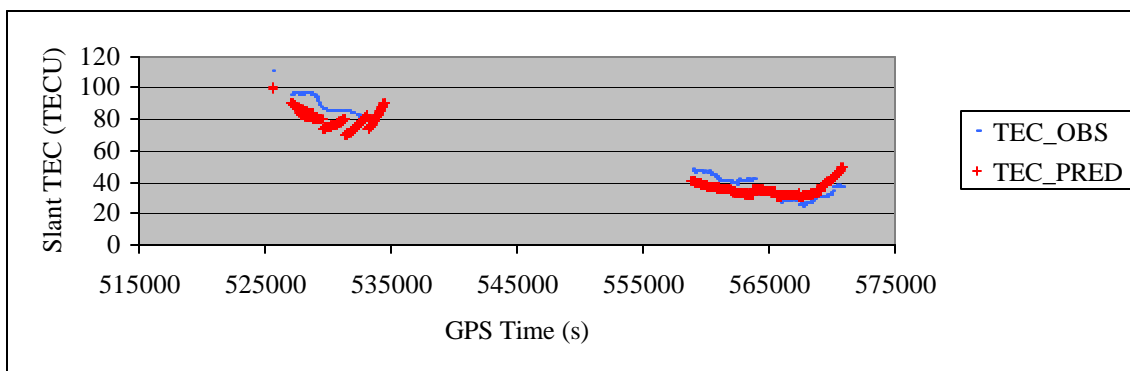


Figure 6.100 Comparison of Observed and Predicted TEC for PRN 31 at PRDS Station on DOY 090 at 20° Cutoff and 30-min Prediction Interval (VTEC RMS= 4.564 TECU, Relative Error = 13.30%)

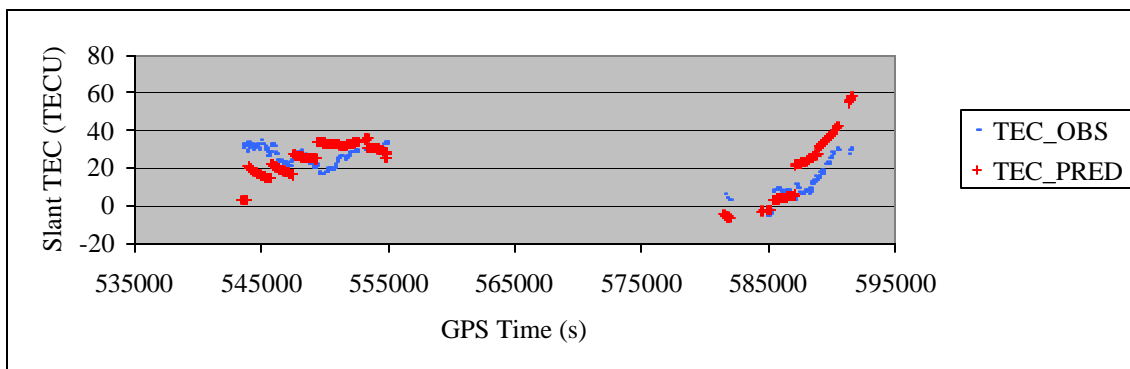


Figure 6.101 Comparison of Observed and Predicted TEC for PRN 04 at FAIR Station on DOY 090 at 20° Cutoff and 30-min Prediction Interval (VTEC RMS= 7.163 TECU, Relative Error = 61.62%)

Table 6.15 Error Statistics for 30-min VTEC Prediction with Cutoff 20° on DOY 090

STATION	VTEC Error RMS (TECU)	Relative Error (%)
ALBH	5.750	31.82%
ALGO	6.281	34.48%
AMC2	5.420	34.63%
CARR	4.946	9.03%
CASP	6.089	16.64%
COSO	4.917	8.99%
DAM2	5.357	8.12%
DRAO	5.509	61.51%
FAIR	5.274	58.64%
FLIN	6.593	38.88%
HOLB	5.422	31.45%
HOPB	4.986	8.53%
KODK	5.097	9.36%
NEAH	5.618	9.93%
NRC1	6.095	8.78%
PRDS	6.527	16.61%
SCH2	5.299	30.05%
STJO	5.419	37.92%
USNO	6.627	36.16%
VNDP	5.216	7.81%
WHIT	5.187	8.59%
WSLR	5.400	24.70%
Mean	5.592	24.21%

Table 6.15 shows a summary of the VTEC prediction error and relative error at individual stations on DOY 090 using Scheme 6 (20°, 30-min). Table 6.15 indicates that the RMS error at most stations is at the order of 5.0~6.0 TECU. It shows that only six stations have an RMS error larger than 6.0 TECU. The RMS errors at other 16 stations are all better than 6.0 TECU. The mean RMS error in the network is 5.592 TECU. Table 6.15 clearly shows that 9 of the 22 stations have a relative error less than 10.0%. Most stations have a relative error smaller than or just slightly over 30.0%. There are just a few stations that have a relative error much larger than 30.0%. The network's mean relative error for this scheme is 24.21%.

6.3.3 Results of high elevation cutoff angle (25°)

6.3.3.1 Results of Scheme 7 (25°, 5 min)

6.3.3.1.1 Results on ionosphere quiet day DOY 089

The results below show the TEC comparisons for Scheme 7 on the ionosphere quiet day using elevation cutoff 25° with a 5-min TEC prediction interval. Figure 6.102 to Figure 6.107 show that the predicted TEC data agree with the observed TEC data very well. The only exception occurs at the first portion of the data at FAIR station. Therefore the VTEC prediction RMS error for PRN 04 at FAIR station becomes much larger than the RMS errors shown in other figures. Compared to the results of Scheme 4 (20°, 5-min), it can be found at the low latitude stations CARR and COSO, the VTEC prediction errors in this scheme is smaller than Scheme 4. However for high latitude stations AMC2, CASP and FAIR stations, the RMS errors of this scheme are larger than Scheme 4. For the whole network, the mean RMS error in this scheme is 3.180 TECU and it is 3.277 TECU for Scheme 4. In terms of relative error, it is 12.41% in Scheme 4 but it is 12.28% in this scheme. The result indicates that the use of 25° as the cutoff angle is better than using 20° for ionosphere modeling over a wide area GPS network under quiet conditions with a 5-min prediction interval.

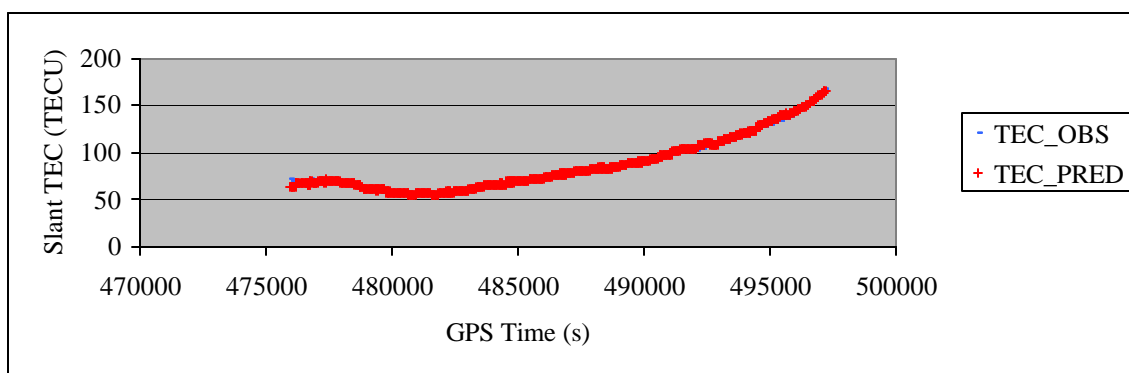


Figure 6.102 Comparison of Observed and Predicted TEC for PRN 02 at CARR Station on DOY 089 at 25° Cutoff and 5-min Prediction Interval
(VTEC RMS= 2.076 TECU, Relative Error = 2.71%)

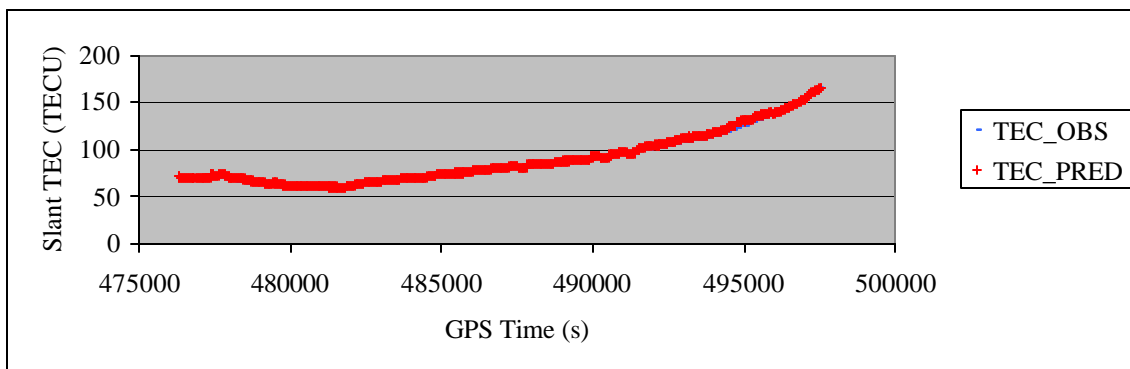


Figure 6.103 Comparison of Observed and Predicted TEC for PRN 02 at COSO Station on DOY 089 at 25° Cutoff and 5-min Prediction Interval (VTEC RMS= 2.324 TECU, Relative Error = 3.04%)

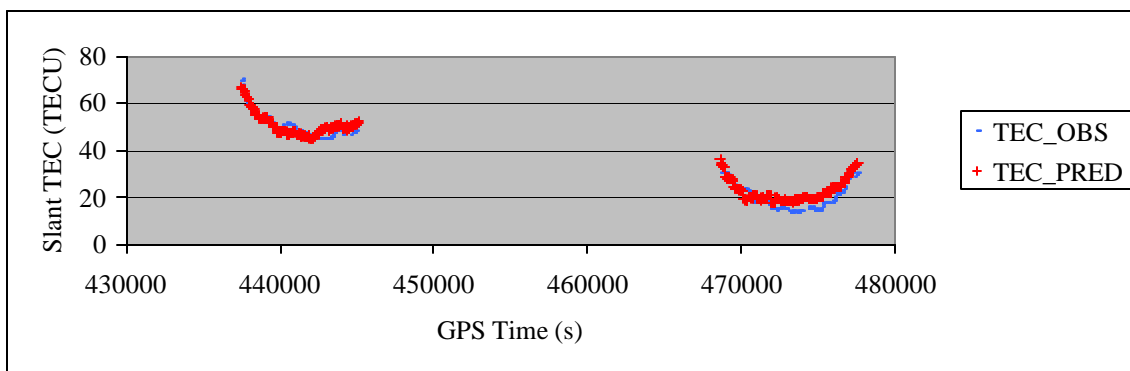


Figure 6.104 Comparison of Observed and Predicted TEC for PRN 03 at AMC2 Station on DOY 089 at 25° Cutoff and 5-min Prediction Interval (VTEC RMS= 2.078 TECU, Relative Error = 12.96%)

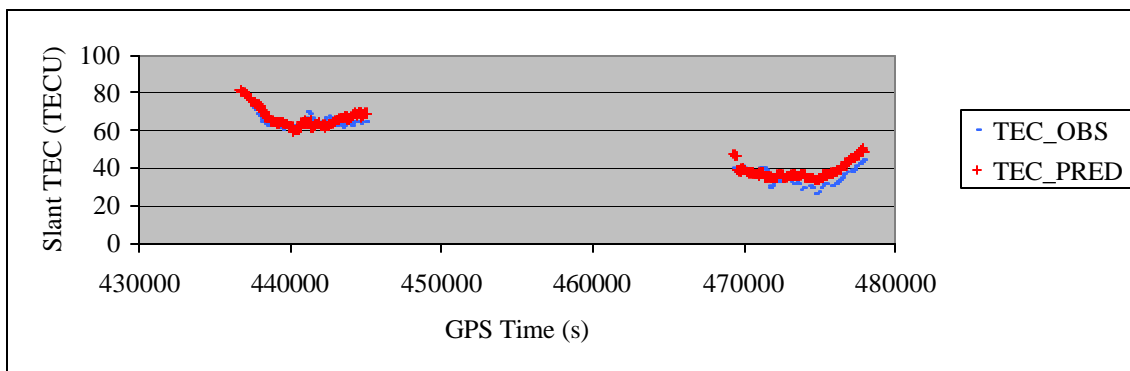


Figure 6.105 Comparison of Observed and Predicted TEC for PRN 03 at CASP Station on DOY 089 at 25° Cutoff and 5-min Prediction Interval (VTEC RMS= 2.764 TECU, Relative Error = 9.40%)

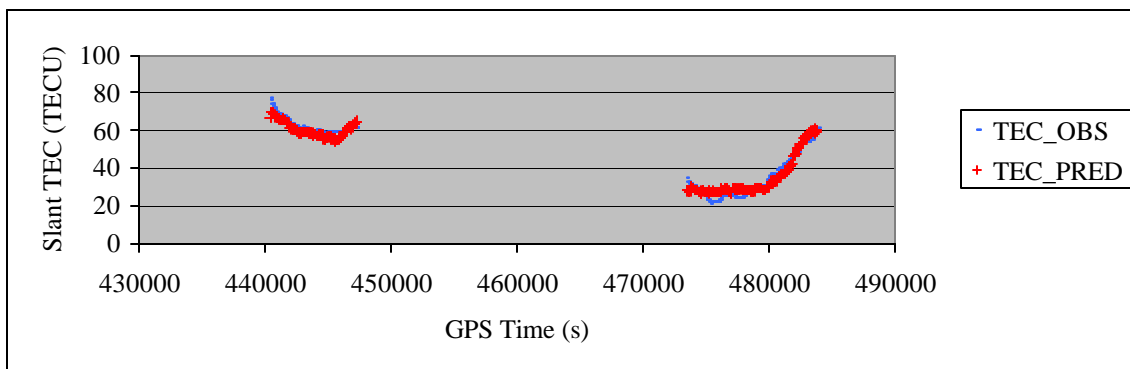


Figure 6.106 Comparison of Observed and Predicted TEC for PRN 31 at PRDS Station on DOY 089 at 25° Cutoff and 5-min Prediction Interval
(VTEC RMS= 2.005 TECU, Relative Error = 7.23%)

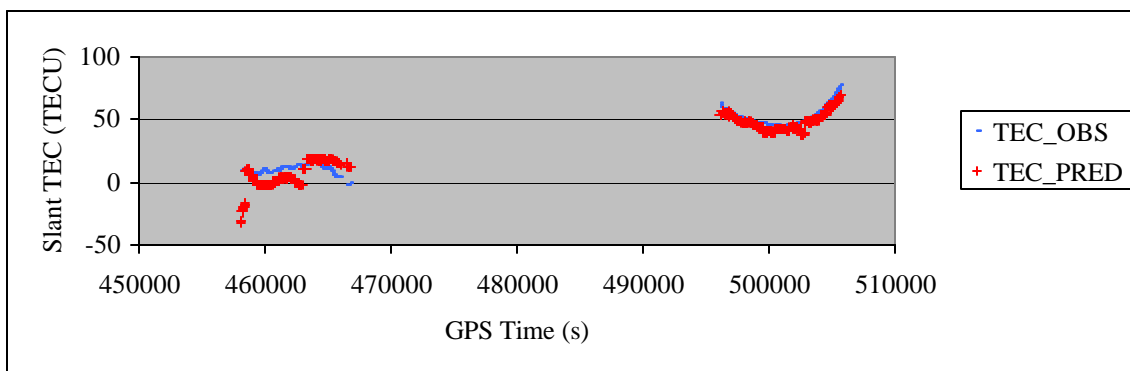


Figure 6.107 Comparison of Observed and Predicted TEC for PRN 04 at FAIR Station on DOY 089 at 25° Cutoff and 5-min Prediction Interval
(VTEC RMS= 5.002 TECU, Relative Error = 67.27%)

Table 6.16 summarizes the VTEC prediction errors and relative errors for all stations on DOY 089. It can be seen that at most stations the VTEC prediction errors are at the level of 2.0~4.0 TECU. Only two stations have a large prediction error over 4.0 TECU. Table 6.16 indicates that most stations have a VTEC prediction RMS error smaller than or only slightly greater than 3.0 TECU. The mean error of the network is 3.180 TECU. As to the relative error, Table 6.16 indicates that 11 of the 22 stations have a relative error less than 10.0%. It also shows that 18 of the 22 stations have a relative error smaller than 20.0%. The rest four stations have a larger relative error but two of them have an error just

slightly over 20.0%. The network's mean relative error for this scheme is as low as 12.28%.

Table 6.16 Error Statistics for 5-min VTEC Prediction with Cutoff 25° on DOY 089

STATION	VTEC Error RMS (TECU)	Relative Error (%)
ALBH	2.881	12.60%
ALGO	2.881	20.28%
AMC2	2.938	17.12%
CARR	3.044	4.45%
CASP	3.031	8.25%
COSO	2.927	4.24%
DAM2	3.338	4.23%
DRAO	2.857	17.68%
FAIR	4.613	35.87%
FLIN	3.501	22.75%
HOLB	2.689	17.48%
HOPB	2.887	4.08%
KODK	4.380	7.26%
NEAH	2.751	4.72%
NRC1	3.095	4.49%
PRDS	3.036	9.17%
SCH2	3.522	20.64%
STJO	3.094	13.74%
USNO	3.039	12.46%
VNDP	3.109	3.83%
WHIT	3.667	5.53%
WSLR	2.682	19.25%
Mean	3.180	12.28%

6.3.3.1.2 Results on ionosphere disturbed day DOY 090

Figure 6.108 to Figure 6.113 present the TEC comparison results for six TEC pairs observed on an ionospherically disturbed day. The goal of this scheme is to analyze the model performance under the condition of using 25° elevation cutoff to perform 5-min TEC predictions. The following plots show the discrepancies between the predicted and observed TEC. It can be seen that in the six pairs of TEC data, the TEC predictions and the observed TEC agree with each other very well. This is verified by the small VTEC

RMS errors shown in the parentheses of the caption line in each figure. Comparing to the results in Scheme 4 (20°, 5-min) on DOY 090, it can be found that the results of this scheme have smaller VTEC RMS values. All stations in this scheme (25°, 5-min) have an improvement of about 0.1~0.7 TECU over the results obtained from Scheme 4 (20°, 5-min) except the station CASP which has a degradation of 0.003 TECU. In terms of the mean RMS error for the whole network, it is found that this scheme has a smaller mean RMS error, 4.554 TECU, than the mean value 4.666 TECU in Scheme 4. The mean relative error for this scheme is 18.75% also lower than 19.61% from Scheme 4. The analysis indicates that ionospheric modeling over a wide area GPS network during ionosphere disturbed time periods with a 5-min TEC prediction interval, the use of 25° as the elevation cutoff angle would provide better prediction accuracies than using 20°.

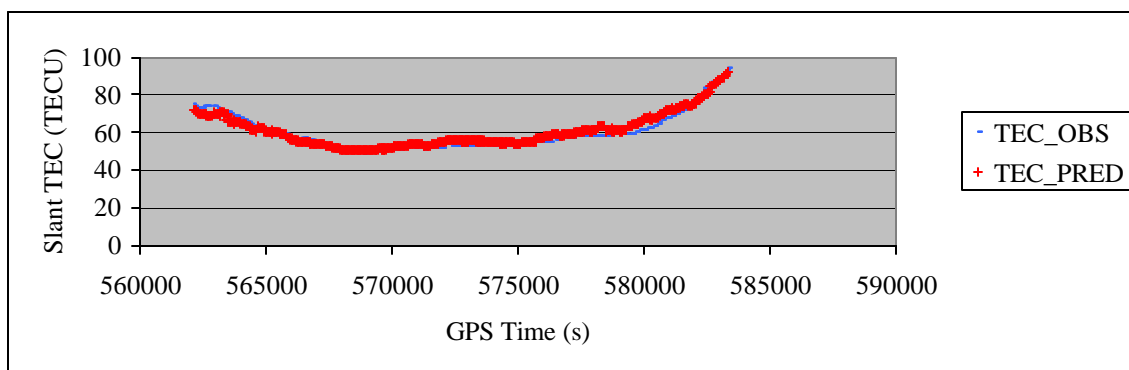


Figure 6.108 Comparison of Observed and Predicted TEC for PRN 02 at CARR Station on DOY 090 at 25° Cutoff and 5-min Prediction Interval
(VTEC RMS= 2.184 TECU, Relative Error = 4.04%)

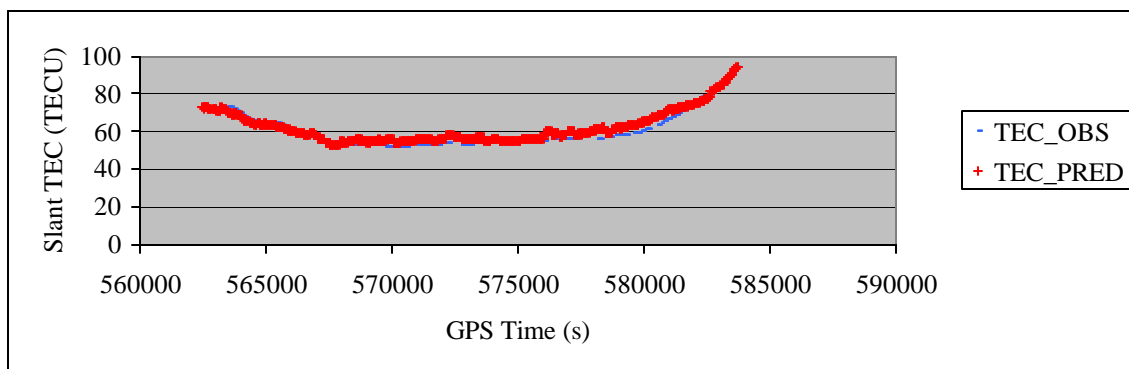


Figure 6.109 Comparison of Observed and Predicted TEC for PRN 02 at COSO Station on DOY 090 at 25° Cutoff and 5-min Prediction Interval
(VTEC RMS= 2.559 TECU, Relative Error = 4.57%)

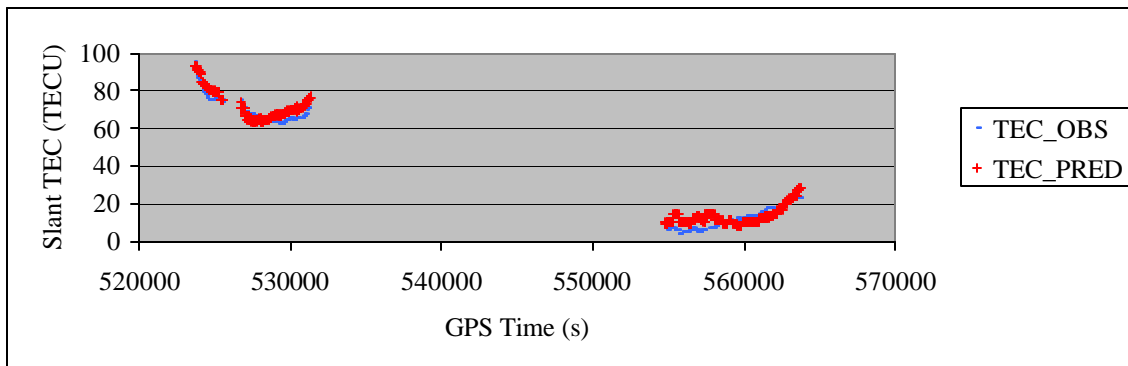


Figure 6.110 Comparison of Observed and Predicted TEC for PRN 03 at AMC2 Station on DOY 090 at 25° Cutoff and 5-min Prediction Interval
(VTEC RMS= 2.569 TECU, Relative Error = 30.67%)

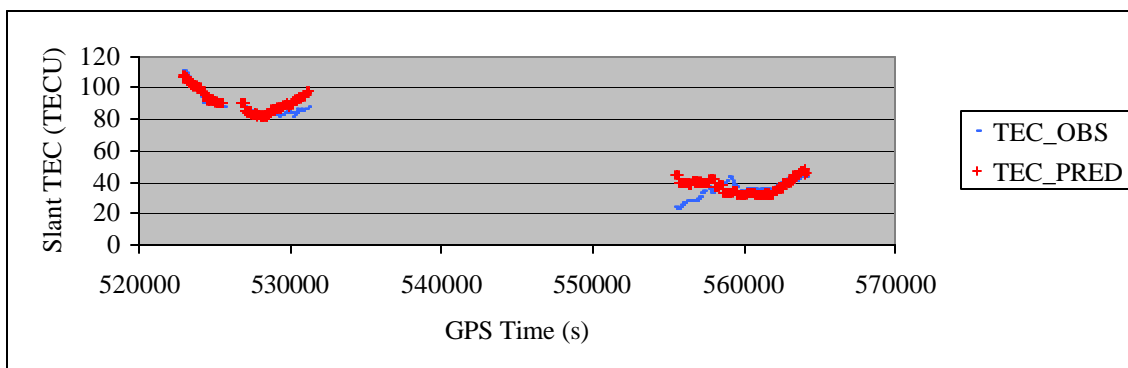


Figure 6.111 Comparison of Observed and Predicted TEC for PRN 03 at CASP Station on DOY 090 at 25° Cutoff and 5-min Prediction Interval
(VTEC RMS= 3.434 TECU, Relative Error = 10.71%)

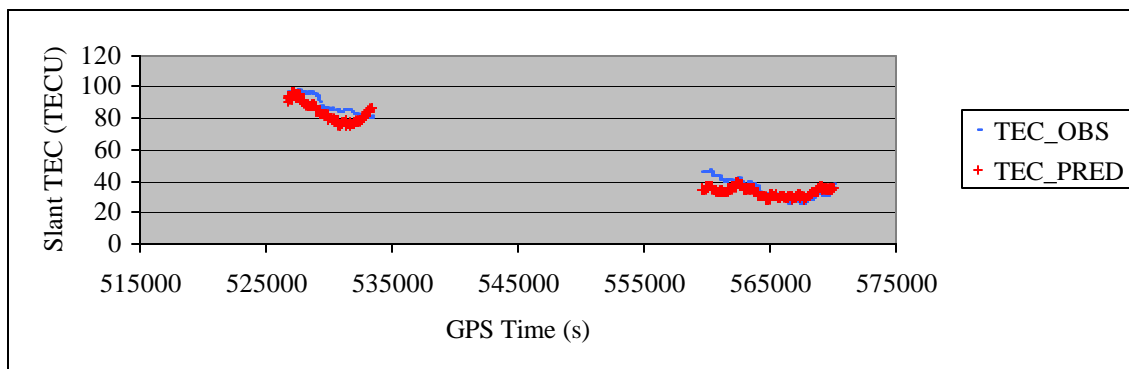


Figure 6.112 Comparison of Observed and Predicted TEC for PRN 31 at PRDS Station on DOY 090 at 25° Cutoff and 5-min Prediction Interval
(VTEC RMS= 2.934 TECU, Relative Error = 8.12%)

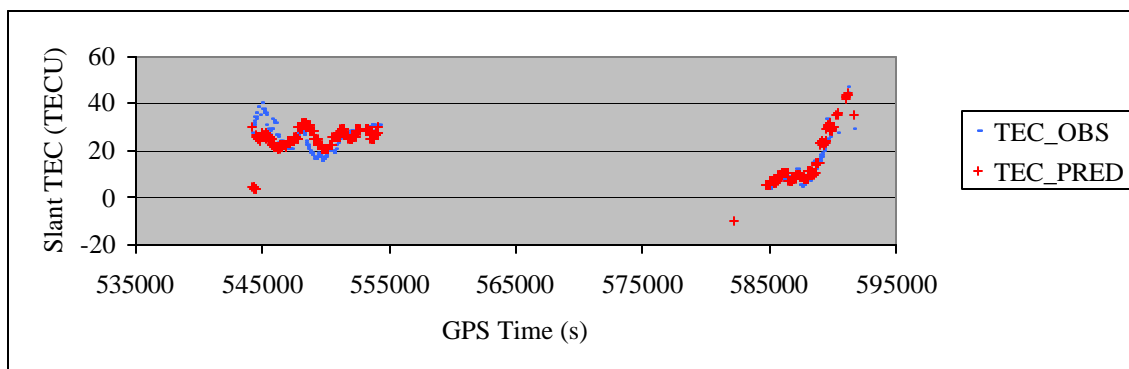


Figure 6.113 Comparison of Observed and Predicted TEC for PRN 04 at FAIR Station on DOY 090 at 25° Cutoff and 5-min Prediction Interval
(VTEC RMS= 3.576 TECU, Relative Error = 21.76%)

The VTEC prediction errors and relative errors from Scheme 7 (25°, 5-min) on DOY 090 are summarized in Table 6.17. The results show that most stations have VTEC prediction errors in the range from 3.0 to 5.0 TECU. Table 6.17 indicates that 16 of the 22 stations have an RMS error smaller than 5.0 TECU. Only six stations have VTEC prediction accuracy worse than 5.0 TECU. It shows that the mean RMS error of the network is 4.554 TECU. Table 6.17 indicates that 5-min TEC predictions can averagely recover 81.25% of the total TEC and the unrecovered TEC error is about 18.75%. It shows that even under extremely disturbed conditions 9 stations have a relative error smaller than 10.0%. It is also shown that the relative errors at 20 of the 22 stations are less than or

around the level of 30.0%. Only 2 stations have a much larger relative error than other stations. But their relative errors are still bounded to the level of 45%.

Table 6.17 Error Statistics for 5-min VTEC Prediction with Cutoff 25° on DOY 090

STATION	VTEC Error RMS (TECU)	Relative Error (%)
ALBH	4.443	24.38%
ALGO	5.516	28.81%
AMC2	4.381	29.10%
CARR	3.805	6.63%
CASP	5.205	13.36%
COSO	3.889	6.78%
DAM2	4.433	6.57%
DRAO	4.282	45.79%
FAIR	4.127	42.11%
FLIN	6.134	32.69%
HOLB	3.989	20.76%
HOPB	3.644	6.14%
KODK	3.878	6.66%
NEAH	4.416	7.26%
NRC1	5.567	7.39%
PRDS	5.574	12.04%
SCH2	4.208	24.80%
STJO	4.470	30.85%
USNO	5.699	30.20%
VNDP	4.205	6.08%
WHIT	4.225	6.75%
WSLR	4.103	17.24%
Mean	4.554	18.75%

6.3.3.2 Results of Scheme 8 (25°, 10 min)

6.3.3.2.1 Results on ionosphere quiet day DOY 089

Figure 6.114 to Figure 6.119 present the comparison results from six pairs of TEC data at six stations on DOY 089 using 25° as the elevation cutoff angle and 10-min prediction interval. The plots show that the predicted TEC data and observed TEC data are in a good agreement with each other. The only large disagreements occur at the first portion of the

data at FAIR station. The VTEC prediction RMS errors shown in the parentheses of the caption of each figure indicate that the RMS errors at five stations are better than 3.0 TECU while the FAIR station with a larger error of 5.710 TECU. Compared to the results from Scheme 5 (20°, 10-min), it can be found that at the stations CARR and COSO, an improvement about 0.1 TECU has been received over Scheme 5. At other stations, the performance of Scheme 5 is superior to the present scheme. But overall the present scheme is better than Scheme 5 according to the mean VTEC prediction error. In Scheme 5, the mean RMS error is 3.357 TECU while the present scheme has a mean RMS error 3.272 TECU. The improvement of Scheme 8 over Scheme 5 is 0.085 TECU.

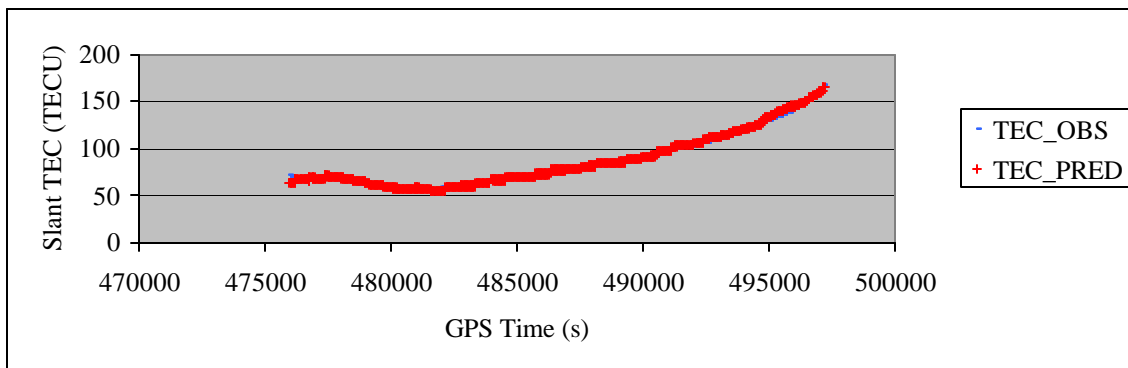


Figure 6.114 Comparison of Observed and Predicted TEC for PRN 02 at CARR Station on DOY 089 at 25° Cutoff and 10-min Prediction Interval
(VTEC RMS= 2.229 TECU, Relative Error = 2.83%)

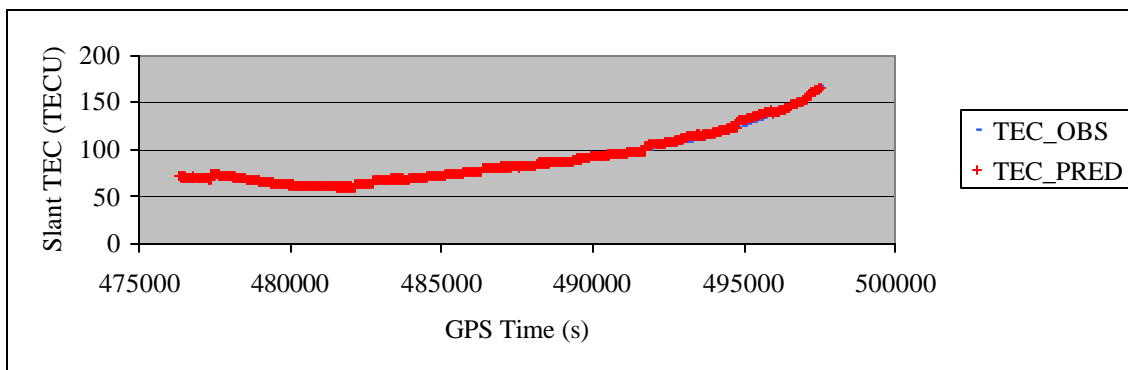


Figure 6.115 Comparison of Observed and Predicted TEC for PRN 02 at COSO Station on DOY 089 at 25° Cutoff and 10-min Prediction Interval
(VTEC RMS= 2.500 TECU, Relative Error = 3.30%)

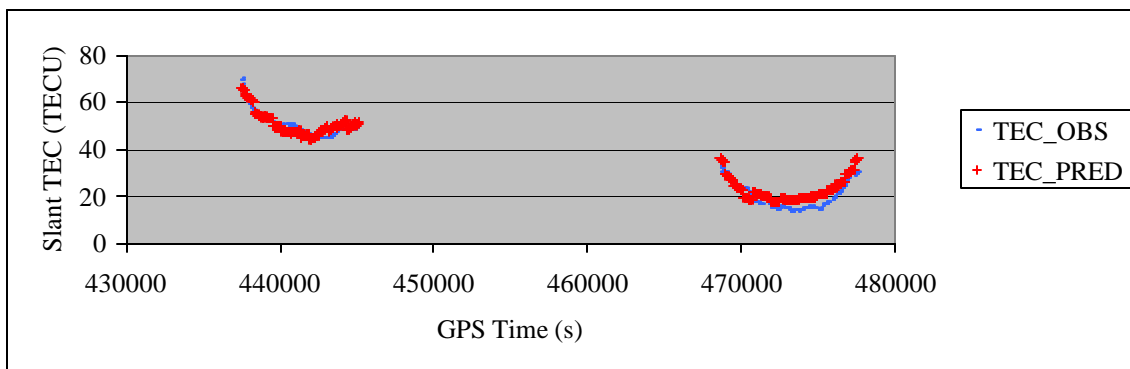


Figure 6.116 Comparison of Observed and Predicted TEC for PRN 03 at AMC2 Station on DOY 089 at 25° Cutoff and 10-min Prediction Interval (VTEC RMS= 2.114 TECU, Relative Error = 13.26%)

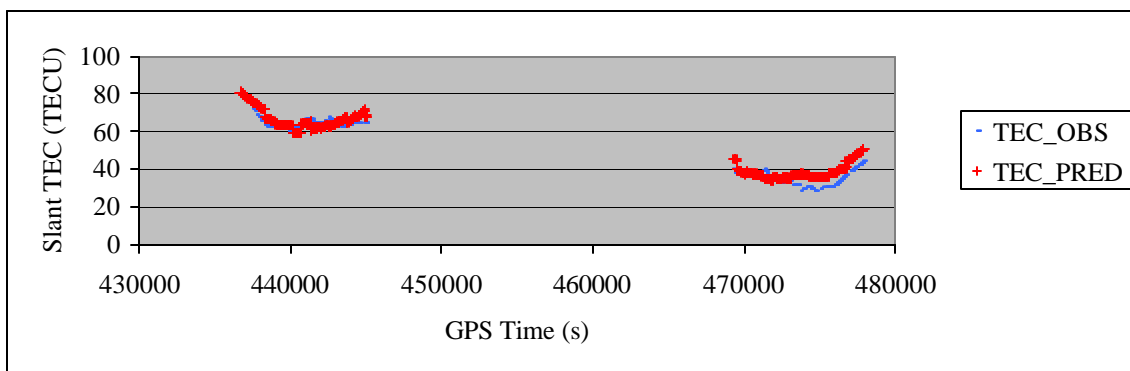


Figure 6.117 Comparison of Observed and Predicted TEC for PRN 03 at CASP Station on DOY 089 at 25° Cutoff and 10-min Prediction Interval (VTEC RMS= 2.800 TECU, Relative Error = 9.37%)

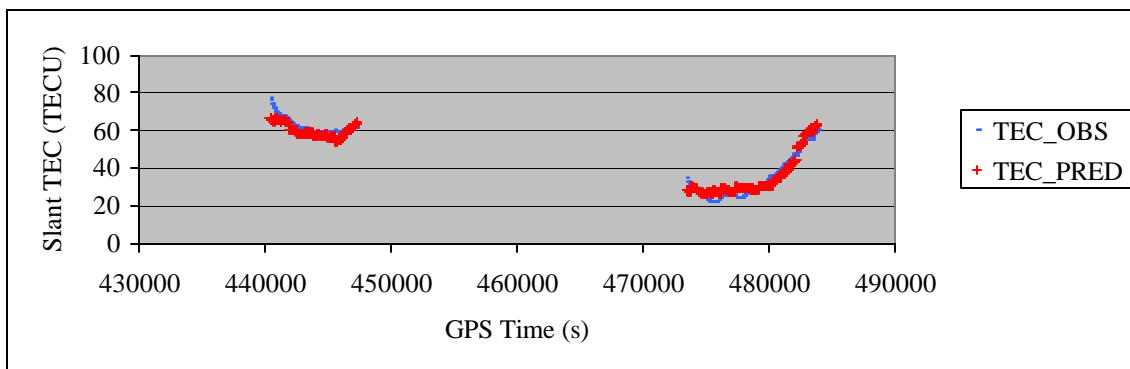


Figure 6.118 Comparison of Observed and Predicted TEC for PRN 31 at PRDS Station on DOY 089 at 25° Cutoff and 10-min Prediction Interval (VTEC RMS= 2.133 TECU, Relative Error = 7.64%)

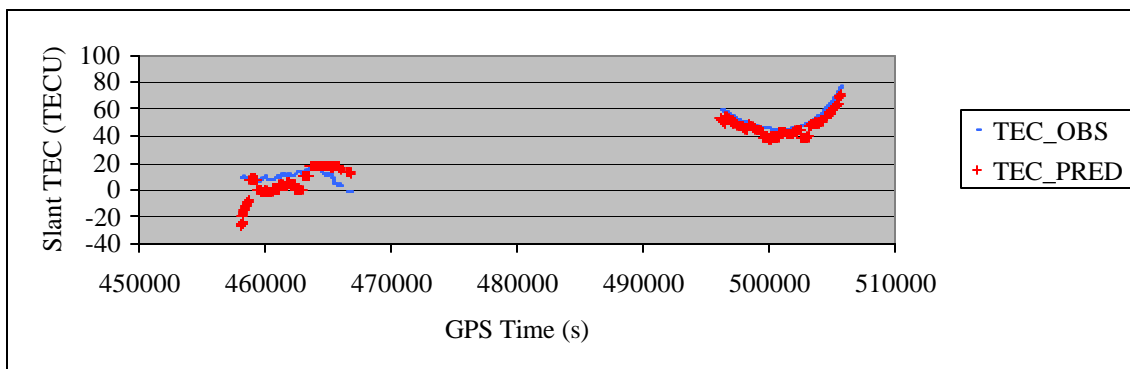


Figure 6.119 Comparison of Observed and Predicted TEC for PRN 04 at FAIR Station on DOY 089 at 25° Cutoff and 10-min Prediction Interval (VTEC RMS= 5.710 TECU, Relative Error = 77.74%)

Table 6.18 Error Statistics for 10-min VTEC Prediction with Cutoff 25° on DOY 089

STATION	VTEC Error RMS (TECU)	Relative Error (%)
ALBH	2.957	12.71%
ALGO	2.981	21.07%
AMC2	3.030	17.58%
CARR	3.147	4.61%
CASP	3.087	8.37%
COSO	3.034	4.40%
DAM2	3.419	4.31%
DRAO	2.947	17.94%
FAIR	4.840	37.30%
FLIN	3.542	22.46%
HOLB	2.786	18.12%
HOPB	2.965	4.22%
KODK	4.243	7.34%
NEAH	2.826	4.89%
NRC1	3.226	4.73%
PRDS	3.144	9.49%
SCH2	3.618	21.47%
STJO	3.284	14.33%
USNO	3.148	12.88%
VNDP	3.176	3.96%
WHIT	3.818	5.82%
WSLR	2.776	20.70%
Mean	3.272	12.67%

Table 6.18 presents the VTEC prediction errors and relative errors for all stations in the network. It can be seen that at most stations the VTEC prediction errors are in the range from 2.0~3.0 TECU. Table 6.18 shows that 7 out of the 22 stations have an RMS error below 3.0 TECU. Ten stations have an RMS error between 3.0~3.5 TECU. The rest five stations have RMS errors between 3.5~5.0 TECU. The mean RMS error of the network is 3.272 TECU. As for the relative errors shown in Table 6.18, it can be seen that 11 out of the 22 stations have a relative error better than 10.0%. Among the 22 stations, 17 stations have a relative error below 20.0%. The other five stations have an error larger than 20.0% but four of them are just slightly more than 20.0%. Table 6.18 shows that the network mean relative error is 12.67%.

6.3.3.2.2 Results on ionosphere disturbed day DOY 090

For the ionosphericly disturbed day, the comparison results of TEC predictions and observations using the elevation cutoff angle 25° and 10-min prediction interval are shown in Figure 6.120 to Figure 6.125. The figures show that two sets of TEC data still have a good agreement with each other though the prediction interval is extended to 10-min from 5-min. After mapping the disagreements of the slant TEC data into the vertical, the VTEC prediction RMS errors of these comparisons show that all of them have accuracies better than 4.0 TECU. Compared to the six figures of Scheme 5 for the same day on DOY 090, it can be found that five out of the six TEC pairs in this scheme have an improvement over Scheme 5. The improvement ranges 0.1~1.3 TECU and varies at different stations. From the network point of view, the mean VTEC RMS error of this scheme also shows an improvement over Scheme 5. The mean RMS error of this scheme is 4.713 TECU while Scheme 5 has an RMS error 4.811 TECU. In this scheme, the mean relative error is 19.50% and in Scheme 5 the value is 20.35%. The analysis results show that for ionospheric modeling over a wide area GPS network during ionosphere disturbed periods with a TEC prediction interval of 10-min, the employment of 25° as the elevation cutoff angle has better VTEC prediction accuracies than the use of 20° .

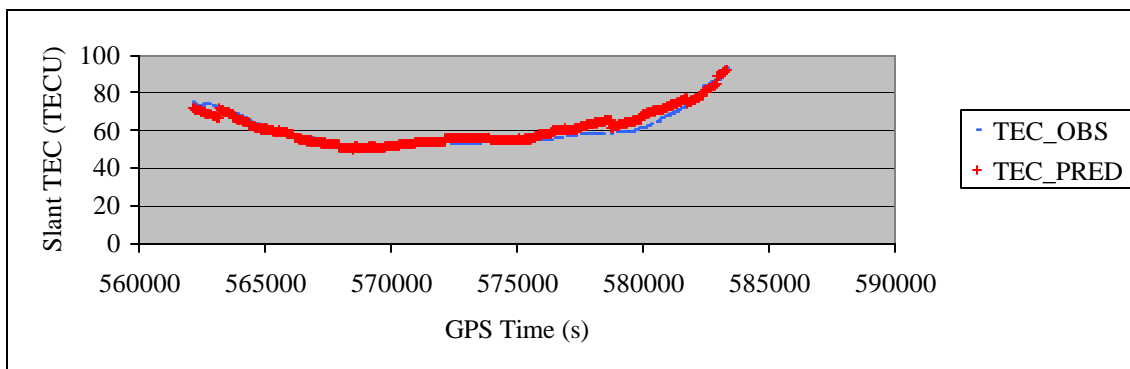


Figure 6.120 Comparison of Observed and Predicted TEC for PRN 02 at CARR Station on DOY 090 at 25° Cutoff and 10-min Prediction Interval (VTEC RMS= 2.646 TECU, Relative Error = 4.69%)

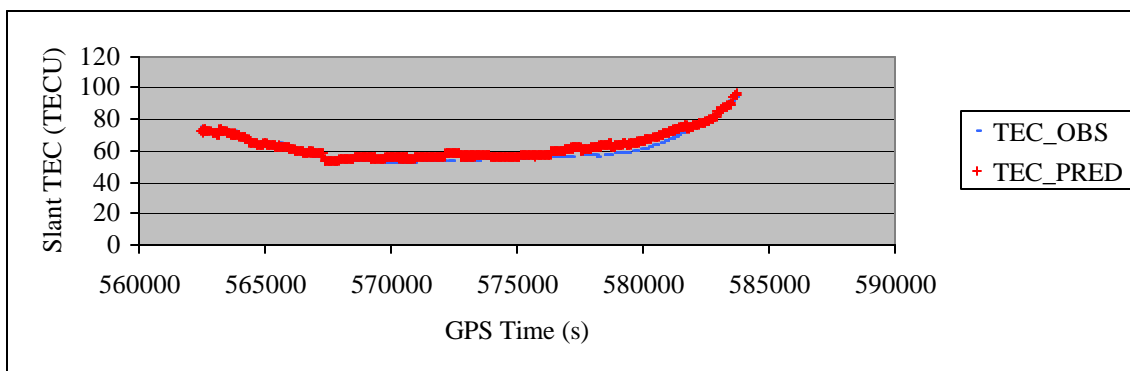


Figure 6.121 Comparison of Observed and Predicted TEC for PRN 02 at COSO Station on DOY 090 at 25° Cutoff and 10-min Prediction Interval (VTEC RMS= 3.045 TECU, Relative Error = 5.33%)

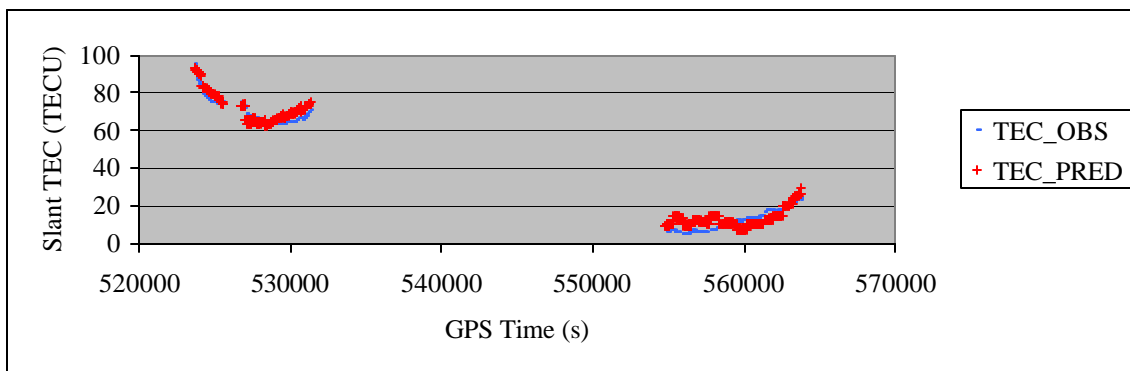


Figure 6.122 Comparison of Observed and Predicted TEC for PRN 03 at AMC2 Station on DOY 090 at 25° Cutoff and 10-min Prediction Interval (VTEC RMS= 2.537 TECU, Relative Error = 29.85%)

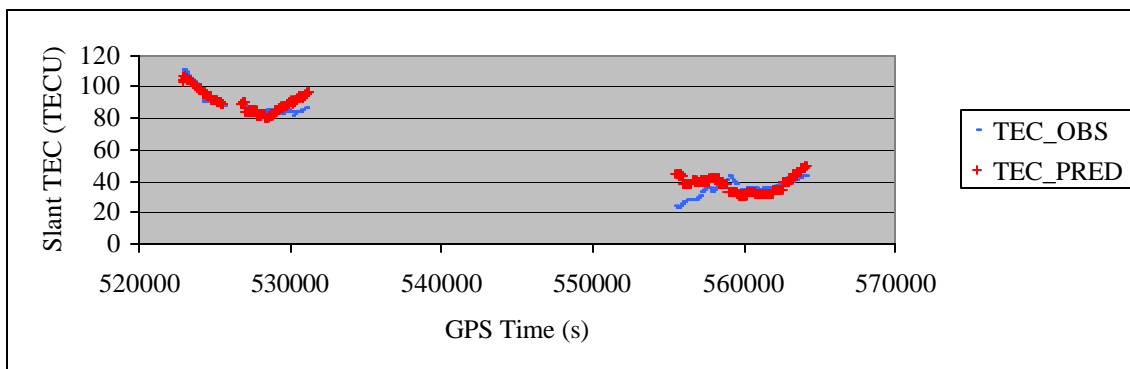


Figure 6.123 Comparison of Observed and Predicted TEC for PRN 03 at CASP Station on DOY 090 at 25° Cutoff and 10-min Prediction Interval (VTEC RMS= 3.572 TECU, Relative Error = 11.48%)

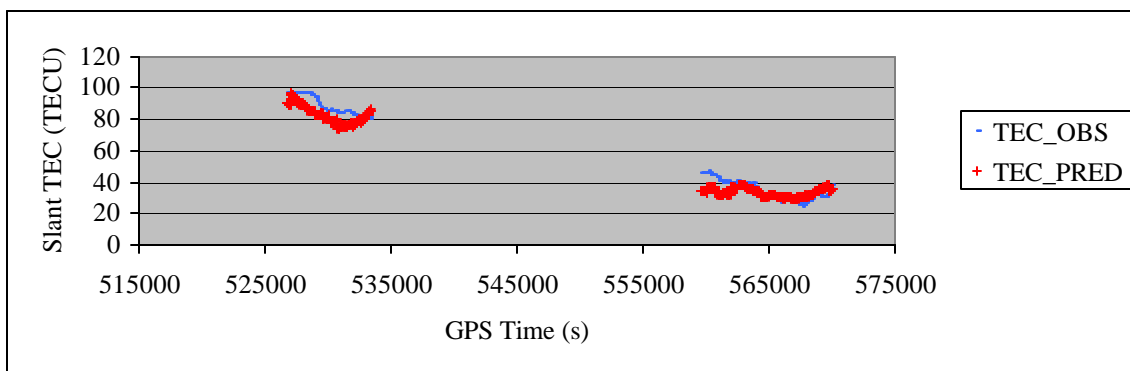


Figure 6.124 Comparison of Observed and Predicted TEC for PRN 31 at PRDS Station on DOY 090 at 25° Cutoff and 10-min Prediction Interval (VTEC RMS= 3.297 TECU, Relative Error = 9.00%)

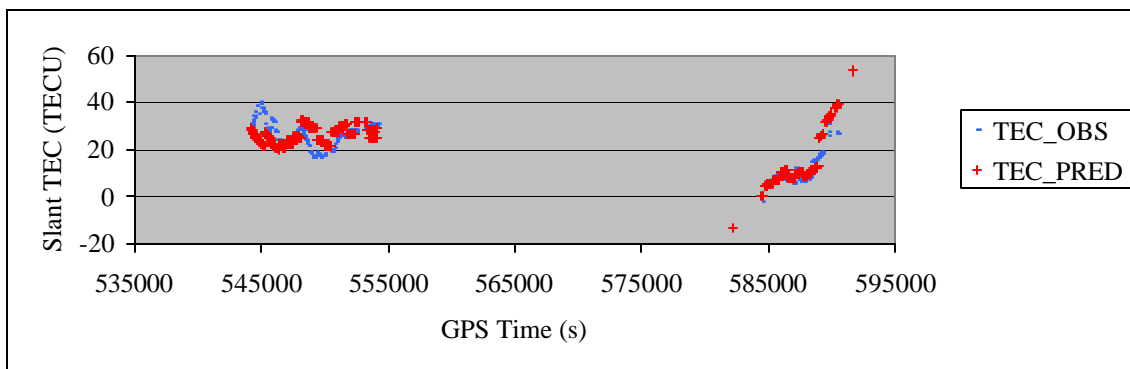


Figure 6.125 Comparison of Observed and Predicted TEC for PRN 04 at FAIR Station on DOY 090 at 25° Cutoff and 10-min Prediction Interval (VTEC RMS= 3.812 TECU, Relative Error = 25.61%)

Table 6.19 Error Statistics for 10-min VTEC Prediction with Cutoff 25° on DOY 090

STATION	VTEC Error RMS (TECU)	Relative Error (%)
ALBH	4.663	25.36%
ALGO	5.719	29.92%
AMC2	4.510	29.45%
CARR	3.887	6.80%
CASP	5.363	13.70%
COSO	3.996	6.97%
DAM2	4.534	6.71%
DRAO	4.466	47.90%
FAIR	4.315	44.60%
FLIN	6.224	33.96%
HOLB	4.215	22.21%
HOPB	3.771	6.39%
KODK	4.037	7.00%
NEAH	4.576	7.50%
NRC1	5.740	7.69%
PRDS	5.777	12.68%
SCH2	4.475	26.23%
STJO	4.683	32.44%
USNO	5.738	30.13%
VNDP	4.344	6.24%
WHIT	4.349	6.90%
WSLR	4.306	18.21%
Mean	4.713	19.50%

Table 6.19 summarizes the VTEC prediction RMS errors and relative errors for all stations and all observed satellites on DOY 090. It shows that most stations have a VTEC prediction RMS error between 4.0~6.0 TECU. Table 6.19 shows that 16 out of the 22 stations have an RMS error below the value of 5.0 TECU and that 21 out of the 22 stations have an RMS error smaller than 6.0 TECU. Only one station has an RMS error over 6.0 TECU. The network's mean RMS error on this ionosphere disturbance day is 4.713 TECU, as shown in last row of Table 6.19. Table 6.19 shows that nine stations have a relative error smaller than 10.0% even under such a severe ionosphere condition. Among the 22 stations, 18 have a relative error less or slightly greater than 30.0%. The mean relative error in the network for the present scheme is 19.50%.

6.3.3.3 Results of Scheme 9 (25°, 30 min)

6.3.3.3.1 Results on ionosphere quiet day DOY 089

Shown in the following are the TEC prediction results against the TEC observations using an elevation cut-off angle of 25° and a 30-min prediction interval. Compared to the results in previous schemes with shorter prediction intervals (5-min and 10-min), the six pairs of TEC data in Figure 6.126 to Figure 6.131 show larger discrepancies. Comparatively, it can be seen that at low latitude stations such as CARR and COSO, the discrepancies between predicted TEC and observed TEC are much smaller than that at high latitude stations. Comparing the six TEC pairs with the results from Scheme 6 (20°, 30-min) on the same day DOY 089, it can be seen that from the network point of view, the mean VTEC RMS error of the current scheme is 3.816 TECU, which is smaller than the mean RMS error of 3.941 TECU from Scheme 6 as shown in Table 6.14. The mean relative error of this scheme is 14.61% as shown in Table 6.20 which is also slightly smaller by 0.24% than that from Scheme 6. The analysis indicates that on DOY 089, the 30-min predictions have an improved VTEC accuracy when using an elevation cutoff angle of 25° compared to using 20°.

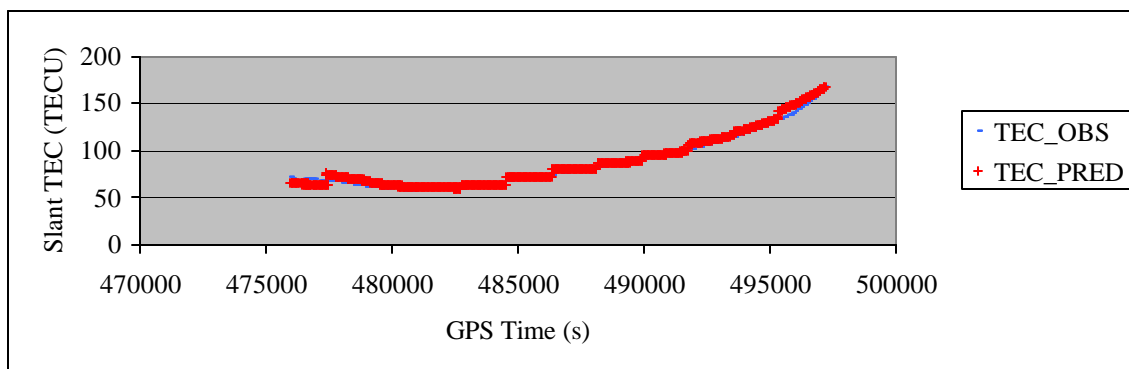


Figure 6.126 Comparison of Observed and Predicted TEC for PRN 02 at CARR Station on DOY 089 at 25° Cutoff and 30-min Prediction Interval
(VTEC RMS= 3.412 TECU, Relative Error = 5.06%)

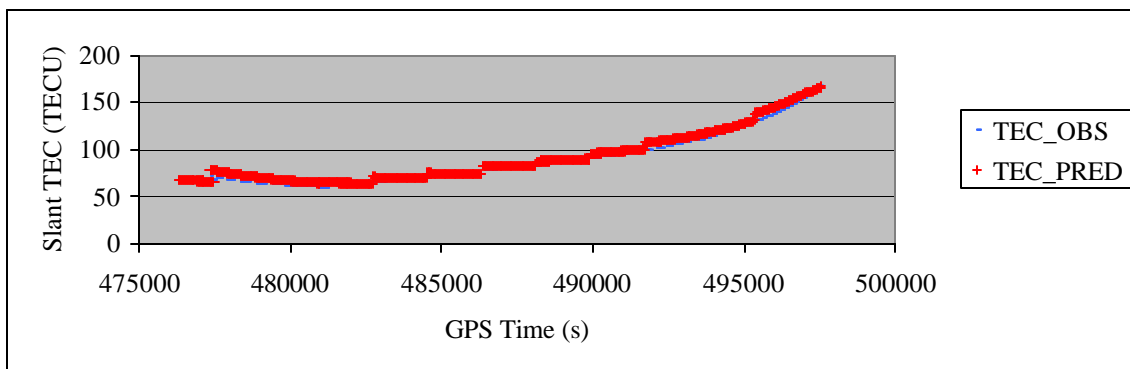


Figure 6.127 Comparison of Observed and Predicted TEC for PRN 02 at COSO Station on DOY 089 at 25° Cutoff and 30-min Prediction Interval (VTEC RMS= 3.962 TECU, Relative Error = 5.62%)

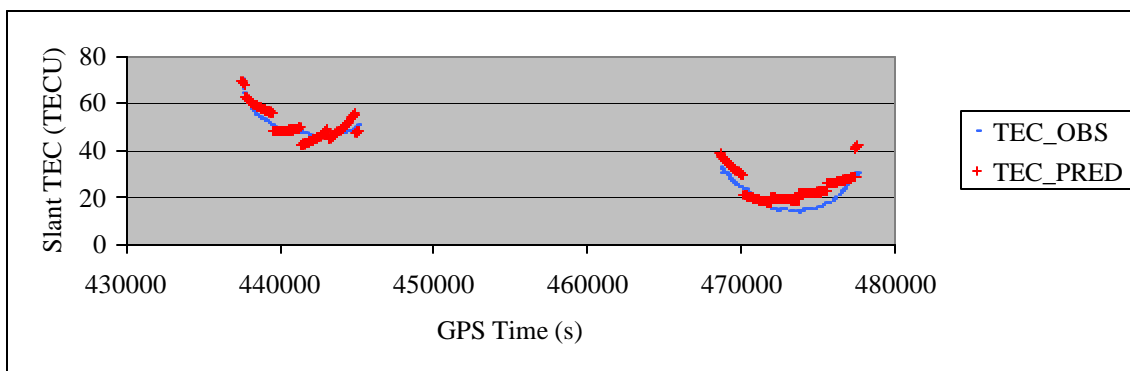


Figure 6.128 Comparison of Observed and Predicted TEC for PRN 03 at AMC2 Station on DOY 089 at 25° Cutoff and 30-min Prediction Interval (VTEC RMS= 2.871 TECU, Relative Error = 17.17%)

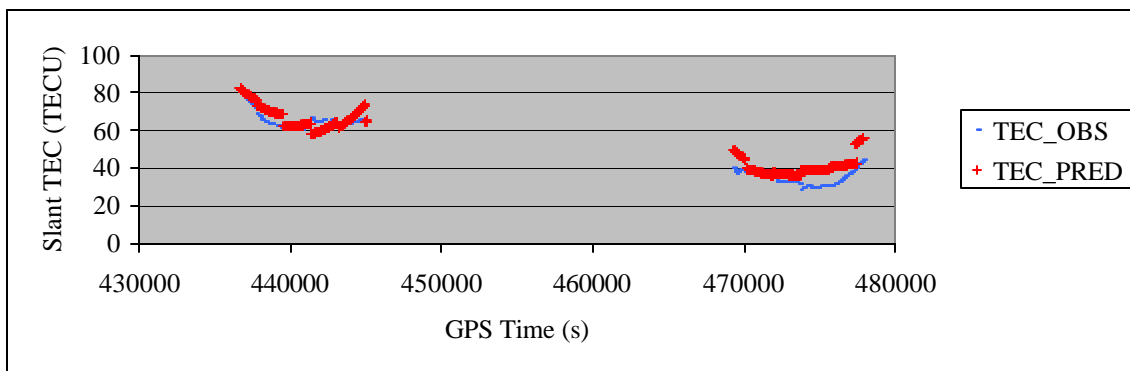


Figure 6.129 Comparison of Observed and Predicted TEC for PRN 03 at CASP Station on DOY 089 at 25° Cutoff and 30-min Prediction Interval (VTEC RMS= 3.877 TECU, Relative Error = 13.27%)

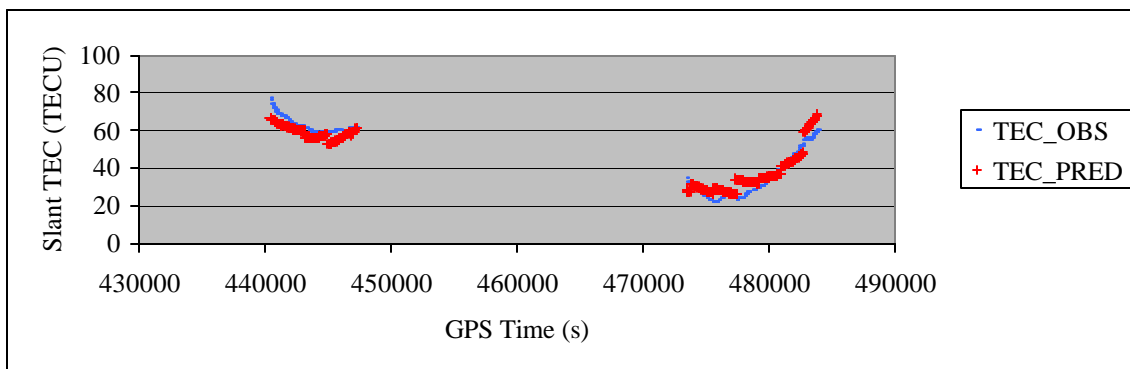


Figure 6.130 Comparison of Observed and Predicted TEC for PRN 31 at PRDS Station on DOY 089 at 25° Cutoff and 30-min Prediction Interval (VTEC RMS= 2.951 TECU, Relative Error = 10.36%)

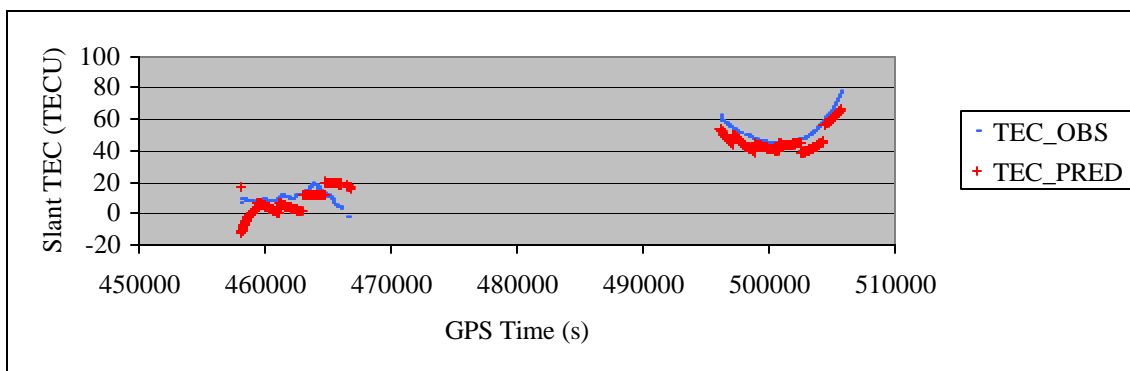


Figure 6.131 Comparison of Observed and Predicted TEC for PRN 04 at FAIR Station on DOY 089 at 25° Cutoff and 30-min Prediction Interval (VTEC RMS= 4.886 TECU, Relative Error = 66.08%)

Table 6.20 summarizes the VTEC prediction RMS errors and relative errors of 30-min TEC prediction for all stations and all observed satellites on DOY 089. It shows that the VTEC prediction errors at most stations are in the range of 3.0~4.0 TECU. Table 6.20 indicates that 17 out of the 22 stations have a VTEC prediction error smaller than 4.0 TECU. The other five stations have an RMS error slightly larger than 4.0 TECU but even the largest error is still smaller than 5.0 TECU. Table 6.20 shows that the mean RMS error for the network is 3.816 TECU. As for the relative error, Table 6.20 shows that 10 of the 22 stations have a relative error smaller than 10.0% and that 15 out of the 22 stations have a relative error smaller than 20.0%. The other seven stations have a relative

error in the range of 20.0%~34.0%. Table 6.20 shows that the network mean relative error is 14.61%.

Table 6.20 Error Statistics for 30-min VTEC Prediction with Cutoff 25° on DOY 089

STATION	VTEC Error RMS (TECU)	Relative Error (%)
ALBH	3.531	14.87%
ALGO	3.630	25.40%
AMC2	3.582	19.57%
CARR	3.758	5.78%
CASP	3.528	9.49%
COSO	3.652	5.50%
DAM2	3.894	5.05%
DRAO	3.531	22.76%
FAIR	4.794	33.03%
FLIN	3.940	23.38%
HOLB	3.240	22.89%
HOPB	3.525	5.21%
KODK	4.422	7.94%
NEAH	3.408	6.26%
NRC1	3.945	5.93%
PRDS	3.798	11.25%
SCH2	4.298	26.09%
STJO	4.179	17.80%
USNO	3.658	14.43%
VNDP	3.764	4.98%
WHIT	4.498	6.97%
WSLR	3.388	26.85%
Mean	3.816	14.61%

6.3.3.3.2 Results on ionosphere disturbed day DOY 090

The following subsection presents comparison results from six pairs TEC using 25° as the elevation cutoff angle and a 30-min prediction interval for the ionosphere disturbed day DOY 090. It can be seen that the disagreements between the predicted and observed TEC in Figure 6.132 to Figure 6.137 are becoming larger than those in the previous schemes with shorter prediction intervals (5-min and 10-min). It implies that the extension of the prediction interval will have a degradation effect on the prediction

accuracies. When compared to the results of Scheme 6 (20° , 30-min) for the same day DOY 090, four pairs of TEC data in the current scheme show an improvement in the vertical TEC prediction RMS error over the results obtained in Scheme 6. If considering all the observed TEC data at all stations in the network, it can be seen that in this network the mean RMS error is 5.560 TECU, which is smaller than the mean value 5.592 TECU from Scheme 6. The mean relative error of current scheme is 23.51%, which is also smaller than the mean error of 24.21% in Scheme 6 shown in Table 6.15. The analysis results show that for ionospheric modeling over a wide area GPS network during ionosphere disturbed periods, the 30-min TEC predictions have a better vertical TEC prediction accuracy using 25° as the elevation cutoff angle than using 20° .

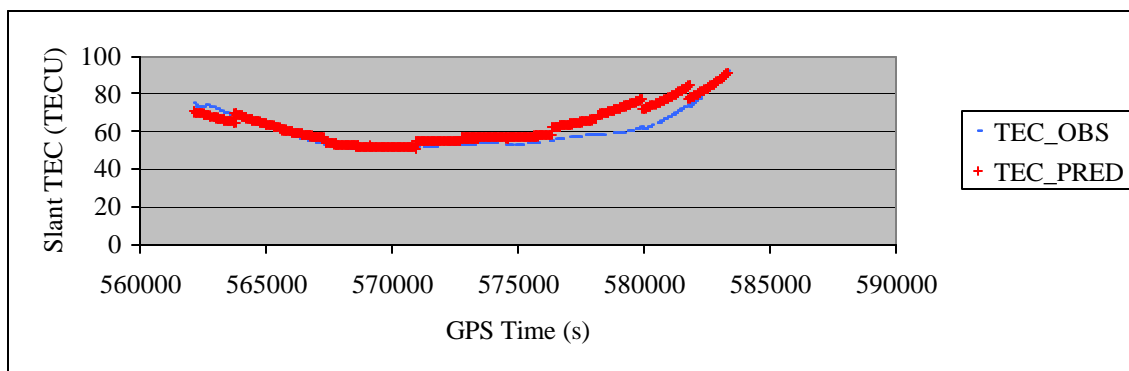


Figure 6.132 Comparison of Observed and Predicted TEC for PRN 02 at CARR Station on DOY 090 at 25° Cutoff and 30-min Prediction Interval
(VTEC RMS= 4.749 TECU, Relative Error = 8.26%)

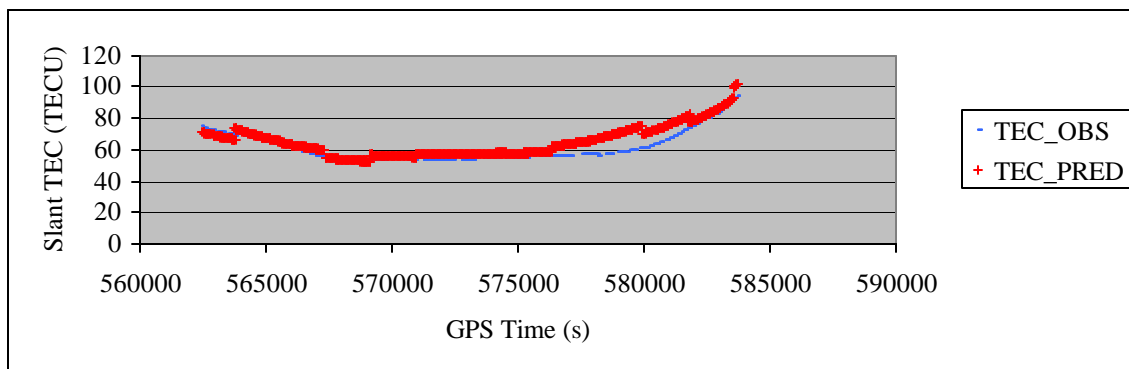


Figure 6.133 Comparison of Observed and Predicted TEC for PRN 02 at COSO Station on DOY 090 at 25° Cutoff and 30-min Prediction Interval
(VTEC RMS= 4.875 TECU, Relative Error = 8.63%)

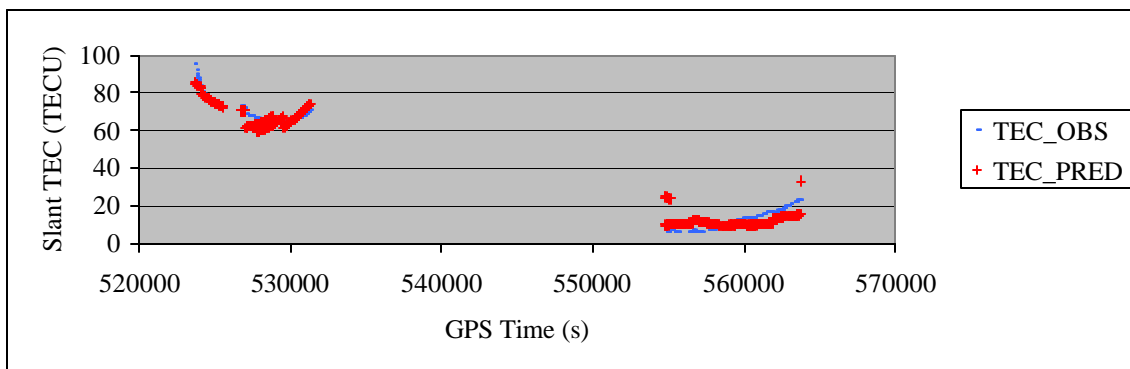


Figure 6.134 Comparison of Observed and Predicted TEC for PRN 03 at AMC2 Station on DOY 090 at 25° Cutoff and 30-min Prediction Interval
 (VTEC RMS= 2.727 TECU, Relative Error = 32.70%)

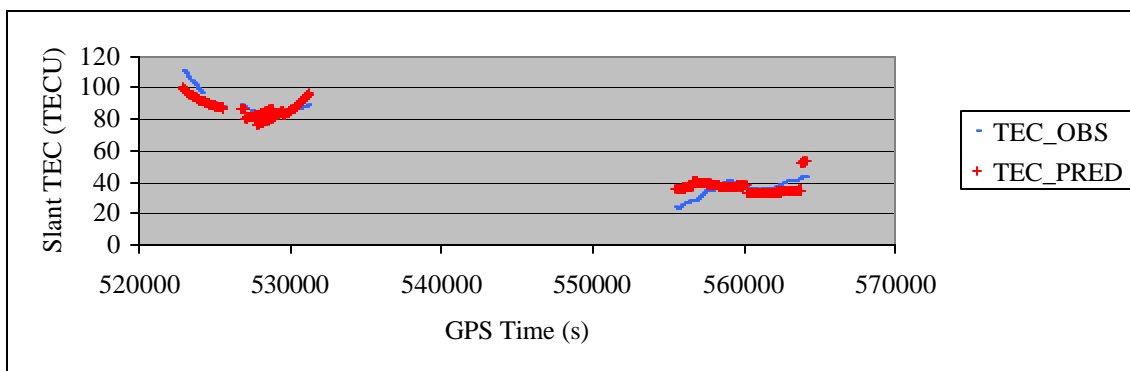


Figure 6.135 Comparison of Observed and Predicted TEC for PRN 03 at CASP Station on DOY 090 at 25° Cutoff and 30-min Prediction Interval
 (VTEC RMS= 3.086 TECU, Relative Error = 9.82%)

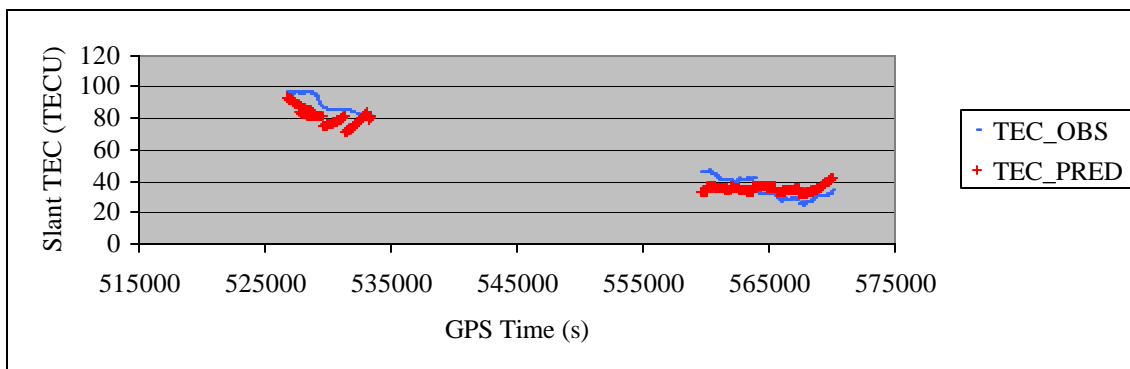


Figure 6.136 Comparison of Observed and Predicted TEC for PRN 31 at PRDS Station on DOY 090 at 25° Cutoff and 30-min Prediction Interval
 (VTEC RMS= 4.710 TECU, Relative Error = 14.44%)

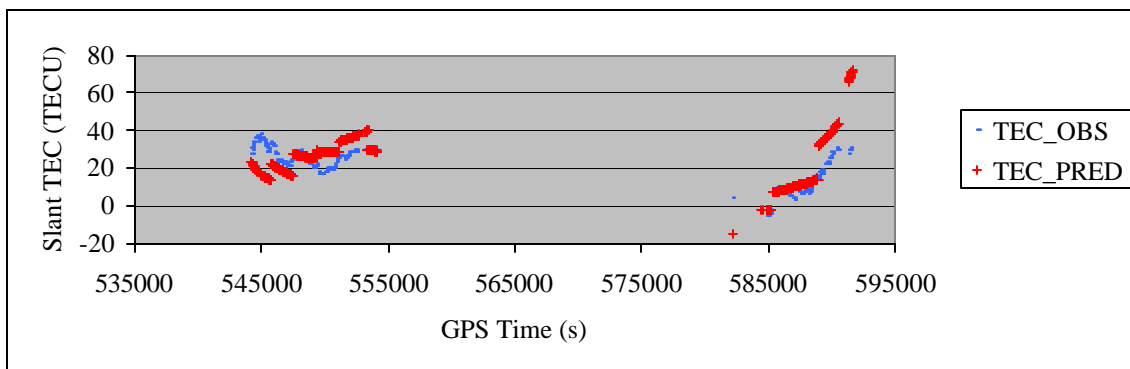


Figure 6.137 Comparison of Observed and Predicted TEC for PRN 04 at FAIR Station on DOY 090 at 25° Cutoff and 30-min Prediction Interval (VTEC RMS= 6.506 TECU, Relative Error = 41.56%)

Table 6.21 Error Statistics for 30-min VTEC Prediction with Cutoff 25° on DOY 090

STATION	VTEC Error RMS (TECU)	Relative Error (%)
ALBH	5.582	29.34%
ALGO	6.529	35.18%
AMC2	5.362	34.42%
CARR	4.760	8.55%
CASP	6.088	16.30%
COSO	4.745	8.53%
DAM2	5.132	7.69%
DRAO	5.353	56.06%
FAIR	5.239	55.07%
FLIN	6.738	38.60%
HOLB	5.281	30.23%
HOPB	4.581	7.84%
KODK	4.872	8.76%
NEAH	5.455	9.28%
NRC1	6.596	9.31%
PRDS	6.133	15.31%
SCH2	5.523	31.14%
STJO	6.286	40.29%
USNO	6.331	34.70%
VNDP	5.093	7.46%
WHIT	5.364	8.62%
WSLR	5.267	24.49%
Mean	5.560	23.51%

Table 6.21 shows the statistics of the VTEC prediction errors and relative errors for all stations on DOY 090. Table 6.21 shows that most stations have VTEC prediction errors at the level of 5.0~7.0 TECU. It shows that 15 of the 22 stations have an RMS error smaller than 6.0 TECU. Only seven stations indicate an error larger than 6.0 TECU. The mean RMS error for the network is 5.560 TECU. Table 6.21 shows that 9 out of 22 stations have relative errors less than 10.0%. It also shows that most stations have a relative error smaller than 30.0%. Only nine stations indicate a relative error over 30.0%. The mean value of the relative error in the network for this scheme is 23.51%.

6.3.4 Summary

Section 6.3.3 presents the ionospheric TEC prediction results corresponding to different modeling schemes using a wide area GPS Network (covering the North America Continent) under different ionospheric activity condition (March 30, 2001 is an ionosphere quiet day and March 31, 2001 is quite disturbed day). For DOY 089, the VTEC predictions accuracy statistics are summarized in Table 6.22 and the relative error statistics are summarized in Table 6.23. The results show that during ionosphere quiet periods the ionospheric TEC predictions have accuracies better than 3.5 TECU in VTEC and 13.0% relative error in STEC for both 5-min and 10-min predictions and that the TEC predictions have accuracies about 4.0 TECU in VTEC and better than 15.0% relative error in STEC for 30-min predictions.

Table 6.22 VTEC Prediction Accuracy Statistics for All Schemes on DOY 089

	5-min	10-min	30-min
15°	3.494	3.558	4.028
20°	3.277	3.357	3.941
25°	3.180	3.272	3.816

Table 6.23 STEC Prediction Relative Error Statistics for All Schemes on DOY 089

	5-min	10-min	30-min
15°	12.75%	12.96%	14.60%
20°	12.41%	12.61%	14.85%
25°	12.28%	12.67%	14.61%

The following Table 6.24 and Table 6.25 summarize the statistics for VTEC predictions accuracy and STEC prediction relative error for DOY 090. The results show that during extremely disturbed ionosphere periods the TEC predictions accuracies are better than 4.9 TECU in VTEC and 21.0% relative error in STEC for both 5-min and 10-min predictions and that they are about 5.5 TECU in VTEC and about 25.0% relative error in STEC for 30-min predictions. Compared to the results of previous quiet day, the ionospheric TEC prediction performance has a degradation in both VTEC RMS value and relative error. The degradation is about 1.4 TECU in VTEC for 5-min and 10-min predictions and is about 1.5 TECU in VTEC for 30-min predictions. For relative error, the degradation is about 8% in STEC for 5-min and 10-min predictions and is about 10% in STEC for 30-min predictions.

Table 6.24 VTEC Prediction Accuracy Statistics for All Schemes on DOY 090

	5-min	10-min	30-min
15°	4.757	4.874	5.546
20°	4.666	4.811	5.592
25°	4.554	4.713	5.560

Table 6.25 STEC Prediction Relative Error Statistics for All Schemes on DOY 090

	5-min	10-min	30-min
15°	20.45%	21.19%	25.09%
20°	19.61%	20.35%	24.21%
25°	18.75%	19.50%	23.51%

Table 6.22 to Table 6.25 show that for both ionosphere quiet and disturbed days, when cutoff angle rises from 15° to 20° and 25°, the accuracies have a slight improvement in both vertical and slant TEC. For ionosphere quiet day, the improvement in VTEC prediction is about 0.1~0.2 TECU and about 0.2%~0.3% in STEC prediction. On ionosphere disturbed day, the improvement is about 0.1 TECU in VTEC prediction and about 0.8%~0.9% in STEC prediction.

For performance analysis conducted at independent stations (the station data not included in ionospheric modeling) on the ionospheric quiet day DOY 089, the 5-min predictions

with a cutoff angle 15° have a vertical RMS of 5.0~5.8 TECU and a relative error of 7.51~34.21%, during ionospheric quiet time periods. The 10-min predictions have a vertical RMS of 5.0~5.8 TECU and a relative error of 7.55~34.84%. The 30-min predictions have a vertical TEC prediction accuracy of 5.5~5.9 TECU and a relative error of 7.62~34.74%. On the ionospheric disturbed day DOY 090, the TEC predictions at independent stations (station data not included for ionospheric modeling) indicates that during ionospheric disturbed periods the 5-min predictions with a cutoff angle of 15° have a vertical RMS 5.2~5.9 TECU and a relative error of 8.09~46.30%. The 10-min predictions have a vertical RMS 5.4~6.1 TECU and a relative error of 8.46~48.21% while the 30-min predictions have a vertical TEC prediction accuracy of 5.8~6.7 TECU and a relative error of 9.81~51.62%.

6.3.5 SPP results

In previous sections, the accuracies of the TEC data predicted by the tomographic model have been evaluated under different modeling conditions. In order to further validate the accuracies of the predicted TEC data, the predicted TEC data are incorporated into a GPS single point positioning (SPP) software package to correct the ionospheric errors on GPS signals. This validation gives another effective assessment of the performance of the TEC predictions generated by the tomographic model. In the following, the predicted TEC data will be applied to support GPS point positioning. For comparison purpose, another two ionospheric models, namely the zero-model and the dual-frequency model, have also been implemented as it was done in Chapter 5.

Although several sets of TEC prediction data are available from the previous data analysis, only the TEC prediction data corresponding to cutoff angle 15° are used here in order to avoid lengthy presentation of results for other schemes. The SPP solutions using the TEC data predicted at three different intervals with an elevation cutoff angle of 15° will be presented.

6.3.5.1 SPP results on DOY 089

The SPP analysis results on the ionosphere quiet day DOY 089 are first described. In the following subsections, the ionospheric TEC data generated at three different prediction intervals (5-min, 10-min and 30-min) with a cutoff angle of 15° are used and incorporated into the SPP software package to correct the ionospheric error for C/A code measurements. For SPP positioning, the cutoff angle used is also 15° to be consistent with the TEC prediction data.

6.3.5.1.1 Use of 5-min TEC Prediction

Figure 6.138 to Figure 6.143 show the single-epoch positioning errors at six different GPS stations with the TEC corrections predicted with a 5-min interval. At each single epoch, the SPP software computes the positioning solution and the positioning solution is then compared to the receiver's known coordinates. Therefore at each single epoch, the positioning error can be obtained. As mentioned before, besides the TEC correction from the ionospheric model's predictions, two other ionospheric models, i.e. the zero-model and the dual-frequency model, have also been implemented into the SPP software. Similar to the tomographic model, the positioning solutions from the zero-model and the dual-frequency model are also compared to the known coordinates and their positioning errors are calculated. Each figure below shows three sets of positioning errors, which correspond to three different ionospheric models. The dark rhombic symbol represents the positioning errors of the zero-model; the pink square denotes the positioning errors for the tomographic model and the positioning errors corresponding to the dual-frequency model are represented by the yellow triangle. From Figure 6.138 to Figure 6.143, it can be found that the positioning errors for the zero-model are considerably larger than those from the use of the tomographic model or the dual-frequency model. The positioning errors for the zero-model generally vary between 5.0~30.0 m. But the positioning errors for the tomographic model and the dual-frequency model are usually better than 5.0 m. Moreover, the positioning errors corresponding to the zero-model vary significantly with time during the 24-hour positioning period. Unlike the positioning errors for the zero-

model, Figure 6.138 to Figure 6.143 show that the positioning errors using the tomographic model and the dual-frequency model do not change much over time. This indicates that the accuracies of the TEC corrections generated from the tomographic model are quite uniform over time and they do not vary much over time. Examining the positioning errors corresponding to zero-model, a large magnitude of positioning errors can be seen. On the contrary, it can be seen that the positioning errors are significantly reduced after using either tomographic model or dual-frequency model. Positioning accuracies for the tomographic model are very comparable to the results for dual-frequency model except at the station FAIR where the positioning errors for the tomographic model are larger than those using the dual-frequency model. This is because of the degraded ionospheric TEC prediction accuracy at FAIR station, which is the far northern station and located at the edge area of the GPS network. It can be seen in Table 6.4 the relative error at FAIR station is much larger than most other stations. Overall the results indicate that the performance of the tomographic model is very close to that of the dual-frequency model in terms of the efficiency to correct ionospheric errors in GPS single point positioning.

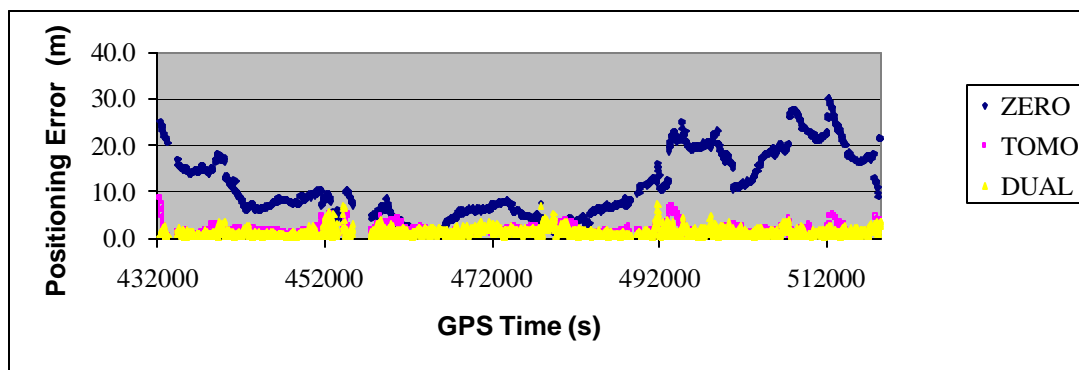


Figure 6.138 Positioning Error at CARR Station Using Three Ionospheric Models, Tomographic Correction Predicted at 15° and 5-min Interval

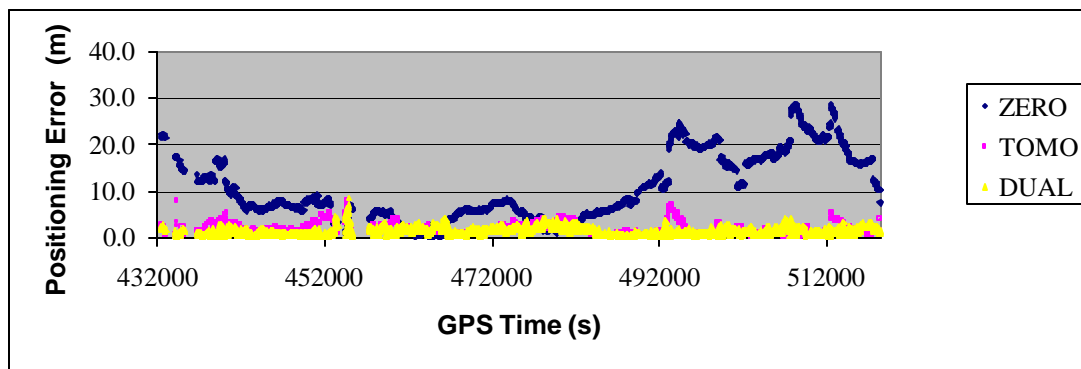


Figure 6.139 Positioning Error at COSO Station Using Three Ionospheric Models, Tomographic Correction Predicted at 15° and 5-min Interval

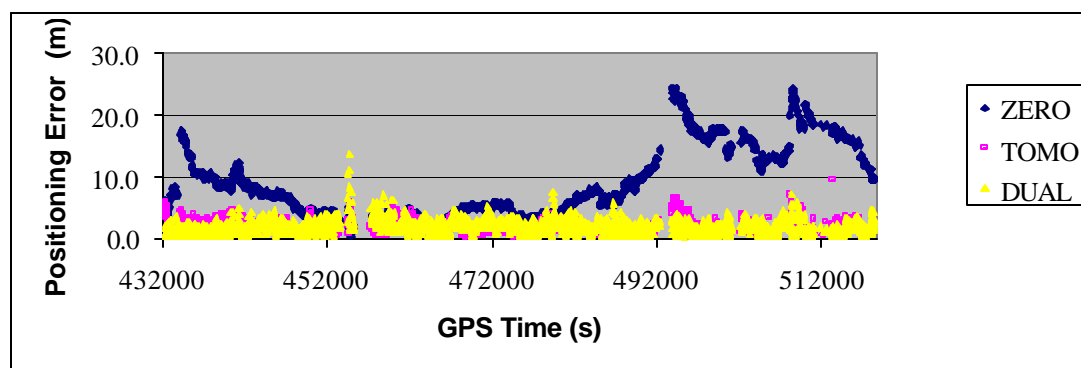


Figure 6.140 Positioning Error at AMC2 Station Using Three Ionospheric Models, Tomographic Correction Predicted at 15° and 5-min Interval

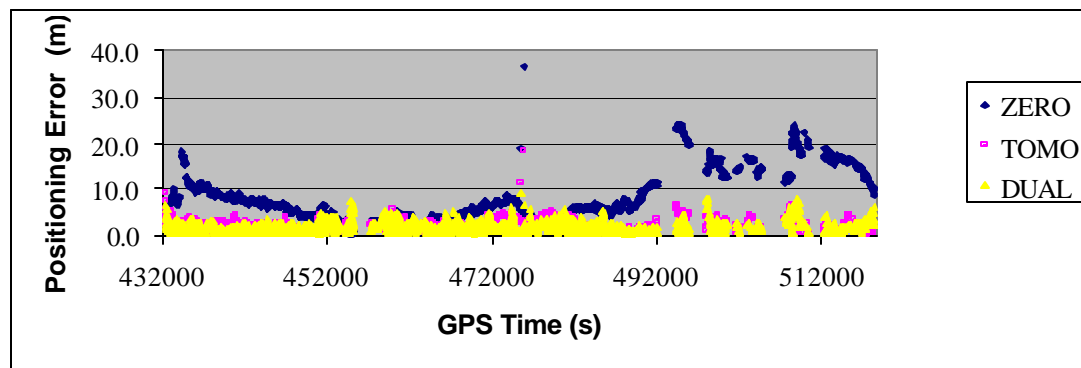


Figure 6.141 Positioning Error at CASP Station Using Three Ionospheric Models, Tomographic Correction Predicted at 15° and 5-min Interval

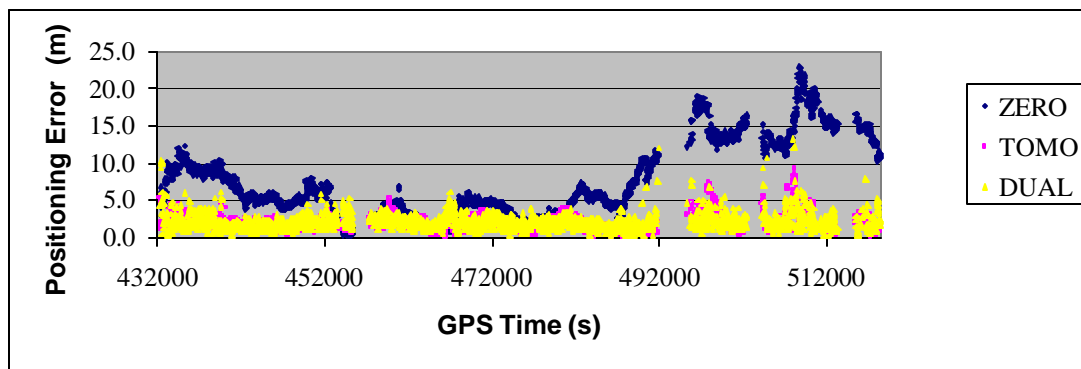


Figure 6.142 Positioning Error at PRDS Station Using Three Ionospheric Models, Tomographic Correction Predicted at 15° and 5-min Interval

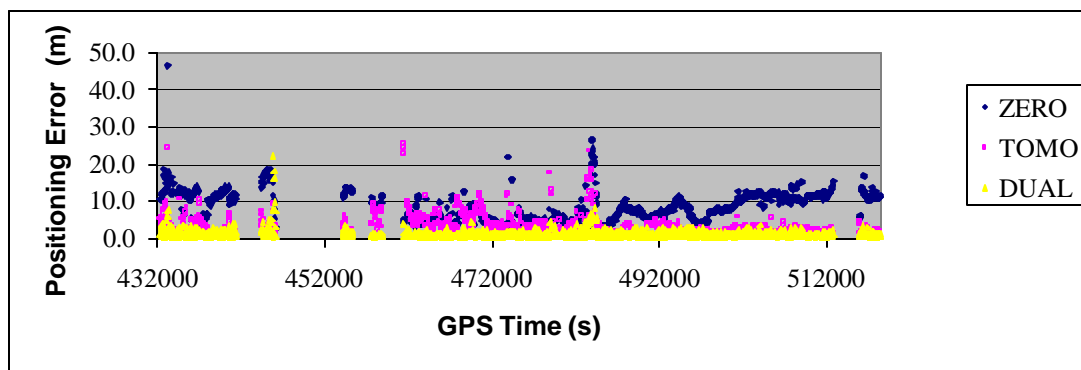


Figure 6.143 Positioning Error at FAIR Station Using Three Ionospheric Models, Tomographic Correction Predicted at 15° and 5-min Interval

Table 6.26 summarizes the positioning errors from using three different ionospheric correction models. The positioning errors in each component, latitude, longitude and height, are also included. The three-dimensional (3D) positioning errors are the total positioning errors calculated from the errors in the three coordinate components. For positioning errors with the zero-model, it can be seen that the ionospheric errors have more significant influences on GPS positioning at low latitude stations than high latitude stations. Table 6.26 shows that without ionospheric corrections the accuracies of GPS point positioning are at the order of 9.0~13.0 m. After the ionospheric correction by the tomographic model, the positioning accuracies are improved to the level of 2.0~4.0 m. If dual-frequency model is used, the point positioning accuracies are further improved to the level of 1.5~2.5 m. Through the comparison of the positioning accuracies from using

different models, it can be seen that the dual-frequency model is the most accurate ionospheric correction method among the three models. Compared to the dual-frequency model, the performance of the tomographic model has a slight degradation but it is quite comparable to it.

Table 6.26 Single-frequency Single Point Positioning RMS Error at 6 Stations Using Tomographic Corrections Predicted at 15° and 5-min Interval (m)

Station	Component	Zero Model	Tomographic Model	Dual-frequency Model
CARR	Latitude	2.056	0.938	0.523
	Longitude	0.370	0.199	0.147
	Height	12.982	1.745	1.434
	3D	13.149	1.991	1.534
COSO	Latitude	1.965	0.847	0.463
	Longitude	0.216	0.127	0.072
	Height	12.427	1.979	1.597
	3D	12.584	2.156	1.664
AMC2	Latitude	1.933	0.804	0.755
	Longitude	0.586	0.351	0.352
	Height	10.163	1.961	2.034
	3D	10.362	2.149	2.198
CASP	Latitude	1.751	0.844	0.707
	Longitude	0.478	0.374	0.332
	Height	8.922	2.284	2.062
	3D	9.105	2.464	2.205
PRDS	Latitude	1.339	0.743	0.813
	Longitude	1.096	0.934	1.198
	Height	8.633	1.912	1.882
	3D	8.805	2.254	2.375
FAIR	Latitude	2.356	1.626	0.554
	Longitude	2.348	1.236	0.537
	Height	8.671	3.400	1.452
	3D	9.287	3.966	1.645

Examining the positioning errors using the zero-model in different coordinate components, it can be seen that the ionospheric errors have a major influence on the height component. The influence of the ionospheric errors on the horizontal component is much smaller compared to the height component. Within the horizontal component, the

latitude component apparently has a greater positioning error than the longitude component. That is to say the ionospheric errors have the least impact on the longitude component. The results in Table 6.26 show that the employment of the tomographic model or dual-frequency model has very little effect on the improvement of the accuracies in the longitude component. A significant improvement however can be seen in the height component after using the tomographic model or dual-frequency model.

Taking the CARR station for example, the use of the dual-frequency model to substitute the zero-model results in a positioning error decrease from 13.149 m to 1.534 m, with an improvement of 11.615 m in the positioning accuracy. The dual-frequency model is considered to have the best performance to correct ionospheric errors. In SPP analysis, all conditions are identical except the different ionospheric models. Therefore the 11.615 m should be considered as the total effect due to ionospheric errors. The positioning error using the tomography model is 1.991 m. The positioning error due to the tomographic model is only 0.457 m greater if compared to the positioning using the dual-frequency model which reflects the modeling error in the tomographic model. The SPP solutions show that the ionospheric residual error after tomographic modeling is about 0.457 m in GPS point positioning at the CARR station. When compared to the total ionospheric error 11.615 m, the residual modeling error is just 3.93% of the total ionospheric error. That is to say the ionosphere tomographic model can recover 96.07% ionospheric delays and the remaining error limited by the model is 3.93%. Similarly the ionosphere recovering efficiency for the tomographic model at other GPS stations can be calculated and they are provided in Table 6.27. Table 6.27 indicates that the mean recovering efficiency at these six stations is 92.91% and the mean residual error is 7.09%. This confirms the use of ionospheric corrections from the 5-min TEC predictions can effectively correct about 92.91% ionospheric errors in the GPS point positioning.

Table 6.27 Ionospheric Recovering Efficiency of 5-min TEC Predictions

Station	Recovering Efficiency (%)	Residual Error (%)
CARR	96.07%	3.93%
COSO	95.49%	4.51%
AMC2	100.00%	0.00%
CASP	96.25%	3.75%
PRDS	100.00%	0.00%
FAIR	69.63%	30.37%
Mean	92.91%	7.09%

The TEC prediction data at stations DRAO and DAM2 obtained by excluding the stations from ionospheric modeling are also examined in the single point positioning. Figure 6.144 and Figure 6.145 show the point positioning results at DRAO and DAM2 stations, respectively. Figure 6.144 shows that at most epochs, the positioning results corresponding to tomographic TEC predictions have much smaller positioning errors than the zero-model. At a large number of epochs, the positioning accuracies for the tomographic model are largely comparable to those using the dual-frequency model. The positioning RMS statistics show that the positioning accuracy is 11.091 m for the zero-model, 3.741 m for the tomographic model and 1.589 m for the dual-frequency model. The recovering efficiency for the 5-min TEC prediction data is 77.35%. The results for DAM2 station also show that the positioning accuracies for the tomographic model gave a significant improvement over those using the zero-model at most epochs. At DAM2 station, the positioning error for the zero-model is 13.645 m and it is 5.856 m for the tomographic model. The positioning solutions using the dual-frequency model to correct the ionospheric errors have an accuracy of 2.552 m. The recovering efficiency at DAM2 station is 70.22%.

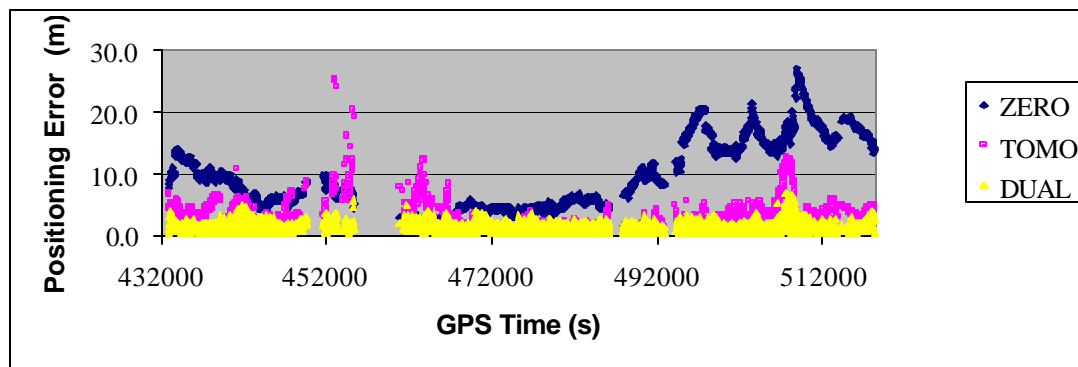


Figure 6.144 Positioning Error at DRAO Station Using Three Ionospheric Models, Tomographic Correction Predicted at 15° and 5-min Interval

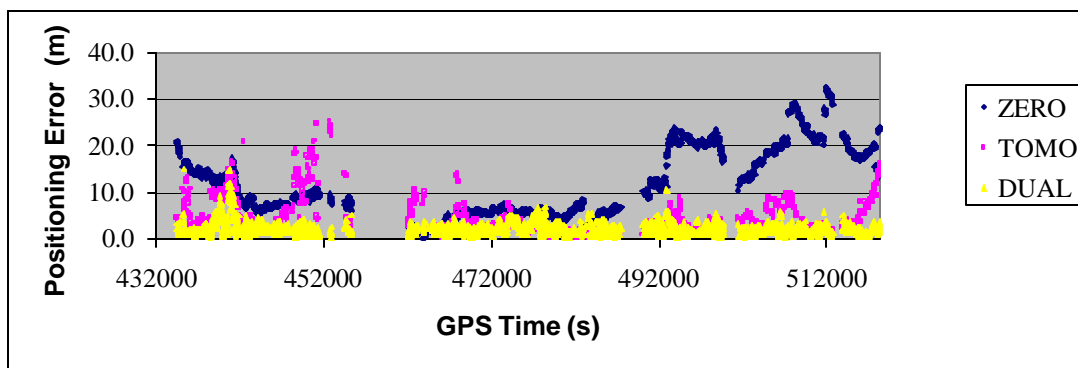


Figure 6.145 Positioning Error at DAM2 Station Using Three Ionospheric Models, Tomographic Correction Predicted at 15° and 5-min Interval

6.3.5.1.2 Use of 10-min TEC Prediction

Figure 6.146 to Figure 6.151 present the positioning results using 10-min TEC predictions from the tomographic model and the other two models. The results in this subsection are compared to those in the previous subsection to assess how the TEC prediction interval will affect the positioning accuracies. Figure 6.146 to Figure 6.151 show that the positioning errors with the zero-model are much bigger than those with the tomographic model and the dual-frequency model. During the 24-hour period, the epoch-by-epoch positioning errors using the zero-model vary between 5.0~30.0 m while the positioning errors using the tomographic model and the dual-frequency model are normally below 5.0 m. Though the TEC prediction interval is extended from 5-min to 10-

min, the positioning solutions indicate that the results from the tomographic model are still quite comparable to those from the dual-frequency model.

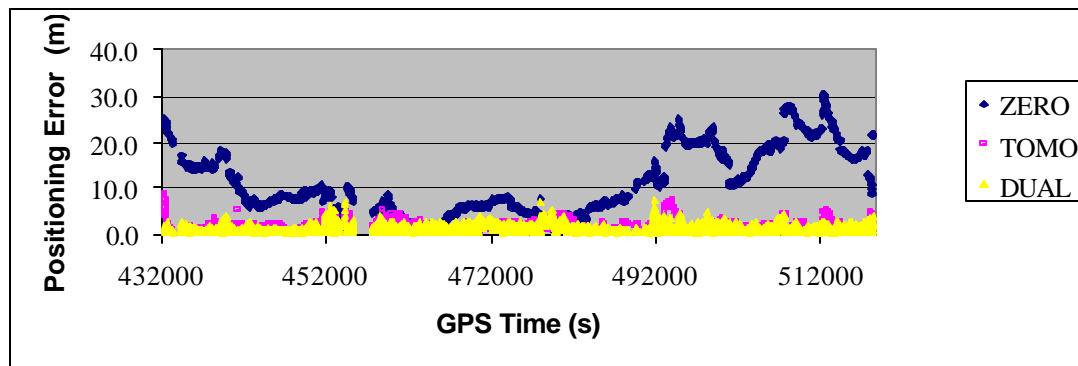


Figure 6.146 Positioning Error at CARR Station Using Three Ionospheric Models, Tomographic Correction Predicted at 15° and 10-min Interval

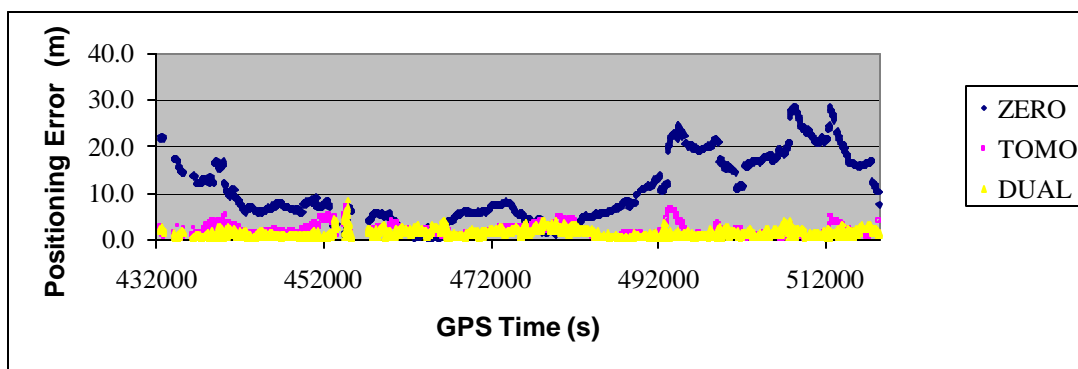


Figure 6.147 Positioning Error at COSO Station Using Three Ionospheric Models, Tomographic Correction Predicted at 15° and 10-min Interval

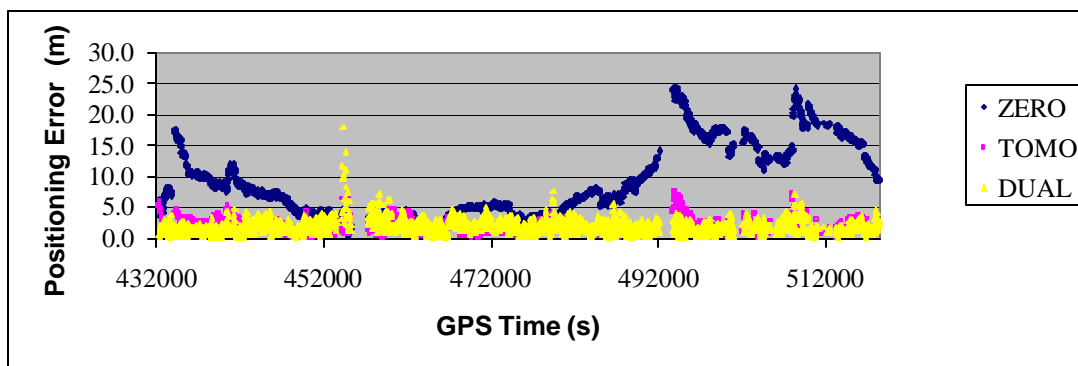


Figure 6.148 Positioning Error at AMC2 Station Using Three Ionospheric Models, Tomographic Correction Predicted at 15° and 10-min Interval

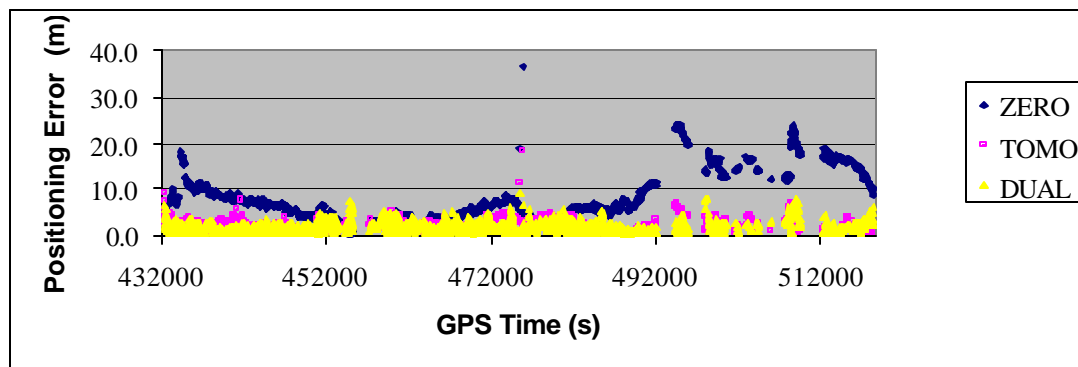


Figure 6.149 Positioning Error at CASP Station Using Three Ionospheric Models, Tomographic Correction Predicted at 15° and 10-min Interval

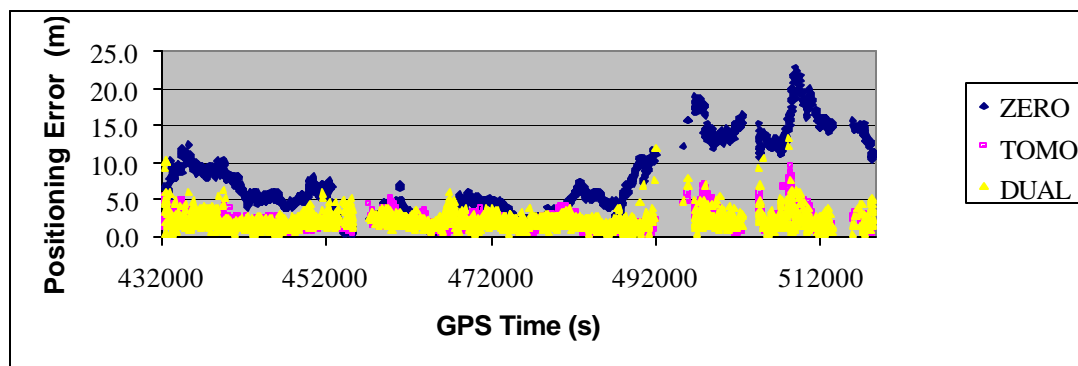


Figure 6.150 Positioning Error at PRDS Station Using Three Ionospheric Models, Tomographic Correction Predicted at 15° and 10-min Interval

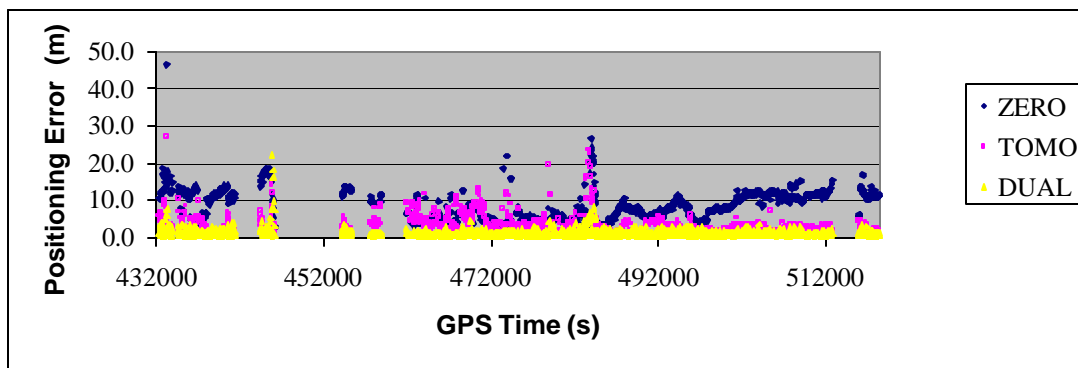


Figure 6.151 Positioning Error at FAIR Station Using Three Ionospheric Models, Tomographic Correction Predicted at 15° and 10-min Interval

Table 6.28 Single-frequency Single Point Positioning RMS Error at 6 Stations Using Tomographic Corrections Predicted at 15° and 10-min Interval (m)

Station	Component	Zero Model	Tomographic Model	Dual-frequency Model
CARR	Latitude	2.076	0.946	0.525
	Longitude	0.370	0.203	0.147
	Height	12.976	1.816	1.435
	3D	13.146	2.058	1.536
COSO	Latitude	1.972	0.847	0.462
	Longitude	0.219	0.129	0.072
	Height	12.426	2.041	1.593
	3D	12.583	2.214	1.660
AMC2	Latitude	1.935	0.805	0.824
	Longitude	0.585	0.357	0.353
	Height	10.116	2.005	2.087
	3D	10.316	2.190	2.271
CASP	Latitude	1.695	0.842	0.706
	Longitude	0.478	0.372	0.334
	Height	8.811	2.342	2.065
	3D	8.985	2.517	2.208
PRDS	Latitude	1.341	0.779	0.814
	Longitude	1.087	0.935	1.199
	Height	8.505	1.972	1.877
	3D	8.679	2.317	2.372
FAIR	Latitude	2.324	1.633	0.561
	Longitude	2.347	1.229	0.539
	Height	8.683	3.519	1.458
	3D	9.291	4.069	1.652

Table 6.29 Ionospheric Recovering Efficiency of 10-min TEC Predictions

Station	Recovering Efficiency (%)	Residual Error (%)
CARR	95.50%	4.50%
COSO	94.93%	5.07%
AMC2	100.0%	0.00%
CASP	95.44%	4.56%
PRDS	100.0%	0.00%
FAIR	68.36%	31.64%
Mean	92.37%	7.63%

Table 6.28 shows that the three-dimensional positioning errors using the tomographic model range between 2.0~4.0 m while the positioning errors using the dual-frequency model vary between 1.5~2.3 m. For the zero-model, its positioning errors are significantly higher than that using the other two ionospheric models and they also change between 8.6~13.1 m. The positioning errors related to the three different ionospheric correction models are summarized in Table 6.28. It can be seen that without ionospheric correction (using the zero-model), the positioning errors are at the order of 10.0 m. With the ionospheric corrections generated from the 10-min TEC predictions, the positioning errors are significantly decreased to a level of 2.0 m. Using the dual-frequency model, the positioning accuracies have a slight improvement over the tomographic model and the positioning accuracies at the stations are about 1.5~2.0 m.

The recovering efficiency of using 10-min TEC predictions from the tomographic model on DOY 089 is given in Table 6.29. It shows that the mean recovering efficiency of the 10-min TEC predictions is about 92.37% and the residual error is 7.63%. Compared to the results of Table 6.27, the employment of 10-min ionospheric predictions has a small degradation in the recovering efficiency. The mean recovering efficiency in Table 6.27 for the 5-min case is 92.91% and in the 10-min TEC predictions, the mean recovering efficiency is 92.37% as shown in Table 6.29. The degradation from using the 5-min TEC predictions to using 10-min TEC predictions to correct the ionospheric errors is 0.54%.

The 10-min TEC prediction data from stations DRAO and DAM2, which are obtained by excluding DRAO and DAM2 during the ionospheric modeling, are also tested. Figure 6.152 and Figure 6.153 show the point positioning results at DRAO and DAM2 stations, respectively. Figure 6.152 shows that at most epochs the tomographic model outperforms the zero-model in the capability of correcting ionospheric errors for single-frequency GPS users. Also at many epochs, the positioning accuracies for the tomographic model are comparable to those of the dual-frequency model. The positioning RMS statistics show that the zero-model has a positioning accuracy of 11.158 m, the tomographic model

3.717 m and the dual-frequency model 1.578 m. The recovering efficiency at DRAO station for the 10-min TEC prediction data is 77.67%. Shown in Figure 6.153 are the SPP results for DAM2 station, indicating that the tomographic model has a significant improvement over the zero-model at most epochs. At DAM2 station, the zero-model positioning accuracy is 13.761 m and the positioning results using tomographic model have an accuracy of 6.220 m. The accuracy of using dual-frequency model to correct ionospheric errors in SPP is 2.552 m. The recovering efficiency at DAM2 station is 67.28%.

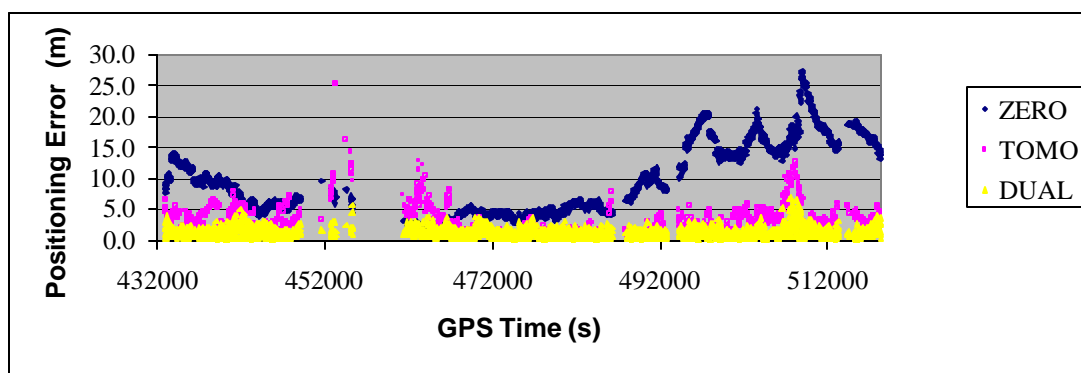


Figure 6.152 Positioning Error at DRAO Station Using Three Ionospheric Models, Tomographic Correction Predicted at 15° and 10-min Interval

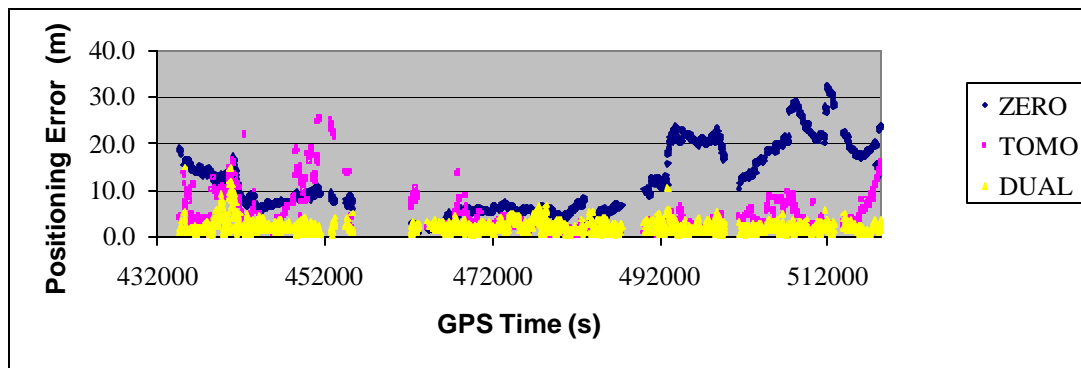


Figure 6.153 Positioning Error at DAM2 Station Using Three Ionospheric Models, Tomographic Correction Predicted at 15° and 10-min Interval

6.3.5.1.3 Use of 30-min TEC Prediction

The results below show the effect of long-term (30-min) TEC predictions on the point positioning accuracy. In this subsection, the ionospheric corrections are based on the 30-

min TEC predictions from the tomographic model while the previous subsections are based on 5-min and 10-min predictions. Comparing the positioning errors using the tomographic model and the dual-frequency model shown in Figure 6.154 to Figure 6.159, respectively, it can be seen that the performance of the tomographic model is very comparable to that from using the dual-frequency model. The only exception is at the FAIR station that is located at the edge of the GPS network and equipped with AOA TurboRogue GPS receiver. Positioning errors using the tomographic model are much larger than those using the dual-frequency model. As said before, tracking performance of codeless AOA TurboRogue receiver is more susceptible to cycle slips than semicodeless ASHTECH Z-12 receivers. Thus the data quality of FAIR station is worse than other stations equipped with ASHTECH Z-12 receivers. Moreover, the location of FAIR station also attributes to the poor TEC prediction accuracy. There is relatively less amount of TEC measurements around FAIR station during the ionospheric modeling than other stations located at central part of the network and this causes a performance degradation at the edge area in the network.

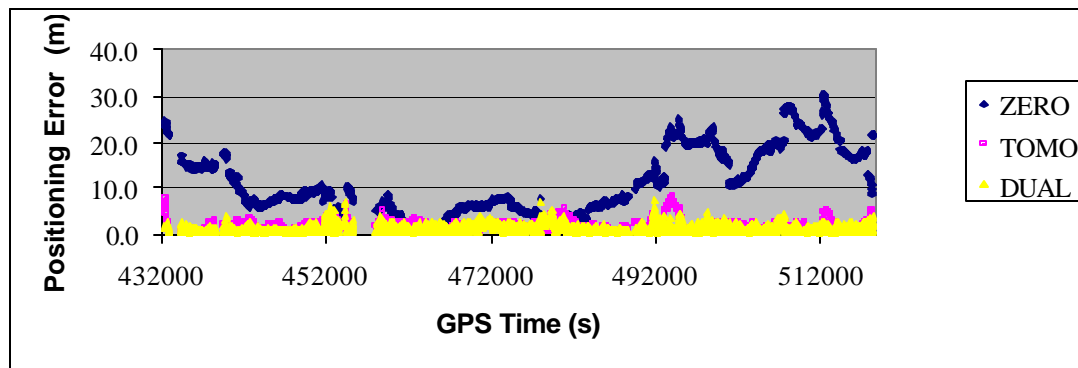


Figure 6.154 Positioning Error at CARR Station Using Three Ionospheric Models, Tomographic Correction Predicted at 15° and 30-min Interval

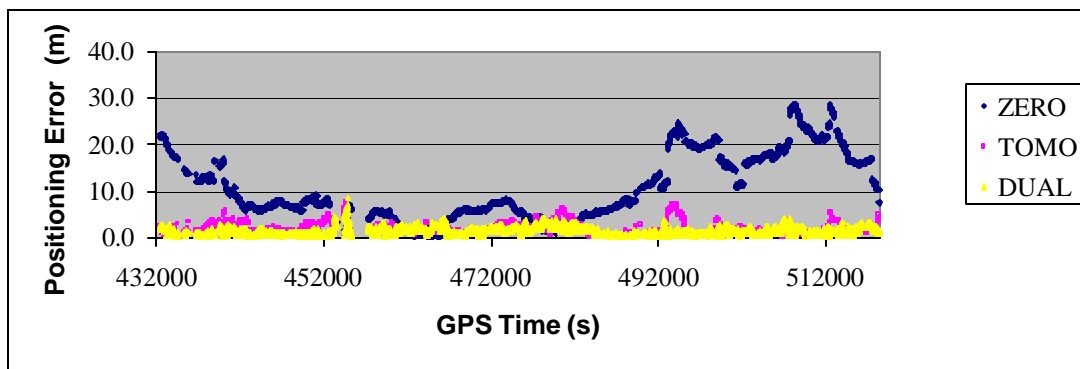


Figure 6.155 Positioning Error at COSO Station Using Three Ionospheric Models, Tomographic Correction Predicted at 15° and 30-min Interval

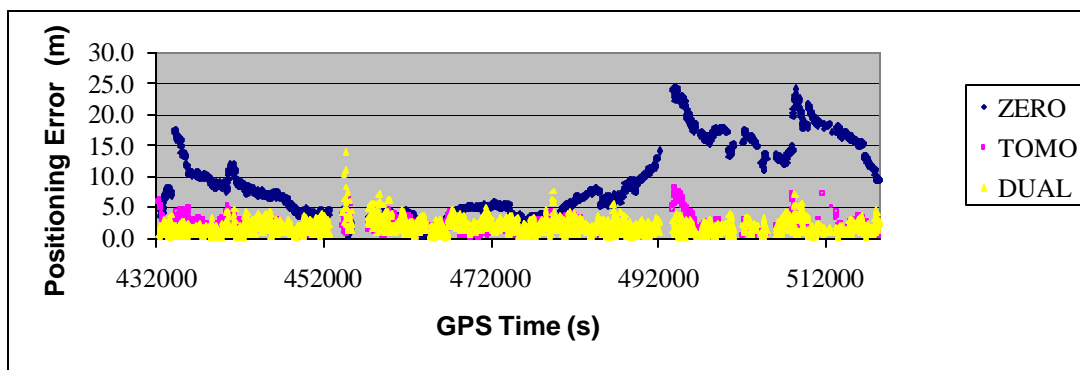


Figure 6.156 Positioning Error at AMC2 Station Using Three Ionospheric Models, Tomographic Correction Predicted at 15° and 30-min Interval

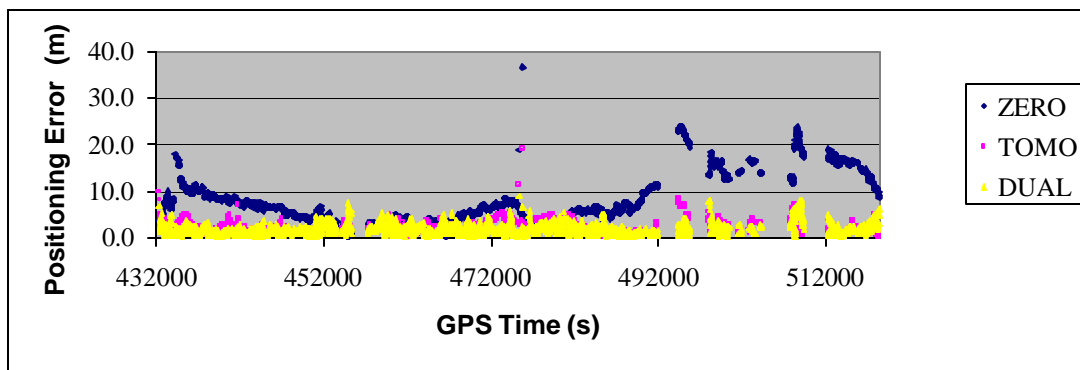


Figure 6.157 Positioning Error at CASP Station Using Three Ionospheric Models, Tomographic Correction Predicted at 15° and 30-min Interval

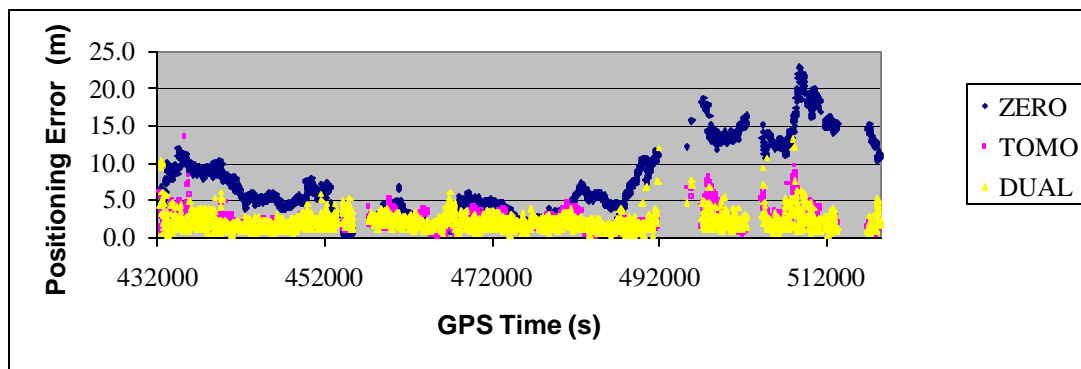


Figure 6.158 Positioning Error at PRDS Station Using Three Ionospheric Models, Tomographic Correction Predicted at 15° and 30-min Interval

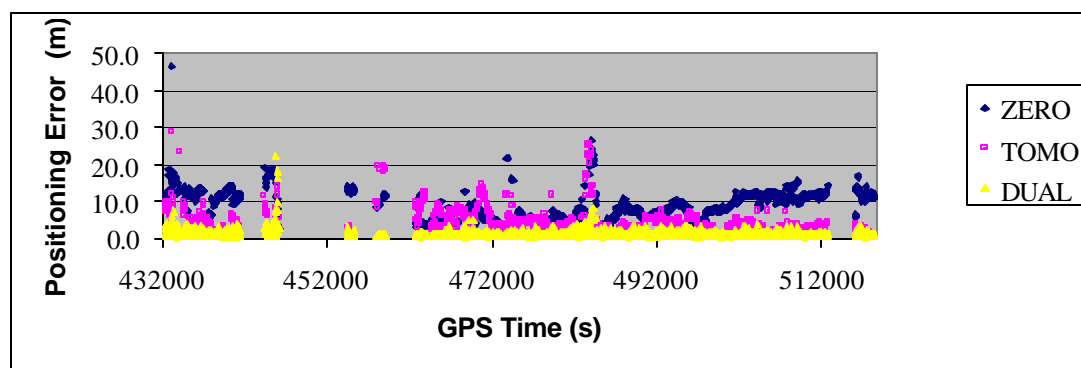


Figure 6.159 Positioning Error at FAIR Station Using Three Ionospheric Models, Tomographic Correction Predicted at 15° and 30-min Interval

Error! Not a valid bookmark self-reference. summarizes the positioning accuracies at each station using different ionospheric models. It clearly shows that the positioning accuracies have a drastic improvement from the zero-model when the 30-min TEC predictions are employed to correct the ionospheric errors in GPS positioning. Using the zero-model, the positioning accuracies are about 8.5~13.0 m. While using the tomographic model, the positioning accuracies are enhanced to a level of 2.1~4.9 m which is basically comparable to the accuracies about 1.5~2.3 m from the dual-frequency model.

Table 6.30 Single-frequency Single Point Positioning RMS Error at 6 Stations Using Tomographic Corrections Predicted at 15° and 30-min Interval (m)

Station	Component	Zero Model	Tomographic Model	Dual-frequency Model
CARR	Latitude	2.054	0.912	0.528
	Longitude	0.368	0.212	0.148
	Height	12.897	1.943	1.437
	3D	13.065	2.157	1.539
COSO	Latitude	2.012	0.854	0.463
	Longitude	0.226	0.137	0.071
	Height	12.511	2.137	1.598
	3D	12.674	2.305	1.665
AMC2	Latitude	1.901	0.829	0.762
	Longitude	0.589	0.384	0.349
	Height	10.153	2.136	2.041
	3D	10.346	2.323	2.207
CASP	Latitude	1.716	0.822	0.701
	Longitude	0.476	0.405	0.336
	Height	8.852	2.539	2.073
	3D	9.030	2.699	2.214
PRDS	Latitude	1.339	0.962	0.812
	Longitude	1.071	1.002	1.199
	Height	8.347	2.162	1.872
	3D	8.522	2.570	2.367
FAIR	Latitude	2.254	1.884	0.544
	Longitude	2.350	1.446	0.541
	Height	8.781	4.330	1.460
	3D	9.366	4.939	1.649

Table 6.31 Ionospheric Recovering Efficiency of 30-min TEC Predictions

Station	Recovering Efficiency (%)	Residual Error (%)
CARR	94.64%	5.36%
COSO	94.19%	5.81%
AMC2	98.57%	1.43%
CASP	92.88%	7.12%
PRDS	96.70%	3.30%
FAIR	57.37%	42.63%
Mean	89.06%	10.94%

Table 6.31 gives the ionospheric recovering efficiency for the 30-min TEC predictions generated from the tomographic model. It can be seen that except the high latitude station FAIR, all other stations have a recovering efficiency better than 92%. The analysis results indicate that the tomographic model has a degraded recovering capability at the high latitude station. The recovering efficiency at FAIR station is just 57.37%. In terms of the mean recovering efficiency for the 30-min TEC predictions, it is 89.06% as indicated by Table 6.31. This value is less than both the mean value 92.91% for the 5-min TEC predictions given in Table 6.27 and the mean value 92.37% for the 10-min TEC predictions given in Table 6.29. It implies that the employment of the 30-min TEC predictions to correct the ionospheric errors in GPS positioning can recover about 89.06% total ionospheric effects but this recovering efficiency is lower than the employment of the TEC predictions with shorter prediction intervals, e.g. 5-min and 10-min.

In the section below, the TEC prediction data, obtained at 30-min interval by excluding the stations DRAO and DAM2 from ionospheric modeling, are tested. Figure 6.160 and Figure 6.161 show the SPP results at DRAO and DAM2 stations obtained on DOY 089, respectively. The results in Figure 6.160 indicate that the tomographic model outperforms the zero-model with respect to the capability to compensate the ionospheric errors. For most epochs, the accuracies of the positioning solutions for the tomographic model are at a comparable level to those using the dual-frequency model. The positioning RMS statistics show that a positioning accuracy of 11.082 m is obtainable for the zero-model, 4.565 m for the tomographic model and 1.573 m for the dual-frequency model. The recovering efficiency for the 30-min TEC prediction data at DRAO station is 68.54%. The results for DAM2 station are depicted in Figure 6.161 and it shows that the tomographic model has a significant improvement over the zero-model. At DAM2 station, the zero-model based positioning accuracy is 13.693 m and the positioning accuracy using the tomographic model is 6.248 m. The positioning using the dual-

frequency model to correct the ionospheric errors has an accuracy of 2.530 m. The obtained recovering efficiency at DAM2 station is 66.69%.

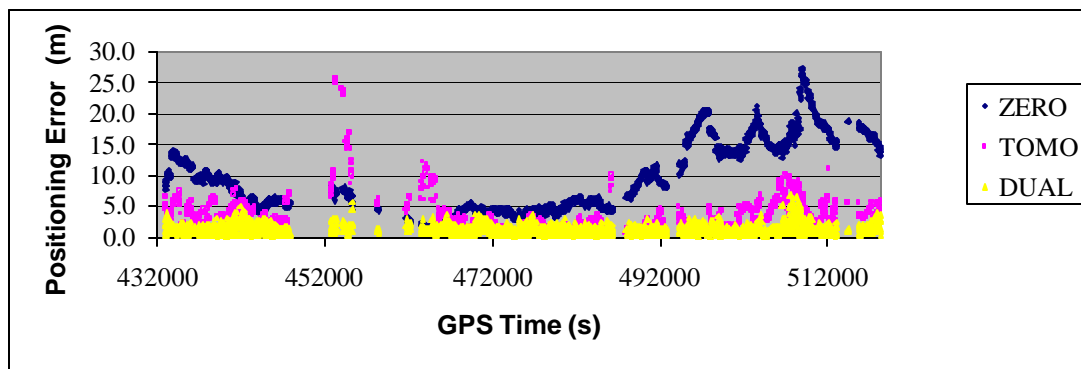


Figure 6.160 Positioning Error at DRAO Station Using Three Ionospheric Models, Tomographic Correction Predicted at 15° and 30-min Interval

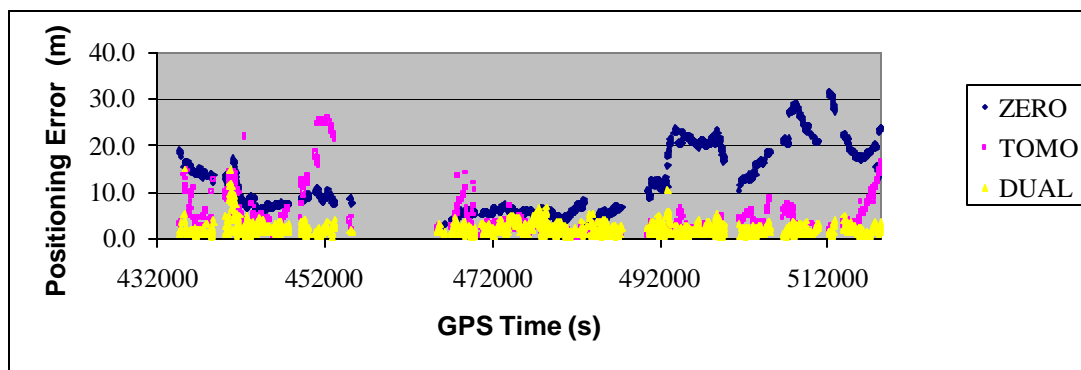


Figure 6.161 Positioning Error at DAM2 Station Using Three Ionospheric Models, Tomographic Correction Predicted at 15° and 30-min Interval

6.3.5.2 SPP results on DOY 090

The above section has analyzed the performance of the TEC predictions obtained on an ionosphere quiet day DOY 089. In order to test the performance of the tomographic model under different ionospheric conditions, the TEC predictions that are obtained on the ionosphere disturbed day are also employed in the SPP analysis and the results are presented in this section. Similar to above section, only the TEC predictions with 15° elevation cutoff angle are used although TEC data for three different elevation cutoff angles are available. Three TEC data sets, which are respectively predicted at 5-min, 10-

min and 30-min intervals, are employed in the positioning processing. In the data analysis, the elevation cutoff angle is set to 15° and the data are processed on the single epoch basis.

6.3.5.2.1 Use of 5-min TEC Prediction

Figure 6.162 to Figure 6.167 illustrate the point positioning results in which the ionospheric errors are corrected using the zero-model, the dual-frequency model and the 5-min TEC predictions generated from the tomographic model, respectively. It can be seen that the positioning errors corresponding to the zero-model are clearly larger than those from using the tomographic model and the dual-frequency model. The positioning errors using the zero-model vary between 10.0~20.0 m. At some epochs, the positioning errors become extremely large to a level of 70.0~80.0 m. This might be due to the drop in the number of the observed satellites. It can be seen that after applying the tomographic model or the dual-frequency model, the positioning accuracies are much better than those using the zero-model. Their accuracies are usually better than 5.0 m. Except for the two stations PRDS and FAIR, the performances of the tomographic model and dual-frequency model at other stations are very similar and comparable. At PRDS and FAIR stations, it can be seen that the positioning errors of the tomographic model are higher than those using the dual-frequency model. Examining the results in Figure 6.162 and Figure 6.163, it is found that during period 553620 s ~ 554040 s, the positioning errors corresponding to the zero-model, tomographic model and dual-frequency model have a big jump. For example, the positioning errors corresponding to zero-model jump from 6-7 m prior to 553620 s to a maximum about 68~78 m at epoch 554040 s. After epoch 554040 s, the positioning errors drop to normal level. Inspecting the raw GPS data for these two stations, it is found that during that period, the number of tracked satellites drops from normally 9-10 satellites to 6 satellites at both CARR and COSO stations. While comparing to the number of tracked satellite during 553620 s ~ 554040 s at other stations AMC2 and CASP, it is found AMC2 station maintains tracking 9-10 satellites and that CASP keeps tracking 8 satellites. At other two stations, PRDS has 9 satellites

tracked and FAIR station tracks 8-9 satellites during period 553620 s ~ 554040 s. At these stations like AMC2, CASP, CASP and FAIR, no such spike errors for the zero-model positioning results are identified in Figure 6.164 to Figure 6.167. Therefore, the spike positioning errors appearing in Figure 6.162 and Figure 6.163 are most likely the effect of reduced number of tracked satellites that deteriorates the observation geometry for single point positioning.

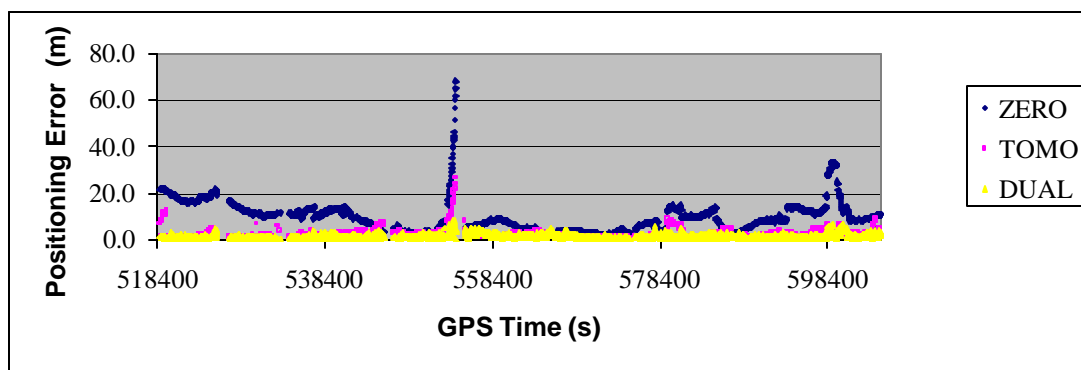


Figure 6.162 Positioning Error at CARR Station Using Three Ionospheric Models, Tomographic Correction Predicted at 15° and 5-min Interval

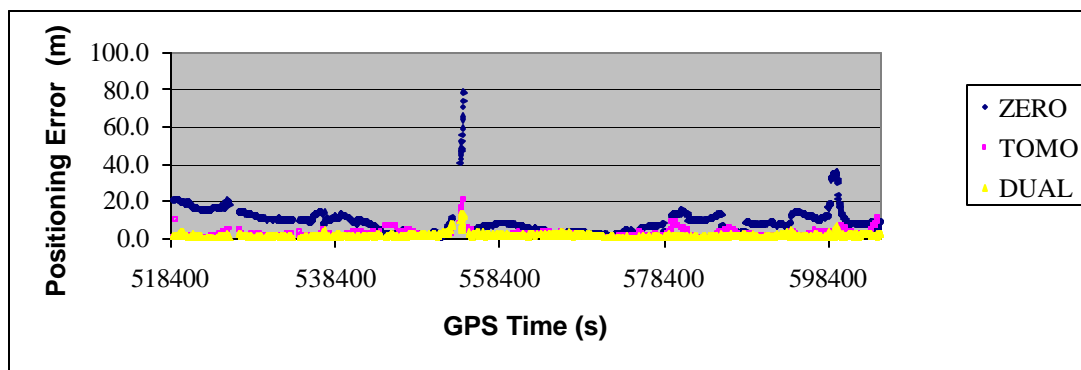


Figure 6.163 Positioning Error at COSO Station Using Three Ionospheric Models, Tomographic Correction Predicted at 15° and 5-min Interval

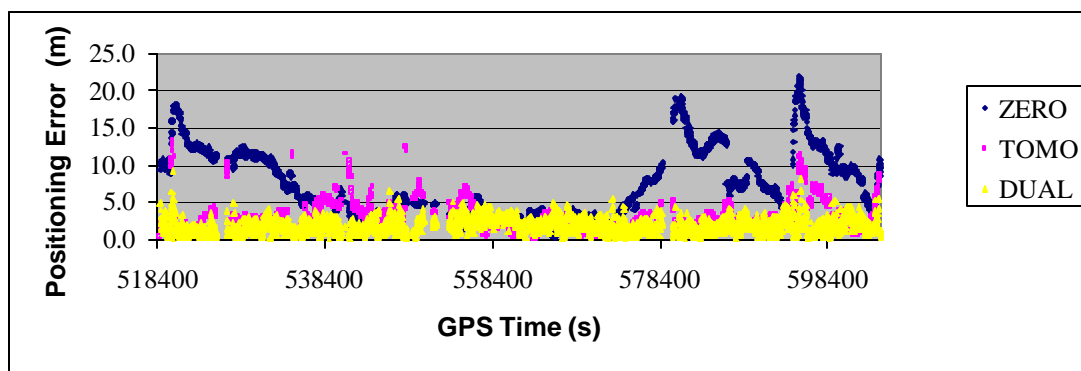


Figure 6.164 Positioning Error at AMC2 Station Using Three Ionospheric Models, Tomographic Correction Predicted at 15° and 5-min Interval

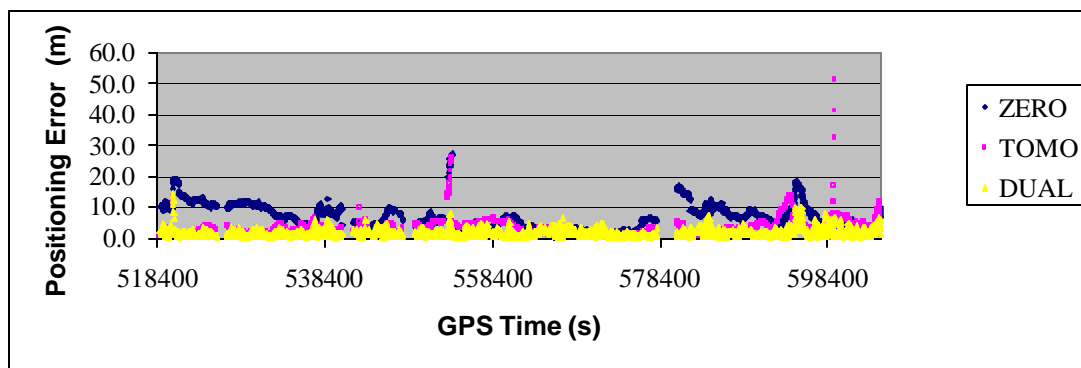


Figure 6.165 Positioning Error at CASP Station Using Three Ionospheric Models, Tomographic Correction Predicted at 15° and 5-min Interval

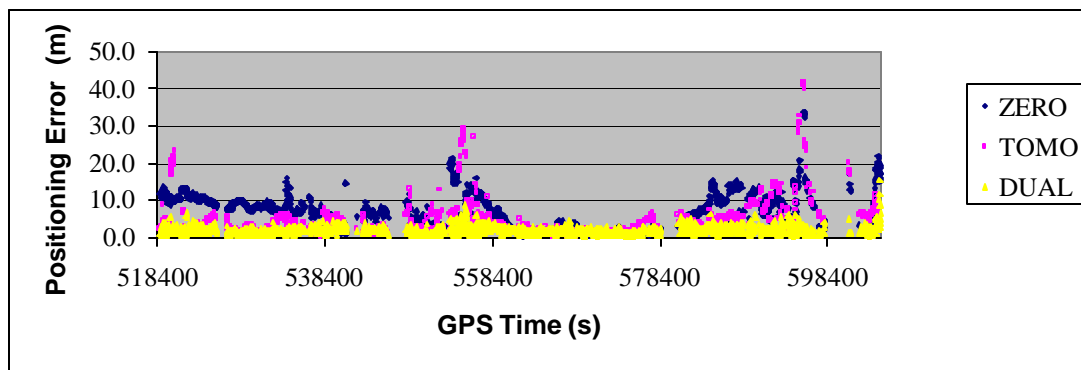


Figure 6.166 Positioning Error at PRDS Station Using Three Ionospheric Models, Tomographic Correction Predicted at 15° and 5-min Interval

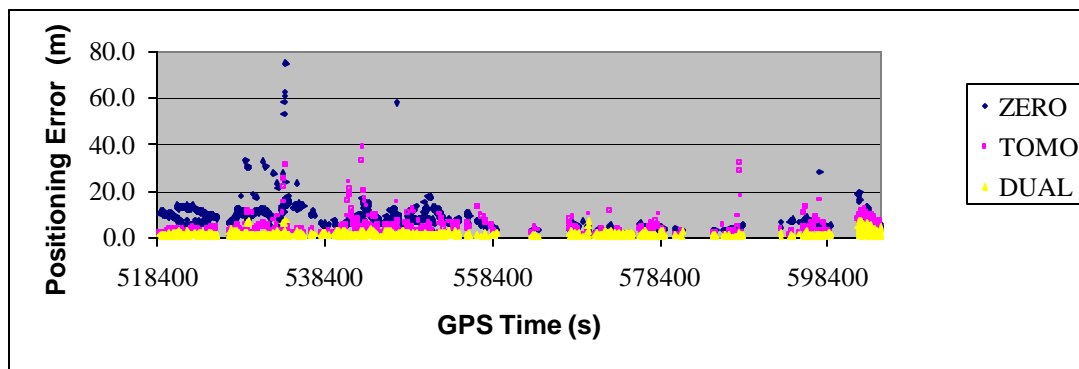


Figure 6.167 Positioning Error at FAIR Station Using Three Ionospheric Models, Tomographic Correction Predicted at 15° and 5-min Interval

Table 6.32 Single-frequency Single Point Positioning RMS Error at 6 Stations Using Tomographic Corrections Predicted at 15° and 5-min Interval (m)

Station	Component	Zero Model	Tomographic Model	Dual-frequency Model
CARR	Latitude	3.296	1.653	0.695
	Longitude	0.722	0.267	0.190
	Height	10.833	2.665	1.559
	3D	11.347	3.147	1.718
COSO	Latitude	3.320	1.645	0.506
	Longitude	0.444	0.153	0.104
	Height	10.484	2.504	1.805
	3D	11.006	2.999	1.877
AMC2	Latitude	2.649	1.636	0.626
	Longitude	1.262	0.703	0.304
	Height	8.032	3.086	2.064
	3D	8.551	3.563	2.179
CASP	Latitude	2.364	2.388	0.868
	Longitude	1.260	0.886	0.359
	Height	7.335	3.514	2.246
	3D	7.809	4.340	2.434
PRDS	Latitude	2.676	2.600	0.844
	Longitude	3.045	2.109	1.161
	Height	6.829	5.474	1.713
	3D	7.942	6.417	2.235
FAIR	Latitude	2.401	1.648	0.486
	Longitude	3.770	1.676	0.519
	Height	8.606	4.918	1.309
	3D	9.698	5.451	1.490

Table 6.32 gives a summary of the positioning errors at each coordinate component obtained from using different ionospheric models. Table 6.32 indicates that the RMS of the positioning errors corresponding to the zero-model is about 8.0~11.0 m. Using the tomographic model to correct ionospheric errors in SPP, the RMS of the positioning errors reduces to a level of 3.0~6.5 m. If the dual-frequency model is applied, the point positioning has shown an even higher accuracy than using the tomographic model. Table 6.32 shows that the RMS of SPP errors after using the dual-frequency model is about 1.5~2.5 m. The ionospheric recovering efficiency of the tomographic model at each station is calculated and presented in Table 6.33.

Table 6.33 indicates that the mean recovering efficiency is 65.69% under the ionosphere disturbance condition. Compared to the SPP results on DOY 089 with the 5-min TEC predictions, the mean recovering efficiency has degraded from 92.91% to 65.69%. It clearly shows the influence of the ionospheric disturbance on the recovering efficiency of the ionospheric TEC predictions. Table 6.33 also shows that at low latitude stations, the recovering efficiencies are still as good as 78%~87%. When the latitude increases, the recovering efficiency of the TEC prediction data has an apparent degradation to the level of 50%~65%. At PRDS, the recovering efficiency is extremely poor. This might be due to a decrease in the number of satellites used in the SPP analysis because of the rejection of some satellites in the SPP software package due to poor ionospheric corrections provided by the TEC prediction data.

Table 6.33 Ionospheric Recovering Efficiency of 5-min TEC Predictions

Station	Recovering Efficiency (%)	Residual Error (%)
CARR	85.16%	14.84%
COSO	87.71%	12.29%
AMC2	78.28%	21.72%
CASP	64.54%	35.46%
PRDS	26.72%	73.28%
FAIR	51.74%	48.26%
Mean	65.69%	34.31%

Presented in Figure 6.168 and Figure 6.169 are the positioning errors at two stations using three different types of ionospheric models and data acquired on an ionospheric disturbed day DOY 090. The predicted TEC data are obtained at a 5-min interval. Figure 6.168 shows that the point positioning results at DRAO station by applying the TEC predictions obtained from the ionospheric modeling. DRAO is considered an independent station since it was not included in the computation of the ionospheric predictions. It shows that on the disturbed day the tomographic model still outperforms the zero-model in the capability of compensating ionospheric errors for single-frequency GPS users. The accuracies of the positioning solutions at many epochs for the tomographic model are close to those obtained using the dual-frequency model. The positioning RMS statistics show that the positioning accuracy is 7.518 m when using the zero-model, and it is 4.018 m using the tomographic model and 1.908 m using the dual-frequency model. The recovering efficiency at DRAO station with 5-min TEC prediction data is 62.39%. Shown in Figure 6.169 are the positioning results for DAM2 station and it shows that the tomographic model has significantly improved the positioning accuracy over the zero-model. At DAM2 station, the zero-model positioning accuracy is 10.478 m and the positioning results using the tomographic model have a positioning error of 5.335 m. The positioning using the dual-frequency model to correct the ionospheric errors has an accuracy of 2.577 m. The recovering efficiency at DAM2 station is 65.09%.

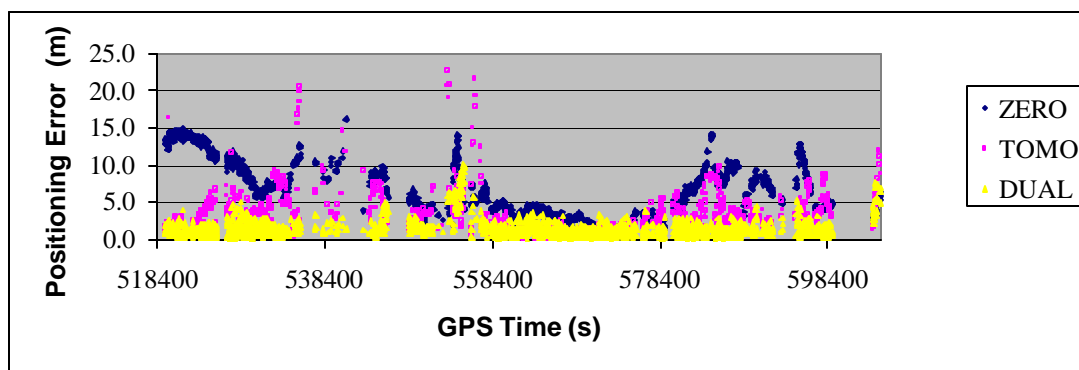


Figure 6.168 Positioning Error at DRAO Station Using Three Ionospheric Models, Tomographic Correction Predicted at 15° and 5-min Interval

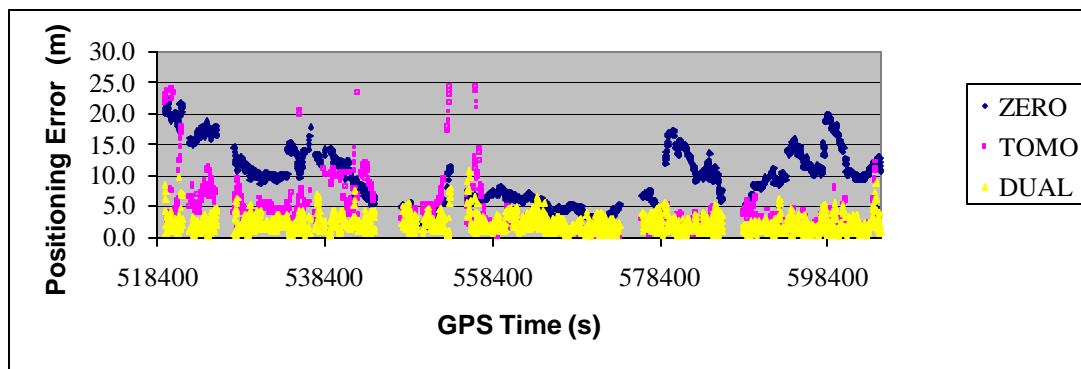


Figure 6.169 Positioning Error at DAM2 Station Using Three Ionospheric Models, Tomographic Correction Predicted at 15° and 5-min Interval

6.3.5.2.2 Use of 10-min TEC Prediction

Shown in Figure 6.170 to Figure 6.175 are point positioning results at six GPS stations using different ionospheric correction models. The tomographic model uses the 10-min TEC prediction data. The SPP solutions using the zero-model have the biggest errors among the three models. At the low latitude stations, the positioning solutions using the ionospheric tomographic models have accuracies comparable to the use of the dual-frequency model. This can be seen from the results shown in Figure 6.170 to Figure 6.173. At stations with high latitudes such as PRDS and FAIR, the 10-min TEC predictions generated from the ionospheric tomographic model have less satisfactory performance than the dual-frequency model. Table 6.34 indicates that the positioning accuracies using the zero-model range from 8.0~11.0 m. As a comparison, the positioning accuracies using the 10-min TEC predictions have been improved to the level of 3.0~6.5 m. Needless to say, the dual-frequency model has the best performance and the positioning accuracy using this model is about 1.5~2.5 m.

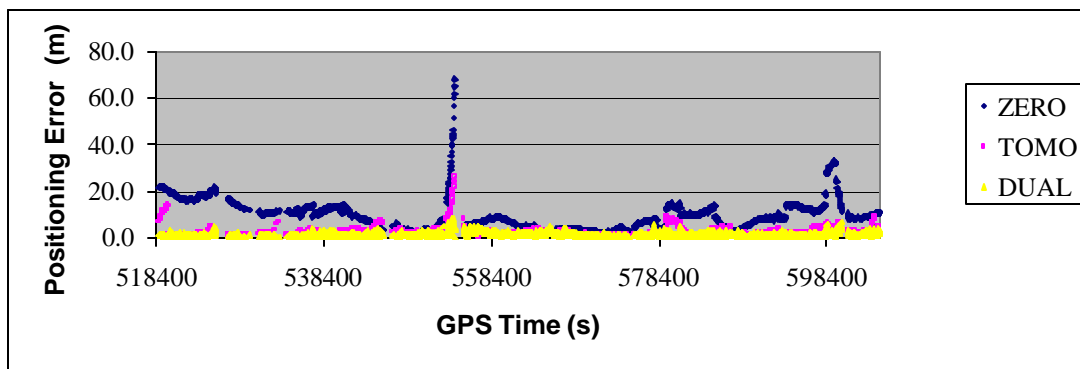


Figure 6.170 Positioning Error at CARR Station Using Three Ionospheric Models, Tomographic Correction Predicted at 15° and 10-min Interval

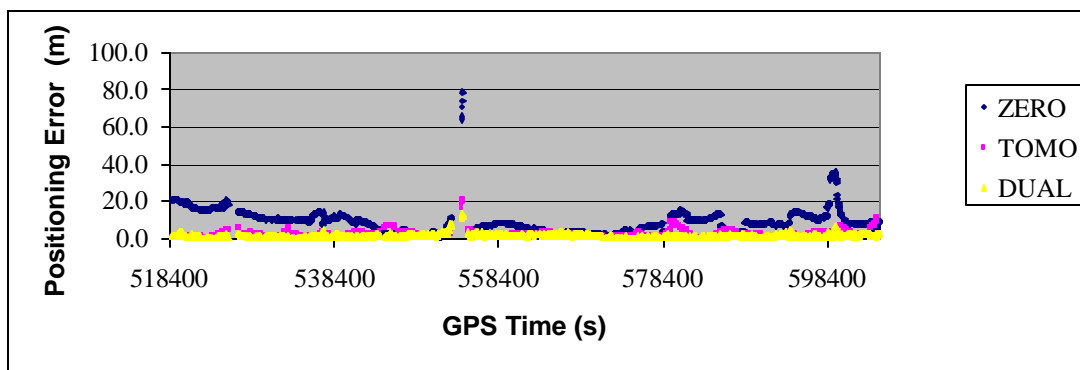


Figure 6.171 Positioning Error at COSO Station Using Three Ionospheric Models, Tomographic Correction Predicted at 15° and 10-min Interval

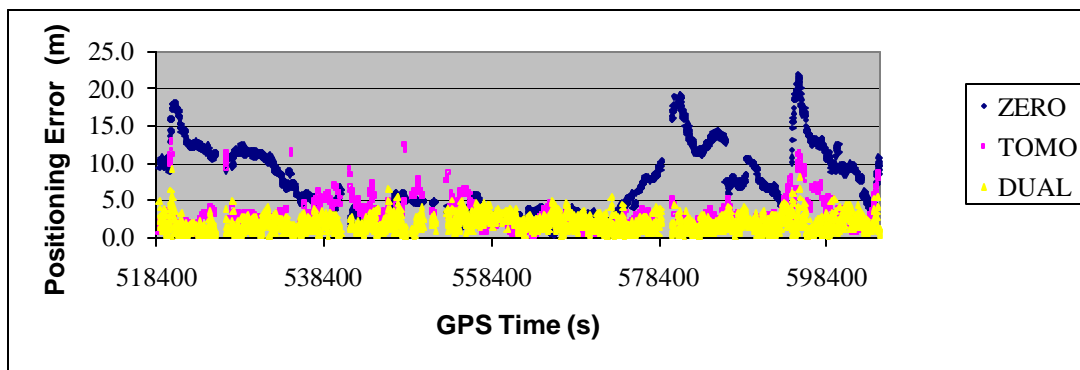


Figure 6.172 Positioning Error at AMC2 Station Using Three Ionospheric Models, Tomographic Correction Predicted at 15° and 10-min Interval

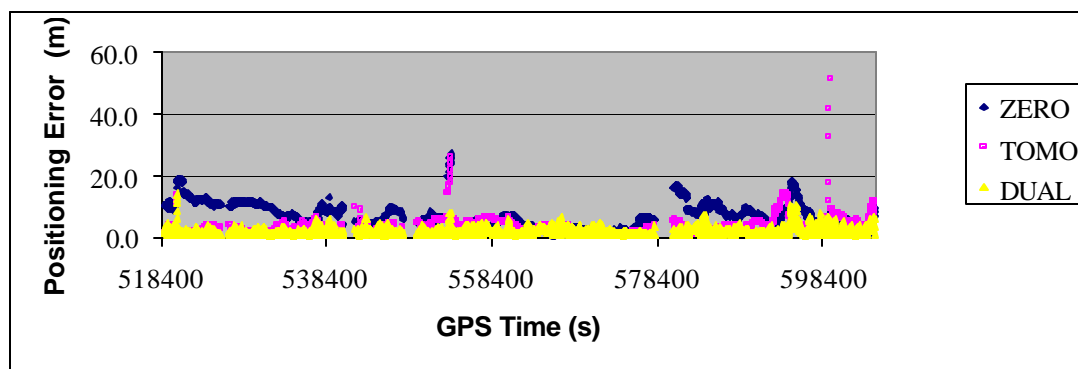


Figure 6.173 Positioning Error at CASP Station Using Three Ionospheric Models, Tomographic Correction Predicted at 15° and 10-min Interval

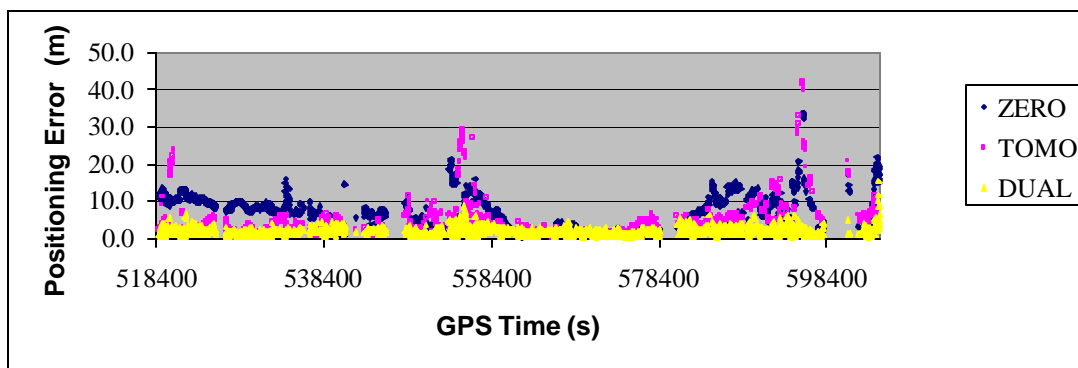


Figure 6.174 Positioning Error at PRDS Station Using Three Ionospheric Models, Tomographic Correction Predicted at 15° and 10-min Interval

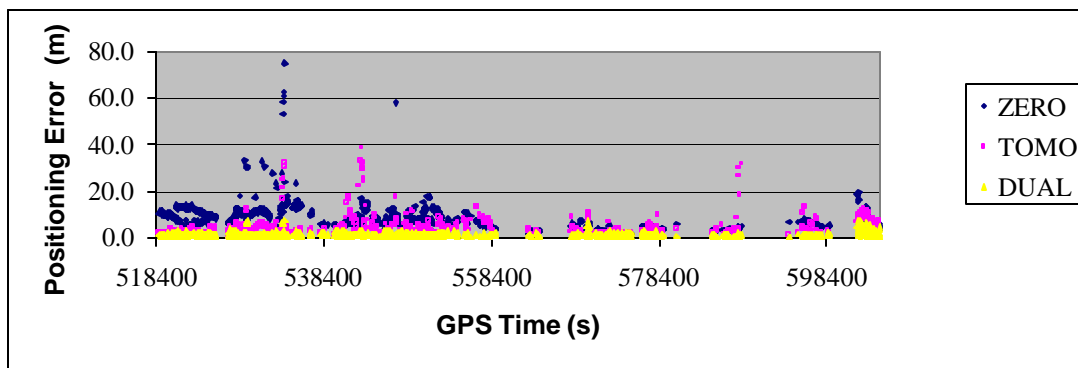


Figure 6.175 Positioning Error at FAIR Station Using Three Ionospheric Models, Tomographic Correction Predicted at 15° and 10-min Interval

Table 6.34 Single-frequency Single Point Positioning RMS Error at 6 Stations Using Tomographic Corrections Predicted at 15° and 10-min Interval (m)

Station	Component	Zero Model	Tomographic Model	Dual-frequency Model
CARR	Latitude	3.328	1.649	0.688
	Longitude	0.695	0.285	0.184
	Height	10.666	2.823	1.551
	3D	11.195	3.282	1.707
COSO	Latitude	3.265	1.630	0.494
	Longitude	0.394	0.153	0.097
	Height	10.095	2.351	1.708
	3D	10.617	2.865	1.781
AMC2	Latitude	2.656	1.648	0.626
	Longitude	1.265	0.707	0.306
	Height	8.040	3.102	2.071
	3D	8.562	3.583	2.185
CASP	Latitude	2.368	2.391	0.866
	Longitude	1.262	0.892	0.358
	Height	7.348	3.599	2.243
	3D	7.822	4.412	2.431
PRDS	Latitude	2.692	2.648	0.843
	Longitude	3.068	2.183	1.161
	Height	6.788	5.539	1.713
	3D	7.920	6.516	2.235
FAIR	Latitude	2.392	1.846	0.480
	Longitude	3.755	1.729	0.514
	Height	8.614	5.187	1.300
	3D	9.697	5.771	1.478

Table 6.35 Ionospheric Recovering Efficiency of 10-min TEC Predictions

Station	Recovering Efficiency (%)	Residual Error (%)
CARR	83.40%	16.60%
COSO	87.73%	12.27%
AMC2	78.08%	21.92%
CASP	63.25%	36.75%
PRDS	24.70%	75.30%
FAIR	47.77%	52.23%
Mean	64.16%	35.84%

Table 6.34 summarizes the performances using different ionospheric models for single-epoch point positioning with a single-frequency GPS receiver. The results clearly show that the application of the 10-min TEC predictions generated by the tomographic model have significantly improved the positioning accuracies over the zero-model. The recovering efficiency of the tomographic model is presented in Table 6.35. It indicates that the performance of the 10-min TEC predictions for SPP positioning would degrade with the increase of the GPS station's latitude. At low latitude stations, the recovering efficiency is about 63%~87%. At high latitude stations, the efficiency degrades to the level of about 25%~48%. But in terms of the mean recovering efficiency, it is still as good as 64.16%. That means the 10-min TEC prediction data obtained under ionospheric disturbance conditions can correct about 64.16% ionospheric effects on GPS positioning. Compared to the performance of the 5-min TEC prediction data, the efficiency of the 10-min predictions has been slightly degraded from 65.69% to 64.16%.

Shown in Figure 6.176 and Figure 6.177 are the positioning errors at DRAO and DAM2 stations using three types of ionospheric models with 10-min TEC predictions for ionospheric disturbed day DOY 090. These TEC predictions are obtained by excluding DRAO or DAM2 station during the ionospheric modeling. Figure 6.176 shows that the point positioning results at DRAO station with 10-min TEC predictions. It shows that on the disturbed day the tomographic model still outperforms the zero-model in compensating the ionospheric errors for single-frequency GPS users. The positioning RMS statistics show that the positioning accuracy is 7.512 m using the zero-model, 4.015 m using the tomographic model and 1.886 m using the dual-frequency model. The recovering efficiency for the 10-min TEC prediction data at DRAO station is 62.16%. The results for DAM2 station are depicted in Figure 6.177 and it shows that the tomographic model has significantly improved the positioning accuracy over the zero-model except at some epochs where the tomographic model has large positioning errors than the zero-model. The large positioning errors at those epochs is due to the poor TEC prediction accuracy for some satellites. At DAM2 station, the positioning accuracy is

10.509 m using the zero-model, 5.376 m using the tomographic model and 2.581 m using the dual-frequency model. The recovering efficiency at DAM2 station is 64.75%.

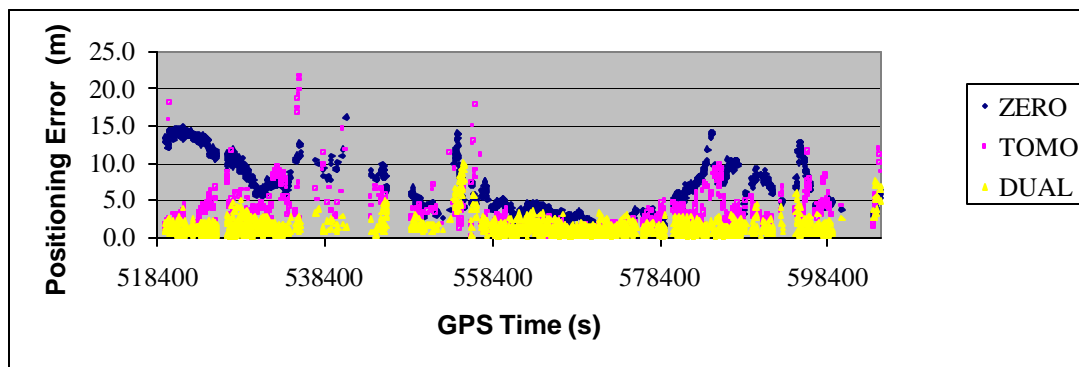


Figure 6.176 Positioning Error at DRAO Station Using Three Ionospheric Models, Tomographic Correction Predicted at 15° and 10-min Interval

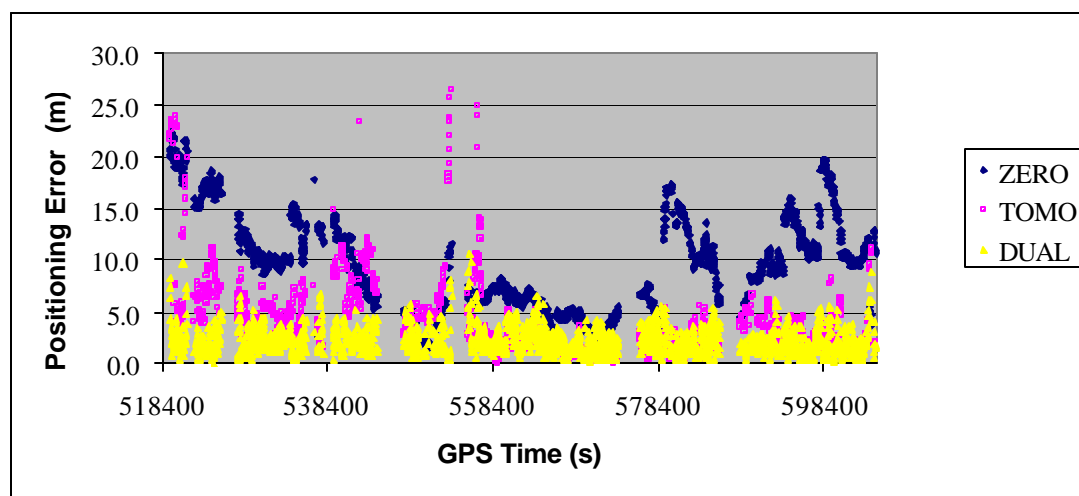


Figure 6.177 Positioning Error at DAM2 Station Using Three Ionospheric Models, Tomographic Correction Predicted at 15° and 10-min Interval

6.3.5.2.3 Use of 30-min TEC Prediction

The subsection below shows the positioning results obtained by using different models to correct ionospheric errors. In this subsection the TEC correction data from the tomographic model are generated at 30-min interval. It can be seen from Figure 6.178 to Figure 6.183 that both the tomographic model and the dual-frequency model show a distinct improvement in positioning accuracies over the zero-model. The SPP solutions have the largest errors when the zero-model is used. The performance of the tomographic

model is very similar to the dual-frequency model at the low latitude stations, as shown in Figure 6.178 to Figure 6.181. However at high latitude stations, the performance of the tomographic model indicates a degraded performance and the positioning solutions using the tomographic model are less satisfactory than the dual-frequency model.

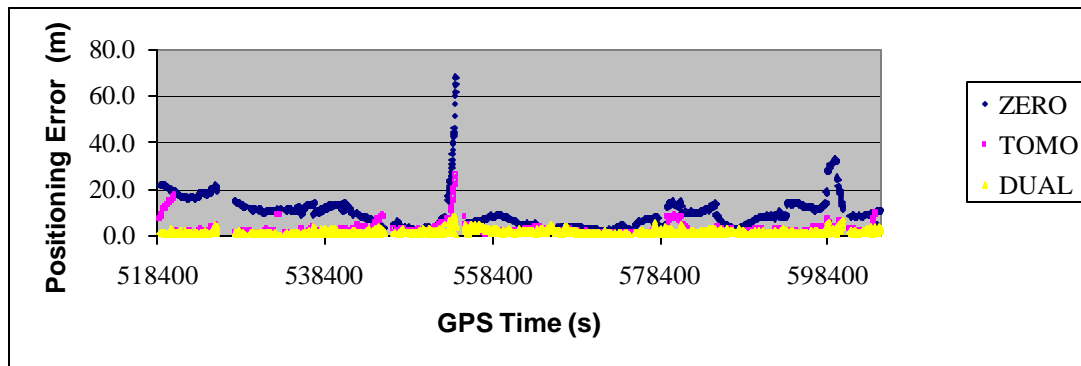


Figure 6.178 Positioning Error at CARR Station Using Three Ionospheric Models, Tomographic Correction Predicted at 15° and 30-min Interval

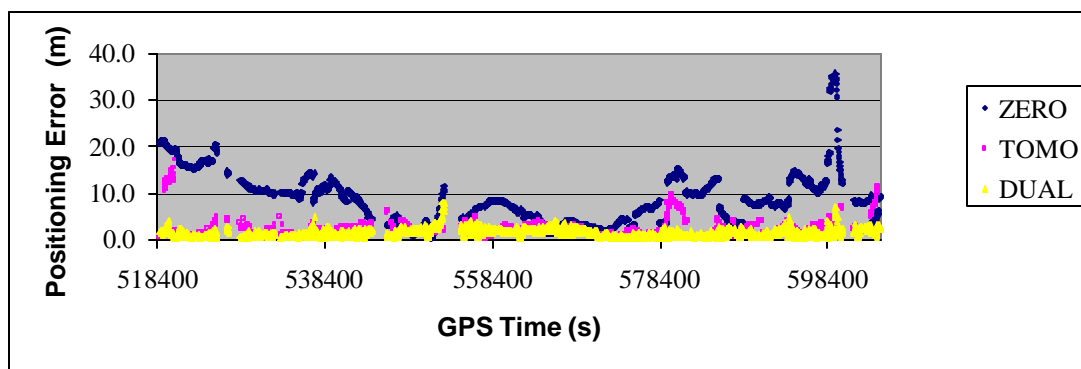


Figure 6.179 Positioning Error at COSO Station Using Three Ionospheric Models, Tomographic Correction Predicted at 15° and 30-min Interval

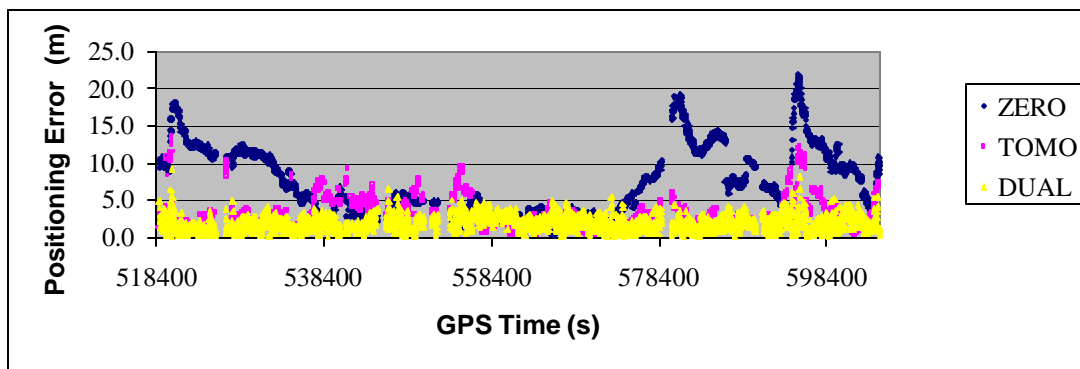


Figure 6.180 Positioning Error at AMC2 Station Using Three Ionospheric Models, Tomographic Correction Predicted at 15° and 30-min Interval

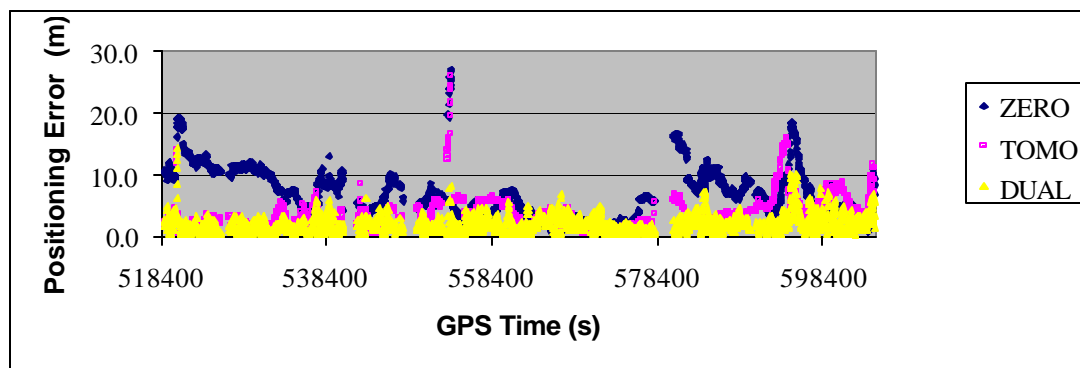


Figure 6.181 Positioning Error at CASP Station Using Three Ionospheric Models, Tomographic Correction Predicted at 15° and 30-min Interval

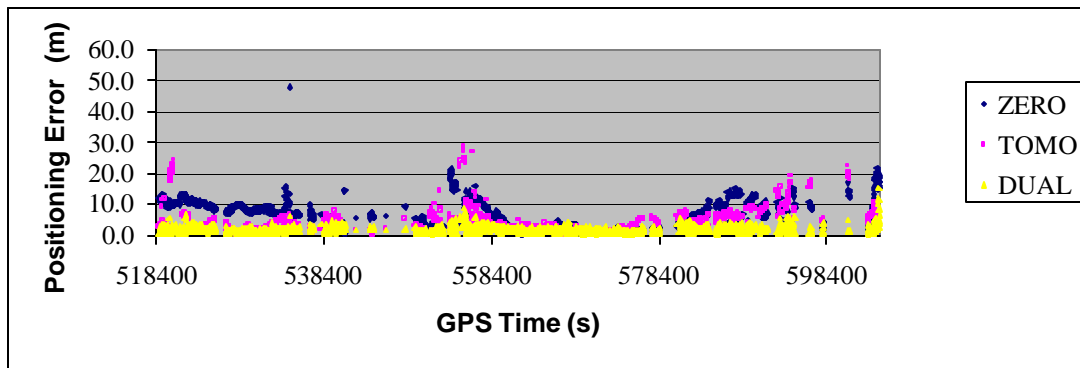


Figure 6.182 Positioning Error at PRDS Station Using Three Ionospheric Models, Tomographic Correction Predicted at 15° and 30-min Interval

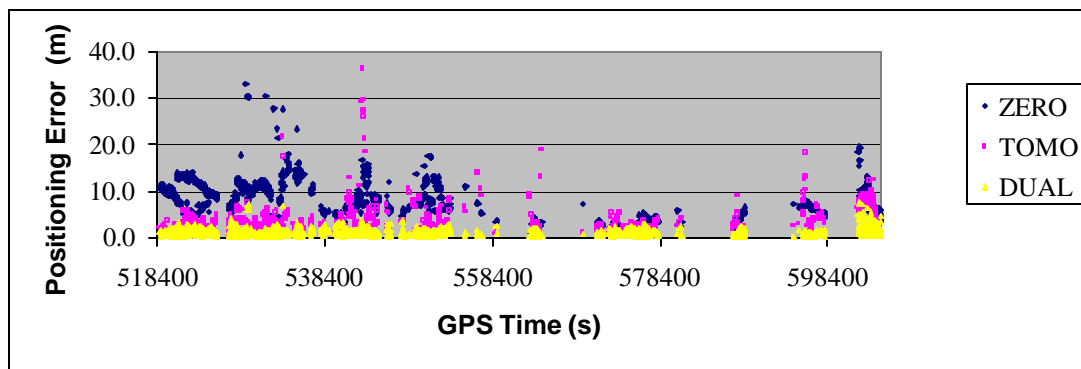


Figure 6.183 Positioning Error at FAIR Station Using Three Ionospheric Models, Tomographic Correction Predicted at 15° and 30-min Interval

Table 6.36 Single-frequency Single Point Positioning RMS Error at 6 Stations Using Tomographic Corrections Predicted at 15° and 30-min Interval (m)

Station	Component	Zero Model	Tomographic Model	Dual-frequency Model
CARR	Latitude	3.312	1.663	0.680
	Longitude	0.692	0.319	0.181
	Height	10.638	3.184	1.540
	3D	11.164	3.606	1.693
COSO	Latitude	3.237	1.568	0.486
	Longitude	0.346	0.167	0.092
	Height	9.661	2.485	1.626
	3D	10.194	2.943	1.700
AMC2	Latitude	2.630	1.750	0.625
	Longitude	1.247	0.712	0.306
	Height	8.118	3.213	2.076
	3D	8.624	3.728	2.189
CASP	Latitude	2.360	2.288	0.871
	Longitude	1.246	0.912	0.360
	Height	7.370	3.564	2.261
	3D	7.838	4.332	2.450
PRDS	Latitude	2.858	2.527	0.833
	Longitude	3.012	2.109	1.153
	Height	6.563	4.362	1.711
	3D	7.766	5.465	2.225
FAIR	Latitude	2.123	2.070	0.463
	Longitude	2.706	1.597	0.488
	Height	8.262	4.296	1.294
	3D	8.949	5.029	1.459

Table 6.36 provides the positioning accuracies at six stations using three different ionospheric correction models. After using the 30-min TEC predictions generated from the tomographic model, the positioning accuracies immediately improve to 3.0~5.5 m from 8.0~11.0 m obtained from the zero-model. However using the dual-frequency model, the positioning accuracies have a further improvement. Table 6.36 indicates that the positioning solutions have an accuracy about 1.5~2.5 m when using the dual-frequency model to correct ionospheric errors in GPS positioning. Based on the positioning accuracies shown in Table 6.36, the ionospheric recovering efficiency of the tomographic model can be determined and they are summarized in Table 6.37.

Table 6.37 Ionospheric Recovering Efficiency of 30-min TEC Predictions

Station	Recovering Efficiency (%)	Residual Error (%)
CARR	79.80%	20.20%
COSO	85.37%	14.63%
AMC2	76.08%	23.92%
CASP	65.07%	34.93%
PRDS	41.53%	58.47%
FAIR	52.34%	47.66%
Mean	66.70%	33.30%

Table 6.37 presents the ionospheric recovering efficiency of the tomographic model at the six stations. The recovering efficiencies in Table 6.37 show a similar variation pattern as demonstrated in Table 6.33 and Table 6.35, i.e., the low latitude stations have higher recovering efficiency than the high latitude stations. Table 6.37 shows that the mean recovering efficiency using the 30-min predicted TEC is 66.70%, slightly higher than that presented in the previous two schemes (5-min and 10-min TEC predictions). The reason is that at some epochs in the previous two schemes the positioning solutions at PRDS station when using the tomographic model have very huge spikes in the positioning errors. This huge spikes drop out in this scheme because at these epochs the positioning solutions are not available. In the SPP software package, when the data of a given satellite is judged to be invalid by the software, e.g. too large residuals, the satellite will be rejected in the positioning solution. This rejection is possibly caused by a large

ionospheric TEC prediction error for a given satellite. When there are not enough valid GPS satellites in the positioning, the positioning results will not be used in the data analysis. Overall, the analysis indicates that using 30-min TEC prediction data, the tomographic model still has an average recovering efficiency about 66.70%.

Shown in Figure 6.184 and Figure 6.185 are the positioning errors at DRAO and DAM2 stations using three ionospheric models with 30-min TEC predictions with data acquired on an ionospheric disturbed day DOY 090. The 30-min TEC predictions at DRAO and DAM2 stations are obtained by excluding the two stations from the ionospheric modeling. Figure 6.184 shows that the point positioning results at DRAO station with 30-min TEC predictions. The results show that the tomographic model can compensate ionospheric errors much better than the zero-model although not as much as when a shorter prediction interval 5-min or 10-min was used. The positioning RMS statistics show that the positioning accuracy is 7.554 m using the zero-model, 4.592 m using the tomographic model and 1.900 m using the dual-frequency model. The recovering efficiency for the 30-min TEC prediction data is 52.39%. The results for DAM2 station are shown in Figure 6.185 and they show that the tomographic model provides greater improvement over the zero-model compared to the results at DRAO station. For DAM2, the positioning accuracy is 10.557 m using the zero-model while it is 5.399 m using the tomographic model. The positioning accuracy using the dual-frequency model is 2.586 m. The recovering efficiency at DAM2 station is 64.71%.

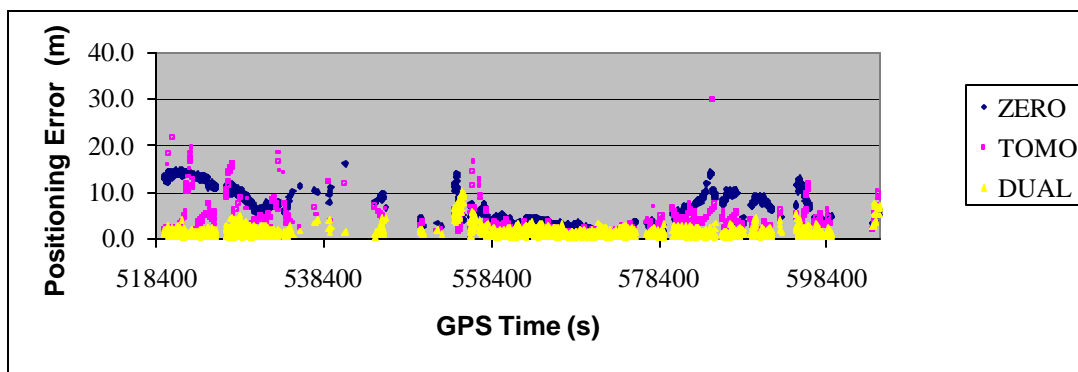


Figure 6.184 Positioning Error at DRAO Station Using Three Ionospheric Models, Tomographic Correction Predicted at 15° and 30-min Interval

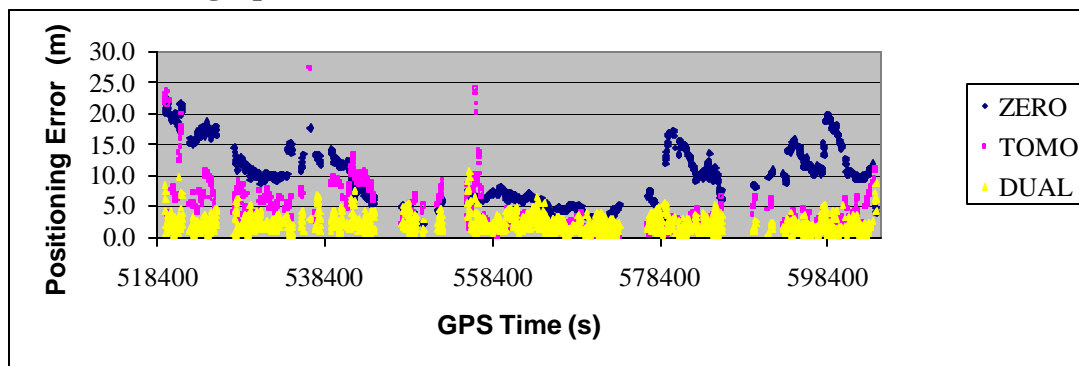


Figure 6.185 Positioning Error at DAM2 Station Using Three Ionospheric Models, Tomographic Correction Predicted at 15° and 30-min Interval

6.3.5.3 Summary

Section 6.3.5 presents the point positioning results with ionospheric corrections from tomographic prediction TEC data as well as two other ionospheric models. Through the comparison of positioning accuracies of three different models, the ionospheric recovering efficiency of the tomographic model predictions is calculated using the formula given by equation (4.68) proposed in Chapter 4. In order to avoid lengthy presentation of the point positioning results, only the TEC predictions with 15° are used in Section 6.3.5. The TEC predictions obtained at 20° and 25° can also be used in the exactly same way to correct the ionospheric errors for single-frequency point positioning but their results are not presented in this research. Table 6.38 summarizes the recovering efficiency of the predicted TEC data in single-frequency point positioning performed on both DOY 089 and 090. Also included in Table 6.38 is the residual of the irrecoverable error in the point positioning, denoted in parentheses.

Table 6.38 Summary of Recovering Efficiency for DOY 089 and 090

	5-min	10-min	30-min
DOY 089	92.91% (7.09%)	92.37% (7.63%)	89.06% (10.94%)
DOY 090	65.69% (34.31%)	64.16% (35.84%)	66.70% (33.30%)

Table 6.38 shows that on ionosphere quiet day DOY 089, the recovering efficiency of the predicted TEC data generated from the tomographic model ranges about 89%~93%. While on the ionosphere disturbed day DOY 090 (for 6 hours with Kp index values at 9), the recovering efficiency of the predicted TEC data has a significant degradation of about 25% from the previous quiet day. The recovering efficiency on DOY 090 is at the level 65%. Table 6.38 also shows that the recovering efficiency does not have a large difference between the schemes of using 5-min, 10-min or 30-min TEC predictions. Basically the shorter prediction interval, the higher recovering efficiency except the 30-min case on ionosphere disturbed day DOY 090. This is possible under the extremely disturbed ionospheric condition. Under this severe ionosphere condition, the quality of GPS data is degraded by such as cycle slips and loss of lock. During to the “time window” for TEC data smoothing, ionospheric modeling and TEC prediction is different for 5-min, 10-min or 30-min, hence quality of the predicted TEC data is different for three prediction intervals. From the statistics point of view, it is possible for that during the 24-hour positioning period, the recovering efficiency of the 30-min prediction data slightly outperforms those of 5-min and 10-min TEC predictions.

The recovering efficiencies of the predicted TEC data obtained from two stations DRAO and DAM2, where their GPS data are excluded during the ionospheric modeling, are also summarized in Table 6.39. It shows that the 5-min and 10-min TEC predictions have similar performances in the single point positioning test. The capability of 10-min ionospheric TEC predictions is quite comparable to the 5-min prediction data although the 10-min interval is double of 5-min interval. This is consistent with the statistics summarized in Table 6.38. Comparing Table 6.38 and Table 6.39, it shows that the performances of the TEC predictions obtained by including the stations in ionospheric modeling and TEC predictions obtained by excluding the stations from ionospheric modeling are quite similar on ionospheric disturbed day DOY 090. On ionospheric quiet day DOY 089, the TEC predictions that include DRAO and DAM2 stations in ionospheric modeling, have smaller recovering efficiency than the case of excluding them

during the modeling stage. But these predictions still have a recovering efficiency over the level of 77% for 5-min and 10-min prediction intervals and over 68% at 30-min prediction interval.

Table 6.39 Summary of Recovering Efficiency for DRAO and DAM2 Predictions

		5-min	10-min	30-min
DOY 089	DRAO	77.35%	77.67%	68.54%
	DAM2	70.22%	67.28%	66.69%
DOY 090	DRAO	62.39%	62.16%	52.39%
	DAM2	65.09%	64.75%	64.71%

CHAPTER 7

CONCLUSIONS AND RECOMMENDATIONS

Precise multiple-layer ionospheric modeling using data from GPS reference networks has been investigated in this thesis. The provision of ionospheric corrections from precise ionospheric models is important for single frequency GPS users to improve their positioning and navigation accuracies and also critical for many applications such as space weather studies. In the following sections, the conclusions obtained from the thesis research as well as recommendations for future studies are summarized.

7.1 Conclusions

An ionospheric modeling system based on the tomographic technique using GPS measurements from operational GPS reference networks has been developed. Unlike other ionospheric modeling methods, the model proposed in this dissertation is constructed on the basis of multiple-layers in a three-dimensional (3D) mode, which can overcome the limitations in current two-dimensional (2D) modeling methods. The scientific significances of 3D ionospheric modeling are twofold. First, it enables the description of the ionospheric electron field in multiple layers instead of a single ionospheric shell. Second, the variable to be modeled by the tomographic method is the electron density rather than the total electron content (TEC). The modeling of the electron density provides a more convenient quantitative basis for other ionosphere-related research than the modeling of TEC quantities. The model also overcomes the drawbacks associated with previous tomographic modeling methods. The modeling system proposed in this thesis has established, for the first time, the link between the smoothed TEC data and function-based tomographic model through a close form analytical expression, which allows the smoothing of TEC data and the estimation of ionospheric model to be carried out simultaneously. The estimation of tomographic model is conducted on an epoch-by-

epoch and station-by-station basis, which can significantly reduce the data processing time as well as the requirement for computational resources. For satellite and receiver inter-frequency bias estimation, a pseudo TEC observation has been introduced to establish a reference.

The methods and algorithms that have been developed in this study have been successfully implemented in a software package “IonoTomo”. This software package can perform ionospheric modeling using the data from GPS reference networks and the software can also perform ionospheric TEC predictions based on the tomographic model parameters. The TEC prediction intervals can be set to 5-min, 10-min or 30-min, with different choice of elevation cutoff angles.

Three quantitative indicators have been developed to assess the performance of the ionospheric TEC predictions based on the tomographic model. For the first quantitative indicator, the predicted TEC data are compared with the observed TEC data and their differences are mapped to the zenith direction. An RMS value is then calculated for the vertical TEC differences. This RMS value is an important indicator to evaluate the agreement between the predicted TEC and the measured TEC. In the second quantitative indicator, a relative error indicator has been proposed, which is determined by dividing the differences between the predicted TEC and the observed TEC data by the measured TEC value. The relative error provides a quantitative measure to assess the prediction errors relative to the total TEC. The third quantitative indicator is used to assess the ionosphere recovering efficiency. The recovering efficiency is defined to describe the efficiency of the tomographic model in correcting the effects due to ionospheric refraction errors on the GPS positioning and navigation results. A combination of the above three evaluation indicators can provide a complete assessment on the performance of the proposed ionosphere tomographic model.

The developed function-based tomographic modeling system has been applied to a local area GPS reference network and a wide area GPS reference network with data acquired under different ionospheric conditions including extremely high level of ionospheric activities ($K_p=8\sim 9$). Similar work has not been done in the past and the data analysis results are summarized in the following.

In the local area GPS network with data acquired under quiet ionospheric activities, performance analysis has been conducted at all network stations (the station data included for both ionospheric modeling and performance analysis) using different elevation cutoff angles, namely low cutoff angle 15° , medium cutoff angle 20° and high cutoff angle 25° . The data analysis results using 15° , 20° or 25° cutoff angle show that the TEC prediction accuracy is better than 2.9 TECU in vertical and that the relative error is about 4.5% in slant TEC for both 5-min and 10-min predictions. For 30-min predictions, the VTEC accuracy is better than 3.8 TECU and slant TEC relative error is about 6.0%. The analysis results indicate that the predicted TEC values in the local area GPS network agree very well with the observed TEC values. The prediction accuracy has a small degradation when the prediction interval is increased from 5-min to 30-min. The degradation is about 0.8 TECU when the elevation cutoff is 15° . The prediction accuracy is not affected much by the change of the elevation cutoff angle. When the TEC predictions obtained at 15° cutoff angle are used to single point positioning, the results show that a recovering efficiency of 98% can be achieved using predicted TEC corrections over a 5-min or 10-min interval. With a prediction interval of 30-min, the predicted TEC have a recovering efficiency better than 92%.

A performance analysis has also been conducted at independent user stations (the station data not included for ionospheric modeling). For TEC predictions using 15° cutoff angle, the 5-min, 10-min and 30-min vertical prediction TEC RMS errors are 3.5 TECU, 4.3 TECU and 5.9 TECU, respectively. The relative errors using the above three prediction intervals are 4.77%, 6.04% and 8.70%, respectively. The research results show that more

than 90% ionospheric range delays could be predicted. The TEC predictions are evaluated with respect to single point positioning and the results show that 5-min and 10-min predictions have a recovering efficiency of 86.06% and 77.79%, respectively. The 30-min predictions have a recovering efficiency of 59.53%.

Similar performance analysis has been conducted using data from a wide area GPS reference network acquired under both ionosphere quiet and disturbed conditions. Different data analysis schemes have been implemented to analyze the performance of the proposed tomographic model under different computational scenarios. For data analysis at all network stations (station data included for both ionospheric modeling and performance analysis), the TEC predictions obtained at 5-min or 10-min prediction interval using 15° , 20° or 25° cutoff angle have an accuracy of about 3.5 TECU in vertical TEC and a relative error better than 13% in slant TEC during ionosphere quiet time periods. With a 30-min prediction interval, the TEC predictions with different cutoff angles have an accuracy of 4.0 TECU in vertical TEC and a relative error better than 15% in slant TEC. Applying the TEC predictions obtained at 15° cutoff angle to single point positioning shows that a recovering efficiency of 92% can be achieved using predictions with 5-min or 10-min intervals. For an interval of 30-min, the predictions have a recovering efficiency of better than 89%. For performance analysis conducted at independent stations (the station data not included in ionospheric modeling), the 5-min predictions with a cutoff angle 15° have a vertical RMS of 5.0~5.8 TECU and a relative error of 7.51~34.21%, during ionospheric quiet time periods. The 10-min predictions have a vertical RMS of 5.0~5.8 TECU and a relative error of 7.55~34.84%. The 30-min predictions have a vertical TEC prediction accuracy of 5.5~5.9 TECU and a relative error of 7.62~34.74%. Application of the TEC predictions obtained at 15° cutoff angle to single point positioning indicates that a recovering efficiency of 70.22~77.35%, 67.28~77.67% and 66.69~68.54% can be achieved with prediction intervals of 5-min, 10-min and 30-min, respectively.

During the ionospheric disturbed period, the TEC predictions (station data included for both ionospheric modeling and performance analysis) obtained at 5-min or 10-min prediction interval using 15° , 20° or 25° cutoff angle have an accuracy of better than 4.9 TECU in vertical TEC and a relative error about 21% in slant TEC. With a 30-min prediction interval, the TEC predictions have an accuracy of about 5.5 TECU in vertical TEC and a relative error about 25% in slant TEC. Single point positioning using predicted TEC corrections obtained at 15° cutoff angle show that a recovering efficiency of 64~66% can be achieved with a prediction interval of 5-min or 10-min or 30-min. On the other hand, the TEC predictions at independent stations (station data not included for ionospheric modeling) indicates that during ionospheric disturbed periods the 5-min predictions with a cutoff angle of 15° have a vertical RMS 5.2~5.9 TECU and a relative error of 8.09~46.30%. The 10-min predictions have a vertical RMS 5.4~6.1 TECU and a relative error of 8.46~48.21% while the 30-min predictions have a vertical TEC prediction accuracy of 5.8~6.7 TECU and a relative error of 9.81~51.62%. Applying the TEC predictions obtained at a cutoff angle of 15° to single point positioning, the results show that a recovering efficiency of 62.39~65.09%, 62.16~64.75% and 52.39~64.71% can be achieved with prediction intervals of 5-min, 10-min and 30-min, respectively.

In summary, the data analysis results indicate that the TEC predictions during ionospheric quiet and disturbed periods in a wide area GPS network have a good agreement with observed TEC values. The results indicate that the increase of the elevation cutoff angle from 15° to 20° and 25° , the model prediction accuracies have a small improvement during both ionosphere quiet and disturbed periods. But this improvement is not significant. The analysis results have indicated that accurate TEC predictions can be obtained from the tomographic model even under severe ionospheric conditions.

7.2 Recommendations

The research work in this dissertation has demonstrated the feasibility of the tomographic modeling technique for precise ionospheric modeling using GPS reference network data. In the future research, the following work should be further investigated:

- 1) Recently some GPS reference networks have attempted to broadcast high-frequency (1 Hz) real-time GPS data to the GPS users. The high-frequency GPS data are able to provide a high-resolution capture of the activities of ionosphere. The ionospheric modeling using the high-frequency GPS data therefore could potentially deliver higher modeling accuracies and provide a better temporal description of the ionospheric activities. In the future, the work of employing high-frequency GPS data sets to construct ionospheric modeling should be conducted.
- 2) The variations of the ionospheric electron density in the time and space domains should be investigated. For the study of ionospheric characteristics, the determination of temporal and spatial variations of the electron density is of special significance. The three-dimensional description of the ionospheric electron density field developed in this thesis would help characterize the ionospheric spatial structure and its variations. In time domain, the ionospheric data observation interval will determine the description of temporal variations. As indicated by the data analysis, the model can characterize the ionospheric variation with variable temporal scales, from 5-min to 30-min. If high-frequency GPS data are employ as suggested in 1), the ionospheric TEC data prediction can correspondingly be performed at a high frequency. In spatial domain, the analysis results showed that the ionospheric model performs well in both local area with dense GPS receiver distribution and wide area GPS network with sparse GPS receiver distribution.
- 3) The 3D ionospheric modeling and analysis has been successfully performed with local area and wide area GPS network data sets. In the future studies, an investigation

should be conducted with respect to global GPS networks to investigate the global characteristics of ionosphere.

- 4) An advantage that the ionospheric tomographic modeling has is its easy assimilation of various TEC data sources into the model. At present time, the ionospheric modeling is based on the TEC data derived from GPS networks. In the future, the synthesis of multiple types of TEC data should be considered. The integration of various TEC data will be beneficial to the enhancement of the modeling accuracy and spatial resolution.

- 5) For ionospheric modeling in either local area GPS network or wide area GPS network, the comprehensive analysis results show that use of 15° elevation cutoff in GPS data edition and ionospheric modeling is the recommended in consideration of both the obtainable TEC prediction accuracy at this cutoff angle and the fact that more prediction data can be obtained at this elevation. Analysis results indicate that either 5-min or 10-min interval can be used in short-term TEC prediction, either of which should be sufficient to serve the positioning purpose for single frequency GPS users.

REFERENCES

Aaron, J. and S. Basu (1994). Ionospheric Amplitude & Phase Fluctuations at the GPS Frequencies, Proceedings of The Institute of Navigation GPS-94, Salt Lake City, Utah, 1994, 1569-1578.

Akasofu, S.I. (1998). Aurora, in the book "From the Sun: Auroras, Magnetic Storms, Solar Flares, Cosmic Rays, edited by S.T. Suess and B.T. Tsurutani, American Geophysical Union, 1998, 172.

Alves, P., G. Lachapelle, M.E. Cannon, J. Park and P. Park (2002). Use of Self-contained Ionospheric Modeling to Enhance Long Baseline Multiple Reference Station RTK Positioning, Proceedings of ION GPS 2002, September 24-27, 2002, Portland, Oregon, 1388-1399.

Baker, D.N. (1986). Statistics Analyses in the Study of Solar Wind-Magnetosphere Coupling, in Kamide, Y. and Slavin, J.A. (eds): Solar-Wind-Magnetosphere Coupling, Terra Scientific Publishing Co., Tokyo.

Bilitza, D. (2001). International Reference Ionosphere 2000, Radio Science, Vol. 36, No. 2, 261-275.

Bishop, G.J., J.A. Klobuchar and P.H. Doherty (1985). Multipath Effects on the Determination of Absolute Ionospheric Time Delay from GPS Signals, Radio Science, Vol. 20, No. 3, 388-396.

Björnsson, H. and S.A. Veregas (1997). A manual for EOF and SVD Analyses of Climate Data, Department of Atmospheric and Oceanic Sciences and Centre for Climate and Global Change Research, McGill University, February, 1997, 53.

Bock, Y. (1998). Reference Systems, in GPS for Geodesy, edited by Peter J.G. Teunissen and Alfred Kleusberg, 2nd Edition, Springer-Verlag, 1998.

Brown, R.G. (1983). Introduction to Random Signal Analysis and Kalman Filtering, John Wiley and Sons Inc., 1983, 347.

Campbell, W.H. (2003). Introduction to Geomagnetic Fields, 2nd edition, Cambridge university press, pp.337.

Cander, L.R. (1993). On the Global and Regional Behaviour of the Mid-latitude Ionosphere, J. Atmos. Terr. Phys., 55, 1543-1551.

Cander, L.R. and S.J. Mihajlovic (1998). Forecasting Ionospheric Structure during the Great Geomagnetic Storms, J. Geophys. Res., 103, 391-398.

Cleveland, F., W. Malcolm, D.E. Nordell and J. Zirker (1992). Solar Effects on Communications, IEEE Transactions on Power Delivery, Vol. 7, No. 2, 460-468.

Colombo, O.L., M. Hernández-Pajares, J.M. Juan and J. Sanz (2002). Wide-Area, Carrier-Phase Ambiguity Resolution Using a Tomographic Model of the Ionosphere, Navigation, Journal of Institute of Navigation, Vol. 49, No. 1, Spring 2002, 61-69.

Colombo, O.L., M. Hernandez-Pajares, J.M. Juan and J. Sanz (2000). Ionospheric Tomography Helps Resolve GPS Ambiguities On The Fly At distances Of Hundreds Of

Kilometers During Increased Geomagnetic Activity, Proceedings of the IEEE PLANS-2000 Symposium, San Diego, CA., March 2000.

Colombo, O.L., M. Hernández-Pajares, J.M. Juan, J. Sanz and J. Talaya (1999). Resolving Carrier-Phase Ambiguities On The Fly, At More Than 100 km From Nearest Reference Site, With The Help Of Ionospheric Tomography, Proceedings of ION GPS-99, Nashville, USA, September, 1999, 1635-1642.

Conker, R.S., M.B. El-Arini, C.J. Hegarty and T. Hsiao (2003). Modeling the Effects of Ionospheric Scintillation on GPS/Satellite-Based Augmentation System Availability, Radio Science, Vol. 38, No. 1.

Coster, A.J., E.M. Gaposchkin and L.E. Thornton (1992). Real-time ionospheric monitoring system using GPS. Navigation, Journal of Institute of Navigation, Vol.39, No.2, 191-204.

Coster, A.J., J. Foster and P. Erickson (2003). Monitoring the Ionosphere with GPS: Space Weather, GPS World, 14 (5), 42-49, 2003.

Cowley, S.W.H. (1998). The Earth's Magnetosphere, in the book "From the Sun: Auroras, Magnetic Storms, Solar Flares, Cosmic Rays, edited by S.T. Suess and B.T. Tsurutani, American Geophysical Union, 1998, 172.

Davies, K. (1990). Ionospheric Radio, Peter Peregrinus Ltd., 1990, 580.

Doherty, P.H., T. Dehel, J.A. Klobuchar, S.H. Delay, S. Datta-Barua, E.R. de Paula and F.S. Rodrigues (2002). Ionospheric Effects on Low-Latitude Space Based Augmentation Systems, Proceedings of ION GPS 2002, September 24-27, 2002, Portland, Oregon, 1321-1329.

El-Arini, M.B., C.J. Hegarty, J.P. Fernow and J.A. Klobuchar (1994). Development of an Error Budget for a GPS Wide-Area Augmentation System (WAAS), Proceedings of The Institute of Navigation NTM-94, San Diego, CA, January, 1994.

El-Arini, M.B., P.A. O'Donnell, P. Kellam, J.A. Klobuchar, T.C. Wisser and P.H. Doherty (1993). The FAA Wide Area Differential GPS (WADGPS) Static Ionospheric Experiment, Proceedings of the Institute of Navigation NTM-93, San Francisco, CA, January, 1993.

El-Arini, M.B., R.S. Conker, T.W. Albertson, J.K. Reagan, J.A. Klobuchar, and P.H. Doherty (1995). Comparison of Real-Time Ionospheric Algorithms for a GPS Wide-Area Augmentation System (WAAS), *Navigation: Journal of The Institute of Navigation*, Vol. 41, No. 4, Winter 1994-1995, 393-413.

El-Arini, M.B., W.A. Poor, R.O. Lejeune, R.S. Conker, J. Fernow and K.R. Markin (1999). An Introduction to WAAS and Its Predicted Performance, Proceedings of Ionospheric Effects Symposium, IES1999, Alexandria, Virginia, May 4-6, 1999, 211-220.

El-Gizawy, M. and S. Skone (2002). A Canadian Ionospheric Warning and Alert System, Proceedings of the Institute of Navigation GPS, Portland, Oregon, USA, Sept. 2002, 1345-1352.

FAA (1997). Specification for the Wide Area Augmentation System, FAA-E-2892C (draft), 1997.

Flores, A., G. Ruffini and A. Rius (2000). 4D tropospheric tomography using GPS slant wet delays, *Annales Geophysicae*, 18, 223-234.

Fu, W., S. Han, C. Rizos, M. Knight and A. Finn (1999). Real-Time Ionospheric Scintillation Monitoring, Proceedings of Institute of Navigation GPS-99, Nashville Convention Center, Nashville, Tennessee, USA, September 14-17, 1999.

Gail, W.B., A.B. Prag, D.S. Coco and C. Coker (1993) A Statistical Characterization of Local Mid-Latitude Total Electron Content, Journal Geophysical Research, 98 (A9), 15,717-15,727.

Gao, Y., P. Heroux and J. Kouba (1994). Estimation of GPS Receiver and Satellite L1/L2 Signal Delay Biases Using Data from CACS, Proceedings of KIS-94, Banff, Canada, Aug. 30 – Sep. 2, 1994.

Gao, Y., X. Liao and Z.Z. Liu (2002a). Ionosphere Modeling Using Carrier Smoothed Ionosphere Observations from a Regional GPS Network, Geomatica, Vol. 56, No. 2, 97-106.

Gao, Y. and Z.Z. Liu (2002). Precise Ionosphere Modeling Using Regional GPS Network Data, Journal of Global Positioning Systems, Vol. 1, No. 1, 18-24.

Gao, Y., Z.Z. Liu and M. Abdel-Salam (2002b). GPS Receiver Benchmarking, Research Report, Department of Geomatics Engineering, The University of Calgary, 76.

Giannini, J.A. and C.C. Kilgus (1997). A Fuzzy Logic Technique for Correcting Climatological Ionospheric Models, IEEE Transactions on Geoscience and Remote Sensing, Vol. 35, No. 2, March 1997, 470-474.

Giraud, A. and M. Petit (1978). Ionospheric Techniques and Phenomena, published by D. Reidel Publishing Company, Dordrecht, Holland, 264.

Goodman, J.M. and J. Aarons (1990). Ionospheric Effects on Modern Electronic Systems, Proceedings of the IEEE, Vol. 78, No. 3, March 1990, 512-528.

Gulyaeva T.L. (2001). Application of the Plasmasphere-ionosphere Model for Short-term forecasting of Total Electron Content, Proceedings of Space Weather Workshop: Looking Towards a European Space Weather Programme, December 17-19, 2001, Noordwijk, The Netherlands.

Hansen, A.J. (1998). Real-time Ionospheric Tomography Using Terrestrial GPS Sensors, Proceedings of Institute of Navigation GPS-98, Nashville, Tennessee, September, 1998, 717-727.

Hansen, A.J., T. Walter and P. Enge (1997). Ionospheric Correction Using Tomography, Proceedings of 10th International Technical Meeting of the Satellite Division of the Institute of Navigation, ION GPS-97, September 16-19, 1997, Kansas City, Missouri, USA, 249-260.

Hargreaves, J.K. (1992). The Solar-terrestrial Environment, Cambridge University Press, 1992, 420.

Hernández-Pajares, M.(2003). Performance of IGS Ionosphere TEC Maps, IGS IONO Working Group Report, Research group of Astronomy and Geomatics, Technical University of Catalonia (gAGE/UPC), Barcelona, Spain, pp.16.

Hernández-Pajares, M., J.M. Juan and J. Sanz (1999). New Approaches in Global Ionospheric Determination Using Ground GPS Data, Journal of Atmospheric and Solar-Terrestrial Physics, 61, 1237-1247, 1999.

Hernández-Pajares, M., J.M. Juan, J. Sanz, O.L. Colombo (2000). Application of Ionospheric Tomography to Real-Time GPS Carrier Phase Ambiguities Resolution, at Scales of 400-1000

km and With High Geomagnetic Activity, *Geophysical Research Letters*, Vol. 27, No. 13, 2009-2012, 1 July 2000.

Hopfield, H.S. (1969). Two-quartic Tropospheric Refractivity Profile for Correcting Satellite Data, *Journal of Geophysical Research*, Vol. 74, No. 18, 4487-4499.

Howe, B.M. (1997). 4-D Simulations of Ionospheric Tomography, *Proceedings of Institute of Navigation National Technical Meeting*, Santa Monica, California, January 14-16, 1997, 269-278.

Howe, B.M., K. Runciman and J.A. Secan (1998). Tomography of Ionosphere: Four-Dimensional Simulations, *Radio Science*, Vol. 33, No. 1, 109-128.

Hu, G., V.H.S. Khoo, P.C. Goh and C.L. Law (2002). Performance of Singapore Integrated Multiple Reference Station Network (SIMRSN) for RTK Positioning, *GPS Solutions*, Vol. 6, No.1-2, 65-71.

Huang, Y.N. and K. Cheng (1991). Ionospheric Disturbances at the Equatorial Anomaly Crest Region during the March 1989 Magnetic Storm, *Journal of Geophysics Research*, 96(A8): 13953-13965.

IGSCB (2004). <http://igsceb.jpl.nasa.gov/components/prods.html>, accessed on January 17, 2004.

ION (2004). <http://ion.le.ac.uk/ionosphere/profile.html>, accessed on March 2, 2004.

Jackson, M. E., C. Meertens, O. Ruud, S. Reeder, W. Gallaher, and C. Rocken (2002), Real-time GPS data transmission using VSAT technology, *GPS Solutions*, Vol. 5, No. 4, 10-19.

Janes, H.W., R.B. Langley and S.P. Newby (1989). A Comparison of Several Models for the Prediction of Tropospheric Propagation Delay, Proceedings of the fifth international geodetic symposium on satellite positioning, Las Cruces, New Mexico, March 13-17, 1989, Vol. 2: 777-788.

Joselyn, J.A. (1998). The Human Impact of Solar Flares and Magnetic Storms, in the book "From the Sun: Auroras, Magnetic Storms, Solar Flares, Cosmic Rays, edited by S.T. Suess and B.T. Tsurutani, American Geophysical Union, 172.

Kamide, Y. and W. Baumjohann (1993). Magnetosphere-Ionosphere Coupling, Springer-Verlag, Berlin Heidelberg, 1993, 175.

Kappernman, J.G. and V.D. Albertson (1990). Bracing for the geomagnetic storms, IEEE Spectrum, Vol.27, No.3, 27-33.

Kasha, M.A. (1969). The Ionosphere and its Interaction with Satellites, Gordon and Breach, Science publishers Inc. New York, 156.

Kelley, M.C. (1989). The Earth's Ionosphere: Plasma Physics and Electrodynamics, Academic Press Inc., 487.

Kleusberg, A. (1993). The Global Positioning System and Ionospheric Conditions, Solar Predictions-IV Workshop, Ottawa, Canada, May 18-22, 1992, NOAA/Dept. of Commerce Pub., Vol. 1, pp.142-146, 1993.

Klobuchar, J.A. (1975). A First-order Worldwide Ionospheric Time Delay Algorithm, Air Force Cambridge Research Laboratories, Hanscom, AFB, MA, AFCRL-TR-75-0502, AD A018862.

Klobuchar, J.A. (1986). Design and Characteristics of the GPS Ionospheric Time Delay Algorithm for Single-Frequency Users, Proceedings of the PLANS-86 conference, Las Vegas, NV, November 4-7, 1986, 280-286.

Klobuchar, J.A. (1987). Ionospheric Time-Delay Algorithm for Single-Frequency GPS Users, IEEE Transactions on aerospace and electronic systems, Vol. AES-23, No.3, 325-331.

Klobuchar, J.A. (1996). Ionospheric effects on GPS, in Global Positioning System: Theory and Applications, Volume I, edited by Bradford W. Parkinson and James J. Spilker Jr., American Institute of Aeronautics and Astronautics, Washington, DC.

Knight, M., M. Cervera and A. Finn (1999). A Comparison of Predicted and Measured GPS Performance in an Ionospheric Scintillation Environment, Proceedings of ION GPS-99, September 14-17, Nashville, TN, 1437-1450.

Komjathy, A. (1997). Global Ionospheric Total Electron Content Mapping Using the Global Positioning System, Ph.D. dissertation, Department of Geodesy and Geomatics Engineering Technical Report NO. 188, University of New Brunswick, Fredericton, New Brunswick, Canada, 248.

Komjathy, A., L. Sparks, T. Mannucci and X. Pi (2002). An Assessment of the Current WAAS Ionospheric Correction Algorithm in the South American Region, Proceedings of ION GPS 2002, Portland, Oregon, September 24-27, 2002, 1286-1296.

Komjathy, A. and R.B. Langley (1996). An Assessment of Predicted and Measured Ionospheric Total Electron Content Using a Regional GPS Network, Proceedings of the National Technical Meeting of the Institute of Navigation, Santa Monica, CA, January 22-24, 1996, 615-624.

Lachapelle, G. (2000). GPS Theory and Applications, Department of Geomatics Engineering, The University of Calgary, Calgary, Alberta, Canada, Fall 2000.

Langley, R.B. (1998a). Propagation of the GPS Signals, in GPS for Geodesy, 2nd Edition, edited by P. J. G. Teunissen and A. Kleusberg, Springer-Verlag Berlin Heidelberg.

Langley, R.B. (1998b). GPS Receivers and the Observables, in GPS for Geodesy, 2nd Edition, edited by P. J. G. Teunissen and A. Kleusberg, Springer-Verlag Berlin Heidelberg.

Lanyi, G. (1984). Tropospheric Calibration in Radio Interferometry, Proceedings of the International Symposium on Space Techniques for Geodynamics, Sopron, Hungary, July 9-13, Vol 2, 184-195.

Leitinger, R., G. Schmidt and A. Taurianien (1975). An Evaluation Method Combining the Differential Doppler Measurements from Two Stations that Enables the Calculation of the Electron Content of the Ionosphere. J. of Geophys. Res., 41, 201-213.

Liao, X. (2000). Carrier Phase Based Ionosphere Recovery Over A Regional Area GPS Network, UCGE Reports, Number 20143, University of Calgary, Calgary, Alberta, Canada, 120.

Liao, X. and Y. Gao (2001). High-Precision Ionospheric TEC Recovery Using a Regional-Area GPS Network, Navigation, Vol. 48, No. 2, Summer, 2001, 101-111.

Liu, Z.Z. and Y. Gao (2001a). Ionospheric Tomography Using GPS Measurements, Proceedings of the International Symposium on Kinematic Systems in Geodesy, Geomatics and Navigation, Banff, Alberta, Canada, June 5-8, 2001, 111-120.

Liu, Z.Z. and Y. Gao (2001b). Optimization of Parameterization in Ionospheric Tomography, Proceedings of Institute of Navigation GPS 2001, Salt Lake City, Utah, USA, September 11-14, 2001, 2277-2285.

Liu, Z.Z. and Y. Gao (2002). Performance Analysis of A 3D Ionosphere Tomographic Model, Proceedings of 2002 International Symposium on GPS/GNSS, the 9th GNSS Workshop, Wuhan, China, November 6-8, 2002.

Loh, R., V. Wulschleger, B. Elrod, M. Lage and F. Haas (1995). The U.S. Wide-Area Augmentation System (WAAS), Navigation: Journal of The Institute of Navigation, Vol. 42, No. 3, Fall 1995, 435-465.

Lyon, J.G. (2000). The Solar Wind-Magnetosphere-Ionosphere System, Science, Vol. 288 Issue 5473.

Malys, S. and J. Slater (1994). Maintenance and Enhancement of the World Geodetic System 1984, Journal of Institute of Navigation, 41, 17-24.

Mannucci, A.J., B. Wilson and C. Edwards (1993). A New Method for Monitoring the Earth's Ionospheric Total Electron Content Using the GPS Global Network, Proceedings of the ION GPS-93, Salt Lake City, Utah, September, 1993, 1323-1332.

Mendes, V.B. (1999). Modelling the Neutral-atmosphere Propagation Delay in Radiometric Space Techniques, Ph.D. dissertation, Department of Geodesy and Geomatics Engineering, Technical Report no. 199, University of New Brunswick, Fredericton, New Brunswick, Canada.

Nichols, J., A. Hansen, T. Walter and P. Enge (2000). High-latitude Measurements of Ionospheric Scintillation Using the NSTB, *Navigation, Journal of The Institute of Navigation*, Vol.47, No. 2, Summer, 2000, 112-120.

Nicholson, N., V. Hoyle, S. Skone, M.E. Cannon, G. Lachapelle (2003). 4-D Troposphere Modeling Using a Regional GPS Network in Southern Alberta, *Proceedings of ION GPS 2003*, Portland, Oregon, September 9-12, 2003, 1718-1727.

NRL (2003). <http://server5550.itd.nrl.navy.mil/projects/HAARP/ion1.html>, accessed on January 13, 2003.

Parkinson, B.W. (1996a). Introduction and Heritage of NAVSTAR, the Global Positioning System, in *Global Positioning System: Theory and Applications, Volume I*, edited by Bradford W. Parkinson and James J. Spilker Jr., American Institute of Aeronautics and Astronautics, Washington, DC.

Parkinson, B.W. (1996b). GPS Error Analysis, in *Global Positioning System: Theory and Applications, Volume I*, edited by Bradford W. Parkinson and James J. Spilker Jr., American Institute of Aeronautics and Astronautics, Washington, DC.

Parkinson, B.W. and P.K. Enge (1996). Differential GPS. in *Global Positioning System: Theory and Applications, Volume II*, edited by Bradford W. Parkinson and James J. Spilker Jr., American Institute of Aeronautics and Astronautics, Washington, DC.

Parks, G.K. (1991). *Physics of Space Plasmas*, Addison-Wesley Publishing Company, 538.

Plasma (2003). www.plasma.org accessed on February 05, 2003.

Preisendorfer, R.W. and C.D. Mobley (1988). *Principal Component Analysis in Meteorology and Oceanography*. Elsevier, Amsterdam, Oxford, New York, Tokyo, 425.

Raymund, T.D. (1995). Comparisons of Several Ionospheric Tomography Algorithms. *Annales Geophysicae*, Vol. 13, No. 12, 1254-1262.

Raymund, T.D., J.R. Austen, S.J. Franke, C.H. Liu, J.A. Klobuchar and J. Stalker (1990). Application of Computerized Tomography to the Investigation of Ionospheric Structures, *Radio Science*, 25(5), 771-789.

Raymund, T.D., Y. Bresler, D.N. Anderson and R.E. Daniell (1994). Model-assisted Ionospheric Tomography: A new algorithm. *Radio Science*, 29(6), 1493-1512.

Rho, H. and R.B. Langley (2002). Assessment of WAAS Correction Data in Eastern Canada, *Proceedings of Ionospheric Effects Symposium, IES2002, Alexandria, Virginia, 7-9 May 2002*.

Richmond, A.D. (1998). The Ionosphere and Upper Atmosphere, in the book "From the Sun: Auroras, Magnetic Storms, Solar Flares, Cosmic Rays, edited by S.T. Suess and B.T. Tsurutani, American Geophysical Union, 1998, 172.

Ros, E., J.M. Marcaide, J.C. Guirado, M.I. Ratner, I.I. Shapiro, T.P. Krichbaum, A. Witzel and R.A. Preston (1999). High Precision Difference Astrometry Applied to the Triplet of S5 Radio Sources B1803+784/Q1928+738/B2007+777, *Astronomy and Astrophysics*, 348, 381-393.

RTCA (1998). *Minimum Operational Performance Standards for Global Positioning System/Wide Area Augmentation System Airborne Equipment*, Document No. RTCA/DO-229A, Prepared by SC-159, RTCA, inc., Washington, DC, June 8, 1998.

Russell, C.T. (1987). The Magnetosphere, in: Akasofu SI, Kamide Y (eds) The Solar Wind and the Earth. Reidel, Dordrecht, 71.

Saastamoinen II (1973). Contribution to the Theory of Atmospheric Refraction, Bulletin Géodésique, 107, 13-34.

Schaer, S. (1999). Mapping and Predicting the Earth's Ionosphere Using the Global Positioning System, Ph.D dissertation, Astronomical Institute, University of Berne, Switzerland, 205.

Schunk, R.W. and A. F. Nagy (2000). Ionospheres: Physics, Plasma Physics, and Chemistry, Cambridge University Press, 554.

Schwarz, K.P. and M. Wei (2000). INS/GPS Integration for Geodetic Applications, The Department of Geomatics Engineering, University of Calgary, Calgary, Alberta, Canada, May 2000, 111.

Seeber, G. (1993). Satellite Geodesy: Foundations, Methods, and Applications, Walter de Gruyter, Berlin and New York, 531.

Skone, S. (1998). Wide Area Ionosphere Grid Modeling in the Auroral Region, UCGE Reports Number 20123, Ph.D thesis, The University of Calgary, Calgary, Alberta, Canada.

Skone, S. (2001). The Impact of Magnetic Storms on GPS Receiver Performance, Journal of Geodesy, 75, 457-268.

Skone, S. and K. Knudsen (2000). Impact of Ionospheric Scintillations on SBAS Performance, Proceedings of Institute of Navigation, ION GPS-2000, Salt Lake City, Utah, September 19-22, 2000, 284-293.

Skone, S. and S.M. Shrestha (2003). 4-D Modeling of Water Vapour using a Regional GPS Network, Proceedings of ION National Technical Meeting, Anaheim, CA, 22-24 January 2003, 809-816.

Skone S., V. Hoyle, S. Lee and S. Poon (2002). Variations in Point Positioning Accuracies for Single Frequency GPS Users during Solar Maximum, *Geomatica*, Vol. 56, No. 2, 131-140.

Spilker Jr., J.J. (1996a). GPS Navigation Data, in *Global Positioning System: Theory and Applications, Volume I*, edited by Bradford W. Parkinson and James J. Spilker Jr., American Institute of Aeronautics and Astronautics, Washington, DC.

Spilker Jr., J.J. (1996b). Tropospheric Effects on GPS, in *Global Positioning System: Theory and Applications, Volume I*, edited by Bradford W. Parkinson and James J. Spilker Jr., American Institute of Aeronautics and Astronautics, Washington, DC.

Spilker Jr., J.J. (1996c). GPS Signal Structure and Theoretical Performance, in *Global Positioning System: Theory and Applications, Volume I*, edited by Bradford W. Parkinson and James J. Spilker Jr., American Institute of Aeronautics and Astronautics, Washington, DC.

Spilker Jr, J.J. and B.W. Parkinson (1996). Overview of GPS Operation and Design, in *Global Positioning System: Theory and Applications, Volume I*, edited by Bradford W. Parkinson and James J. Spilker Jr., American Institute of Aeronautics and Astronautics, Washington, DC.

Stankov, S.M., I.S. Kutiev, N. Jakowski, A. Wehrenpfennig (2001). A New Method for Total Electron Content Forecasting Using Global Positioning System Measurements, Proceedings

of Space Weather Workshop: Looking Towards a European Space Weather Programme, December 17-19, 2001, Noordwijk, The Netherlands.

Svensson, C. (1999). Empirical Orthogonal Function Analysis of Daily Rainfall in the Upper Reaches of the Huai River Basin, China, *Theoretical and Applied Climatology*, 62, 147-161.

Tsurutani, B.T. and W.D. Gonzalez (1998). Magnetic Storm, in the book "From the Sun: Auroras, Magnetic Storms, Solar Flares, Cosmic Rays, edited by S.T. Suess and B.T. Tsurutani, American Geophysical Union, 1998, 172.

USNO (2003) <ftp://tycho.usno.navy.mil/pub/gps/gpssy.txt>, accessed on January 06, 2003.

UTK (2003a). <http://csep10.phys.utk.edu/astr161/lect/earth/magnetic.html>, accessed on January 15, 2003.

UTK (2003b). <http://csep10.phys.utk.edu/astr161/lect/earth/magnetic.html>, accessed on January 15, 2003.

Walker, J.K. (1989). Spherical Cap Harmonic Modeling of High Latitude Magnetic Activity and Equivalent Sources with Sparse Observations, *Journal of Atmospheric and Terrestrial Physics*, Vol.51, No.2, 1989, 67-80.

Wells, D.E., N. Beck, D. Delikaraoglou, A. Kleusberg, E.J. Krakiwsky, G. Lachapelle, R.B. Langley, M. Nakiboglu, K.P. Schwarz, J.M. Tranquilla, and P. Vanicek (1987). *Guide to GPS Positioning*. Canadian GPS Associates, Fredericton, New Brunswick, Canada, 2nd edition, 600.

Xenos, Th.D., S.S. Kouris and A. Casimiro (2003). Time-dependent Prediction Degradation Assessment of Neural-networks-based TEC Forecasting Models, *Nonlinear Processes in Geophysics*, Vol. 10, 585–587.